

Nighttime radical NO_x chemistry by CRD

Justin Shenolikar

Max Planck Institute for Chemistry
Mainz, Germany

SEPTEMBER 2020

Abstract

The following work presents measurements of NO_2 , NO_3 , N_2O_5 , and organic nitrates (ΣPNs ($\text{R}(\text{O})\text{O}_2\text{NO}_2$; and ΣANs (RONO_2)) made by 3 years of measurements by a 5-channel cavity ringdown spectroscopy (5-CRD) instrument over the course of two field campaigns and multiple laboratory experiments. The results of these two campaigns are discussed within.

The 2017 AQABA ship campaign reports measurements of NO_2 , NO_3 and N_2O_5 from a mixture of highly-polluted and clean marine environments around the Arabian Peninsula and eastern Mediterranean Sea. NO_3 and N_2O_5 mixing ratios over the detection limits seen over 30 of a possible 60 nights during the nights, with mixing ratios of 12 ± 18 ppt for NO_3 (max: 146 ppt) and 23 ± 35 ppt (max: 295 ppt) for N_2O_5 , respectively. This corresponds to a median NO_3 lifetime of 65.5 seconds ($\sim 0.0153 \text{ s}^{-1}$ reactivity) across the entire campaign, although this was found to be highly variable according to the region. DMS was found to be the single largest contributor (20 – 25%) in each region to controlling the lifetime of NO_3 , though reactions with anthropogenic VOCs, while generally negligible were a regionally important sink in the Persian Gulf. Heterogeneous uptake onto the surface of particles was limited by high temperatures and contributed only a small fraction to reactivity ($\sim 5\%$). Most reactivity (40 – 80%, depending on region) could not be accounted for in the measurements made during AQABA, though an analysis within suggests that ship emissions may contribute strongly to this and shows that SO_2 can be used marker to estimate reactivity.

Results further suggest that nighttime removal of NO_x was considerably more efficient (factor 2 – 3) than during the day in 4 out of 5 of the AQABA regions, despite longer days, high $[\text{OH}]$ concentrations and approximately similar NO_2 loss rates with OH and O_3 .

The 2018 SAPHIR campaign reports measurements of NO_2 , NO_3 , N_2O_5 , ΣPNs and ΣANs from a series of chamber experiments studying the reaction of NO_3 + isoprene. Measurements of NO_2 , NO_3 and N_2O_5 are presented in a statistical intercomparison against other instruments. NO_2 measurements from three instruments, including the 5-CRD, report strong agreement in linear regression analysis with high slopes (> 0.9), high R^2 values (> 0.9) and generally insignificant intercepts. NO_3 and N_2O_5 comparisons report high levels of agreement with slopes within instrument uncertainties (1.0 and 0.95); high R^2 (> 0.9) and intercepts generally consistent with limits of detection.

ΣPNs and ΣANs data show possibility of thermal dissociation of isoprene nitrates at temperatures far lower than previously expected (beginning at 430 K), the implications of which are discussed. Gas phase yields of RONO_2 from the reaction of NO_3 + isoprene were determined as 0.81 ± 0.17 when taken all together but yields from individual experiments were found to be highly variable with significant uncertainty.

Zusammenfassung

In der folgenden Arbeit werden Messungen von NO_2 , NO_3 , N_2O_5 und organischen Nitraten (ΣPNs ($\text{R}(\text{O})\text{O}_2\text{NO}_2$; und ΣANs (RONO_2)) vorgestellt, die in 3 Jahren Messungen mit einem 5-channel cavity ringdown spectroscopy (5-CRD) Instrument durchgeführt wurden. Im Verlauf von zwei Feldkampagnen und mehreren Laborexperimenten werden die Ergebnisse dieser beiden Kampagnen diskutiert.

Die AQABA-Schiffskampagne im Jahr 2017 weißt Messungen von NO_2 , NO_3 und N_2O_5 aus einem Wechsel stark verschmutzter und sauberer maritimer Luftmassen auf. Die untersuchten Regionen umfassen die arabische Halbinsel und das östliche Mittelmeer. NO_3 und N_2O_5 Mischungsverhältnisse oberhalb der Nachweisgrenze, wurden in über 30 der insgesamt 60 Nächte beobachtet, mit Mischungsverhältnissen von 12 ± 18 ppt für NO_3 (max: 146 ppt) und 23 ± 35 ppt (max: 295 ppt) für N_2O_5 entsprechend. Dies entspricht einer mittleren NO_3 -Lebensdauer von 65,5 Sekunden ($\sim 0,0153 \text{ s}^{-1}$ Reaktivitätsrate) über den gesamten Kampagnenzeitraum. Dabei ist zu beachten, dass es große regionale Unterschiede gibt. DMS hat in allen Regionen den größten Beitrag zur Kontrolle der NO_3 Lebensdauer (20 - 25%). Jedoch stellen auch Reaktionen mit anthropogene VOCs regional wichtige Senken im Persischen Golf dar. Über den gesamten Kampagnenzeitraum sind sie jedoch vernachlässigbar. Die heterogene Aufnahme wurde durch hohe Temperaturen begrenzt und trug nur einen kleinen Teil zur Reaktivität bei ($\sim 5\%$). Die meiste Reaktivität (40 - 80%, abhängig von der Region) konnte bei den während der AQABA durchgeführten Messungen nicht berücksichtigt werden, obwohl eine Analyse darin nahe legt, dass Schiffsemissionen stark dazu beigetragen haben können und zeigt, dass SO_2 als Marker zur Abschätzung der Reaktivität verwendet werden kann.

Die Ergebnisse legen ferner nahe, dass die nächtlichen Senken von NO_x in 4 von 5 der AQABA-Regionen trotz längerer Tage, hoher $[\text{OH}]$ -Konzentrationen und annähernd ähnlicher NO_2 -Verlustraten mit OH und O_3 wesentlich effizienter war als tagsüber (Faktor 2 - 3).

Bei der SAPHIR-Kampagne 2018 wurden Kammermessungen von NO_2 , NO_3 , N_2O_5 , ΣPNs und ΣANs durchgeführt, in denen die Reaktion von NO_3 + Isopren untersucht wurde. Die Messungen von NO_2 , NO_3 und N_2O_5 werden statistisch, im Vergleich mit anderen Instrumenten dargestellt. NO_2 -Messungen von drei Instrumenten, einschließlich der 5-CRD, zeigen in der linearen Regressionsanalyse starke Übereinstimmung mit hohen Steigungen ($> 0,9$), hohen Bestimmtheitsmaß ($> 0,9$) und insignifikanten Achsenabschnitten. NO_3 - und N_2O_5 -Vergleiche zeigen ein hohes Maß an Übereinstimmung in der Steigung, innerhalb der Instrumentenunsicherheiten (1,0 und 0,95), ein hohes Bestimmtheitsmaß ($> 0,9$) und Achsenabschnitte, die grundsätzlich mit den Nachweisgrenzen übereinstimmen.

Die Daten von ΣPNs und ΣANs zeigen eine mögliche thermische Dissoziation von Isopren-Nitraten bei Temperaturen, die weit unter den zuvor erwarteten Temperaturen liegen (beginnend bei 430 K). Deren Auswirkungen werden im Folgenden diskutiert. Die Gasphasenausbeuten von RONO_2 aus der Reaktion von NO_3 + Isopren beträgt zusammengenommen $0,81 \pm 0,17$, jedoch stellen sich die Gasphasenausbeuten der einzelnen Experimenten als sehr variabel mit signifikanter Unsicherheit dar.

Contents

Abstract.....	1
Zusammenfassung	2
1. Introduction	7
2. Chemistry of reactive nitrogen in the atmosphere.....	11
2.1.1 Sources of oxides of Nitrogen (NO _x)	11
2.1.2 Sinks of Nitrogen Oxides	13
2.2.1 Sources of the Nitrate Radical and N ₂ O ₅	14
2.2.2 Sinks of Nitrate radical	15
2.2.3 Gas Phase reactions of N ₂ O ₅	16
2.3.1 Heterogeneous Chemistry of NO ₃ and N ₂ O ₅	16
2.3.2 Halogen activation from N ₂ O ₅	20
2.3.3 Interaction with SO _x cycle	20
2.3.4 Interaction with RO _x cycle.....	21
2.3.5 Influence on SOA formation	21
2.4.1 Organic Nitrate chemistry.....	22
2.4.2 Peroxy(acyl) Nitrates.....	22
2.4.3 Alkyl Nitrates.....	23
2.5.1 Atmospheric Isoprene Chemistry	25
2.5.2 Formation of Alkyl Nitrates.....	26
2.6.1 Relationship between ΣANs, ΣPNs, NO ₃ , N ₂ O ₅ and NO _x	30
3. Instrumentation & Methods.....	31
3.1.1 Principles of Cavity Ringdown Spectroscopy	31
3.2.1 Instrument Design.....	34
3.2.2 Detection of NO ₂ at 405 nm.....	35
3.2.3 Detection of NO ₂ via thermal dissociation.....	36
3.3.1 Data Corrections	37
3.3.2 The <i>I/d</i> ratio	37
3.3.3 Effective laser cross section	38
3.3.4 Transmission losses of NO ₂	38
3.3.5 Effects due to Rayleigh scattering.....	39
3.3.6 Radical Chemistry in the heated sections.....	39
3.3.7 Detection of NO ₂ from thermal decomposition of HNO ₃	42

3.3.8	Detection of NO ₂ from thermal decomposition of N ₂ O ₅ and ClNO ₂	42
3.3.9	Total Uncertainty and limit of detection	43
3.4.1	Detection of NO ₃ at 662 nm.....	44
3.4.2	Detection of NO ₃ via thermal dissociation.....	45
3.4.3	The <i>l/d</i> ratio	45
3.4.4	Effective laser cross section	46
3.4.5	Transmission losses across the cavities	46
3.4.6	Losses across the automatic filter changer.....	46
3.4.7	Losses in the sampling line.....	47
3.4.8	Total uncertainty and limit of detection	47
4.	Campaign Description and Set-up.....	48
4.1.1	The 2017 AQABA ship campaign.....	48
4.1.2	Measurements of NO ₃ and N ₂ O ₅ by cavity ringdown spectroscopy	49
4.1.3	NO and NO ₂	50
4.1.4	NO _x and NO _y	50
4.1.5	Volatile Organic Compounds (VOCs)	50
4.1.6	O ₃ , SO ₂ , and OH.....	51
4.1.7	Aerosol Measurements.....	51
4.1.8	Meteorological data.....	51
4.1.9	Boundary Layer data	51
4.1.10	OH Reactivity.....	51
4.2.1	2018 SAPHIR NO ₃ -Isoprene campaign	51
4.2.2	NO ₃ and N ₂ O ₅	54
4.2.3	NO, NO ₂ , NO _x and O ₃	55
4.2.4	Peroxyacyl and Alkyl Nitrates.....	55
4.2.5	Direct measurements of NO ₃ reactivity	56
4.3.6	Isoprene and other VOCs	56
4.3.8	The SAPHIR chamber	56
5.	NO ₃ reactivity during the AQABA campaign	57
5.1.1	Overview of measurements made during AQABA.....	57
5.1.2	NO ₃ First order loss rates	60
5.1.3	Regional variability of k(NO ₃)	61
5.2.1	Assigning reactivity 22 – 23 August (North Red Sea).....	67

5.2.2 Gas-Phase reactions of NO ₃	70
5.2.2.1 Reaction with NO	70
5.2.2.2 Reaction with DMS.....	71
5.2.2.3 Reaction with other VOCs	72
5.2.2.4 Heterogeneous reactions of NO ₃ and N ₂ O ₅	73
5.2.3 Unknown loss processes	76
5.2.3.1 – Reactions with NO.....	76
5.2.3.2 – Reactions with RO ₂ radicals	76
5.2.3.3 – Reactivity from ship-based emissions.....	78
5.2.4 Reactivity from Ship Emissions.	79
5.2.5 comparison with OH reactivity	82
5.2.6 Simulations.....	83
5.2.7 Summary of losses	85
5.3.1 Integrated NO _x Loss	86
5.3.1.1 NO _x loss in the Persian Gulf	88
5.3.1.2 NO _x Loss in the Indian Ocean.....	89
5.3.1.3 NO _x Loss in the Red Sea	89
5.3.1.4 NO _x loss in the Mediterranean Sea	91
5.3.1.5 Summary of NO _x Losses	93
5.3.2 Day time losses due to NO ₃ formation	95
5.4.1 Summary	96
6. NO ₃ during the 2018 SAPHIR NO ₃ -Isoprene Campaign.....	97
6.1.1 Overview of Measurements	97
6.2.1 Intercomparison of NO ₂ measurements.....	97
6.2.2 Comparison by experiment.....	98
6.2.3 Conclusion and comparison with previous NO ₂ intercomparison campaign.	103
6.3.1 Intercomparisons of NO ₃ / N ₂ O ₅ measurements	104
6.3.2 Comparison by experiment.....	104
6.3.3 Comparison to previous intercomparisons.....	111
6.3.4 Conclusions	111
7. Organic Nitrates during the SAPHIR campaign	113
7.1.1 Oxidation of Isoprene by NO ₃	113
7.2.1 Detection of Isoprene Nitrates via TD-CRD.....	113

7.2.2 Detection of 'PANs' at 448 K.....	113
7.2.3 Nighttime generation of PANs.....	114
7.2.4 Surface Catalyzed breakdown of ANs.....	116
7.2.5 Thermal Dissociation of Alkyl Nitrates at $T < 690$ K.....	116
7.3.1 Yields of Alkyl Nitrates.....	118
7.3.2 Comparisons by experiment.....	119
7.3.3 Technical issues in ANs measurements.....	122
7.3.4 Discussion.....	126
7.4.1. Summary and conclusions.....	128
8. Outlook.....	130
9. Appendix.....	132
Appendix A – Supplementary Figures AQABA.....	132
Appendix B – Supplementary Figures SAPHIR.....	137
Appendix C – List of abbreviations.....	139
Appendix D – FACSIMILE Codes.....	140
Appendix E – List of figures and tables.....	145
Figures.....	145
Tables.....	147
Appendix F – Bibliography.....	149
References.....	149

1. Introduction

Since the beginning of industrialization, which started in the United Kingdom in the latter half of the 19th century, the atmosphere has undergone significant chemical changes, driven by anthropogenic activities, which have had numerous consequences for air quality and environmental sustainability. Worsening of ambient air quality has had consequences for human health and is linked to an estimated 4.2 million premature deaths annually (Stanaway et al. 2018) according to the WHO, contributing to major health problems ranging from lung cancer and respiratory infections to strokes and heart disease. Within the wider environment, air pollution causes damage to ecosystems by, among other mechanisms, catalyzing chemical reactions which lead to the building up of concentrations of molecules with potentially dangerous outcomes. Tropospheric ozone (O₃), for example, has been shown to reduce crop yields (Avnery et al. 2011) raising concerns over long-term food security and is damaging to other plant life; sulfur pollution can lead to acid rain events which are harmful to pH sensitive environments and infrastructure; Carbon emissions continue to be an international issue with climate change, and so on.

Ambient air pollution and its effects on human activities are not a new problem and many laws and regulations have been enacted, usually in response to high-profile pollution incidents, which have been well-documented throughout history. The first instance of attempts to limit the effects of air pollution can be found nearly two millennia ago, with the Mishnah laws of first and second century Israel which prevented tanneries to being too close to settlements because of offensive smells. In 1272, King Edward I of England regulated the use of coal as fuel in London due to the increasing smoke problems.

In the modern age, in October 1948 the town of Donora, Pennsylvania in the United States was enveloped in a hazy smog (smog = smoke + fog) which was caused by local emissions of air pollutants and a simultaneously occurring strong thermal inversion, as a warmer air mass passed over the town, trapping the colder more polluted air at ground level. This resulting smog caused the deaths of 40 people and led to respiratory or cardiovascular health problems amongst half of the town's 14,000 residents. Far from Donora a different, but equally significant, phenomenon was observed beginning in the 1940's in Los Angeles, California. In the bright solar irradiance and hot temperatures of summer the city's ambient air had become distinctly irritating to the eyes of residents, while also causing respiratory issues and leading to school closures, cancelling of public events and a host of other problems (Special 1972). The air was found to contain high concentrations of strongly oxidizing molecules, which in turn would promote the formation unhealthy, long-lasting, secondary pollution molecules which would prevent outdoor activities, and this would have negative consequences upon the health and economic activities of the Los Angeles residents.

Since the investigations into the 1944 Los Angeles photosmog events, this type of pollution has been recognized as a world-wide problem in many major cities (IQAir 2019). It is now understood to be the consequence of emissions of large concentrations of primary pollutants, such as NO_x (NO_x = NO + NO₂) and Volatile Organic Compounds (VOCs) and other trace gases into the local ambient air, in many cases exacerbated by the local geography and meteorological events. The dynamic cycling of NO_x between NO and NO₂ and the interactions of these molecules with other trace gases, many of which are in dynamic cycles of their own, is now known to be directly responsible for the building-up of harmful species and creating events like the Los Angeles photosmog.

Both NO_x and VOCs have a multitude of sources, both natural and anthropogenic. During the day, reactivity of VOCs is driven by the OH radical, the so-called 'detergent of the atmosphere' - a term coined by the Nobel prize-winning atmospheric scientist Paul Crutzen - well-known as one of the most important molecules for driving oxidation of trace gases. VOCs react with OH to form intermediate, peroxy radicals (RO_2 , where R = carbon chain). These can directly influence the NO_x budget by reaction with NO to form NO_2 , or branching off to form organic nitrates (RONO_2), a longer-lived reservoir species. In either case, these reactions convert NO into a different form (typically favoring the formation of NO_2) without consuming O_3 . Consequently, this leads to build up of O_3 , as the reaction which forms O_3 requires the photolysis of NO_2 . Additionally, reaction with OH of a VOC containing a carbonyl ($\text{C}=\text{O}$) group or the photolysis of certain organic trace gases such as acetone ($(\text{CH}_3)_2\text{CO}$) or methylglyoxal ($\text{CH}_3(\text{CO})\text{CHO}$), leads to the formation of the short lived $\text{R}(\text{O})\text{O}_2$ species which can undergo reaction with NO, to form NO_2 or with NO_2 to form Peroxyacyl Nitrates (PNs). These longer lived, secondary pollutants are either themselves harmful, or else can be transported away from their sources into the surrounding areas becoming a significant source of NO_x and therefore O_3 in rural regions.

During the night however, without the input of energy from the sun reactive nitrogen chemistry is dominated by the nitrate radical (NO_3). During daylight hours photolysis converts NO_2 to NO and reaction with, amongst others, O_3 reproduces NO_2 . Without this photochemical cycling the relatively slow reaction between NO_2 and O_3 leads to an increase in the ambient mixing ratios of the reactive nitrate radical NO_3 . This radical quickly establishes an equilibrium with NO_2 , reacting together to form Dinitrogen Pentoxide (N_2O_5). Nighttime radical chemistry is a significant sink of both NO_x and VOCs as NO_3 reacts with VOCs form a variety of products, including organic nitrates and nitric acid (HNO_3), while N_2O_5 undergoes heterogeneous reactions on the surface particles suspended in aerosol – colloids of liquid or solid particles dispersed in a gaseous medium.

The Nitrate radical was postulated to exist over 100 years ago through observation of absorption bands produced in the region 500-700 nm in optical absorption spectra which did not belong to O_3 (Hautefeuille and Chappuis 1882). Following identification, the role which NO_3 was thought to play was negligible compared to daytime photochemistry. This understanding began to change during the late 1970s and 1980s when the first direct observations of NO_3 were made (Ulrich Platt et al. 1980). Since then, numerous field studies – both in continental and maritime settings (e.g. (McLaren et al. 2010; Crowley, Schuster, et al. 2010; Sobanski, Tang, et al. 2016; S. S. Brown et al. 2004; Aldener et al. 2006) – have attempted to measure NO_3 (and N_2O_5) concentrations and consequently understand what factor(s) control its reactivity and what impact its oxidation of VOCs and interaction with aerosol particles has on the atmosphere more broadly.

Moreover, global emissions of NO_x have been on the rise. In 1985, global anthropogenic NO_x emissions from all combustion processes were estimated to be 21 Teragrams Nitrogen per year (TgN yr^{-1}) but estimates had risen significantly to 33 TgN yr^{-1} by 2000 (Enhalt and Prather 2001). Currently, the most recent assessment of the global NO_x burden from combustion is 28.3 Tg N yr^{-1} , according to the IPCC AR5 report. (IPCC 2013), or 37.5 Tg N yr^{-1} for all anthropogenic sources, including agriculture and anthropogenic biomass burning. The next edition of this report by the IPCC (AR6) is underway and is expected to be released in 2022. This increase will undoubtedly increase the importance of reactive nitrogen chemistry in the decades to come. While some national governments have pledged reduce NO_x emissions, and have had some degree of success in this (European Environment Agency, 2003) the global trend is clear and much still needs to be done to understand the ultimate fate of reactive nitrogen in

places which have seen a marked reduction (or increase) in emissions in recent history. An industry of particular interest in the conversation of global NO_x is the shipping industry, where global freight demands are predicted to triple by 2050 and where the warming of the climate is set to open new, trade routes for ships to traverse (ITF 2019). Previous examination of shipping emissions has shown that a significant proportion of NO_x emissions in the transportation sector ($3.08 \text{ Tg N yr}^{-1}$, accounting for 14% of all nitrogen from fossil fuel combustion.) (Corbett, Fischbeck, and Pandis 1999) are attributable to shipping. More recently, (Eyring et al. 2005) showed that emissions of NO_x from ships (estimated as 6.5 Tg N yr^{-1}) were comparable to emissions from road traffic (8.3 Tg N yr^{-1}) or approximately 22.9% of all NO_x emissions from combustion processes ($28.3 \text{ Tg N yr}^{-1}$) (IPCC 2013).

Thesis Outline

This thesis aims to investigate the reactivity of various nitrogen species in the lower troposphere with measurements made by a Thermal Dissociation Cavity Ringdown Spectrometer (TD-CRDs), deployed in two different field studies. Section 2 details the sources of reactive nitrogen species studied within this thesis including NO_x , Organic Nitrates, NO_3 and N_2O_5 and the reactions of these with other trace gases and interactions with other atmospheric cycles.

Section 3 will look at the TD-CRDs technique for detecting NO_2 and NO_3 , the principles behind the method and the data corrections which need to be made in order to analyze the results gathered from the field campaigns or the laboratory.

Section 4 shall detail the specific the background and scientific motivations of the field campaigns on which the TD-CRD instrument was deployed. It shall discuss the specific set-ups used for data acquisition and a description of the set-ups of other instruments which provided relevant data for the analysis of the CRD measurements. These two campaigns were The Air Quality and Climate Change in the Arabian Basin (AQABA) campaign, wherein shipborne measurements were made on route from the port of La-Seynes-sur-Mer in the south of France to Kuwait City and back during the summer of 2017 and the Simulation of Atmospheric Photochemistry in a large Reaction chamber (SAPHIR) / NO_3 + Isoprene campaign of summer 2018, where the reaction between the ubiquitous and biogenic VOC isoprene and the nitrate radical were studied in series of experiments inside a large chamber capable of simulating a range of atmospheric conditions.

The sections which follow (5, 6 and 7) will discuss the results from these campaigns. Section 5 considers the factors which control the reactivity of NO_3 around the Arabian Peninsula and in the eastern Mediterranean Sea, regions with many highly polluted air masses. Additionally, the role of ship emissions will also be analyzed as these contribute greatly to local air pollution, producing large concentrations of NO_x , SO_2 and VOCs leading to high rates of NO_3 production but also NO_3 losses.

Section 6 discusses the measurements of both NO_2 and NO_3 in the context of the NO_3 + Isoprene experiments during the SAPHIR campaign. The results of an intercomparison between five different instruments which measure NO_2 and for two different instruments which measure NO_3 are presented, and the results of the analysis used to generate a harmonized dataset.

Section 7 will discuss the organic nitrates, in the form of the sum of all peroxy nitrates (ΣPNs) and the sum of all alkyl nitrates (ΣANs), measured during the SAPHIR chamber experiments and the total contribution of these organic nitrates to the sum of all reactive nitrogen (known as NO_y , where $\text{NO}_y = \text{NO}, \text{NO}_2, \text{NO}_3$,

N_2O_5 , ΣPNs , ΣANs , Nitric Acid (HNO_3), Nitryl Chloride (ClNO_2) and particulate nitrate $\text{p}(\text{NO}_3^-)$). The results regarding the partitioning of organic nitrates, which run counter to expectations based on knowledge from within the literature about the chemical mechanism of NO_3 's addition to isoprene, are discussed and from this data an estimate of the yield(s) of alkyl nitrates from this reaction is given.

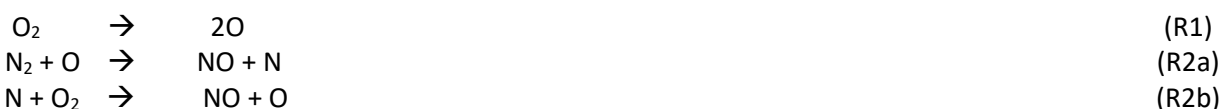
Finally, section 8 details and outlook of potential future studies which could be undertaken in the future based on the observations made and the results gathered during the course of this thesis and some potential improvements or changes to the instrument will be suggested.

2. Chemistry of reactive nitrogen in the atmosphere

This section will give an overview of some of the most important molecules in the troposphere, particularly the trace gas species of NO, NO₂, NO₃, N₂O₅ and organic nitrates such as PN_s and AN_s. It will focus on their sources, sinks and reactivity.

2.1.1 Sources of oxides of Nitrogen (NO_x)

Nitrogen Oxides (NO_x) are formed from the reaction of atmospheric nitrogen (N₂) with oxygen atoms (O), dissociated from atmospheric oxygen (O₂). Due to the presence of the highly stable nitrogen-nitrogen triple bond (bond dissociation energy 945 kJ mol⁻¹ at 298 K), this reaction has a very high activation energy, requiring very high temperatures. The mechanism of the formation of NO in this way was first described by the Zel'dovich (Zeldovich 1947) mechanism:



The newly-formed N=O bonds are also strong (626 kJ mol⁻¹ at 298 K) therefore the activation energy for the reaction in the reverse direction (i.e. (re)forming N₂ and O₂ from NO_x) are similarly high, also requiring high temperatures. Thus, the kinetics conditions best suited to the formation of NO_x are those where intense heating of air is followed by rapid cooling (Park and Calderer 2008). Such conditions can be found under several natural processes (e.g. lightning strikes) but ideal conditions are additionally created by anthropogenic processes as well, e.g. in internal combustion engines and (anthropogenic) biomass burning. Human activities dominate NO_x emissions on a global scale with fossil fuel burning contributing ~50% to the global budget and biomass burning contributing a further ~20% (Delmas, Serça, and Jambert 1997). Other sources of NO_x, representing ~30% of total emissions, are either natural and include the previously mentioned lightning strikes; direct emissions from microbial activity in the soil; derived from other natural and anthropogenic sources of nitrogen, such as the oxidation of atmospheric NH₃; or transport of nitrogen (e.g. NO_x from N₂O) down from the stratosphere.

Table 1. Global Sources of NO_x (in TgN yr⁻¹) adapted from (Enhalt and Prather 2001) to include most recent IPCC (2014) estimate. The next IPCC report (AR6) is predicted to be released in 2022.

Reference	AR5/IPCC	TAR/IPCC	Enhalt	Holland <i>et al.</i>	Penner <i>et al.</i>	Lee <i>et al.</i>
Year	<u>2013</u>	<u>2000</u>	<u>1985</u>	<u>1985</u>	<u>1992</u>	<u>1997</u>
Fossil Fuel	28.3	33.0	21.0	20-21	21.0	22.0
Aircraft		0.7	0.45	0.23-0.6	0.5	0.85
Biomass Burning	5.5	7.1	7.5	3-13	5-12	7.9
Agriculture	3.7	-	-	-	-	-
Soils	7.3	5.6	5.5	4-21	4-6	7.0
NH₃ oxidation	-	-	3.0	0.5-3	-	0.9
Lightning	4	5.0	7.0	3-13	3-5	5.0
Stratosphere		< 0.5	0.15	0.1-0.6	-	0.6
Total	48.8	51.9	44.6	-	-	44.3

In the Stratosphere, NO_x can be formed via photolysis to give N₂ and the highly reactive O (¹D) atom. This O atom will then react with another N₂O molecule giving two equivalents of NO (R3c) or N₂ and O₂ (R3b):



Approximately 90% of stratospheric NO_x comes from these reactions with tropospheric N₂O (Mohanakumar 2008). Stratospheric NO_x plays a key role in ozone depletion by catalyzing conversion into O₂, however as this thesis focuses on reactive nitrogen in the lower troposphere and stratospheric NO_x is a minor contributor to the global tropospheric NO_x budget (< 1% from the data in Table 1), the reactivity of NO_x in the stratosphere and the associated environmental problems will not further be considered.

In the troposphere ambient NO_x levels show substantial variation by area, ranging from a few ppt (parts-per-trillion) near the surface in remote regions, both continental and oceanic, to > 100 ppb (parts-per-billion) in urban or industrial areas. This spatial variability is related to the concentration of sources, the reactivity of NO_x with other trace gases and other factors including geography, weather and climate. This uneven distribution profile also extends vertically, leading to potentially stratified layers of NO_x and other reactive nitrogen compounds throughout the atmosphere.

A comprehensive review of several of the chemical reactions presented here, and many others, are given by (Finlayson-Pitts and Pitts Jr. 1999) in their book *Chemistry of the Upper and Lower Atmosphere* and sources therein.

Most NO_x produced by the rapid heating and cooling mechanism is in the form of NO. While NO₂ can be directly emitted by the same processes that produce NO, most NO₂ is derived from the chemistry of NO in the troposphere. These reactions cycle NO_x between the NO and NO₂ forms:



Reaction (R4) shows the production of NO₂ from the reaction between O₃ with NO. While reaction (R5) shows that during the day NO₂ undergoes photolysis at wavelengths of light of λ < 420 nm, producing a molecule of NO and an oxygen atom, O (³P). The rate coefficient which governs this photolytic reaction is known as J(NO₂). These two reactions combine with reaction (R6) where the oxygen atom combines with O₂, which is highly abundant in the atmosphere, to reform O₃. This completes a null cycle wherein there is no net production or loss of the trace gases involved, a condition known as steady state and an important concept in atmospheric chemistry. As O (³P) is very reactive and short-lived, under most circumstances, we can assume it is in steady state and therefore we can predict the concentration of ambient [O₃], or [NO_x], as long as the other and the relevant J(NO₂) are known. This cycling is known as the Leighton relationship (Leighton 1961).

Other atmospheric trace gases, such as VOCs or the hydroperoxyl radical (HO₂), generate NO₂ from NO which modify the available concentration of [NO₂] without consuming O₃, modifying the Leighton relationship:



Following these reactions can NO_2 undergo photolysis, as per reaction (R5), reproducing NO and $\text{O} (^3\text{P})$. This oxygen atom reacts as in reaction (R6) to give O_3 , resulting in a net gain rather than a null cycle. Through this mechanism, ambient $[\text{O}_3]$ can build up locally, potentially to dangerous levels. High concentrations of tropospheric O_3 is a major component of photochemical smog.

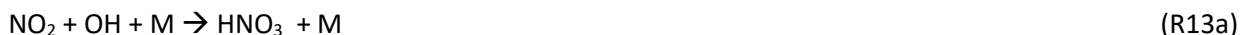
Reactions which are sources of NO_x but are not combustive are either biogenic from, e.g., soil bacteria involving enzymes which convert complex, nitrogen-containing molecules in the soil into different forms, including gas-phase NO , which are then emitted into the atmosphere; or NO_x sources derived from reservoirs, such as nitryl halogens (ClNO_2 or BrNO_2), NO_3 , N_2O_5 , HNO_3 or organic nitrates. These reservoirs are the result of reactions involving gas-phase NO_x and serve to transport it away from the source(s) into other areas. Some of the most important reactions include:



Where X is a halogen ($\text{X} = \text{Cl}, \text{Br}$) and R is a carbon-based chain or cycle. (R9) is a photolysis reaction which generates a free halogen radical and NO_2 . A typical example of this is the reaction of ClNO_2 in coastal and maritime environments. (R10) and (R11) are thermal decomposition reactions of organic nitrates to produce peroxy (RO_2) radicals and NO_2 , and are an example of how NO_x/VOC reactivity can transport NO_x away from its source(s) and into more rural areas. These reactions will be discussed further below.

2.1.2 Sinks of Nitrogen Oxides

The chemical lifetime of NO_x in the troposphere is quite short, compared with other common trace gas pollutants (e.g. SO_2) ranging from ~ 1 day in polluted lower troposphere regions to a few days in the upper troposphere. As several reactions which remove gas-phase NO_x involve photochemically generated trace gases, sinks for NO_x are different between the day and night. During the day, a major sink for NO_x is reaction with the OH radical:



Reactions (R12) and (R13b) are highly reversible as they produce relatively short-lived species which thermally decompose or are photolyzed back to NO_x and thus they act only as temporary reservoirs. Reaction (R13a) produces gas-phase nitric acid, which is a thermally stable and highly water-soluble, ionic molecule. Formation of HNO_3 via OH oxidation has been shown over many field studies (see section 5 for discussion) to be either the most important loss mechanism (or amongst the most efficient) of NO_x .

Therefore, the ultimate fate of NO_x is closely tied to the losses of HNO_3 . An important loss mechanism of HNO_3 from the atmosphere is loss via deposition of HNO_3 molecules, of which there are two different mechanisms. HNO_3 which adheres directly on to exterior surfaces is known as dry deposition, while dissolution of HNO_3 into suspended water droplets, which go on to form clouds or mist resulting in precipitation (snow, rain, etc.) is known as wet deposition. HNO_3 can also interact with and become incorporated into aerosols (as ionic nitrate, NO_3^-), which are a colloidal suspension of solid or liquid particles within a gaseous medium, creating an equilibrium between the gas-phase and other phases. Much like gas-phase HNO_3 , these aerosols will be lost to the atmosphere via dry deposition processes and thus represent a significant loss pathway for NO_x .

Other sinks of NO_x include the formation of the temporary sinks the nitrate radical (NO_3) and its equilibrium partner dinitrogen pentoxide (N_2O_5) at night. These sinks are temporary as NO_x is efficiently recycled via photolysis beginning at sunrise. NO_3 and N_2O_5 can however become more permanent sinks via direct reaction of NO_3 with other trace gases, most notably volatile organic carbon (VOC) species, to form nitric acid (HNO_3) and alkyl nitrates (RONO_2). N_2O_5 can become incorporated into aerosol particles leading to hydrolysis and formation of NO_3^- . During the day, radical initiated VOC chemistry (e.g. by OH) can create a temporary sink by incorporating NO_x in a carbon skeleton, forming peroxy acyl nitrates ($\text{R(O)O}_2\text{NO}_2$) or the longer lived alkyl nitrates (RONO_2). Each of these shall be discussed below in addition to the impact that reactive nitrogen species can have on other atmospheric cycles.

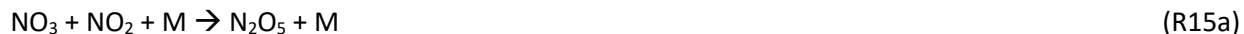
2.2.1 Sources of the Nitrate Radical and N_2O_5

Excellent reviews of the nitrate radical, N_2O_5 , their physical properties, reactions and atmospheric importance have been detailed before by (Wayne, et al. 1990) and (Steven S. Brown and Stutz 2012). What follows is an overview of the most important reactions of the nitrate radical within the context of the chemical systems studied during the course of this thesis.

The nitrate radical is produced from the reaction of NO_2 and O_3 :



Nearly all formation of NO_3 comes from oxidation of NO_2 by ozone. Once formed, NO_3 reacts with another molecule of NO_2 to form N_2O_5 quickly establishing an equilibrium:



The partitioning between NO_3 and N_2O_5 is strongly dependent on levels of NO_2 and the ambient temperature. Under most atmospheric conditions the equilibrium between NO_3 , NO_2 and N_2O_5 will be established on the order of a few minutes (Wayne, et al. 1990), allowing for calculation of one of the trace gases as long as the other two and the ambient temperature, which determines the value of the equilibrium constant $K_{\text{eq}}(T)$, are known. As N_2O_5 is both thermally labile and in equilibrium with NO_3 , N_2O_5 is therefore also a source of NO_3 by thermal dissociation back to NO_3 and NO_2 :



Separate from the reaction of NO_2 with O_3 , studies have suggested the possibility of an additional NO_3 source due to the reaction of NO_2 with carbonyl oxides (C(O)O) generated by stabilized Criegee

intermediates (see below) (Presto and Donahue 2004), particularly when sinks for the nitrate radical are few and the chemical lifetimes are long. This has been posited as an explanation for data gathered in rural sites where strong agreements for measurements of NO₂ and O₃ imply an accurate determination of the production rates of NO₃, but combined losses by heterogeneous uptake and gas phase reactivity do not account for steady-state lifetimes of NO₃ (Sobanski, Tang, et al. 2016).

2.2.2 Sinks of Nitrate radical

Nitrogen oxides are recycled from NO₃ via reaction with NO:



During daylight hours however, NO_x is also recycled from NO₃ via photochemistry:



As both of these reactions reform NO_x, reactive nitrogen is not lost to the atmosphere due to these processes as both NO and NO₂ can reform NO₃ via reactions (R4) and (R14). This means under certain conditions in the atmosphere where nocturnal losses are inefficient, NO₃ and N₂O₅ represent only a temporary reservoir of NO_x, undergoing rapid photolysis or reaction with the photochemically produced NO following sunrise the next day.

While highly regionally dependent, generally the largest sink of the NO₃ radical which does not directly reproduce NO_x is the gas-phase reaction with a VOC. NO₃ oxidations of VOCs are more selective than oxidation by the OH radical with typically smaller rate coefficients for the same trace gas, although there are several important exceptions to this such as the reaction with NO. Despite the lower rate coefficients, VOC oxidation by NO₃ can be comparable to OH as atmospheric concentrations of NO₃ can regularly exceed OH concentrations by several orders of magnitude.

VOC reactions with NO₃ in the case of saturated VOCs (e.g. C₄H₁₀) proceed via direct H-abstraction to form a peroxy radical (RO₂) after addition of abundant O₂ from the intermediate alkyl radical (R) and HNO₃. Compared with addition reactions, rate coefficients for NO₃ H-abstractions tend to be smaller and relatively unimportant, though there are some important exceptions (e.g. dimethyl sulfide) where NO₃ H-abstraction is far more rapid and significant. Therefore, is often the case that H-abstraction reactions with OH at day represent the more important loss mechanism for saturated VOCs than NO₃ reactions at night. For example, the rate coefficient for the reaction of NO₃ with n-C₄H₁₀ is $k_{(\text{NO}_3+\text{C}_4\text{H}_{10})} = 4.6 \times 10^{-17} \text{ cm}^3 \text{ molecule}^{-1} \text{ s}^{-1}$ at 298 K compared with $k_{(\text{OH}+\text{C}_4\text{H}_{10})} = 2.35 \times 10^{-12} \text{ cm}^3 \text{ molecule}^{-1} \text{ s}^{-1}$ at 298 K (IUPAC, 2020) for the same VOC with OH.

If the VOC in question contains a carbon-carbon double bond (aliphatic), reaction with NO₃ will typically proceed via an electrophilic addition across the double bond system (e.g. Isoprene, C₅H₈). However, the rate coefficients which govern addition reactions of NO₃ on to short-chain, lighter VOCs (≤ C3) tend to be small, e.g. $k_{(\text{NO}_3+\text{C}_2\text{H}_4)} = 2.1 \times 10^{-16} \text{ cm}^3 \text{ molecule}^{-1} \text{ s}^{-1}$ but these increase quickly with longer carbon-chain VOCs. For some larger (C10-C15) biogenic VOCs, such as various mono- or sesquiterpenes, rate coefficients on the order of $> 10^{-10} \text{ cm}^3 \text{ molecule}^{-1} \text{ s}^{-1}$ are known. In the case of aromatic carbon-carbon double bond systems, NO₃ reacts slowly to abstract hydrogen from the aromatic ring system (e.g. benzene, $k_{(\text{NO}_3+\text{C}_6\text{H}_6)} \approx$

$3 \times 10^{-17} \text{ cm}^3 \text{ molecule}^{-1} \text{ s}^{-1}$) or from hydrogen-containing electron donating groups (e.g. $-\text{CH}_3$) in substituted benzene rings such as toluene or various xylenes. Conversely, NO_3 reactions with aromatics substituted with electron withdrawing groups (e.g. $-\text{OH}$ in phenol) tend to be much faster, with rate coefficients several orders of magnitude larger than benzene, even if they contain other electron donating groups, such as cresols ($k_{(\text{NO}_3+\text{p-cresol})} = 1.1 \times 10^{-11} \text{ cm}^3 \text{ molecule}^{-1} \text{ s}^{-1}$).



In the case of reaction (R18) the reaction with NO_3 produces HNO_3 , and a peroxy radical (RO_2), while in reaction (R19) NO_3 adds to the double bond and a nitrooxy peroxy radical is formed. The functionalized peroxy group is also able to undergo reactions with NO_3 to form NO_2 , O_2 and an alkoxy radical (RO):



2.2.3 Gas Phase reactions of N_2O_5

The only known gas phase reaction of N_2O_5 is with water vapor:



Both rate coefficients are known to be extremely small, with $k_{(\text{H}_2\text{O}+\text{N}_2\text{O}_5)} < 10^{-22} \text{ cm}^3 \text{ molecule}^{-1} \text{ s}^{-1}$ for (R21a) and $k_{(2\text{H}_2\text{O}+\text{N}_2\text{O}_5)} = 1.8 \times 10^{-39} [\text{H}_2\text{O}] \text{ cm}^3 \text{ molecule}^{-1} \text{ s}^{-1}$ for (R22b). More recent experimental evidence however, has shown that in the atmosphere a purely gas phase reaction between N_2O_5 and H_2O is likely significantly slower than even this, at least a factor of 3 than $k_{(\text{H}_2\text{O}+\text{N}_2\text{O}_5)}$ would suggest at 280 – 290 K according to field measurements by (Crowley, Schuster, et al. 2010).

2.3.1 Heterogeneous Chemistry of NO_3 and N_2O_5

Both NO_3 and N_2O_5 are known to undergo uptake into aerosols, reacting on the surface of particles and establishing equilibria between the gas and particle phases. This is followed by hydrolysis to nitrate ions:



The rates of these processes are controlled according to:

$$k_{\text{Het}}(\text{NO}_3) = \frac{1}{4} \gamma(\text{NO}_3) \bar{c} \text{ASA} \quad (\text{Equation 1})$$

$$k_{\text{Het}}(\text{N}_2\text{O}_5) = \frac{1}{4} \gamma(\text{N}_2\text{O}_5) \bar{c} \text{ASA} K_{\text{eq}}(\text{T})[\text{NO}_2] \quad (\text{Equation 2})$$

Where k_{Het} describes the rate coefficient for NO_3 and N_2O_5 (in s^{-1}) according to the dimensionless uptake coefficient γ , which describes the efficiency of N_2O_5 or NO_3 loss being defined as the percentage of molecules colliding with particles which produce a net loss in the gas phase. \bar{c} is the temperature dependent average molecular velocity (cm s^{-1}) and ASA is the aerosol surface area concentration ($\mu\text{m}^2 \text{cm}^{-3}$). The rate of uptake of a gas to a particle can be reduced however, due to concentration gradients close to the surface of the particle, therefore introducing an error which needs to be corrected for gas-phase diffusion. This corrected γ , $\gamma_{\text{effective}}$, was estimated by (Sutugin and Fuchs 1971):

$$\frac{1}{\gamma_{\text{effective}}} = \frac{1}{\gamma} + \frac{0.75 + 0.283Kn}{Kn(Kn+1)} \quad (\text{Equation 3})$$

With Knudsen's number, $Kn = \frac{3D_g}{\bar{c}r_{\text{sw}}}$. r_{sw} is the radius of the particle and D_g is the gas phase diffusion constant for NO_3 or N_2O_5 at a given temperature and pressure. The magnitude of this correction depends on the size of γ and the size of the particle(s). If the dominant particle size during a field study was $\approx 0.2 \mu\text{m}$, and this particle size was the dominant contributor to aerosol surface area, as was the case during the AQABA campaign (see section 5), then only large values of γ (≥ 0.1) would require significant correction. For example, as the D_g for N_2O_5 is $0.085 \text{ cm}^2 \text{ s}^{-1}$ at 298 K and atmospheric pressure, a $\gamma = 1$ would reduce down to ≈ 0.5 , whereas a $\gamma = 0.03$ would reduce down to $\gamma > 0.02999$, a negligible difference compared to the accuracy of the measurements.

Values of γ are highly variable according to the chemical composition of the particles, the size of particles, temperature and relative humidity. In general, NO_3 uptake to the surface of aerosols is only significant in environments where all other loss processes of NO_3 and N_2O_5 are small. Such environments may include deserts or clean marine environments (Steven S. Brown and Stutz 2012), where VOC emissions are limited, the air masses are significantly aged and temperatures are sufficiently high to reduce the thermochemical lifetimes of N_2O_5 , inhibiting $k_{\text{het}}(\text{N}_2\text{O}_5)$. Attempts to quantify the NO_3 uptake coefficient on the surface of differing types of aerosol under field measurements have proven to be extremely difficult, due to the difficulty inherent in separating out the other gas-phase loss processes. While the laboratory studies which have been attempted typically present a large range of possible γ (see Table 2).

In contrast to NO_3 , values of γ for N_2O_5 are easier to determine as losses of N_2O_5 are easily separated out between insignificant gas phase reactions and heterogeneous chemistry and accurate determinations of N_2O_5 concentrations are possible either from calculation with NO_2 and NO_3 , or direct measurements. As a result, values of $\gamma(\text{N}_2\text{O}_5)$ are much better understood and successful determinations have been inferred from field measurements in environments with favorable conditions, i.e. with fairly constant, gas-phase loss rates of NO_3 , significant ASA and variable NO_2 mixing ratios. In such conditions the first order loss rates of NO_3 ($k(\text{NO}_3)$) will show a linear dependence on NO_2 and γ can be calculated according to (Equation 2) as a slope of a linear regression analysis of $K_{\text{eq}}(\text{T})[\text{NO}_2]$ vs. $k(\text{NO}_3)$. For example, (Aldener et al. 2006) derived a value of $\gamma \approx 0.03$ in a polluted marine environment, which is consistent with laboratory studies of N_2O_5 uptake onto the surface of sea salt (Zetzsch and Behnke 1992); while (Gavin J. Phillips et al. 2016) inferred N_2O_5 uptake coefficients from ambient measurements of NO_3 , N_2O_5 , ClNO_2 and particulate nitrates concentrations at a semi-rural mountain site during the 2011 PARADE campaign.

$\gamma(\text{N}_2\text{O}_5)$ has also been the subject of several laboratory studies, testing the efficiency of N_2O_5 uptake with aerosols of a certain type of particle composition. To date, studies of $\gamma(\text{N}_2\text{O}_5)$ on water, ice, soot, minerals,

organics and inorganics have all been reported in the literature (Table 3). As noted above, good agreement can be found between laboratory studies and field measurements, particularly in regions where a certain type of particle composition dominates the heterogeneous chemistry, such as mineral dust particles in arid regions. This agreement between laboratory and field determinations has led to parameterizations for the calculation of γ , assuming knowledge of particle chemical composition which are common measurements during field campaigns (e.g. Aerosol Mass Spectrometer). A parameterization technique developed by (Bertram, Thornton and Riedel, 2009), quantifies the contributions of Cl^- , NO_3^- and H_2O to calculate values of γ :

$$\gamma = \frac{4V}{\bar{c} ASA} K_H k'_f \left(1 - \frac{1}{\frac{k_a[\text{H}_2\text{O}(l)]}{k_b[\text{NO}_3^-]} + 1 + \frac{k_c[\text{Cl}^-]}{k_d[\text{NO}_3^-]}} \right) \quad (\text{Equation 4})$$

Where V is the total volume concentration of the particle ($\text{cm}^3 \text{ cm}^{-3}$), \bar{c} is the temperature dependent average molecular velocity of N_2O_5 (cm s^{-1}), ASA is the aerosol surface area concentration ($\text{cm}^2 \text{ cm}^{-3}$), K_H is the dimensionless Henry's law coefficient for the partition of N_2O_5 between the gas and liquid phases, and k_a , k_b , k_c , and k_d are rate coefficients governing the reactions of N_2O_5 with $[\text{H}_2\text{O}]$, $[\text{NO}_3^-]$ and $[\text{Cl}^-]$. k_f describes a function of H_2O limited uptake observed in nitrate-free particles. This analysis explains observations where the uptake of N_2O_5 is dependent on the water content of the particle (relative humidity) and suppressed by particles containing nitrate, but are negated by the presence of chloride in the particle.

Table 2. NO_3 uptake coefficients with ranges. Adapted from (Steven S. Brown and Stutz 2012). All γ coefficients given at 298 K.

Particle	$\gamma(\text{NO}_3)$ range	Comment	Reference
Water	$1.5 - 60 \times 10^{-4}$	Increasing with ionic content	(Rudich et al. 1996)
Ice	$< 10^{-3}$		(Fenter and Rossi 2010)
H_2SO_4	$< 10^{-3}$		(Kane, Caloz, and Leu 2001)
NaCl	0.002 – 0.49	Dry	(Seisel et al. 1997)
Dust	0.009 – 0.12	Varies by mineral type	(Tang et al. 2010)
Organic	$4.5 \times 10^{-4} - 1.0$	Varies by type	(Gross and Bertram 2009; Steven S. Brown and Stutz 2012)
Soot	$< 4 \times 10^{-4} - 0.33$	Varies by type	(Tang et al. 2010)

Table 3. N_2O_5 uptake coefficients with ranges. Adapted from (Steven S. Brown and Stutz 2012). All γ coefficients given at 298 K

Particle	$\gamma(N_2O_5)$ range	Comment	Reference
Water	< 0.01 – 0.06	Increasing with decreasing T	(George, et al. 1994)
NH_4HSO_4	0.02 – 0.2	Increasing with decreasing T	(Davis, Bhawe, and Foley 2008; Kane, Caloz, and Leu 2001)
$(NH_4)_2SO_4$	~ 0.02		(Steven S. Brown and Stutz 2012)
$NaNO_3$ or NH_4NO_3	$2 - 3 \times 10^{-3}$	0.02 at RH > 90%	(Fenter, Caloz, and Rossi 1996)
NaCl	$5 \times 10^{-3} - 0.03$	Sea Salt = 0.03	(Fenter, Caloz, and Rossi 1996; Mogili et al. 2006)
Dust	$5 \times 10^{-3} - 0.2$	Varies by mineral type	(Tang, Schuster, and Crowley 2014; Tang et al. 2010)
Organic	$1.5 \times 10^{-4} - 0.047$	Varies by type	(Steven S. Brown and Stutz 2012)
Soot	$4 \times 10^{-6} - 6 \times 10^{-3}$	Varies by type	(Tang et al. 2010)

Table 2 and

Table 3 outline the range(s) of value(s) of γ from laboratory studies of the heterogeneous uptake of NO_3 and N_2O_5 onto surfaces of aerosols of various chemical compositions. It shows to what extent heterogeneous reactivity could come to influence nighttime chemistry and loss of NO_x particularly in the absence of direct, gas-phase NO_3 reactivity (i.e. in regions with little local emissions or/and aged air masses, e.g. desert, oceanic, polar) and the dependence of the uptake coefficients on other factors such as RH and temperature.

2.3.2 Halogen activation from N_2O_5

After uptake onto the surface of aerosol, N_2O_5 undergoes hydrolysis reactions forming nitrate (NO_3^-). In the presence of aerosol containing chloride, N_2O_5 can also undergo a reaction to form gas-phase ClNO_2 :



With f being the yield of ClNO_2 , determined by the ratio of Cl^- to H_2O in a given aerosol sample (Finlayson-Pitts and Pitts Jr. 1999). ClNO_2 can be important to regional NO_x cycling, particularly in coastal regions and over oceans where there is a strong source of chloride (sea salt). It has also been measured at elevated levels away from the influence of the coasts in continental Europe near Frankfurt, Germany (G. J. Phillips et al. 2012) and at several locations across North America such as Colorado (Riedel et al. 2013), the source of chloride coming from either transport from the coastal regions or local generation of soluble chlorides from power plant emissions. As it requires the first step of N_2O_5 uptake (leading to the NO_2^+ cation) into chloride containing particles and N_2O_5 only builds up to significant concentrations at night due to the rapid photolysis of nocturnal nitrates, ClNO_2 is also formed almost exclusively at night. After formation and partition out of the particle phase into the gas phase, ClNO_2 undergoes rapid photolysis in sunlight, releasing NO_2 and Cl radicals:



Photochemically generated $\text{Cl}\cdot$ radicals have been shown to enhance oxidation rates of VOCs and can be competitive with oxidation rates of OH , especially in the early morning when generation of OH is relatively small compared with later in the day (Eger et al. 2019; G. Sarwar et al. 2012; Golam Sarwar et al. 2014).

2.3.3 Interaction with SO_x cycle

DiMethyl Sulfide (DMS, CH_3SCH_3) is a biogenic VOC released by ocean-dwelling phytoplankton which reacts readily with both OH and NO_3 , thus NO_3 can impact the sulfur cycle. As sources of DMS are dominated by emissions of phytoplankton and other ocean dwelling species, DMS can be a major sink of NO_3 in coastal and oceanic regions. The reaction of DMS with NO_3 proceeds via H-abstraction to form HNO_3 and an organosulfur radical $\text{CH}_3\text{SCH}_2\cdot$, which will react rapidly with atmospheric oxygen to form a peroxy radical.

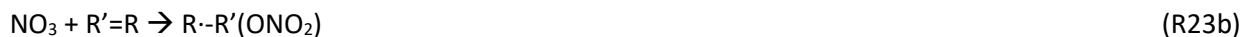


Further reaction of the sulfur peroxy radical with OH or NO_3 is possible and will result in methanesulfonic acid (MSA, $\text{CH}_3\text{SO}_3\text{H}$) and sulfur dioxide (SO_2) and through these, eventually sulfate (SO_4^{2-}) and H_2SO_4 , meaning that radical DMS oxidation introduces an additional, indirect, anthropogenic source of SO_2 ,

supplementing direct emissions from stationary (e.g. coal-fired power plants) or mobile (e.g. ship exhaust fumes) sources. This is important as sulfates play an important role as condensation nuclei for clouds, which determine the cloud droplet number concentration which, for the same content of liquid water, leads to greater concentration of cloud droplets with smaller radii, thereby increasing cloud reflectivity (Boucher and Lohmann 1995). As DMS is the largest source of natural sulfur (40-50%) in the atmosphere (Andreae 1990) its oxidation acts as a significant source of SO_4^{2-} in coastal environments, particularly in more polluted regions where NO_x emissions are large leading to higher production of NO_3 radicals, which react quickly with DMS. Numerous studies have documented the importance of DMS in controlling NO_3 lifetimes (Aldener et al. 2006; Sommariva et al. 2007; Matsumoto et al. 2006; Carslaw et al. 1997; Allan et al. 1999) in the marine boundary layer (MBL) or inferred its importance from stratified concentration gradients of NO_3 in flights over the MBL (Steven S. Brown et al. 2007).

2.3.4 Interaction with RO_x cycle

NO_3 interacts with VOCs via the reactions shown in (R15) and (R16). Regardless of how it is initiated, both the abstraction and addition mechanisms produce a highly reactive alkyl radical ($\text{R}\cdot$) which reacts immediately with abundant atmospheric O_2 to give the peroxy (RO_2) radical:



As described above (2.1.1), RO_2 radicals can interact with NO during the day to generate NO_2 (or organic nitrates) without consuming O_3 , therefore the NO_3 radical reactions which give rise to RO_2 affect regional NO_x cycling and subsequent ozone concentrations. During the night, NO_3 and RO_2 may act as a source of nighttime HO_2 and OH radicals via the alkoxy radical, which can be formed by reaction of RO_2 with NO_3 or another RO_2 . Alkoxy radicals can decompose to release HO_2 or NO_2 (in the case of nitrooxy peroxy radicals), forming a stabilized carbonyl group. HO_2 formed from this decomposition will react with other RO_2 radicals to give OH , which then can enhance oxidation rates of VOCs at night. These mechanisms can thus lead to a wide variety of organic products and inorganic trace gases at night, influencing the chemistry of the region on the following day and beyond. For example, nocturnal NO_3 chemistry with biogenic VOCs such as isoprene or monoterpenes directly contributes to the sequestration of nitrogen into alkyl nitrates but also indirectly to, in addition to the above described O_3 concentrations, regional concentrations of PAN, formaldehyde, CO and eventually to organic aerosols.

2.3.5 Influence on SOA formation

Organic aerosols are either directly emitted from anthropogenic combustion sources in urban areas or biomass burning (referred to as Primary Organic Aerosol, or POA) or are the result of gas-phase organic VOCs being oxidized and partitioning into the aerosol phase over time (referred to as Secondary Organic Aerosol, or SOA). According to modelling studies, SOAs make up a considerable fraction of the global organic aerosol budget (20 – 60%) in the northern hemisphere (Q. Zhang et al. 2007), including up to 90% in forested regions (Kanakidou et al. 2005) due to the presence of ubiquitous biogenic VOC (BVOC) emissions. NO_3 drives this partition from the gas phase by fast reaction with BVOCs to give alkyl nitrates (ANs) and other oxidized products, which after further oxidation lead to semi-volatile molecules which

can condense into the particle phase. As a result, the nitrate ester bonding group (R-ONO₂), the functional group which defines ANs, has been identified in and contributes significant mass to SOA particles in field studies in forested regions in California, United States (Rollins et al. 2013). While all main atmospheric oxidants contribute to AN formation, NO₃ is currently understood to be strongest source of ANs (Horowitz et al. 2007) and thus is likely one of the single largest contributors to global SOA. The global yields of SOA via BVOC oxidation remain quite uncertain however, estimated at 90 ± 90 TgC yr⁻¹ (Hallquist et al. 2009). Much of this uncertainty can be attributed to the uncertainty in the reported SOA yields from different studies of BVOCs reactions with radicals. As a result there have been large ranges in SOA yields reported for NO₃ reactions with: for example, isoprene of 2 – 24% (Rollins et al. 2009; Juliane L. Fry et al. 2018; Ng et al. 2008); Limonene (14 – 57%) (J. L. Fry et al. 2011; Juliane L. Fry et al. 2014); or β-Caryophyllene (86 – 146%) (Jaoui et al. 2013).

2.4.1 Organic Nitrate chemistry

Alkyl Nitrates are organic molecules which contain the functional group RONO₂, together with peroxy nitrates (RO₂NO₂) or peroxyacyl nitrates (R(O)O₂NO₂) they are formed with NO_x reactions with VOCs in the atmosphere and can collectively be referred to as Organic Nitrates (ONs). For the purposes of this thesis, they can also be considered as any organic molecule which releases NO₂ when undergoing thermal decomposition. Photochemical lifetimes of ONs in the atmosphere are typically on the order of several days, therefore they act as a reservoir transporting NO_x away from its sources and into remote regions. An exception to this are the alkyl nitrates form by reaction of the highly prevalent isoprene with NO₃ during the night where the multiple functional groups, especially the electron-withdrawing C=O group, in the molecules act to promote weaker bonding in the nitrate ester group, resulting in quantum yields near unity and lifetimes on the order of several hours following sunrise (Müller, Peeters, and Stavrou 2014).

2.4.2 Peroxy(acyl) Nitrates

Peroxynitrates (RO₂NO₂) and Peroxyacyl Nitrates (R(O)O₂NO₂) (PNs) are formed from photochemically produced alkyl peroxy radicals (RO₂) reacting in the presence of NO₂:



By far the most common PN is peroxyacetyl nitrate (PAN) though higher carbon chain analogues are known, the most common being peroxypropyl nitrate (PPN) and methacrolein peroxyacyl nitrate (MPAN). PAN itself typically makes up, according to field studies, approximately 70 – 90% of the peroxy nitrate budget e.g. (Roberts et al. 1998, 2002). PAN is formed from the photochemical reaction of acetaldehyde with OH to give a carbonyl (C=O) functionalized RO₂ or acylperoxy radical.



OH initiated oxidation of acetaldehyde is not the only source of PAN however, as other routes to generation of the $\text{CH}_3\text{C}(\text{O})\text{O}_2$ radical, or longer carbon chain analogues, are possible and known (Roberts et al. 1998; Bertman and Roberts 1991). PAN can also be generated from the photolysis of acetone, followed by reaction (R30):



Or by photolysis of methylglyoxal (MGLY), followed by reaction (R30):



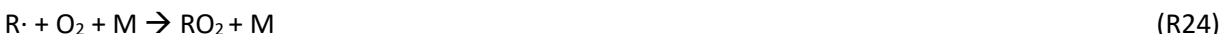
The reaction (R30) has the key feature that it is reversible, indeed most PAN in the atmosphere is lost due to thermal decomposition which occurs at lower temperatures and pressures compared to other organic nitrates (Fischer et al. 2014). PAN lifetimes are strongly dependent on ambient temperatures and range from a few hours under most conditions and up to months at low temperatures and high altitudes (Singh 1987). This means PAN, its analogues, and PNs act as a temporary reservoir for NO_x and organic radicals, and to varying degrees as a source of transport into remote areas where they may act as a considerable source of NO_x , RO_2 and ultimately HO_x in the dark.

Much of the precursor molecules to the acylperoxy radical (and therefore PAN) detailed are themselves generated by VOC reactivity. Larger carbon chain molecules will undergo oxidation with OH to give peroxy radicals which will undergo a series of possible reactions, including decomposition reactions, resulting in some of the carbonyl-containing molecules described above, or longer chain analogues. If the VOC in question also contains a carbon-carbon double bond, reactivity towards NO_3 and O_3 increases offering more routes to these PAN precursors. In this way, isoprene degradation is one of the most significant sources of PAN globally, contributing up to 37% (Fischer et al. 2014).

PNs of all kinds are understood to be a major component of photochemical smog, where it has been shown that PAN production becomes more efficient relative to O_3 in highly polluted air masses (Fischer et al. 2014). In some cases PAN mixing ratios as high as 70 ppb have been reported (Finlayson-Pitts and Pitts Jr. 1999), which are significant as it is a strong lachrymator (eye irritant), and has been shown to cause respiratory problems in acute exposure, comparable to O_3 , NO/NO_2 and SO_2 (Vyskocil, Viau, and Lamy 1998). Long term chronic exposure to PANs studies are currently underway with links to respiratory and cardiac health problems. They are also mutagenic and phytotoxic to plant species (Sun and Huang 1995), raising concerns about potential negative effects on agriculture or ecosystems, either directly or indirectly by transport of NO_x into more rural areas and thereby impacting local O_3 concentrations.

2.4.3 Alkyl Nitrates

Alkyl nitrates (ANs) are organic molecules which contain the functional group RONO_2 (also known as a nitrate ester). They are formed through both photochemically driven processes with the OH radical during the day as well as nocturnal oxidation with NO_3 radicals.





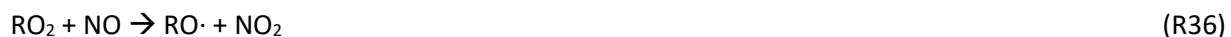
Both of these mechanisms of RONO_2 can proceed via addition across a carbon-carbon double bond or initiated by H-abstraction from a saturated VOC. The H-abstraction mechanism requires the presence of NO , which reacts quickly with O_3 to form NO_2 at night and therefore not present in large concentrations, limiting nighttime formation of ANs via this mechanism.

AN formation is additionally supplemented by the Criegee mechanism of O_3 radical with unsaturated organics:



In this mechanism, ozone adds across a carbon-carbon double bond via a 1,3-dipolar cycloaddition. While different work ups will lead to different organic products in a laboratory setting, in the atmosphere this is followed by a decomposition yielding a carbonyl ($\text{R}=\text{O}$) group and a peroxy (RO_2) radical. In the presence of NO , this can generate a stable alkyl nitrate molecule.

The reaction of RO_2 with NO also has the possibility to proceed in a different route, where NO_2 and an alkoxy ($\text{RO}\cdot$) radical are generated instead of an alkyl nitrate:



Similarly, at night the reaction with NO_3 with RO_2 can also regenerate NO_2 and an alkoxy radical as per (R20).

The yield of ANs relative to $\text{RO}\cdot$ can be described as a branching ratio and is determined by the size and functionality of the R group. Smaller R groups (e.g. C1-3 hydrocarbon chains) tend to give smaller yields of just a few percent, while R groups larger than this can give a yield of ~30 – 35% (Finlayson-Pitts and Pitts Jr. 1999). The yields of the NO_3 addition mechanism also depend strongly on the R group, but for larger VOCs, particularly BVOCs, tend to be quite large. A review of several common BVOCs, such as isoprene and monoterpenes, found yields with NO_3 in the range of ~50 – 70% (Lee Ng et al. 2017) for such molecules. This makes ANs of particular interest in remote, 'clean' regions – typically with low background NO_x – where modelling studies have shown that 30 – 70% of NO_y is sequestered in the form of alkyl nitrates (Madronich and Calvert 1990). Forested regions, in particular, are important to alkyl nitrate chemistry as

they are a very strong source of BVOCs, from foliage which tend to be larger (C5-10), contain carbon-carbon double bonds, and have large rate coefficients with NO_3 and OH.

The major sinks for ANs are dry deposition on to surfaces, photolysis or further oxidation. Chemical lifetimes with respect to oxidation and photolysis tend to be quite long for many kinds of ANs, on the order of days to weeks (Finlayson-Pitts and Pitts Jnr. 1999) and thus, similar as with PNs, ANs are able to transport NO_x away from polluted regions and into more remote ones. This is not the case with all ANs however, as the lifetime is highly dependent on the R group and intramolecular interactions in many biogenic ANs can weaken the bonding in the RONO_2 group leading to relatively short (hours to days) photochemical lifetimes (Müller, Peeters, and Stavrakou 2014). Short lifetimes contribute to higher rates of NO_x recycling and consequently affect regional O_3 levels. Further oxidations of ANs can lead to increased partitioning into the aerosol phase to form SOA (see 2.3.5) due to reduced volatility. This link into the particle phase means that ANs chemistry is directly tied into the global aerosol budget, both in terms of contribution the growth of carbon mass in particles and their hygroscopic properties, or tendency to take up water. High O:C ratios, typical in the highly-oxidized, semi-volatile BVOC products, are associated with higher hygroscopic growth factor and higher cloud condensation activity (Massoli et al. 2010; Boucher et al. 2013), modifying the amount light scattered by particles and therefore modifying the radiative forcing properties, with consequences for global climate.

2.5.1 Atmospheric Isoprene Chemistry

Isoprene (C_5H_8) or 2-methyl-1,3-butadiene is a biogenic, volatile organic molecule, emitted by many types of plant species. Isoprene was discovered as a plant emission by (Sanadze and Kursanov 1966) in the 1960's after researchers had previously identified isoprene as a product of burning rubber and heating terpenes. Despite this, it was not universally accepted at the time that plants produced isoprene until it was proven by mass spectroscopy in the early 1970's (Sharkey and Yeh 2001). In the late 1860's, studies of many natural organic products, such as essential oils and resins, revealed a common ratio of carbon to hydrogen (5:8), leading to compounds which were shown to exhibit this ratio being coined 'terpenes'. Isoprene is the simplest terpene (sometimes referred to as a hemiterpene) and when repeating units of the isoprene skeleton are joined together this results in monoterpenes (2 isoprene units), sesquiterpenes (3 isoprene units), diterpenes (4 isoprene units) and so forth, up to long polymer chains – called polyterpenes – present in e.g. plant-derived rubber. This makes isoprene an important biomolecule in the atmosphere-biosphere exchange both as a direct emission and as the building block of other larger volatile species released into the atmosphere. Today, we understand that isoprene is the single largest non-methane hydrocarbon (NMHC) emission into the atmosphere and constitutes nearly 50% of all global VOC emissions with a flux of $\sim 600 \text{ TgC yr}^{-1}$ (Guenther, et al. 2006). As the source strength is so strong products of radical-initiated reactions which eventually result in ANs, SOA, and other atmospherically important VOCs and trace gases can represent large shares of the relevant local, regional and even global budgets, even if the yields of those reactions are small.

In the atmosphere, isoprene reacts quickly with all three of the atmospheres' main oxidants: OH, NO_3 and O_3 . Reactions with OH will proceed by addition of OH to one of isoprene's double bonds, leaving an unpaired electron which rapidly reacts with molecular oxygen forming the peroxy radical. This is similar to the addition of NO_3 , producing an RONO_2 functionalized nitrooxy peroxy radical and the 1,3-dipolar addition of O_3 , forming Criegee intermediates which decompose to give a carbonyl and a peroxy radical. The rate coefficients of these addition reactions are $k(\text{OH} + \text{Isoprene}) > k(\text{NO}_3 + \text{Isoprene}) > k(\text{O}_3 + \text{Isoprene})$, which is the reverse of typical atmospheric concentrations of each of these oxidizers, where O_3

concentrations are usually orders of magnitude (10^{10} - 10^{12} molecule cm^{-3}) higher than NO_3 (10^7 - 10^9 molecule cm^{-3}) which are orders of magnitude higher than OH (10^5 - 10^6 molecule cm^{-3}).

Following an addition reaction and subsequent generation of an isoprene peroxy radical, these radicals are able to further react with oxidizers, including NO_3 , HO_2 and other RO_2 molecules resulting in alkoxy radicals, which are further able to decompose to release NO_2 , HO_2 (and therefore OH) and organics, shortening the carbon chain. The results of all these different reactions is a suite of multi-functionalized organic products based on the isoprene skeleton (isoprenoids) or C3-4 organic molecules from decompositions. For example, according to the master chemical model (MCM, (Jenkin, Young, and Rickard 2015)) OH-initiated radical oxidation will generate products containing carbonyls (e.g. HCHO, methacrolein ($\text{C}_4\text{H}_6\text{O}$)), hydroperoxides (ROOH), hydroxyls (ROH) and, in the presence of NO_x , ANs and PNs. Likewise, NO_3 -initiated reactions of isoprene, which have been reported on in the literature (Perring et al. 2009; Schwantes et al. 2015; Lee Ng et al. 2017), will similarly generate a variety of products with carbonyl, hydroxyl-, epoxy- and hydroperoxy- functionalized isoprenoids in addition to the RONO_2 functional group that results from the initial electrophilic addition of NO_3 to the isoprene double bond.

2.5.2 Formation of Alkyl Nitrates

A full reaction scheme for the oxidation of isoprene by NO_3 is available in appendix B.

The first step in the NO_3 -isoprene reaction scheme is the addition of NO_3 to isoprene, attacking at the electron rich conjugated double bond system. This produces a short-lived, unstable organic radical which quickly reacts with abundant atmospheric oxygen to form two major products: a β -nitrooxy peroxy radical and a δ -nitrooxy peroxy radical (INP), with other minor isomers also formed:

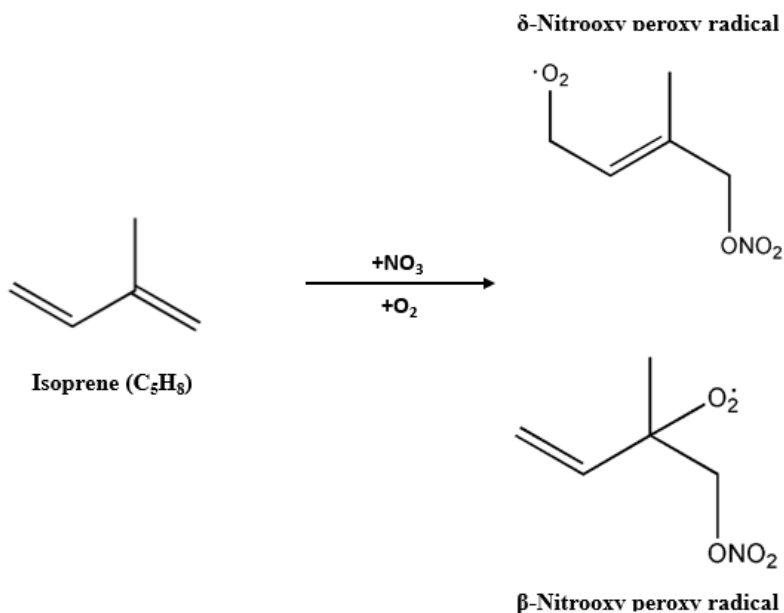


Figure 1. Isoprene + NO_3 reaction forming β - and δ -nitrooxy peroxy isoprene (INP).

These nitrooxy peroxy radicals (RO₂) are short-lived and undergo reactions with other trace gases to form more stable products. A reaction with second equivalent of NO₃, HO₂ or another RO₂ can reduce the INP molecules to give an alkoxy radical:

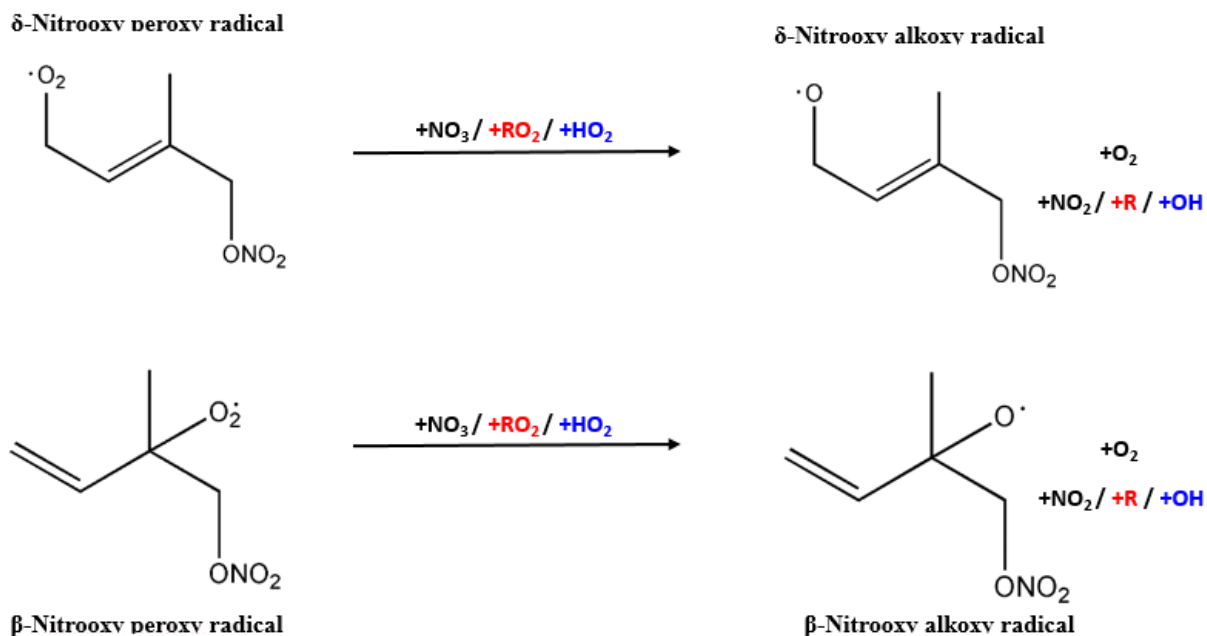
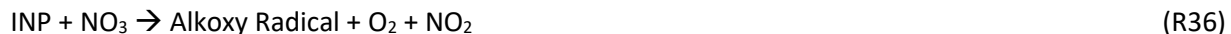
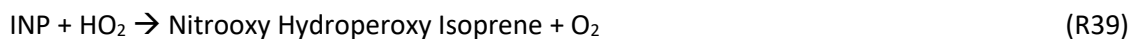
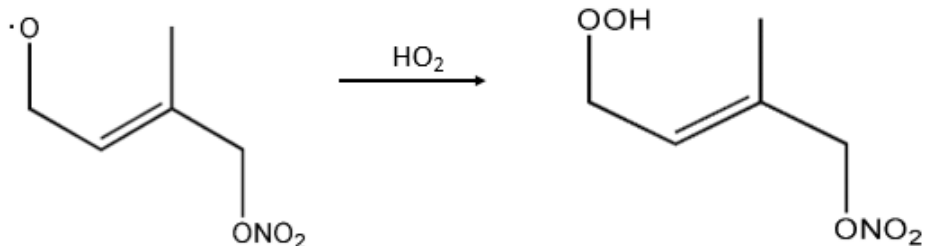


Figure 2. Reaction of INP with NO₃/RO₂/HO₂, producing alkoxy radicals

However, there are other branching pathways which occur in the reaction between INP and RO₂ or HO₂. In the case of reaction with HO₂, a substitution of O₂ can occur creating a relatively stable product:



δ -Nitrooxy alkoxy radical



β -Nitrooxy alkoxy radical

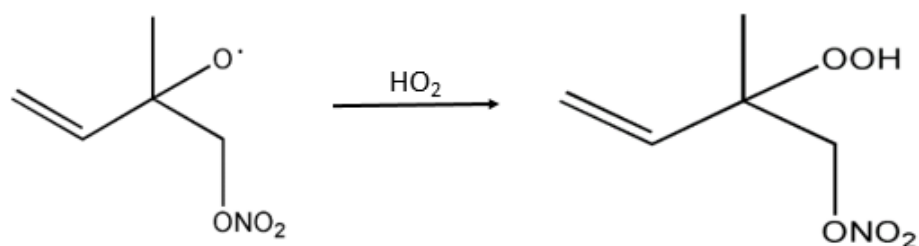
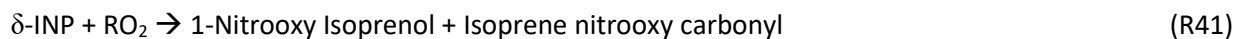
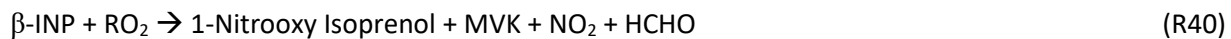
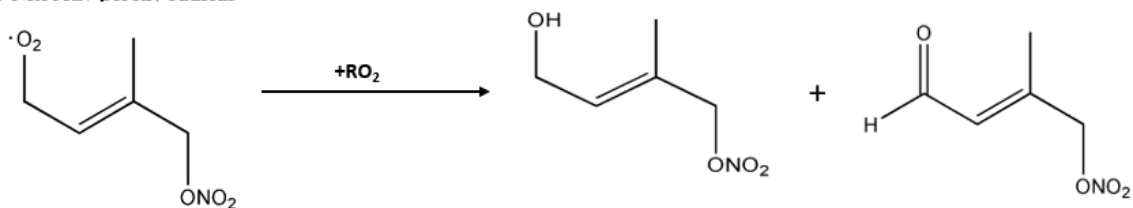


Figure 3. INP reaction with HO_2 , producing hydroperoxy functionalized molecules

While the reactions between RO_2 molecules can yield a variety of different functionalized products including carbonyls ($C=O$), hydroxyls (OH), or in the case of the β -INP isomer, a rearrangement to form methyl vinyl ketone (MVK) and HCHO:



δ -Nitrooxy peroxy radical



β -Nitrooxy peroxy radical

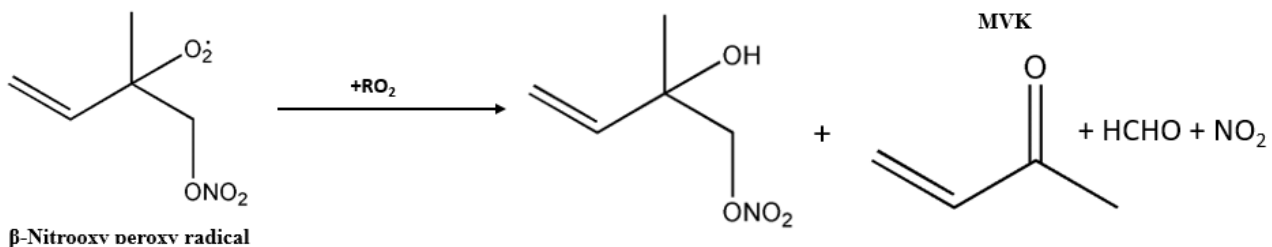


Figure 4. Reaction of INP with RO_2 , forming carbonyl and hydroxyl functional groups

The alkoxy radicals (RO) generated in (R36), (R37) and (R38) will also undergo rearrangements to remove NO₂ or HO₂, in the case of the δ -isomer, or NO₂ and HCHO (forming MVK) in the case of the β -isomer:

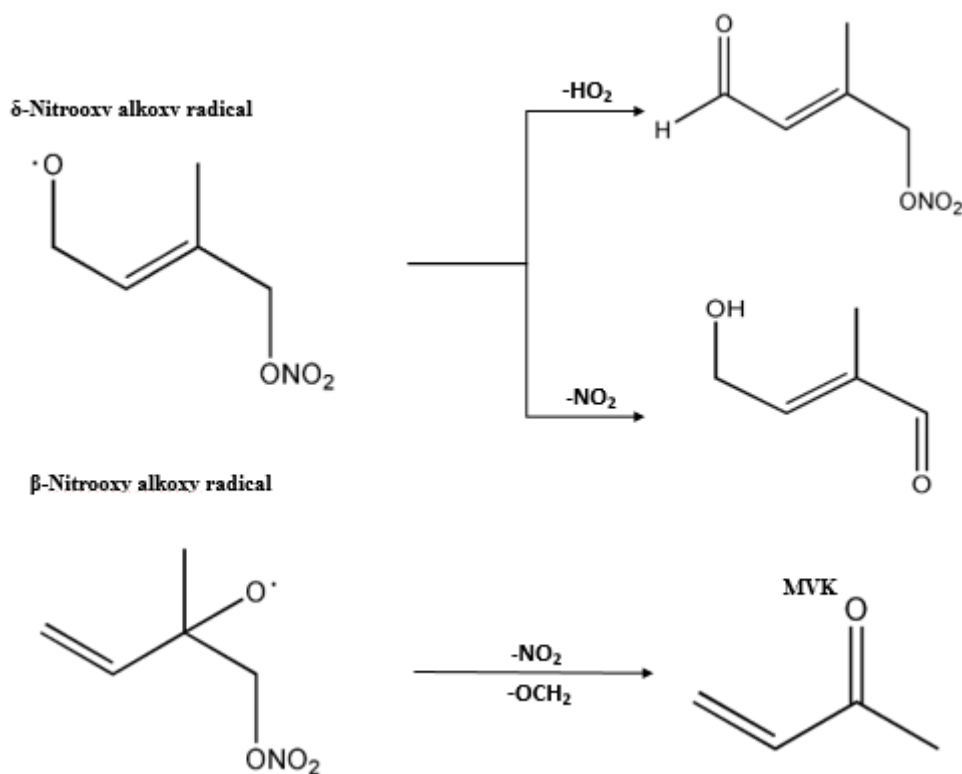
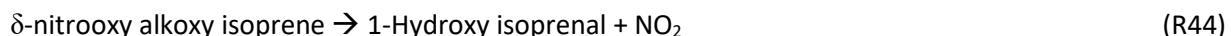
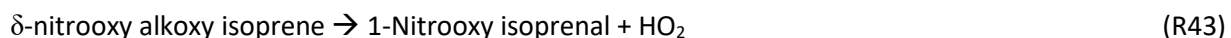
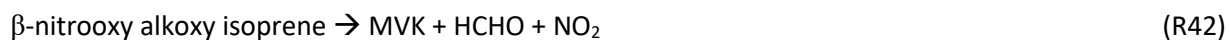


Figure 5. Rearrangement of isoprene nitrooxy alkoxy radicals to give multi-functionalized products

Most reactions in this scheme produce organic nitrates of the form (RONO₂). Of those that do not (R42, R44) these regenerate and release NO₂, which is able to react with O₃ to reform NO₃. Past the first isoprene oxidation, further oxidations are possible with NO₃ attacks possible at the remaining carbon double bonds – forming dinitrate species – or H-abstractions forming new, RO₂ radicals including acylperoxy. Product studies (Schwantes et al. 2015) have identified a suite of different molecules based on the nitrooxy isoprene skeleton, including epoxides generated from the nitrooxy hydroperoxy product (R39); dihydroxy-functionalized nitrate species; and shorter carbon-chain nitrates (e.g. Propanone Nitrate).

2.6.1 Relationship between Σ ANs, Σ PNs, NO_3 , N_2O_5 and NO_x

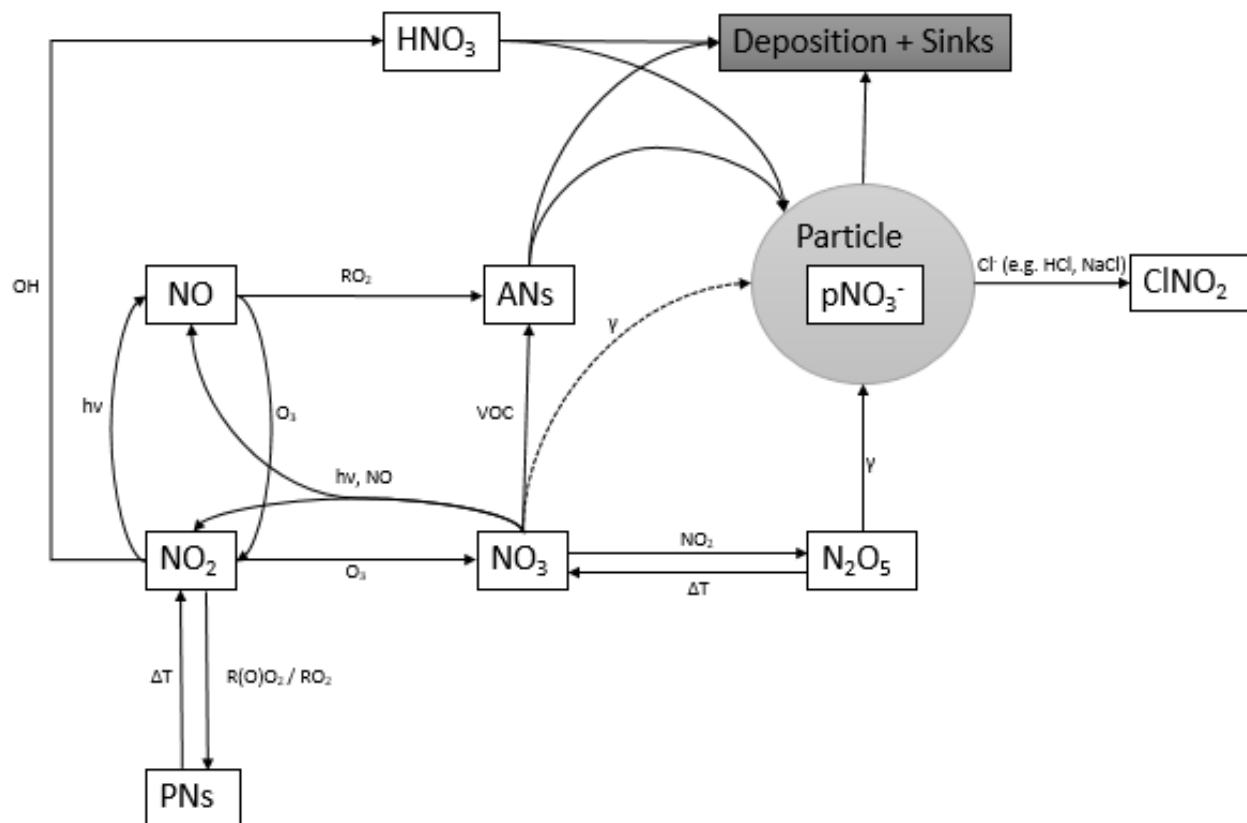


Figure 6. Reaction scheme of NO_x chemistry explored in this thesis. Includes major NO_x reactions from both day and nighttime processes

Figure 6 summarizes the reactions outlined in section 2 and shows the role of NO_x chemistry in the atmosphere, both during the day and during the night, including some of the most important interconversions between NO_x and NO_y trace gases. Photolysis drives the formation of O_3 from NO_2 , while O_3 drives the formation of NO_3 , which is the most important nocturnal oxidizer. NO and NO_3 react with VOCs to form alkyl nitrates, while NO_2 can react with VOCs to give peroxy nitrates and peroxyacyl nitrates. NO_3 and N_2O_5 undergo uptake onto the surfaces of particles to give particle nitrates (pNO_3^-) during the night, while NO_2 can react with the daytime oxidizer OH to give HNO_3 , which may also transition into the particle phase. NO_x can then be recycled from the particle phase by halogen activation, yielding e.g. ClNO_2 , or undergo deposition via NO_y molecules, primarily in the form of ANs , HNO_3 or as pNO_3^- in the particle phase.

The 5-CRD instrument is able to directly measure atmospheric concentrations of NO_2 , NO_3 , N_2O_5 , Σ PNs and Σ ANs. The main aims of this thesis are to take the measurements of these trace gases from laboratory experiments and field campaigns and discuss the importance of nighttime NO_x chemistry in controlling the NO_x and VOC budgets under the chemical processes outlined in this section.

3. Instrumentation & Methods

NO₂, NO₃, N₂O₅ and the sum of organic Nitrates (ΣPNs and ΣANs) were measured during this project by cavity ringdown spectroscopy. The instrument used for these measurements was constructed by a research group at the Max Planck Institut für Chemie, Mainz, Germany and has previously been described in detail and deployed for measurements before (Sobanski, Schuladen, et al. 2016; Sobanski, Tang, et al. 2016). In the following chapter, the principles of Cavity Ringdown spectroscopy will be explored and a description of the technical information for the acquisition and analysis of data from the 5-channel cavity ringdown system (5-CRD) will follow. Reviews in the literature which detail the principles of different cavity ringdown systems and the applications of CRD to atmospheric measurements are available from (Berden, Peeters, and Meijer 2000; Steven S. Brown 2003).

3.1.1 Principles of Cavity Ringdown Spectroscopy

In its simplest form, cavity ringdown spectroscopy consists of two highly reflective mirrors positioned either side of an optical cavity. The cavity itself is a straight, hollow tube normally a few mm in diameter and made from a durable material such as steel or quartz glass. It differs from differential absorption spectroscopy, which measures optical extinction from absolute differences in light intensity. By contrast, A CRD set-up measures a time-dependent exponential decay in light intensity following a pulse of light into the cavity. The name 'ringdown' comes from the similarity of the signal to the signal of a sound decay after ringing a bell. Cavity ringdown techniques have first been described in the 1980's and 1990's (O'Keefe and Deacon 1988), where they were developed initially as a method of testing the reflectivity of mirrors (Scheret et al. 1997). Cavity ringdown set-ups take advantage of the time dependent exponential decay by relating this measurement to a concentration of an absorbing, trace gas species.

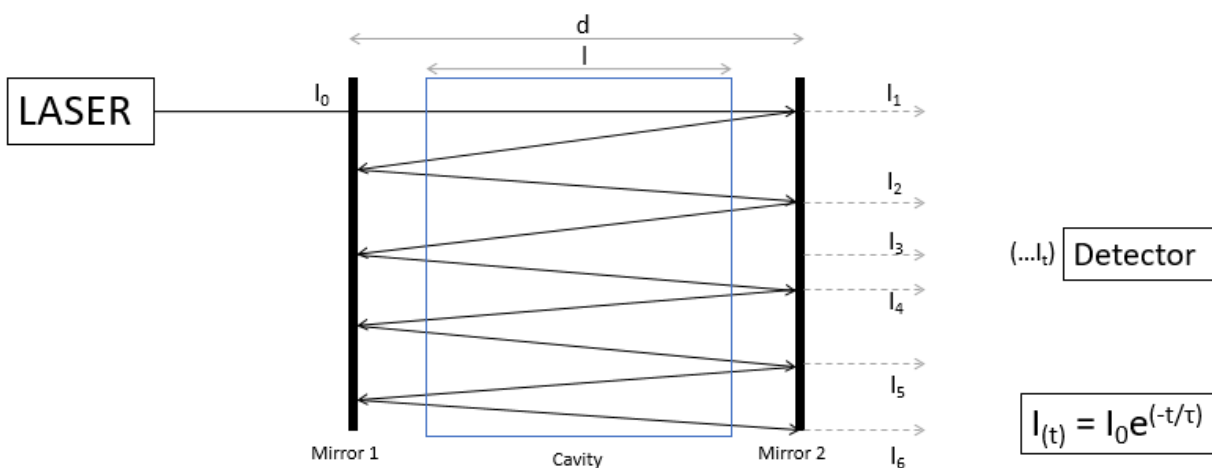


Figure 7. Cavity Ringdown set-up showing the initial laser intensity, I_0 , entering the cavity and a transmitted intensity ($I_1, I_2, I_3...$) leaving the cavity and arriving at the detector. This produces an exponential decay function where $I(t) = I_0 e^{(-t/\tau)}$

Figure 7 is a simplified diagram representing a cavity ringdown set up. The optical cavity of length l sits between two, highly reflective mirrors ($R > 99.9998\%$ at the selected wavelength) of light positioned with a distance d apart to provide a long path for extinction spectroscopy. Initial light intensity entering the

cavity, I_0 , is determined by the source (In this example: a monochromatic laser) and the transmittance of the mirrors ($T = 1 - R$), through which the light enters when the source is on. A pulsed cavity set up makes use of modulated, laser pulses (10 – 100 ns) with a coherence length short enough to ensure no interference becomes established within the cavity (O’Keefe and Deacon 1988). Inside the cavity, photon propagate between the two mirrors and with each reflection, assuming negligible absorbance on the mirrors themselves, a small fraction of the light is transmitted according the current intensity within the cavity and T . When the laser is switched off, photons within the cavity continue to leak out with every pass between the mirrors. The intensity of light seen by the detector at every at any given pass, $I_{1,2,3...}$, forms the basis of a time-dependent exponential decay curve, as the light intensity lost via transmission through the mirrors is governed by $(I_{0,1,2,3...} \cdot T)$. It is this exponential decay which is the signal measured in CRD. The intensity of light seen at the detector at time t can therefore be predicted:

$$I(t) = I_0 e^{(-t/\tau)} \quad \text{(Equation 5)}$$

The many passes between the two mirrors effectively increases the path length several orders of magnitude compared to the length of the cavity (cm to km). In spectroscopy, a high path length is associated with high sensitivity, and this is the case for CRD set-ups, allowing for the measurement of even trace amounts of absorbing gases including down to the parts-per-trillion range. In the presence of a molecule which absorbs or scatters light with absorption coefficient α , the intensity of light will appear at the detector to reduce faster, as each traverse of light through cavity will reduce intensity by a further $(\alpha \times l)$, where l is the length of the cavity and not be confused with the distance between the mirrors, d . This implies that if α is known, the difference between the light intensity seen at the detector in the presence and absence of an absorbing or scattering molecule can be related back to its concentration:

$$[X] = \frac{l}{dc\sigma_{(x,\lambda)}} \left(\frac{1}{\tau} - \frac{1}{\tau_0} \right) \quad \text{(Equation 6)}$$

Where the concentration of absorbing/scattering molecule X , $[X]$ (molecule cm^{-3}), is related to the ringdown time in the presence of an absorber, (τ) ; the ringdown time in the absence of an absorber (τ_0) (both in s); the speed of light, c (cm s^{-1}); and σ , the effective absorbing cross section ($\text{cm}^2 \text{ molecule}^{-1}$) of molecule X at wavelength λ (nm). As the decay occurs on short time scales (on the order of microseconds) several thousand ringdowns can be collected and averaged every second.

A cavity ringdown set up for the use of measuring atmospheric trace gases will compare an artificially generated null signal (known as a zero) against the signal in ambient air. When an absorbing or scattering molecule enters the cavity during the measurement period, the intensity of light will build up less and will decay faster, relative to the zero signal (Figure 8).

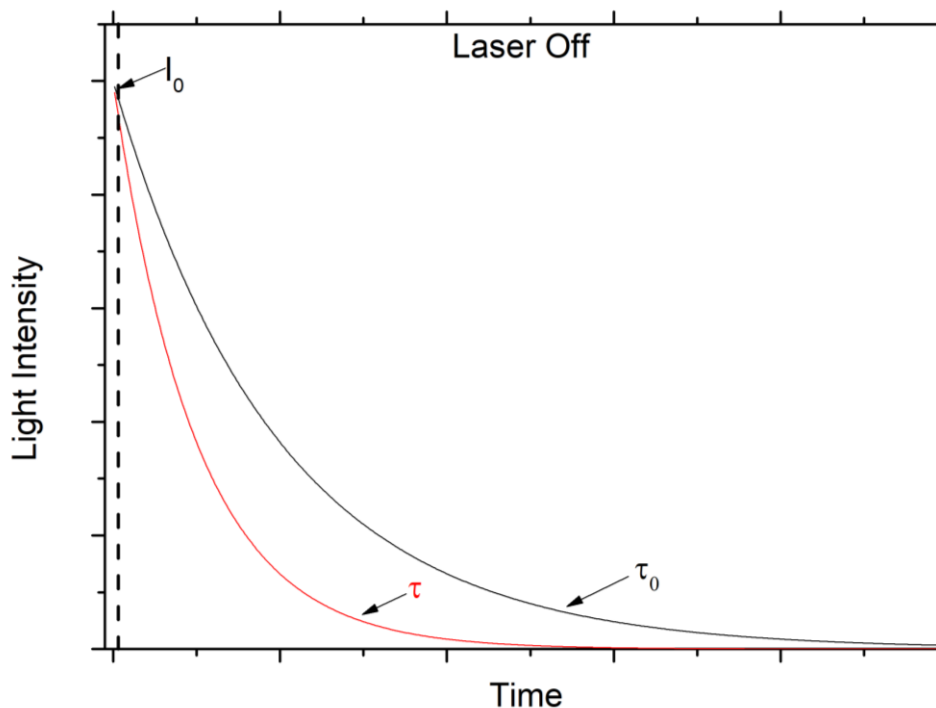


Figure 8. A ringdown signal comparing τ with τ_0 . The difference between the two is caused by the presence of a molecule which absorbs or scatters light at the wavelength(s) of the light source.

In the context of atmospheric chemistry measurements, advantages of the CRD method include the previously mentioned high measurement sensitivity due to the long effective path length over which molecules absorb (> 10 km). Monochromatic light-sources can additionally be used to ensure high selectivity of the particular molecule of interest. If multiple cavities are working in concert, one can take advantage of molecules which are easily converted (e.g. by photolysis, oxidation or thermal decomposition) to allow for accurate, comparative determination of concentrations. For example, two cavities which both detect NO_2 could, in principle, be designed to give all NO_x (and thus, NO by subtraction) if one of these cavities has a feature which could rapidly convert NO to NO_2 or vice-versa (e.g. by reaction with excess O_3). Cavity ringdown systems are also relatively insensitive to short-term fluctuations in light source intensity, as they relate an extinction within the cavity to a decay time. Cavity ringdown is also an absolute measurement technique, where the concentration of the molecule(s) of interest are directly inferred from the measurements, thereby eliminating the need for regular calibrations and preventing the additional associated uncertainties.

3.2.1 Instrument Design

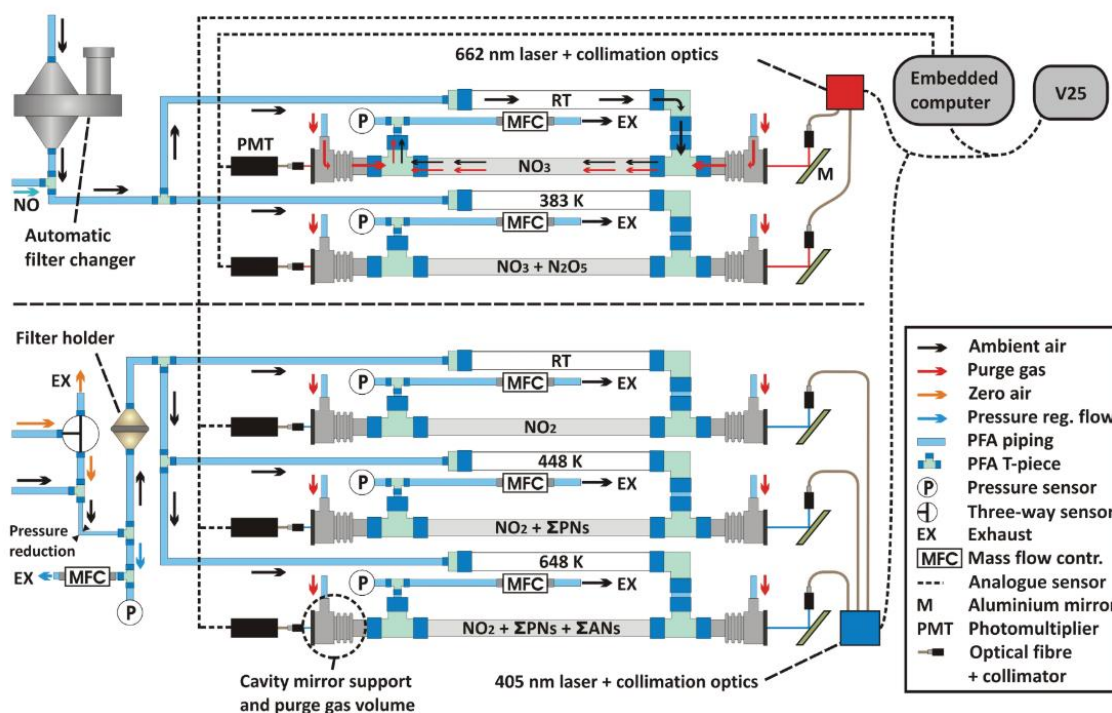


Figure 9. Instrument schematic of the five-channel cavity ringdown (5-CRD) system from (Sobanski, Schuladen, et al. 2016).

The five channel cavity ringdown (5-CRD, Figure 9) system consists of five Teflon-lined (DuPont, FEP, TE9568), stainless-steel cavities, 70 cm in length, approximately 1 mm thick with an inner diameter \approx 8 mm. The cavities are temperature-controlled with heated jackets (HORST GmbH MA07059) to reduce mechanic stress caused by temperature fluctuations at the measurement site. The cavities are fixed into two PFA T-pieces (Swagelok) which are attached to two adjustable metal supports that house the mirrors, which are at a distance of 90 cm apart. This set-up allows for proper alignment of the lasers. A small flow of (\sim 160 standard cubic centimeters per minute, sccm) synthetically generated zero-air (Fuhr GmbH, CAP180 air purifier) is added near the ends of the supports for protection of the mirrors. Using a purge flow in this way has the side-effect of reducing the effective length over which the analytes (ambient gas) flow within the cavity, thus the sensitivity, but allows for continuous use over long measurement periods (i.e. during field campaigns).

Physical parameters (e.g. temperature, pressure, valves) are read and controlled by the self-designed control unit known as a V25. The V25 regulates flows both in and out of the cavities with mass-flow controller units (MKS) attached to a pump. Pressure reduction in the cavities is achieved by the use of a $\frac{1}{4}$ " PFA line, positioned near the main inlet, and is recorded by the use of a pressure sensor for each cavity. The 5-CRD system additionally makes use of a dynamic pressure regulation system which uses a mass-flow controller to selectively siphon air away from the main flow (6.3 standard litres per minute, SLM) to reduce or increase pressure to a set-value determined by an additional pressure sensor, measured shortly after the main inlet and pressure reduction but before the flow is split into the three cavities.

The V25 unit also controls the modulation of the lasers. The 5-CRD uses two laser diodes at 405 nm and 662 nm. The lasers are housed in two self-build casings with optical components for isolation and beam collimation. The light is coupled into the cavities using 50 μm core fibre optic cables, which are spliced to split the light intensity into two (for the 662 nm laser) or four (for the 405 nm laser). The fibre optics are focused onto aluminum mirrors positioned behind the cavity mirrors which direct the light into the cavities. Light intensity escaping the cavities is measured and transformed into an electrical signal by photomultiplier tubes (Hamamatsu H10492-012 at 662nm, H10492-002 at 405 nm) positioned just behind the mirrors. Data acquisition for the 5-CRD is performed by an embedded computer system (National Instruments PXIe-8135). Determination of the of the decay constants (ringdowns) is achieved using the linear regression of sums (LRS) fitting method (Everest and Atkinson 2008), allowing for the acquisition of data at a time resolution of up to and exceeding one data point per second.

The 405 nm channels measure NO_2 at ambient temperature (but the cavity is maintained at 306 K); NO_2 and the sum of peroxy nitrates and acylperoxy nitrates (RO_2NO_2 and $\text{R(O)O}_2\text{NO}_2$, respectively. Collectively referred to as ΣPNs) at 448 K; and NO_2 , ΣPNs and the sum of alkyl nitrates (RONO_2 , referred to as ΣANs) at 648 K. The 662 nm channels measure NO_3 at ambient temperature, and the sum of NO_3 and N_2O_5 at 383 K. A zero signal (τ_0) was obtained in the 405 nm channels by use of a three-way valve controlled by the embedded computer unit, which alternates between ambient measurement and flooding the cavities with synthetically generated zero air with negligible concentrations of NO_2 . The zero signal in the 662 nm channels was generated by use of introducing a small flow (~ 8 sccm) of concentrated NO (100 ppm in N_2) into the main flow (15 SLM) allowing it to react with the ambient NO_3 , and NO_3 generated via thermal decomposition of N_2O_5 . The residence time of ~ 1.2 seconds in the inlet has been previously shown (Sobanski, Schuladen, et al. 2016) to be sufficient enough to completely titrate all NO_3 under realistic atmospheric concentration conditions.

3.2.2 Detection of NO_2 at 405 nm

As described above, a cavity ringdown set-up compares the time-dependent ringdown signal in the presence of an absorber against the signal in the absence of one. The absorption spectrum of NO_2 has been characterized several times (Voigt, Orphal, and Burrows 2002; Vandaele et al. 2003) with the presence of strong absorption bands known in the region of 390 – 420 nm. Within this range the absorption band at 405 nm ($\approx 6 \times 10^{-19} \text{ cm}^2 \text{ molecule}^{-1}$, Figure 10) is a particularly useful region as 405 nm laser diodes are commercially available and relatively cheap (e.g. Blu-ray disk readers). Absorption of NO_2 at 405 nm allows the modification of Equation 6:

$$[\text{NO}_2] = \frac{l}{d} \times \frac{1}{c\sigma(\text{NO}_2)} \left(\frac{1}{\tau} - \frac{1}{\tau_0} \right) \quad \lambda = 405 \text{ nm} \quad (\text{Equation 7})$$

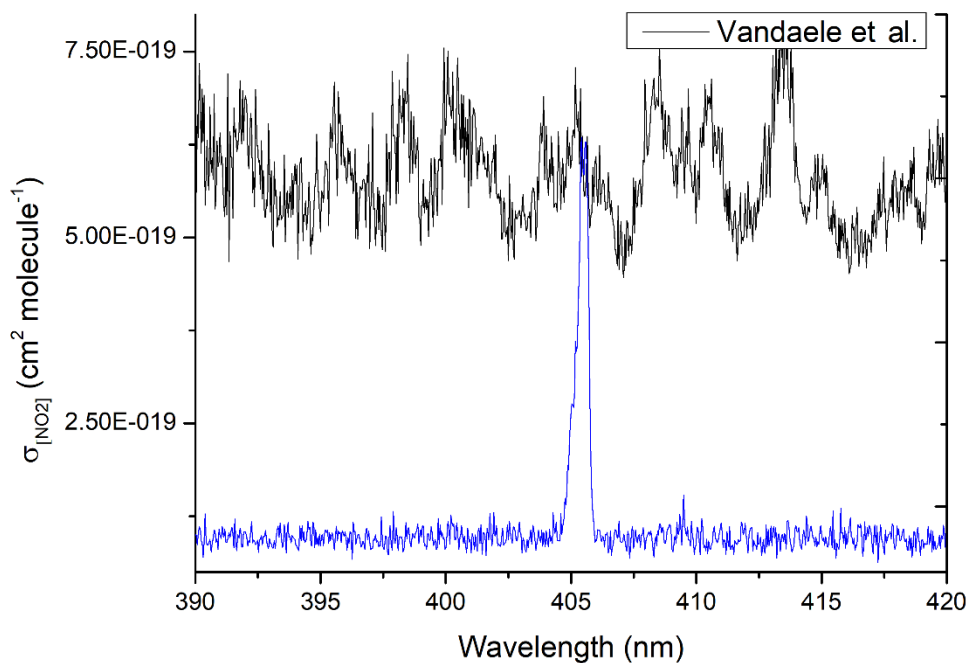


Figure 10. Absorption cross section of NO_2 (Vandaele et al. 2003) with a typical 405 nm laser emission spectrum.

3.2.3 Detection of NO_2 via thermal dissociation

The 5-CRD makes use of two, vertically mounted, quartz-glass ovens, approximately 50 cm long and positioned ahead of two of the 405 nm cavities, for detection of species which decompose to NO_2 upon heating. The ovens design consists of a heating wire, which can be selectively controlled by a voltage signal provided by the V25, wrapped around the first ~ 10 cm of the quartz-glass with a thermocouple positioned between the wire and the glass. These ovens are then wrapped in several layers of heat-resistant fabric for insulation. The heated section of the ovens is filled with glass beads (400-600 μm diameter, Sigma-Aldrich G9268) resting on top of a 2 cm long, fritted glass surface approximately 15 cm downstream from the entrance to the ovens. The beads and the frits serve to increase the instrument's surface area in order to scavenge organic radical species formed with NO_2 via thermal dissociation (see below). The oven set temperatures are determined in laboratory experiments by passing a source of a representative organic nitrate molecule through the oven(s) and increasing the temperature until no more signal can be obtained. In the case of the ΣPNs channel, the representative molecule selected was peroxyacetyl nitrate (PAN), for the ΣANs channel the representative molecule selected was isopropyl nitrate (iPN).

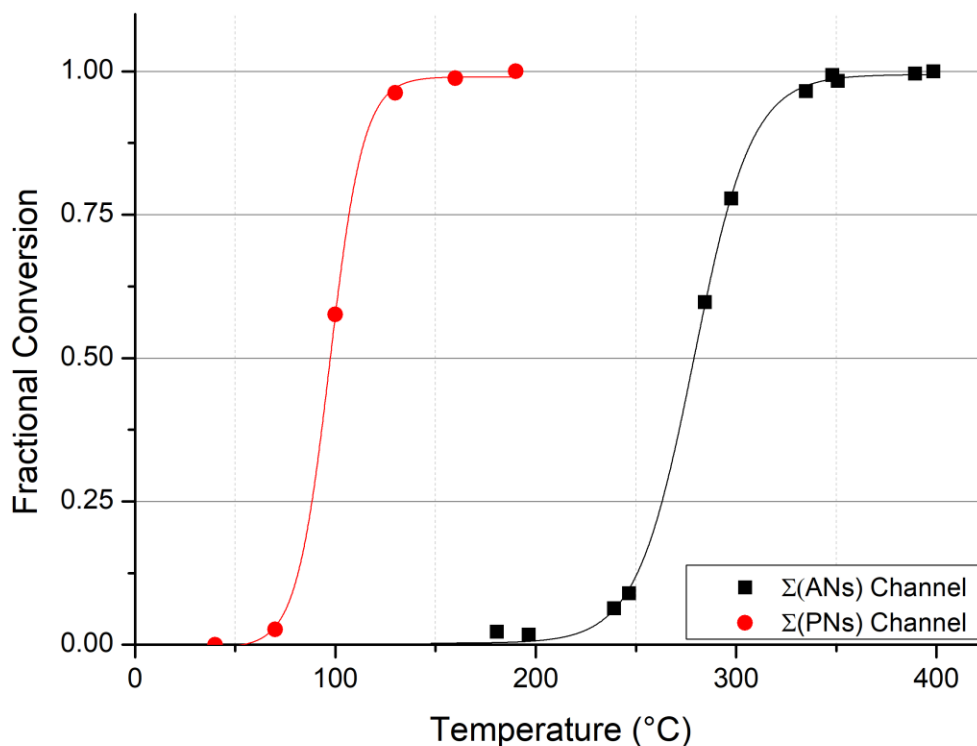


Figure 11. Thermogram of NO_2 yield from peroxyacetyl nitrate (PAN) and isopropyl nitrate (iPN) as a function of set temperature.

Figure 11 details the NO_2 yield from this approach, referred to as a thermogram. The ΣPNs channel reaches a maximum signal at $\sim 150^\circ\text{C}$ (423 K) and the ΣANs channel reaches maximum signal at $\sim 350^\circ\text{C}$ (623 K). The set temperatures (448 K and 648 K, respectively) were chosen as to be well within the plateau (maximum conversion) but lower than that required to start decomposing ANs (for ΣPNs) or HNO_3 (for ΣANs). Note that the thermal dissociation of PAN reaches 100% efficiency before significant decomposition of iPN begins, allowing for the determination of the ΣPNs and ΣANs from the differences in signal between the 3 channels.

3.3.1 Data Corrections

The raw data acquired by the 5-CRD is subject to a number of corrections of both a chemical and physical nature, many of which are temperature or time dependent. Below, these corrections are laid out for both the 405 nm and 662 nm channels.

3.3.2 The l/d ratio

As described in (Equation 7), the sensitivity of the measurements is determined not just by the difference in ringdown time but also by the ratio between the length of the cavity, over which the absorbing gas flows (l), and the total distance the between the mirrors, over which light travels (d). This ratio defines the path length which is several kilometers long. As the distances of l and d are known at 70 and 90 cm respectively, the theoretical maximum l/d ratio is simply $70/90 = 0.77$. However, the use of the purge flow,

which protects the mirrors, has the side-effect of reducing the l/d ratio by reducing the distance over which the measurement gas flows in the cavities. The magnitude of this reduction was estimated in laboratory experiments where the total purge flow to all the cavities was varied from 0 sccm to 1,500 sccm for a constant source of NO_2 (1 ppm in N_2 from a calibrated bottle) and a constant outflow from the cavities. The l/d ratios for each of the 405 nm cavities were determined to be $0.73 \pm 3\%$, in agreement with the 0.69 ± 0.02 reported by (Sobanski, Schuladen, et al. 2016).

3.3.3 Effective laser cross section

Laser diode emissions are not infinitely sharp, emitting light over a small range of $\pm \sim 0.5$ nm centered about 405 nm. Absorption of light by NO_2 is therefore over a range of several nanometers and this can affect the measurement of the concentration according to (Equation 7). For the purposes for data acquisition a default value of $\sigma(\text{NO}_2) = 6 \times 10^{-19} \text{ cm}^2 \text{ molecule}^{-1}$ is used. The real emission spectra of the laser were found to be temperature dependent, fluctuating as a function of the laser diode temperature which was influenced by the changes in the ambient temperature at the measurement site or in the laboratory. In order to correct for these fluctuations in wavelength, emission spectra of the laser diodes were recorded during measurement periods at a rate of up to once per hour during use in the field. From these spectra an effective absorbing cross section, $\sigma_{\text{effective}}$, can be calculated by normalizing the contributions of each wavelength, as detected by an on-board spectrometer (Ocean Optics HR4000, 350 – 486 nm, spectral resolution: 0.02 nm) to a reference NO_2 absorption spectrum (Vandaele et al. 2003) and summing up the contributing components. The correction is then given by the ratio of the default value to $\sigma_{\text{effective}}$:

$$\text{Correction Factor} = \sigma_{\text{DAQ}} / \sigma_{\text{Effective}} \quad (\text{Equation 8})$$

With $\sigma_{\text{DAQ}} = 6.0 \times 10^{-19} \text{ cm}^2 \text{ molecule}^{-1}$. The uncertainty associated with the measurement of the spectra is $\approx 5\%$ while the reference spectrum of Vandaele *et al.* reports a total uncertainty of 5%. Spectra were applied to acquired data by tracing a linear interpolation between determined $\sigma_{\text{effective}}$ values onto the relevant CRD-Data time axis (generally averaged to 1 minute) then applying the Correction Factor calculated according to (Equation 8) directly to ppt mixing ratios.

3.3.4 Transmission losses of NO_2

Significant disagreement of ppt mixing ratios between the three 405 nm cavities when sampling from the same NO_2 source (bottle) has been observed, likely a result of the previously described glass bead set-up in the Σ PNs and Σ ANs ovens. The observed NO_2 mixing ratios passing through the ambient temperature channel which does not have a quartz glass oven, instead utilizing a $\frac{1}{2}$ " PFA line, are larger than those seen in both heated channels, presumably as a result of chemical interactions between NO_2 and the surfaces of the instrument. Glass beads introduce a large surface area into the ovens increasing the possible sites for NO_2 to interact with leading to a decline in the signal observed at the detector. While no rigorous attempts have been undertaken to verify this surface-catalyzed removal hypothesis, the observed losses were quantified by varying mixing ratios of NO_2 in dry synthetic air into all three cavities, from 0.5 to 5 ppb, and comparing the signal obtained in the ambient temperature cavity, where it is assumed that surface losses of NO_2 are negligible, against the signal obtained in the heated cavities in a linear regression analysis. The transmissions of NO_2 were determined to be $99.0 \pm 1\%$ for Σ PNs cavity and $96.0 \pm 2\%$ for the Σ ANs cavity. This is in agreement with values reported by (Sobanski, Schuladen, et al. 2016) who determined the transmissions to be $98.5 \pm 2\%$ and $95.5 \pm 2\%$, respectively.

3.3.5 Effects due to Rayleigh scattering

Use of dry zero air to derive a τ_0 requires a correction for the fact that the Rayleigh scattering cross section of water vapor is smaller than that of dry air. (Thieser et al. 2016) investigated the size of this effect by comparing the τ_0 obtained with dry synthetic air and that obtained at various relative humidities (RH) from 10 to 70 %. The obtained cross sectional difference between humid air and dry air was $\Delta\sigma_{\text{Rayleigh}} = (-4.0 \pm 0.4) \times 10^{-27} \text{ cm}^2 \text{ molecule}^{-1}$. This is broadly in line with the value of $\Delta\sigma_{\text{Rayleigh}} = (-5.0 \pm 0.2) \times 10^{-27} \text{ cm}^2 \text{ molecule}^{-1}$ reported by (Fuchs, Dubé, et al. 2009). This value (Thieser *et al.*) implies for a measurement of NO_2 made at 50% RH, 30 °C temperature and 1 bar of pressure a correction of ≈ 200 ppt of $[\text{NO}_2]$ must be applied. In order to reduce the magnitude of this humidity error during the AQABA ship campaign (see section 4), an automatic zero air humidification system was used in which RH sensors actively monitored ambient relative humidity conditions (controlled and measured by a separate V25 unit) and achieved matching of the ambient RH by adjusting the proportion of the of zero air used for the determination of τ_0 into a self-built glass bubbler, filled with deionized water, or into a dry bypass line with two separate mass flow controller units. These two lines then rejoin into a single combined airstream with a second sensor positioned shortly downstream to read the RH of this recombined outflow before entering into the main inlet. The V25 unit compares this reading against the ambient RH measurement and automatically adjusts the flow rate through or bypassing the bubbler to match. The 20% difference between Fuchs *et al.* and Thieser *et al.* determinations of $\Delta\sigma_{\text{Rayleigh}}$ introduces significant source of uncertainty when measuring at high RH and low NO_2 however, this RH matching system reduces the 20% error implied by the difference such that the uncertainty associated with this error in the 5-CRD reduces down from ± 20 ppt to ± 10 ppt.

3.3.6 Radical Chemistry in the heated sections

Thermal decomposition of PNs or ANs in the heated ovens leads to a molecule of NO_2 and the associated organic radical (R(O)O_2 or RO). The organic radicals produced can initiate radical chemistry which may serve to bias the final results in different ways by influencing the concentration of NO_2 . (Day et al. 2002) discusses the influence of these biases in the context of measurements of PNs and ANs, which are dependent on concentrations of non-target trace gases such as NO , HO_2 and O_3 . For example, the thermal decomposition of PN is a reversible reaction and as such organic radicals which are not scavenged by the glass surfaces while passing through the oven can recombine with the thermally-liberated NO_2 , negatively biasing the measurements:



However, in the presence of NO the radical chemistry can generate NO_2 , positively biasing measurements by up to a factor of 3, in the most extreme cases, per peroxyacyl radical:

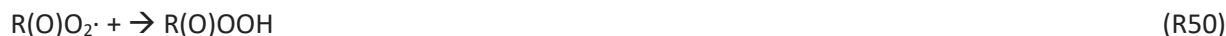


OH generated via this mechanism can also negatively bias measurements by reacting with NO₂ to produce HNO₃, which is not seen by the 5-CRD:

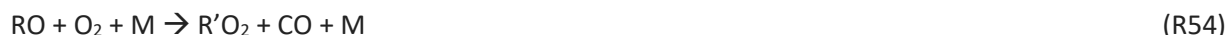


These reactions show that the detection of PN in the cavity is dependent on ambient concentrations of NO and NO₂ as, conceivably, in the presence of high mixing ratios of either trace gas the PN could either completely recombine or generate 3 times the anticipated NO₂ per R(O)O₂ radical. In order to reduce the magnitude of these effects one can take advantage of the fact that there is a significant wall loss of organic radicals onto the quartz-glass surfaces of the ovens, preventing further reaction, by increasing the surface area which organic radicals pass over and therefore the number of sites they interact with. To this end, the heated section of the ovens was filled with 400 – 600 μm glass beads.

In the 648 K ANs oven the increased temperatures compared to the ΣPNs oven make the thermally-derived peroxy acyl radicals thermally unstable, leading to greatly reduced biasing effects with NO and NO₂, due to the number of R(O)O₂ radicals being available to interact with NO_x being reduced. The reactions which bias measurements at these temperatures were posited by (Carr, et al. 2011) and (Chen and Lee 2010) where R(O)O₂ can form an α-lactone and generate OH which, if not lost to the walls, can react with NO₂ forming HNO₃.



Additionally, a thermal decomposition of the alkoxy radical RO· can release CO and an alkyl radical which reacts with oxygen to produce a peroxy radical (R'O₂) and CO. R'O₂ can then react in the presence of NO to form NO₂ if not lost to the wall, introducing a positive bias to measurements under high NO conditions:



Finally, another potentially important source of positive bias is the reaction of NO with O₃ in the inlet to form NO₂. This reaction, unlike the others specified above is significant even at ambient temperatures seen in the unheated cavity.



In order to quantify the magnitude of each of these competing effects, a series of controlled laboratory experiments was performed. For the simple reaction of NO + O₃, a source of NO (1 ppb in N₂) from a bottle was sampled into the instrument, diluted in dry zero air, and mixed with a simultaneous flow of zero air containing varying mixing ratios of photochemically generated O₃ (50 – 200 ppb). By varying the concentrations of NO and/or O₃ for each cavity an effective, time-independent rate coefficient could be obtained as a function of the [NO₂] increase seen in each cavity, when corrected for the previously

discussed effects. These pseudo rate coefficients were determined to be 2.14×10^{-14} , 4.00×10^{-14} , and $5.8 \times 10^{-14} \text{ cm}^3 \text{ molecule}^{-1}$ for the NO_2 , ΣPNs and ΣANs channels, respectively.

For the radical chemistry in the heated channels, experiments were undertaken in the laboratory to determine the magnitude of the effects on the $[\text{NO}_2]$ signal. Experiments sampled a diffusion source of PAN (varied between 0.5 – 10 ppb) in dry zero air into the instrument and added step-wise increasing mixing ratios of NO and then later NO_2 (0 – 8 ppb). PAN was sampled into both ovens as the temperature profiles are different resulting in different chemical processes. Similarly, in further experiments iPN was sampled in dry zero air into the instrument (only seen in the ΣANs channel) in approximately the same varied mixing ratios (0.8 – 12 ppb) with the same approximate mixing ratios of NO then later NO_2 to test the effects on the ΣANs $[\text{NO}_2]$ signal.

These results cannot be fit in a normal linear regression analysis as towards the extremes, i.e. when $[\text{NO}]$ or $[\text{NO}_2]$ approach zero, the dependence of PAN or iPN begins to display non-linear behavior. Thus, the dependence of PAN or iPN on NO or NO_2 necessarily must be simulated to accurately estimate the ‘true’ PAN at zero NO_x , which was achieved using a numerical modelling software FACSIMILE (Curtis and Sweetenham 1987), which solves differential equations, a requirement to understand the complicated, competing chemical reactions in the ovens. In essence, FACSIMILE takes a determined concentration of PAN or iPN and generates the predicted evolution of this over time. This requires the chemical input of concentrations of NO_2 , ΣPNs (represented by PAN), ΣANs (represented by iPN), NO and O_3 ; the accurate profile of the oven temperatures, pressures, and wall surface area; and the complete set of the relevant rate coefficients for each reaction from the literature. The surface area of the walls can be easily estimated according to approximation of the ovens as a series of hollow cylinders or, in the case of the glass beads, as a perfect sphere and the appropriate geometry calculations with the measured dimensions. (Sobanski, Schuladen, et al. 2016) used these geometric approximations to estimate a total reactive surface area (A) of the 5-CRD as $100 \text{ cm}^2 \text{ cm}^{-3}$, which can be used to determine the wall loss rate (k_w) according uptake coefficient of organic radicals, γ :

$$k_w = \frac{\gamma \bar{c} A}{4} \quad (\text{Equation 9})$$

With \bar{c} being the average molecular velocity of the organic trace gas radical. Values of γ are dependent on temperature and are limited by diffusion. These were previously described by (Crowley, Ammann, et al. 2010). The temperature profile was estimated by physically moving a thermocouple up the length of the ovens, measuring the temperature at several points along the length and creating a linear interpolation between measurements. It is assumed that these temperature profiles begin from ambient (298 K, in the case of the laboratory) to internal cavity temperature (306 K), assumed to be uniform. Analyzing the data from these experiments reveals that without correction PAN mixing ratios would be approximately 50% overestimated in the presence of ~ 8 ppb of NO and approximately 40% underestimated in the presence of ~ 8 ppb of NO_2 , while iPN mixing ratios would be 17% overestimated (NO) and 10% underestimated (NO_2), respectively.

To evaluate field data from campaigns, the reverse of this approach was taken where measured datasets of corrected NO, NO_2 , O_3 and either the raw $\text{NO}_2 + \Sigma\text{PNs}$ data; or else the corrected ΣPNs and the raw $\text{NO}_2 + \Sigma\text{PNs} + \Sigma\text{ANs}$ data are entered into the FACSIMILE model. Using the data from the PAN and iPN dependence on NO_x experiments explained above, together with the temperature and pressure profiles

which determine the organic radical wall losses, ‘true’ Σ PN and Σ AN concentrations are reconstructed from the directly measured concentrations of $[\text{NO}_2]$ in each heated channel. The uncertainty of this approach is discussed in 3.3.9.

3.3.7 Detection of NO_2 from thermal decomposition of HNO_3

Nitric acid, HNO_3 , is a major sink of NO_x in the atmosphere, and is thermally stable up to temperatures of ~ 700 K. At higher temperatures HNO_3 undergoes thermal decomposition to NO_2 and thus can represent a significant source of bias in the 405 nm heated channels. Although both the Σ PNs and Σ ANs channels run significantly colder than this, (Wild et al. 2014) reported a 95% conversion of HNO_3 at 650 K, suggesting oven design can have an impact on thermal decomposition functions. This runs counter to findings by (Thieser et al. 2016) who reported a conversion of no more than 10% at 723 K. Previous characterizations of the 5-CRD by (Sobanski, Schuladen, et al. 2016) determined that the upper limit to HNO_3 conversion was $< 0.5\%$ at 648 K by injecting a calibrated source of HNO_3 (~ 30 ppb) into the instrument at the point before the flow splits into three, in order to minimize wall losses. In these experiments thermal decomposition of HNO_3 was not observed in either channel, a finding qualitatively backed up by field data taken over the course of this thesis. For example, during the 2018 SAPHIR campaign (see section 7) chamber experiments, on several occasions the chamber was observed to contain a non-organic source of reactive nitrogen which was detected by another TD-CRD instrument, which measures the sum of all NO_y , but not seen by the 5-CRD at either temperature. During SAPHIR, direct measurements of HNO_3 were made and thus the fraction of NO_y which this represents is known at any given time and can be compared to the 5-CRD.

3.3.8 Detection of NO_2 from thermal decomposition of N_2O_5 and ClNO_2

During the nighttime, or in specific laboratory experiments, N_2O_5 mixing ratios can build up to ppb levels and thus represent a significant bias on the measurements of both Σ PNs and Σ ANs as N_2O_5 decomposition to NO_3 and NO_2 was found to be 100% efficient in both heated cavities and thus requires independent measurements of N_2O_5 in order to be corrected. The correction is made by subtracting the ppt mixing ratios of the corrected N_2O_5 signal (e.g. from the 5-CRD’s N_2O_5 cavity) directly from the $\text{NO}_2 + \Sigma$ PNs or $\text{NO}_2 + \Sigma$ PNs + Σ ANs cavity signals, after correction for the l/d ratio, effective laser cross section and Rayleigh scattering effects, but before correction with the FACSIMILE models as $\text{NO}_3 / \text{N}_2\text{O}_5$ are not considered in the model.

At very high temperatures (> 700 K) the unimolecular thermal decomposition of NO_3 (and NO_3 from N_2O_5) to NO_2 becomes possible, though decomposition to NO and molecular oxygen is strongly thermodynamically favored and thus dominates (Wayne, et al. 1990). This can result in minor positive bias as while the 5-CRD cannot detect NO , the newly formed NO molecules can interact with organic radicals and O_3 in the reactions detailed in 3.3.6 to form NO_2 . For the NO_3 radical directly sampled from the air (i.e. not from the dissociation of N_2O_5) residence time-dependent, exponential surface losses are known (see below) in the 662 nm cavities. In order to reduce the magnitude of the correction these cavities operate under a much greater flow rate compared to the 405 nm cavities, as such it can be expected that the transmission of NO_3 in the 405 nm set-up, though it has not been rigorously determined, is likely very small. These observations suggest that, under most atmospheric conditions, the magnitude of the corrections from the dissociation of NO_3 in the ANs oven is negligible.

Detection of other inorganic reactive nitrogen molecules such as ClNO_2 or BrNO_2 is possible in the 5-CRD, as shown in the laboratory experiments by (Sobanski, Schuladen, et al. 2016), who reported the fractional

yield of NO₂ from ClNO₂, generated by flowing Cl₂ gas in synthetic air over sodium nitrite crystals, as a function of set oven temperature (thermogram) overlaps significantly with the thermogram of ΣANs. As ClNO₂ observations in the atmosphere can reach mixing ratios of a few 100 ppt to several ppb, this introduces a significant bias in the measurement of ΣANs and requires an independent, selective measurement of ClNO₂ to apply the appropriate data correction.

3.3.9 Total Uncertainty and limit of detection

The total uncertainty of the final NO₂, PNs and ANs data from the 405 nm cavities is dependent on several variables, which account for both the systematic uncertainties which affect the entire signal, such as the l/d ratio and the uncertainties associated with the laser spectra; or uncertainties which make variable contributions depending on measurements of other trace gases, such as Rayleigh scattering effects of H₂O or the relative contribution of the reaction of NO + O₃ in the cavity to the total NO₂. For the ambient NO₂ cavity, the uncertainty of the reference laser spectrum (Vandaele et al. 2002) reports 5% uncertainty while the uncertainty in the measurements of the laser spectrum adds an additional 5% uncertainty due to spectrum-to-spectrum variability. The uncertainty of the l/d ratio is estimated at 2%. Combining these, in quadrature a total of 7.34% is reached (2σ) for the NO₂ cavity plus a variable contribution from Rayleigh scattering due to relative humidity, pressure differences between the zero signal and measurement signal, and the reaction of different trace gases with NO to form NO₂, of which O₃ is the major contributor. Considering a ~10% uncertainty for $k_{(\text{NO} + \text{O}_3)}$ and 5% total uncertainty each on measurements of [NO] and [O₃], and ambient mixing ratios of [NO₂], [NO] and [O₃] of 1, 0.5 and 50 ppb, we obtain a total uncertainty ~0.1% in the NO₂ signal due to this reaction. Rayleigh scattering effects caused by the differences in pressure between zero and measurement are negligible due to the presence of the active pressure regulation system discussed above. The effect of humidity is more important as the previously installed bubbler system for matching ambient relative humidity described in (Sobanski, Schuladen, et al. 2016) was no longer in place (for the SAPHIR campaign), therefore the correction relies on the uncertainty of in both the measurement of relative humidity, temperature and the relative cross section between synthetic air and water ($\Delta\sigma$) which was estimated at ~20% by (Thieser et al. 2016) due to the difference between this measurement and similar measurements by (Fuchs, Dubé, et al. 2009). This uncertainty, assuming no uncertainty in RH or temperature measurements, converts to an error of ~20 ppt at 100% RH. Additional possible sources of error, including other absorbers at 405 nm or the slow thermal decomposition of N₂O₅ at ambient temperatures are variable and thus must be evaluated on a case-by-case basis. Other than the previously discussed losses across the ovens, no additional perceivable losses of gas-phase NO₂ across the inlet were observed nor memory effects. Thus, for the NO₂ channels we arrive at a total uncertainty of $7.34\% \pm 20$ ppt.

In the PNs cavity, the major source of uncertainty, beyond what was discussed above, comes from the behavior of the radical organic fragments in the ovens, as they interact with ambient NO and NO₂. Because the behavior of PNs in the presence of these traces gases is non-linear, no single value uncertainty can be obtained. Under laboratory conditions, (Sobanski, Schuladen, et al. 2016) argue that the ability to simulate experimental data with a high degree of accuracy implies a total uncertainty of < 15% when considering the various rate coefficients governing the reactions in the heated ovens. However, when considering that these rate coefficients consider input only from the molecule PAN (C₂H₃NO₅) specifically, as opposed to other PNs or PAN analogues such as PPN or MPAN, this estimate according to Sobanski *et al.* was doubled to a conservative estimate of 30% to account for differences in different R groups.

Total uncertainty in the ANs channel is also determined by the uncertainties in the behavior of the radical organic fragments in the oven, but in this case these are derived from both PNs and ANs. As the final mixing ratios from the NO₂ + ΣPNs + ΣANs channel are obtained by subtraction of both NO₂ and ΣPNs, this introduces the total uncertainties of both into the final ΣANs, amplifying them and leading to large uncertainties in air masses contain large concentrations of PNs (or NO₂) relative to ANs. Additionally, as with the ΣPNs channel, the dependence of ANs on NO or NO₂ is non-linear and thus the uncertainty in the signal is variable according to the concentration of these trace gases. To give some idea of the magnitude of the uncertainty at typical atmospheric conditions, 1 ppb [NO] and 1 ppb [PAN] results in ~16% uncertainty in the final ANs data, increasing to > 50% when [NO] is increased to 5 ppb. Finally, additional sources of NO₂ in the ΣPNs or ΣANs channels which need to be subtracted from the final mixing ratios will also add to the uncertainty (e.g. N₂O₅, ClNO₂), sometimes considerably, depending on the contribution of each trace gas to the total ΣPNs or ΣANs signal, and therefore need to be evaluated on a case-to-case basis. Memory effects on the inlets were generally not observed in either of the heated channels under laboratory or field measurements, however during the 2018 SAPHIR campaign a significant delay, presumed to be caused by gas-wall partition of biogenic organic nitrate molecules, affected the accuracy of the measurements. These effects occurred in both heated channels and are discussed within the results in section 7.

The limit of detection (LOD) of each of the 405 nm cavities is defined by the reproducibility of the zero signal, which is subject to change with time due to thermal and mechanical stress, which may affect the alignment of the optics, and can be estimated as the 2σ standard deviation of one zero to the next over the course of some period of measurement. During field campaigns this period was usually one hour. This 2σ definition results in a LOD which is continually changing during operation but implies that in 95% of cases the difference between one zero and the next is less than the quoted LOD. To give an example of the typical magnitudes of the LOD during field operations, during the AQABA campaign the LOD for the NO₂ cavity ranged from 32 to 75 ppt, 90 – 120 ppt for PAN and 100 – 187 ppt for AN.

3.4.1 Detection of NO₃ at 662 nm

As with NO₂, the concentration of NO₃ can be detected as a function of the decay of light in the presence of NO₃ compared with the decay in the absence of NO₃. Here, the relevant wavelengths are in the visible region of the electromagnetic spectrum, located between 650 – 680 nm. The absorption spectrum of NO₃ has been characterized before (Orphal, Fellows, and Flaud 2003; Osthoff et al. 2007), the primary absorption band is located at 662 nm (Figure 12) and is approximately $\approx 2.3 \times 10^{-17} \text{ cm}^2 \text{ molecule}^{-1}$. Absorption of NO₃ at 662 nm allows the modification of (Equation 6):

$$[\text{NO}_3] = \frac{l}{d} \times \frac{1}{c\sigma_{(\text{NO}_3)}} \left(\frac{1}{\tau} - \frac{1}{\tau_0} \right) \quad \lambda = 662 \text{ nm} \quad (\text{Equation 10})$$

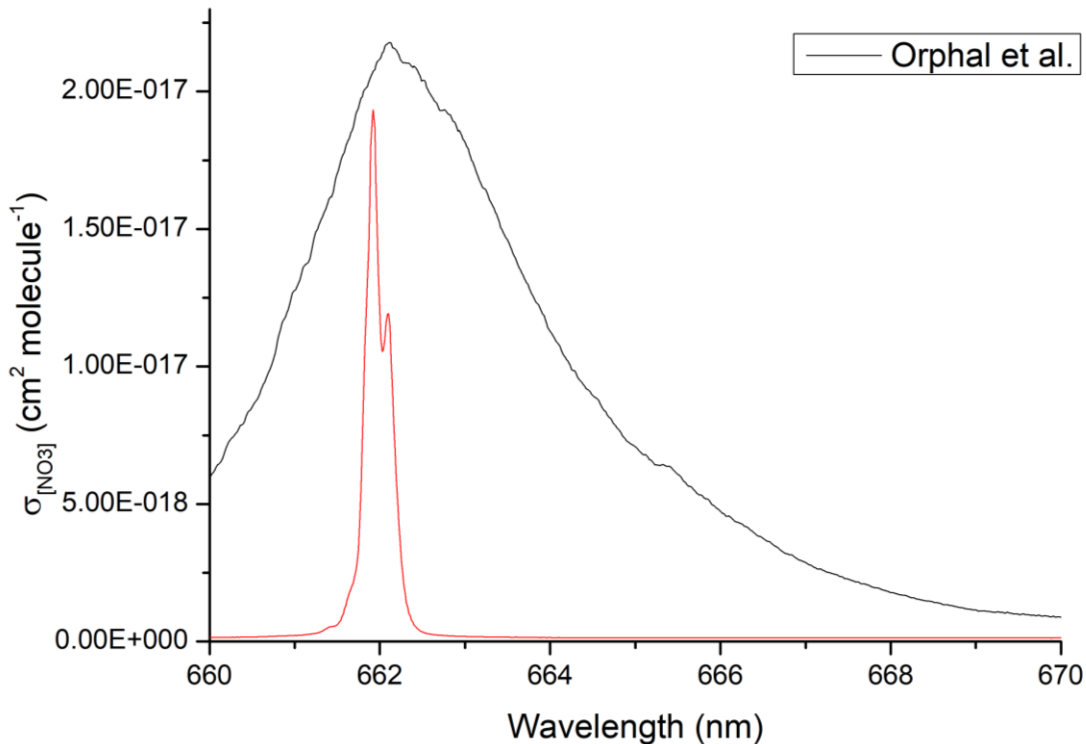


Figure 12. NO_3 absorption spectrum from (Orphal et al., 2003) and a typical 5-CRD laser diode emission spectrum centered about 662 nm.

3.4.2 Detection of NO_3 via thermal dissociation

N_2O_5 thermally decomposes to a molecule of NO_3 and NO_2 , therefore the data from heated 662 nm cavity can be described as the sum of N_2O_5 and NO_3 . The heating begins in an insulated, quartz-glass volume positioned horizontally before the entrance into the cavity. The N_2O_5 cavity was set to 398 K, the temperature was selected by laboratory experiment; passing N_2O_5 through the oven and into the cavity and gradually raising the temperature of the oven until no more signal could be acquired, also implying that the residence time in the oven before the cavity is sufficient to decompose all N_2O_5 . Unlike the heated 405 nm cavities, the N_2O_5 cavity maintains a temperature of 398 K throughout the entire length of the cavity in order to prevent recombination between NO_3 and NO_2 through the cavity.

3.4.3 The l/d ratio

The flow rate through the NO_3 and N_2O_5 cavities was considerably greater than those in the 405 nm cavities in order to reduce residence time, and therefore losses of NO_3 due to interaction with the cavity walls. As the flow rate in these cavities was so high (7 SLM and 8 SLM for NO_3 and N_2O_5 cavities, respectively) the purge gas flow (200 sccm) used to protect the mirrors represented a much smaller fraction of the overall outflow of the cavities, therefore the l/d ratio, was close to the upper limit of the ratio determined by the distance between the mirrors and length of the cavity. By varying the purge gas flow (0 – 1000 sccm) while maintaining total outflow, temperature and pressures in the 662 nm cavities the l/d ratio was determined to be $0.77 \pm 1.5\%$ for both the NO_3 and N_2O_5 cavities.

3.4.4 Effective laser cross section

Several wavelengths centered about 662 nm contribute to the absorbance of NO_3 , as was the case for NO_2 detection in the 405 nm cavities, each with a slightly different σ which affects the final determination of $[\text{NO}_3]$ according to (Equation 10). The emission spectra of the laser diode were collected at a rate of up to one spectrum per hour during operation in the field. These were used for determining the effective cross section, $\sigma_{\text{effective}}$, or the absorbance seen by NO_3 in the cavity by the sum of all the wavelengths emitted by the laser diode, normalized according to a reference spectrum of NO_3 by (Osthoff et al. 2007) for the AQABA and (Orphal, Fellows, and Flaud 2003) for the SAPHIR campaign (see section 6). The emission spectra of the laser are known to be temperature dependent, according to both and as such are influenced by the ambient temperature of the measurement site or laboratory. For the purposes of data acquisition, a set value of $\sigma_{\text{DAQ}} = 2.3 \times 10^{-17} \text{ cm}^2 \text{ molecule}^{-1}$ was used with the correction factor calculated as:

$$\text{Correction Factor} = \sigma_{\text{DAQ}} / \sigma_{\text{Effective}} \quad (\text{Equation 8})$$

Both the (Osthoff et al. 2007) and (Orphal, Fellows, and Flaud 2003) spectra report a total uncertainty of $\sim 10\%$ (2σ) while the uncertainty associated with gathering laser spectra provides an extra $\sim 5\%$ due to the spectrum-to-spectrum variability. As is the case with the 405 nm spectral data, the calculated $\sigma_{\text{effective}}$ were interpolated onto the 5-CRD data time resolution and Correction Factor was applied directly to $\text{NO}_3 / \text{N}_2\text{O}_5$ ppt mixing ratios.

3.4.5 Transmission losses across the cavities

As a highly reactive radical trace gas, NO_3 interacts with the surfaces in the instrument, removing it from the gas phase and resulting in a negative bias in the NO_3 and N_2O_5 data. These interactions are both time dependent and exponential so in order to minimize these gas-wall reactions a high sampling flow is used (15 SLM) to reduce the total residence times in the instrument. In order to quantify the magnitude of this effect, NO_3 was generated in a darkened glass, Teflon-lined volume which could be filled with a calibrated NO_2 source (bottle) and O_3 generated by reacting dry zero-air from the generator in a quartz tube with an ultraviolet Pen-ray lamp. The outflow of this volume was then sampled into the NO_3 and $\text{NO}_3 + \text{N}_2\text{O}_5$ cavities, where the flow rate across each cavity was varied (0 – 10 SLM) while maintaining total outflow. A correction factor was derived by an extrapolation of the experimental data to infinite flow (zero residence time), where this theoretical maximum can be compared against the flow rate under standard operating conditions. For NO_3 the transmission across the cavity was determined to be by $87.7 \pm 3\%$ and $88.0 \pm 3\%$ for N_2O_5 .

3.4.6 Losses across the automatic filter changer

Protecting the internal PFA tubing of the instrument and the cavities themselves is a self-built, pneumatic, automatic filter changer. The filter changer is capable of holding up to 20, $2 \mu\text{m}$ pore-size, Teflon filters which are changed at a rate of one per hour while in operation during field measurements and generally more frequently during laboratory work. These filters serve to remove aerosol particles which may scatter light in the cavity, positively biasing results or by coating the internal PFA tubing making the instrument reactive towards NO_3 and / or N_2O_5 , negatively biasing results by removal from the gas phase. Unlike the transmission across the cavity, the filter changer can be treated as a point loss and so was characterized by alternately sampling NO_3 and N_2O_5 either over the filter changer or through a $\frac{1}{4}$ " PFA bypass line of equivalent total volume. Transmission of NO_3 was determined to be $70 \pm 5\%$ while no perceivable losses of N_2O_5 were observed over the filter changer.

3.4.7 Losses in the sampling line

When taking measurements during a field campaign, a ½" PFA sampling inlet line of several meters (3 or 4 m, depending on the campaign) was utilized to bring ambient air to the instrument. Although PFA is generally inert, a prolonged residence time in the sampling line will still contribute to potentially large losses of NO₃. The 5-CRD achieves low total residence time, both in the sampling inlet and in the main internal tubing of the instrument and cavities by using a very high flow rate. The instrument cavities are attached to a pump and controlled by mass flow control units which draw 15 SLM, under standard operating conditions, into the 5-CRD from a larger bypass line set to 25 SLM. This results in a total flow rate from the end of the inlet system, where ambient air enters, to the point where 15 SLM is siphoned into the 5-CRD of 40 SLM. Losses of NO₃ in this sampling line were characterized in the same manner as for the cavities themselves, i.e. by adjusting the flow rate through the bypass line and extrapolating the observed mixing ratios for several flow rates (and therefore residence times) to infinite flow and comparing this signal at the set flow rate. The transmission of NO₃ across ~4 m of PFA tubing at 40 SLM (corresponding to a residence time of ~0.14 s) was determined to be $89.3 \pm 1\%$ for a correction factor of 1.12. No losses of N₂O₅ were observed over a range of bypass flows.

3.4.8 Total uncertainty and limit of detection

Total uncertainty in the NO₃ and N₂O₅ cavities are functions of the series of systematic errors in the corrections for NO₃ interaction with the walls, filters, etc. combined with uncertainties in the laser cross section. The reference laser cross section (Osthoff et al. 2007) reports an uncertainty of ~10 % while the uncertainty associated with measuring the emission spectra of the laser diode contributes an additional 5%. Additional systematic uncertainties are also added to the NO₃ signal by transmission across the cavity (3%), transmission across the filter changer (5%) and transmission in the bypass lines (generally ≈ 1%). Combining these together, we arrive a total uncertainty of 23% (2σ) in the measurement of NO₃. As it is corrected for by the subtraction on NO₃, the total uncertainty of the N₂O₅ measurement depends on the relative contribution of NO₃ to the total signal and therefore this uncertainty can be highly significant at N₂O₅/NO₃ ratios close to 1. Combining the NO₃ uncertainty of 23% in the N₂O₅ cavity together with mixing ratios between 50 ppt and 500 ppt, results in a total uncertainty of ~25%.

The limits of detection for both NO₃ and N₂O₅ cavities were defined in exactly the same manner as the previously discussed 405 nm cavities, based on the reproducibility of the zero signal. This was estimated by measuring the 2σ standard deviation from one zeroing period to the next over an hour of campaign zeros and is thus continually variable. To give an example of the magnitude of the LOD during field operation, during the AQABA campaign the LOD of the NO₃ cavity ranged from 0.5 ppt to 2 ppt and the LOD of the N₂O₅ cavity ranged from 3.2 ppt to 7 ppt.

4. Campaign Description and Set-up

In this section, an overview of the field work campaigns analyzed in this thesis will be provided, discussing the scientific motives and specific set-up of the 5-CRD and other instruments necessary to analyze the reactive nitrogen data. The results of the data analysis for the AQABA campaign are provided in section 5 and the results of the data analysis of the SAPHIR campaign are presented in sections 6 and 7. For a description of the 5-CRD system see section 3.

4.1.1 The 2017 AQABA ship campaign

At the crossroads between huge industrial and economic centres in Europe and Asia, the Arabian Basin is an area with a large and growing population (Yüceşahin and Tulga 2017) of nearly 500 million (in 2015) with large, industrialized cities which have, in recent years, seen rapid growth. With year-round high temperatures and strong solar irradiation, the Arabian Peninsula, with its population concentrated around the Persian Gulf (also known as the Arabian Gulf), has become a global hot spot for atmospheric chemistry. The region has been strongly affected by the consequences of rising global temperatures and is subject to intense heat and falling rainfall, leading to droughts, both of which are predicted to intensify in the future (X. Zhang et al. 2005; Terink, Immerzeel, and Droogers 2013), and strong air pollution originating from anthropogenic sources and intensified and distributed across the Peninsula and wider Middle Eastern region by local geography, population trends and meteorology events (e.g. dust storms). Primary gas-phase pollutants such as VOCs, NO_x, SO₂ and CO / CO₂ are a direct consequence of combustion processes, where much of the increase can be traced to growth of cities and land traffic (NO_x and CO₂), power generation (NO_x, CO, SO₂), desalination (SO₂), concrete for infrastructure projects (CO₂), shipping (NO_x, SO₂, CO, VOCs) and the growth in the oil and gas industry (Farahat 2016). Further, the strong sources of emissions combined with intense, year-round sunlight leads to the formation of secondary pollutants, including fine particulate matter and photochemically formed pollutant molecules such as PAN and ozone. The O₃ concentrations in the Persian Gulf are already among some of the most severe in the world with up to 150 nmol mol⁻¹ (Smoydzin, Fnais, and Lelieveld 2012) not atypical, and these higher levels are predicted to grow greater still in the future (Lelieveld et al. 2009).

Despite this however, measurements relating to atmospheric processes are few with most limited to NO_x / O₃ air quality studies, primarily in urban sites, as well as a few relatively recent studies of pollution emitted by port areas and refineries (Barkley et al. 2017; Simpson et al. 2014). The 2017 Air Quality and climate change in the Arabian Basin (AQABA) ship campaign was an attempt to close some of the gaps by making shipborne measurements of aerosols and trace gases around the Arabian Peninsula and in the eastern Mediterranean. These measurements were made by a suite of different instruments outfitted on board of the *Kommandor Iona* research vessel, setting sail from La-Seyne-sur-Mer near Toulon, France to Kuwait City, Kuwait and back from June 26th, 2017 to September 1st, 2017. Measurements were taken in the eastern Mediterranean near Malta and Crete, through the Suez Canal, across the length of the Red Sea (with a port call made in Jeddah, Saudi Arabia between 10 – 12th July), through the Gulf of Aden and into the Indian Ocean off the south coasts of Yemen and Oman (Arabian Sea), before heading north and sailing up the Persian Gulf. These regions of influence ranged from ‘clean’ maritime environments, such as the Indian Ocean or Mediterranean Sea, where the influence of anthropogenic emissions was limited

due to a lack of local sources and aged (oxidized) air masses, to heavily polluted regions influenced by petrochemical industries (Persian Gulf) or shipping emissions (Red Sea and Suez).

In particular, little-to-no observations of atmospheric nitrate radical (NO_3) and dinitrogen tetroxide (N_2O_5) have been made around the Arabian Peninsula. The high NO_x and VOC emissions which characterize much of the region have been shown to lead to a net-production of O_3 (Tadic et al. 2019), leading to elevated mixing ratios. As O_3 persists into the night NO_3 production will be large, potentially leading to large mixing ratios of NO_3 and N_2O_5 , (in the absence of reaction partners) and enhanced oxidation rates of VOCs, including the anthropogenic VOCs produced by ships (Eyring et al. 2005) and petrochemical industries (Bourtsoukidis et al. 2019; Zheng et al. 2018) in polluted regions, or biogenic VOCs like dimethyl sulfide (DMS), produced by ocean dwelling phytoplankton, which link the biosphere sulfur budget with the NO_x budget via the fast reaction with NO_3 . As the main product of the reaction of DMS with NO_3 is HNO_3 , it has been suggested that DMS is involved with regulating local O_3 levels in marine environment by removing NO_x from the atmosphere in favor of the highly soluble product (U. Platt and Le Bras 1997). Interactions between the NO_x and sulfur cycles are also important on a global scale, as the oxidation of DMS will lead to, in time, the formation of SO_2 and H_2SO_4 , the latter of which may transfer into the aerosol phase where the sulfur particles act as cloud condensation nuclei, linking reactive nocturnal nitrogen in marine environments to questions of global temperature and weather patterns (Andreae 1990).

Furthermore, the heterogeneous chemistry of NO_3 and N_2O_5 on the surface of aerosols provides another link between local NO_x emissions and the global aerosol budget. Despite typically low rates of reaction via the heterogeneous mechanism compared to gas-phase reaction with VOC, these reactions may represent an important loss process for NO_x away from sources, such as over the desert where one may expect VOC reactivity to be reduced compared to heterogeneous uptake onto dust particles (U. F. Platt, et al. 1984), and uptake coefficients (γ) have been shown to be relatively large (e.g. up to 0.2 for Saharan Dust (Karagulian, Santschi, and Rossi 2006)). In oceanic regions, N_2O_5 uptake onto chloride-containing (sea salt) particles indirectly increases the oxidation rates of VOCs in as this results in the activation of halogens via release of ClNO_2 from the particle phase. ClNO_2 undergoes rapid photolysis to NO_x and free halogen radicals (Cl) during the day. The oxidation of VOCs by these Cl radicals has been shown to be competitive during the early hours of the morning with other atmospheric oxidants (Eger et al. 2019).

The ultimate goals for the AQABA campaign with regards to this thesis are to use the measured ambient mixing ratios of NO_3 / N_2O_5 in a region where little-to-no previous measurements have been made to provide some insight into NO_3 's role as an oxidant, attempting to identify what are the most important mechanisms for controlling the lifetime of NO_3 in the seas around the Arabian Peninsula and finally to demonstrate the importance of nighttime chemistry as a sink for regional NO_x .

4.1.2 Measurements of NO_3 and N_2O_5 by cavity ringdown spectroscopy

NO_3 and N_2O_5 were measured by using a five-channel, thermal dissociation cavity-ring down system (TD-CRDs), which was described in detail before (Sobanski, Schuladen, et al. 2016) and section 3. This set-up uses one channel to measure NO_3 directly at 662 nm, while the second channel measures the sum of ambient NO_3 and NO_3 from thermal dissociation of ambient N_2O_5 .

The instrument was situated within a temperature-controlled shipping container which was positioned on the front deck of the *Kommandor Iona*. This positioning ensured that sampling inlets were ahead of any potential contamination sources from the vessel's exhaust when headed into the direction of the

wind. The air sampling was performed with a high-flow, cylindrical, stainless-steel inlet (height: 5.5 m; diameter: 0.2 m). Ambient air was sampled from the middle of the high-flow inlet with the use of a ½" PFA line at a flow rate of 40 SLM (Standard Litres per Minute) in order to reduce inlet residence time. From this bypass line 15 SLM (7+8) were subsampled into ¼" PFA inlet line, leading to the 5-CRD cavities. A 2 µm pore Teflon filter (diameter 47 mm) was positioned near the end of the inlet line inside an automatic filter changer. During operation the filter was changed at a rate of once per hour. The limit of detection of both channels is defined by the reproducibility of the zero signal, described in detail in section 3. The zero signal achieved by adding a small flow (8 sccm in the 15 SLM sampling flow) of 100 ppm NO into the inlet, leading to complete titration (residence time ≈ 1.2 seconds) of all NO₃ in the sampled ambient air. For the AQABA campaign, the LOD was variable due in part to temperature fluctuations in the container and, in particular, the motion of the ship on the waves both of which affected the alignment of the lasers. As a result, depending on the weather, the LOD ranged from 0.5 to 1.8 ppt for NO₃ and 3.2 to 7.0 ppt for N₂O₅. Total uncertainty for the NO₃ channel was estimated at 25% and ~28% for N₂O₅ between 50 and 500 ppt, which covers the range of values seen (max: 300 ppt) during the AQABA campaign.

4.1.3 NO and NO₂

NO₂ was measured by the same TD-CRD instrument which measured NO₃ and N₂O₅. The method and instrument was described before by (Sobanski, Schuladen, et al. 2016) and section 3. The analysis of the NO₂ data from the AQABA campaign gave a total measurement uncertainty of 7.4% ± 10 ppt and a limit of detection of ~50 ppt. The reference spectrum used for NO₂ data correction was (Vandaele et al. 2002). NO and additional NO₂ measurements were made by I. Tadic with a modified commercial chemiluminescence detector (CLD 790 SR)(ECO Physics, Duernten, Switzerland) (Fontijn, Sabadell, and Ronco 1970). The limit of detection of the NO signal is estimated between 5 – 9 ppt (integration time 5 s), with total uncertainty of 5.5% (1σ). The NO₂ CLD data reports a total uncertainty of ~7% ± 112 ppt (1σ). The agreement of the two NO₂ measurements was good, within combined uncertainty of the two instruments, with an average (mean) deviation of ~6%.

4.1.4 NO_x and NO_y

The sum of NO and NO₂ (NO_x) and all reactive nitrogen (NO_y) was measured by N. Friedrich with a two-channel thermal dissociation cavity ringdown. This instrument has been described in (Thieser et al. 2016) but has since undergone modifications which are described in (Friedrich *et al.* 2020, in preparation). The limit of detection of this instrument was 98 ppt and the total uncertainty was 11% ± 20 ppt.

4.1.5 Volatile Organic Compounds (VOCs)

Non-methane hydrocarbons (NMHC) were measured by E. Bourtsoukidis and L. Ernle with a Gas Chromatography-flame ionization detector (GC-FID), the set-up and operation of which was discussed in detail for the AQABA campaign specifically in (Bourtsoukidis et al. 2019). This method was used both for the evaluation of light hydrocarbons (C₂-C₆) and heavier hydrocarbons and aromatic compounds (C₆-C₈). Compounds evaluated in this analysis include: ethene, ethane, propane, propene, i-butane, n-butane, trans-2-butene, 1-butene, i-pentane, n-pentane, isoprene and 1-pentene. Additional VOC species were measured by a Proton-Transfer-Reaction Time-of-Flight Mass Spectrometer (PTR-ToF-MS) (Jordan et al. 2009)(Graus, Müller, and Hansel 2010), including dimethyl sulphide (DMS), Benzene and Toluene. The set-up and operation of the PTR-ToF-MS during the AQABA campaign were described in (Edtbauer *et al.* 2019).

4.1.6 O₃, SO₂, and OH

Ozone was measured by a commercial ozone monitor (2B Technologies, Model 202) with a detection limit of 3 ppb (integration time of 10 s) and a total uncertainty of 2%. Measurements of SO₂ were made with Chemical Ionization Quadrupole Mass Spectroscopy (CI-QMS) (Eger et al. 2019), with a limit of detection of 38 ppt and a total uncertainty of 20%. Ambient concentrations of the OH radical were measured by S. Tauer and R. Rohloff with the HORUS (HydrOxyl Radical measurement Unit based on fluorescence Spectroscopy) instrument which has been previously described in (M. Martinez et al. 2010).

4.1.7 Aerosol Measurements

Aerosol Mass Spectrometry (Aerodyne HR-ToF-AMS) was used to measure PM₁₀, PM_{2.5}, and aerosol composition including total organics, nitrate, sulfate, chloride and ammonium with a total uncertainty of 35%. A Fast Mobility Particle Sizer (FMPS, TSI model 3091) measured particle size distribution with a range of 5.6 nm to 560 nm. An Optical Particle Spectrometer (OPC, Grimm Model 1.109) measured the sized distribution in the range 250 nm to 32 μm. From the particle size measurements (FMPS, OPS) the particle surface concentration (ASA) could be calculated with an uncertainty estimated to be ~30%. These measurements were made by J. Brooks of Manchester University, UK.

4.1.8 Meteorological data

A commercial NEPTUNE weather station (Sterela) was positioned near the bow of the ship, and recorded various parameters including temperature, air pressure (including at sea level), wind speed and direction, and the speed and location (via GPS) of the vessel. Photolysis rates (JNO₃) were calculated from actinic flux measured by a spectral radiometer (Metcon GmbH), positioned on top of a shipping container on the front deck, close to the sampling inlet. Cross sections and quantum yields were taken from (Demore et al. 1985).

4.1.9 Boundary Layer data

Marine boundary layer information was provided by ECMWF ERA5 (Copernicus Climate Change Service (C3S) 2017). The data covers a 30 km² grid and a height of up to 80 km covering a large number of terrestrial, oceanic and atmospheric variables.

4.1.10 OH Reactivity

Direct measurements of the per-second reactivity of the OH radical (k(OH)) were made by E. Pfannerstill and N. Wang using the comparative reactivity method, described in (Pfannerstill et al. 2019), which uses a competitive reaction between reactive compounds in ambient air and a reagent of pyrrole. The 5-minute averaged data averaged a 5.4 s⁻¹ detection limit (2σ) for the entire campaign. The instrument reports a ~50% total uncertainty (1σ).

4.2.1 2018 SAPHIR NO₃-Isoprene campaign

The 2018 SAPHIR NO₃-Isoprene campaign was a series of experiments undertaken in the SAPHIR (see below) chamber in Jülich, Germany in the summer of 2018. The experiments were focused on the gas-phase radical reaction between the nitrate radical, NO₃, and Isoprene (2-methyl-1,3-butadiene, C₅H₈). Isoprene, which is emitted by many, but not all, plant species is the single most emitted non-methane hydrocarbon into the atmosphere (Guenther, et al. 2012) with an estimated flux of 600 TgC yr⁻¹ (Guenther, et al. 2006). Its reactivity is therefore highly important on local, regional and global scales. On a local scale, isoprene is a strong source of alkyl peroxy (RO₂) radicals which are formed when isoprene reacts with any

of the atmosphere's main oxidants (OH, NO₃ or O₃). In the presence of NO, these radicals produce NO₂ leading to a net gain of ozone during daylight hours. For a practical example, one can take the city of Atlanta, Georgia which in the 1980's suffered from photochemical smog production when isoprene emissions from nearby Oak forests reacted with local NO_x to catalyze the local production of ozone (Chameides et al. 1988). Similar effects have been noted in other sub-tropical urban cities such as Taipei, Taiwan (Sun and Huang 1995) or Sacramento, California (Dreyfus, Schade, and Goldstein 2002). Moving to a regional and global scale, isoprene oxidation contributes strongly to the formation of secondary organic aerosol (SOA), which in turn contributes to fine particulate matter – suspensions of solid or liquid particles dispersed into a gaseous medium – with a diameter of 2.5 μm or less (also known as PM_{2.5}). Regionally, inhalation of PM_{2.5} is linked to increased rates of cardiovascular disease, respiratory problems and lung cancers (Dockery et al. 1993; Pope and Dockery 2006). On global scales PM_{2.5}, and SOA more generally, influence climate patterns directly, by absorbing and scattering solar and terrestrial radiation (Kanakidou et al. 2005), or indirectly, through the formation of clouds to by acting as condensation nuclei (Boucher et al. 2013).

Despite the high profile nature of these issues and the prevalence of isoprene emissions, the path to organic aerosols by isoprene and other biogenic VOC oxidation remains highly uncertain. The total contribution of isoprene, monoterpenes (C₁₀H₁₆), and sesquiterpenes (C₁₅H₂₄) by reaction with OH, NO₃ and O₃ to the global SOA budget was estimated by (Hallquist et al. 2009) to be 90 ± 90 TgC yr⁻¹. While there exist many possible reasons for the wide ranges reported in global modelling studies, including the simple uncertainties associated with estimates of global VOC emissions, as isoprene's source strength is so great, even compared to higher terpenes, global SOA estimates rely highly on isoprene oxidation and SOA yields. To give some idea of the uncertainty, modelling studies have suggested that isoprene oxidation alone could be responsible for between 27% (Hoyle et al. 2007) and 78% (C. L. Heald et al. 2008) of the global SOA budget.

The difficulty in making accurate estimates of the isoprene contribution to global SOA budgets comes in part from the variability in the production of isoprene, as different plants emit isoprene at different rates depending on the species (Sharkey, Wiberley, and Donohue 2008) and at different times of the day, which can make estimating total emissions difficult in regions of multiple kinds of plant species, such as forests. Losses of isoprene are also highly variable as, depending on the region, different oxidizing trace gases will be more or less important in the removal of isoprene, the products of which might have vastly different chemical fates. For instance, in urban environments isoprene tracers in aerosols have been shown to correlate strongly with O₃ concentrations, implying an increased importance of Criegee ozonolysis mechanisms in such regions (Rattanavaraha et al. 2016) to PM_{2.5} formation. In more remote, forested regions reactivity with NO₃ is more important, as ozone concentrations tend to be lower, and photochemistry is suppressed (contributing to formation of OH and NO, which reacts quickly with NO₃) in the canopy regions, where isoprene emissions are strong. While NO₃ concentrations are also reduced during the day due to rapid photolysis and reaction with NO, yields of ANs tend to be higher (0.6 – 0.9, IUPAC; 0.7 ± 0.08 (Rollins et al. 2009); 0.75 – 0.78 (Schwantes et al. 2015)) than the OH initiated pathway.

The route to SOA via NO₃-initiated oxidation of isoprene, or other terpenes, involves the formation of alkyl nitrates some of which partition into the aerosol phase over time. (Rollins et al. 2013) estimated that 17 – 23% of molecules in organic aerosols contained nitrate ester (RO-NO₂) functional groups in Bakersfield, California, highlighting the role an important role of NO₃ in oxidation of terpenes. More recently, the assumption that NO₃ reactions with isoprene and other BVOCs such as monoterpenes during the day are

generally unimportant due to fast photolysis back to NO_x has been challenged. (J. Liebmann et al. 2019) showed that a majority (70%) of ΣANs formed in the Boreal forest were a result of reaction with NO_3 , with 49% of the total ANs generated from nighttime NO_3 reactions and 21% of the total from daytime NO_3 reactions. While it should be noted that isoprene nitrates made up a small contribution to the total ΣANs in the Liebmann *et al.* study due to the relative prevalence of monoterpene emissions; isoprene-derived nitrates are thought to be the largest source of all ANs globally (Fisher et al. 2016) and observations of elevated levels of isoprene nitrates have been noted in the forest canopy (Grossenbacher et al. 2001), where direct measurements of NO_3 reactivity have suggested that the BVOC reactivity is large enough to be competitive with NO_3 reactions with NO and the photolysis rates (J. Liebmann et al. 2018). This interpretation fits with previous work on atmosphere-biosphere interactions of isoprene (Sharkey and Yeh 2001; Sharkey, Wiberley, and Donohue 2008) which show that it is generally only released by plants in large amounts during the day, implying that concentrations are potentially higher during the day, which would in principle lead to higher NO_3 loss rates.

The aims of the SAPHIR NO_3 -Isoprene experiments are to understand the gas-phase mechanism of this reaction, and the ultimate fate of the products thereby reducing some of the uncertainty surrounding the questions of AN yields, product identification, the relative importance of RO_2 , HO_2 and NO_3 chemistry under different conditions and SOA mass yields – which have proven to be highly uncertain ranging from a few percent (4.3 % (Ng et al. 2008); 0.7% (Rollins et al. 2009)) when only semi-volatile, first-generation isoprene oxidation products are considered to larger values when the total mass yields from second generation oxidation product are considered (23.8% (Ng et al. 2008); 14% (Rollins et al. 2009)). The SAPHIR experiments will examine this with a suite of instruments and under a variety of different conditions.

4.2.2 NO₃ and N₂O₅

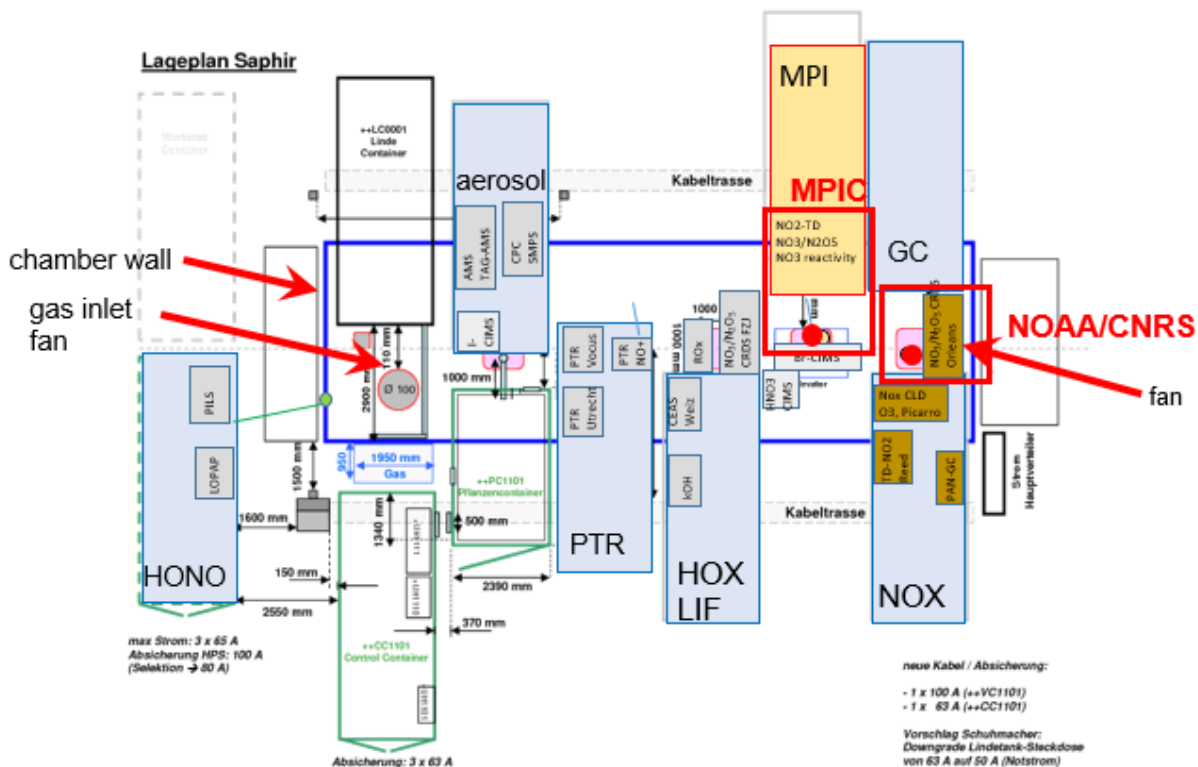


Figure 13. Schematic of instrument locations relative to the SAPHIR campaign. MPIC = Max Planck Institut fuer Chemie, where the 5-CRD was located. NOAA/CNRS = Location of the other NO₃ / N₂O₅ instrument.

NO₃ and NO₃ from the thermal dissociation of N₂O₅ were measured by cavity ringdown spectroscopy located in a shipping container at the base of the SAPHIR chamber. The set-up of this instrument has been explained in section 3. The sampling method used an approximately 4 m, ½", PFA sampling line connected to the base of the SAPHIR chamber with a high flow rate (40 SLM) in order to reduce residence time in the sampling line. From this large flow, 15 SLM (8+7) were subsampled into the instrument perpendicular to the bypass flow. A characterization of this sampling line indicated that the transmission of NO₃ was 87.7 ± 2% at the set flow rate compared to the extrapolation to zero residence time, requiring the application of a correction factor of 1.14 directly to the NO₃ mixing ratios. No losses of N₂O₅ were observed in the sampling inlet. Total uncertainty was estimated at 25% for the NO₃ cavity and an average of 28% for N₂O₅, which varies according to the absolute values of the mixing ratios of NO₃ and N₂O₅. The limits of detection, which rely on the reproducibility of the zero signal (see section 3) were variable due to temperature fluctuations in the container leading to mechanical stress on the cavities causing slight realignments in the laser. In general, the LOD of NO₃ varied from 0.8 to 1.2 ppt and 2.0 to 3.4 ppt for N₂O₅.

Additional measurements of NO₃ and N₂O₅ were made by F. Bernard by another cavity ringdown system built by the NOAA Earth System Research laboratory (Dubé, et al. 2006) and operated by Centre national de la recherche scientifique (CNRS). The sampling method used by this instrument employed a much lower flow rate of 12.5 SLM (5.5+7) and no additional bypass flow, favoring reducing the residence time in the

inlet by positioning the system closer to the SAPHIR chamber. The total uncertainty of this instrument is 20% for NO₃ and 15% for N₂O₅, with a LOD of 0.9 and 0.25 ppt, respectively.

4.2.3 NO, NO₂, NO_x and O₃

NO₂ was measured by the same cavity ringdown system as NO₃ and N₂O₅ (the 5-CRD) via a separate 4 m PFA inlet line, which also was used for sampling ΣPNs and ΣANs (see below). The cavities were protected by a 2 μm Teflon filter, changed once per experiment, to prevent aerosol contamination in the cavities. Unlike the AQABA campaign, this set up did not include an active monitoring and matching of ambient (chamber) humidity with the zero air, requiring an additional correction and increased uncertainty in the NO₂ signal based on the difference of absorption cross section ($\Delta\sigma$) between dry and wet air. As such, the total uncertainty in the NO₂ channel was estimated as 9% ± 20 ppt, with the additional systematic uncertainty coming from a difficulty in maintaining the temperature of the laser diode, thus the laser emission spectrum and effective NO₂ cross section, due to high ambient temperatures in the container (often over 30°C) and a newly deployed, self-built housing for the laser diode. The limit of detection of the 5-CRD was determined to be 54 ppt.

Several other measurements of NO₂ were additionally made, including via cavity ringdown spectroscopy. A second cavity ringdown system, operated by P. Dewald, the primary purpose of which is to measure NO₃ reactivity (see below) contained a secondary cavity for the measurement of NO₂ with a total uncertainty of 9% and a LOD of 150 ppt. Another cavity instrument, described in (Keehan *et al.*, 2019 In preparation) and operated by B. Brownwood and J. Fry of Reed College, Portland, Oregon measured NO₂ with relative uncertainty of ~10% and a LOD of ~1 ppb.

NO_x measurements were made by a fourth TD-CRD instrument, operated by N. Friedrich, using a photochemical source (a UV penray lamp) to generate O₃ to react NO into NO₂. This instrument was described before in (Thieser *et al.* 2016) but has since undergone modifications which are described in (Friedrich *et al.* 2020, in preparation). Since this study focused on the reaction of NO₃ with isoprene and must necessarily be undertaken in the dark, in most cases NO mixing ratios were at the detection limit, thus the NO_x measurement essentially acts as another measurement for NO₂. The limit of detection of this instrument was 98 ppt and the total uncertainty was 11% ± 20 ppt.

NO was measured by F. Rohrer with a Chemiluminescence detector (CLD, (Ridley, Grahek, and Walega 1992)) ECO Physics, model TR780 with a detection limit of 4 ppt. Ozone was measured with an LOD of 1 ppbv by ultraviolet absorption spectroscopy at 254 nm (Ansyco, ozone analyser 41M). Both instruments operate with accuracy (1σ) of 5%.

4.2.4 Peroxyacyl and Alkyl Nitrates

The sum of all peroxyacyl nitrates (ΣPNs) and the sum of all alkyl nitrates (ΣANs) were measured by thermal dissociation cavity ringdown spectroscopy by the same 5-CRD which measured NO₂, NO₃ and N₂O₅ using two vertically mounted, quartz glass ovens with set temperatures of 473 K and 693 K, respectively based on the thermal yields of NO₂ characterized by the laboratory thermogram experiments, described in section 3. The LOD of ΣPNs channel was determined to be ~120 ppt, while the LOD of ΣANs was found to vary considerably due to fluctuations in the mass flow controller unit which was found to reduce the flow rate in the cavity, compared to the NO₂ and ΣPNs cavities by up to 5% (2 SLM vs. 2.1 SLM). This fluctuation in flow led to differences in pressure (1 – 5 torr) which would impact the Rayleigh scattering coefficient leading to an error in the signal. As such, using the difference in the Rayleigh scattering ($\Delta\sigma$) coefficient

derived by (Thieser et al. 2016) the final LOD is estimated by adding the ppt values derived from pressure differences to the LOD calculated according to the difference in consecutive zeros method detailed in section 3, arriving at values between 307 – 500 ppt. The total uncertainty in the Σ PNs and Σ ANs, as discussed in section 3, is dependent on the absolute values of PNs and ANs as well as NO_2 and NO . This is difficult to estimate due to the presence of significant, non- NO_2 signal in the 473 K cavity which is unlikely to be PNs, described in more detail in section 7. Taking the assumption that there is no PN nor significant NO in the chamber, the FACSIMILE numerical model gives an average correction of 1.02 which, considering the 30% uncertainty in the model estimated by (Thieser et al. 2016; Sobanski, Schuladen, et al. 2016) results in a total uncertainty for the ANs channel of ~9% rising to 11% at high AN mixing ratios (10 ppb).

4.2.5 Direct measurements of NO_3 reactivity

The first-order loss rates (measured in s^{-1}) of NO_3 in ambient air, $k(\text{NO}_3)$, were measured by a cavity ringdown instrument, described in detail in (Dewald et al. 2020; J. M. Liebmann et al. 2017), by introducing air from the chamber into a cavity containing a constant mixing ratio of NO_3 radicals. This approach has the advantage compared to the 5-CRD approach of measuring NO_3 and calculating steady state (see sections 2, 5) as this instrument does not see NO_3 losses due to interaction of the radical with surfaces or heterogeneous chemistry of N_2O_5 . The LOD of this instrument was estimated at 0.005 s^{-1} , the total uncertainty is dependent on the absolute concentration of NO_2 and this varies from 36% to >100% depending on the experiment.

4.3.6 Isoprene and other VOCs

Isoprene and other VOC were measured by two different PTR-ToF-MS (Proton Transfer Reaction-Time-of-Flight-Mass Spectroscopy) instruments. The PTR-ToF-1000 (IONICON Analytic GmbH) has a mass resolution of $>1500 \text{ m}/\Delta\text{m}$. At m/z of mass 69 (Isoprene) this instrument performs with a sensitivity of 60 counts ppb^{-1} and a LOD of 20 ppt min^{-1} . The Vocus PTR (Tofwerk AG/Aerodyne Research Inc.) features a focusing ion-molecule reactor resulting in an increased resolving power of $12000 \text{ m}/\Delta\text{m}$ (Krechmer et al. 2018). The two instruments generally agreed within the combined uncertainties. The uncertainty of the final isoprene dataset, generated by a combination of both instruments, has been estimated at 10% with 2σ confidence.

4.3.8 The SAPHIR chamber

The SAPHIR atmospheric simulation chamber (Simulation of Atmospheric PHotochemistry In a large Reaction Chamber) consists of a double-layer of PFA material, creating an approximately cylindrical shape with a total internal volume of $\sim 270 \text{ m}^3$. The SAPHIR chamber has been described numerous times (e.g. (Rohrer et al. 2005; Fuchs, Ball, et al. 2009; Bossmeyer et al. 2006)) before in the literature. The chamber is surrounded by an interlocking, retractable shutter system which allows for quick opening and closing for exposure to, or shielding from, sunlight. An integrated fan system allows for quick mixing of gases in the chamber within ~ 2 minutes. High-purity synthetic air in the chamber was generated from on-site containers of N_2 and O_2 , and this was additionally used to flush the chamber between experiments. Leakages of the chamber, combined with the gas-volume consumption of the instruments on the NO_3 -Isoprene campaign led to an estimated dilution rate of $1.4 \times 10^{-5} \text{ s}^{-1}$.

5. NO₃ reactivity during the AQABA campaign

Below, the results of the data analysis following measurements of 5-CRD measurements of NO₂, NO₃ and N₂O₅ during the 2017 AQABA ship campaign are discussed.

5.1.1 Overview of measurements made during AQABA

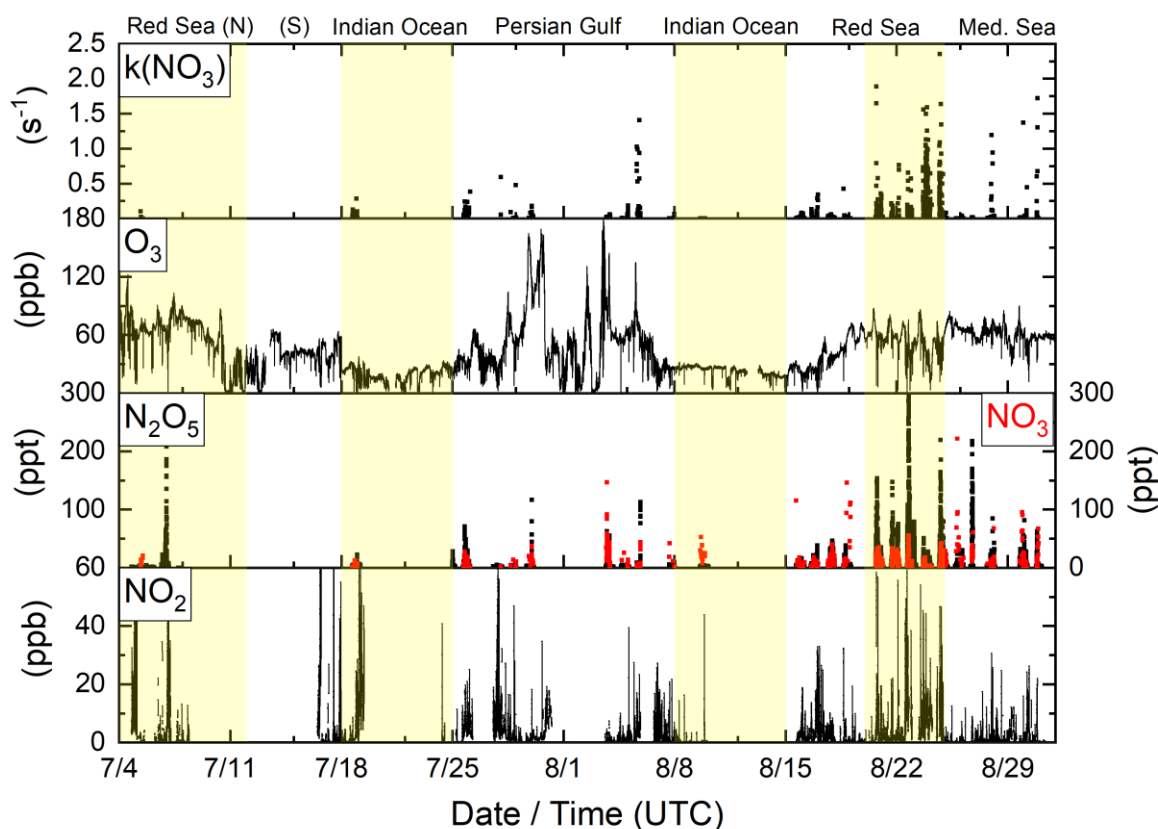
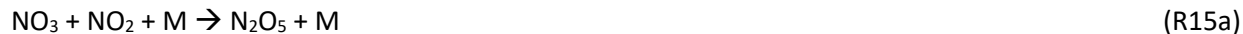


Figure 14. Overview of measurements of O₃, NO₂, NO₃, N₂O₅ made during the 2017 AQABA ship campaign. $k(\text{NO}_3)$ is the loss rate (in s^{-1}) of NO₃ due to all processes, direct and indirect. Mixing ratios of NO₃ shown are derived from calculations from [NO₂], [N₂O₅] measurements and the equilibrium constant K_{eq} from the literature. (N) = North, (S) = South.

The Air Quality and climate change in the Arabian Basin (AQABA) campaign was ship-based study of various trace gases and aerosol measurements conducted in the seas around the Arabian Peninsula and Mediterranean Sea during the summer (June – August) of 2017. As part of the campaign, the reactive nitrogen trace gases of NO₂, NO₃, and N₂O₅ were measured by the 5-CRD instrument. An overview of these measurements, broken down by the five regions of interest studied during the campaign (north Red Sea, south Red Sea, Indian Ocean (in the Arabian Sea), Persian Gulf (also known as the Arabian Gulf) and Mediterranean Sea), is shown in Figure 14 together with ozone (O₃) and the calculated first-order loss rate of NO₃ ($k(\text{NO}_3)$). During the nights of the campaign, NO₃ and N₂O₅ were produced via reaction with NO₂ and O₃ according to:





With

$$P(\text{NO}_3) = k_1[\text{NO}_2][\text{O}_3] \quad (\text{Equation 11})$$

And

$$K_{\text{eq}}(\text{T}) = \frac{[\text{N}_2\text{O}_5]}{[\text{NO}_2][\text{NO}_3]} \quad (\text{Equation 12})$$

$P(\text{NO}_3)$ describes the rate of production of NO_3 (molecule $\text{cm}^{-3} \text{s}^{-1}$) from $[\text{NO}_2]$ and $[\text{NO}_3]$ (molecule cm^{-3}) with k_1 , a rate coefficient ($\text{cm}^3 \text{molecule}^{-1} \text{s}^{-1}$). $K_{\text{eq}}(\text{T})$ describes the equilibrium coefficient which is established between N_2O_5 , NO_3 and NO_2 at a given temperature T (K), with: $K_{\text{eq}}(\text{T}) = 5.8 \times 10^{-27} e^{(10840/\text{T})}$ (JPL Recommended (DeMore et al. 1997)).

During the AQABA campaign NO_3 and N_2O_5 nighttime mixing ratios varied from below the detection limit to over 100 ppt for NO_3 and from the below the detection limit to approximately 300 ppt for N_2O_5 . The NO_2 and O_3 mixing ratios were also highly variable according to region; NO_2 background levels were at or below the detection limit in the ‘clean’ marine environment regions, such as the Indian Ocean (August 7 – August 14), and at much higher levels in the more polluted regions (several ppb), such as the Persian Gulf. Due to the near constant presence of ship emissions, it is difficult to quantitatively define background NO_2 in these regions. O_3 mixing ratios were lower in the Indian Ocean (20 – 30 ppb) and much higher in the Red Sea (4 – 18 July and 15 – 24 August; 50 – 80 ppb) and the Persian Gulf regions (24 July – 7 Aug; 60 – > 150 ppb).

Measurements of NO_3 and N_2O_5 were made on 30 campaign nights (of a total of 60 possible), with each geographic region covered at least once on either of the two legs (La Seyne sur-mer to Kuwait or Kuwait to La Seyne sur-mer (Figure 18, shown below)). The nights on which $\text{NO}_3 / \text{N}_2\text{O}_5$ were not measured were a result of instrument failures in the Mediterranean and Red Sea regions in the first leg of the campaign, and a ship-wide power failure in the Indian Ocean on the second leg of the campaign. NO_3 , throughout most of the campaign, was typically not observed in continuous, long stretches of time, rather it was observed sporadically appearing a few times throughout the nights, often alongside sudden rapid increases (from several 10s of ppb and up to 100 ppb) and decreases in the signal of NO_2 , referred to as a plume event, as an increase in $[\text{NO}_2]$ drives an increase in $P(\text{NO}_3)$, according to (Equation 11).

While NO_3 was directly observed on several nights, mixing ratios predicted according to the equilibrium between NO_3 , NO_2 and N_2O_5 (Equation 12) were significantly higher than observed mixing ratios, with sometimes as much as a factor of 5 difference. As ambient temperatures (controlling K_{eq}) were high throughout the campaign, generally 25 – 35°C (min \approx 21°C), and higher temperatures tend to favor partition towards NO_3 , this small signal compared to N_2O_5 was surprising and suggests local losses at the measurement site.

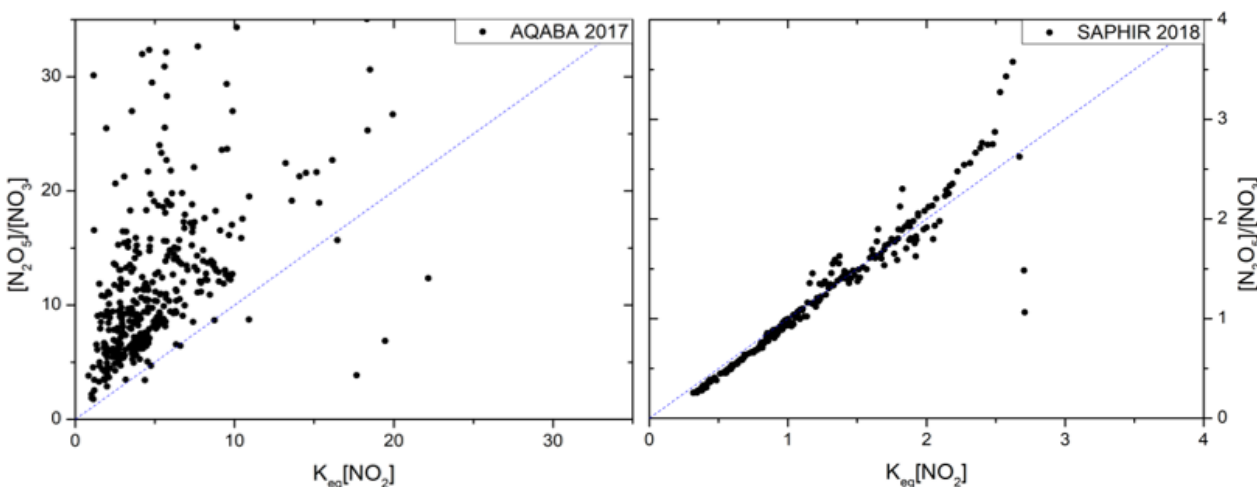


Figure 15. $K_{eq}(T)[NO_2]$ vs. $[N_2O_5]/[NO_3]$ for one night (22-23 August, north Red Sea) in the SAPHIR campaign compared with one experiment conducted during the 2018 SAPHIR campaign. Blue line indicates the 1:1 ratio.

A potential source of these local losses was in the PFA sampling inlet with similar sampling losses having been reported before (Steven S. Brown et al. 2017; Crowley, Thieser, Tang, Schuster, Bozem, Beygi, et al. 2011). The inlet strategy (1/2" PFA piping with a large flow rate to reduce residence time) has been used before (Sobanski, Tang, et al. 2016) and after the AQABA without similar or reported losses of NO_3 . Figure 15 compares $K_{eq}[NO_2]$ against $[N_2O_5]/[NO_3]$ from a typical case during a night where NO_3 was directly measured during the AQABA campaign (left) against a typical case during the latter 2018 SAPHIR campaign. While the apparent NO_3 losses reported here did not appear to become more severe with time (i.e. a greater deviation from 1:1 against $K_{eq}[NO_2]$), replacement of the PFA line did not result in an increase of NO_3 signal, even temporarily. At times the inlet line would become visually discolored as a result of sampling over long periods. These observations demonstrate the importance of regularly checking the transmission efficiencies on inlets and internal tubing during field measurements.

A possible explanation for these observations would be the inlet line, when exposed to ambient air, may act as large surface area which becomes reactive towards NO_3 due to heterogeneous chemical processes occurring as a result of being coated in a layer of, e.g., unsaturated organics. The correction implied by the calculation of $K_{eq}[NO_2]$ always resulted in an increase to the mixing ratios of NO_3 or else a decrease in the mixing ratios of N_2O_5 , the latter of which implies an error in the data correction procedures outlined in section 3. As these correction procedures were shown to be consistent before and after the AQABA campaign and/or the corrections affect both cavities in the same manner (e.g. the l/d ratio or effective laser cross section) it is more likely that the disagreement between measured and calculated $K_{eq}[NO_2]$ was a result of NO_3 loss and not an overestimation of N_2O_5 . While this does not rule out losses of N_2O_5 on the inlet system, for the analysis which follows, it is assumed that NO_3 losses were caused by gas phase organics partitioning to the walls of the instrument. As N_2O_5 does not generally react with organics, and the inner PFA tubing was protected by a 2 μm Teflon filter preventing the PFA from being coated in reactive aerosol, it is not anticipated that there were further losses of N_2O_5 .

Continuing with the assumption that losses of NO_3 were a result of the inlet becoming reactive to NO_3 after exposure to ambient air, the residence time of NO_3 and N_2O_5 in the instrument's internal tubing and across the cavities (~ 1 s) would be considerably shorter than the thermal lifetime of N_2O_5 (minutes). Therefore, the NO_3 mixing ratios can be calculated from the measured $[N_2O_5]$, $[NO_2]$ and K_{eq} , modified

from (Equation 12). A disadvantage of this indirect calculation of NO₃ is that it relies on a complete set of accurate, low-noise NO₂ and N₂O₅ measurements. At low mixing ratios of NO₂, the production of NO₃ is limited and the uncertainties in the NO₂ measurements dominate, particularly under humid conditions. If mixing ratios NO₂ are comparatively large, but mixing ratios of N₂O₅ are low then uncertainty in this measurement (~25%) dominates the calculation of NO₃.

5.1.2 NO₃ First order loss rates

Understanding the role of NO₃ as an oxidizing species requires a detailed understanding of its production rate, P(NO₃), and the first order loss rates, k(NO₃), which can be calculated directly from observations of NO₃, NO₂ and O₃:

$$k(\text{NO}_3) = \frac{k_1[\text{NO}_2][\text{O}_3]}{[\text{NO}_3]} \quad (\text{Equation 13})$$

Where the term “NO₃ reactivity” is used, we refer to k(NO₃) (in units s⁻¹). “NO₃ lifetimes” refers to the inverse of this parameter (i.e. 1/k(NO₃)).

The analysis of data as described in (Equation 12) requires certain conditions to be fulfilled. It is necessary that the system is in a steady-state (Steven S. Brown, Stark, and Ravishankara 2003), this being achieved when the rates of change of NO₃ and N₂O₅ are zero. More rigorously, this means steady-state has been achieved when $\delta[\text{NO}_3]/\delta t = k_1[\text{NO}_2][\text{O}_3] + k_2'[\text{N}_2\text{O}_5] - k_2[\text{NO}_2][\text{NO}_3] - k_x[\text{NO}_3] = 0$ and $\delta[\text{N}_2\text{O}_5]/\delta t = k_2'[\text{NO}_2][\text{NO}_3] - k_2'[\text{N}_2\text{O}_5] - k_y[\text{N}_2\text{O}_5] = 0$, where k_x and k_y represent the total of all first-order loss processes of NO₃ and N₂O₅, respectively.

The time required to achieve a steady-state depends upon the both rate of formation of NO₃ (reaction between NO₂ and O₃) and the loss rates of both NO₃ and N₂O₅, in addition to the ambient air temperature. Chemistry can also have an influence as a rapid injection of NO into an air mass (e.g. from a local ship emission) can rapidly remove NO₃, disrupting an existing equilibrium. If an air mass was measured directly after one of these NO events, and as the chemical lifetime of NO at night is short, particularly in conditions of high ambient ozone (minutes), a steady-state may not have been reestablished. As a result, the k(NO₃) calculated would be positively biased, even if all removal sources are accurately accounted for.

In principle, under steady-state conditions, the different contributions to the total loss rates of NO₃ can be assigned if all the loss processes are known. Losses can be direct, such as VOC reactions with NO₃ in the gas phase, or indirect where N₂O₅ (formed from NO₃) is lost onto the surfaces of aerosols in a heterogeneous reaction. Assigning these losses, both direct and indirect, requires knowledge of all relevant species and their associated rate coefficients describing their reactions with NO₃. This method of describing total loss rate, k(NO₃), has been described before (U. F. Platt, et al. 1984) and used on numerous occasions to evaluate field data (Crowley, Thieser, Tang, Schuster, Bozem, Beygi, et al. 2011; Aldener et al. 2006; Matsumoto et al. 2006; McLaren et al. 2010) and is equal to:

$$\sum_{k(\text{NO}_3)} = (k_x[\text{X}]) + (0.25\bar{c}\gamma(\text{NO}_3)\text{ASA}) + (0.25\bar{c}\gamma(\text{N}_2\text{O}_5)\text{ASA})K_{eq}[\text{NO}_2] \quad (\text{Equation 14})$$

Where k_x (cm³ molecule⁻¹ s⁻¹) is the rate coefficient for a reaction of NO₃ with a trace gas [X] (molecule cm⁻³); \bar{c} is the mean molecular velocity (cm s⁻¹); γ represents the dimensionless uptake coefficients of NO₃ and N₂O₅ on the surface of particles; and ASA is the aerosol surface area concentration (cm² cm⁻³). Throughout the nights of the campaign, calculated values of $\gamma(\text{N}_2\text{O}_5)$ were $\approx 0.033 \pm 0.003$ for the aerosol

chemical composition (T. H. Bertram, Thornton, and Riedel 2009) (see section 2). The standard deviation in γ reflects the small region-to-region variability observed during the campaign. The dominant contribution to the aerosol surface area was by particles with a diameter of $< 0.200 \mu\text{m}$. As described in section 2, the uptake coefficient can be reduced due to large particle sizes and high γ due to gas-phase diffusion of NO_3 and N_2O_5 being limited by a concentration gradient close to the surface of particles. Under these conditions, at 298 K and atmospheric pressure, according to (Equation 3), we would expect to see a reduction of the γ from ≈ 0.03 to > 0.02999 . As this difference is essentially negligible, it is not considered further in this analysis.

(Equation 14) represents a simplified statement of all potential losses, as a complete description of all loss processes of NO_3 and N_2O_5 at any point in time would necessarily require knowledge of gas-phase losses of N_2O_5 as well as the relevant photolysis and dry deposition rates. In the gas phase, reaction partners of N_2O_5 are not known, except H_2O , which is generally seen as insignificant (Crowley, Schuster, et al. 2010). Taking the current IUPAC recommendation of $\text{N}_2\text{O}_5 + \text{H}_2\text{O}$ results in an average loss rate of $7.25 \times 10^{-5} \text{ s}^{-1}$ or a lifetime of > 4 hours. Photolysis rates of NO_3 and N_2O_5 were calculated from spectral radiometer data (see section 4). Beginning at sunrise, photolysis quickly becomes the biggest loss pathway for NO_3 . As all measurements of NO_3 during AQABA were conducted during the night, where photolysis rates approach zero, photolysis rates were not a significant contributor to $k(\text{NO}_3)$ except at dusk and dawn. Direct deposition rates of N_2O_5 can be a significant loss mechanism in regions where other loss processes of both NO_3 and N_2O_5 are inefficient and where the marine boundary layer (MBL) height is low and wind speeds are high. During the AQABA campaign the average true wind speeds measured were $5.4 \pm 2.9 \text{ m s}^{-1}$ which contributes to an exchange velocity (V_{ex}) to the ocean surface of between $0.5 - 2.0 \text{ cm s}^{-1}$ (Liss and Slater 1974). A more recent estimate (Kim, Farmer, and Bertram 2014) suggests a value of -1.66 cm s^{-1} . Proceeding with this estimate of N_2O_5 deposition, the deposition rate, k_{dep} , can be estimated as:

$$k_{\text{dep}} = -\frac{V_{\text{ex}}}{\text{MBL}} \quad (\text{Equation 15})$$

With, MBL being the marine boundary layer height (m) provided by the ERA5 dataset described in section 4. The average marine boundary layer height in AQABA was $691 \pm 192 \text{ m}$, with the standard deviation representing the region-to-region variability rather than the minimum-maximum differences in a diurnal profile. For example, in the Indian Ocean, where the MBL height was lowest, the MBL height was $587 \pm 122 \text{ m}$, while in north Red Sea it was $964 \pm 161 \text{ m}$. Calculating k_{dep} as per (Equation 15) with these conditions results in a loss rate of $2.83 \times 10^{-5} \text{ s}^{-1}$ in the Indian Ocean, which would represent highest average in the campaign, or a lifetime of 16 hours. This contribution to the overall loss of NO_3 and N_2O_5 is far smaller than the lifetimes observed in most regions (minutes) and even in the clean maritime environment of the Indian Ocean (< 1 hour) and therefore is not further considered in the analysis which follows.

5.1.3 Regional variability of $k(\text{NO}_3)$

Below, the results of the AQABA NO_3 -Lifetime analysis (calculated indirectly from measurements of N_2O_5) are displayed in a series of histograms (Figure 16 and Figure 17). $k(\text{NO}_3)$ was calculated according to (Equation 13) with NO_3 calculated according to (Equation 12). Where there were no $\text{NO}_3 / \text{N}_2\text{O}_5$ signals from which to calculate $k(\text{NO}_3)$ the limit of detection has been taken to describe a lower limit to reactivity, i.e. what the loss rate of NO_3 would have to have been to reduce NO_3 to below the limit of detection. These data points are shown in red while the black data points are associated with a calculation of $k(\text{NO}_3)$ from a measurement of N_2O_5 . The data is also summarized in Table 4.

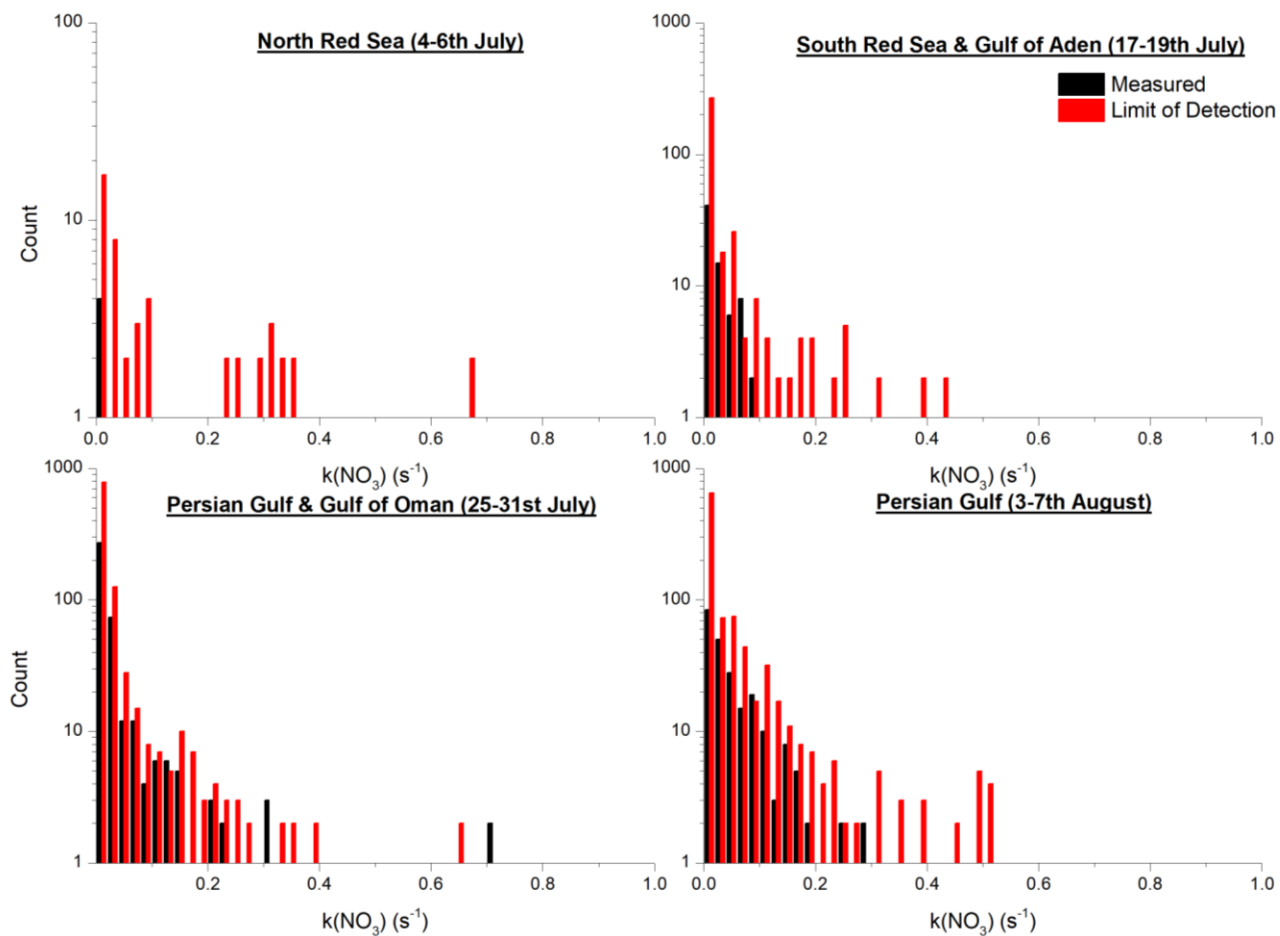


Figure 16. Histograms of NO_3 reactivity from the AQABA campaign. This figure details the first leg of the campaign (La Seyne-sur-Mer to Kuwait). The histograms show $k(\text{NO}_3)$ calculated directly from measurements of $K_{eq}(T) \times \text{N}_2\text{O}_5 (= \text{NO}_3)$ in black, while the red bars show the lower-limit to $k(\text{NO}_3)$, calculated from the limit of detection (LOD).

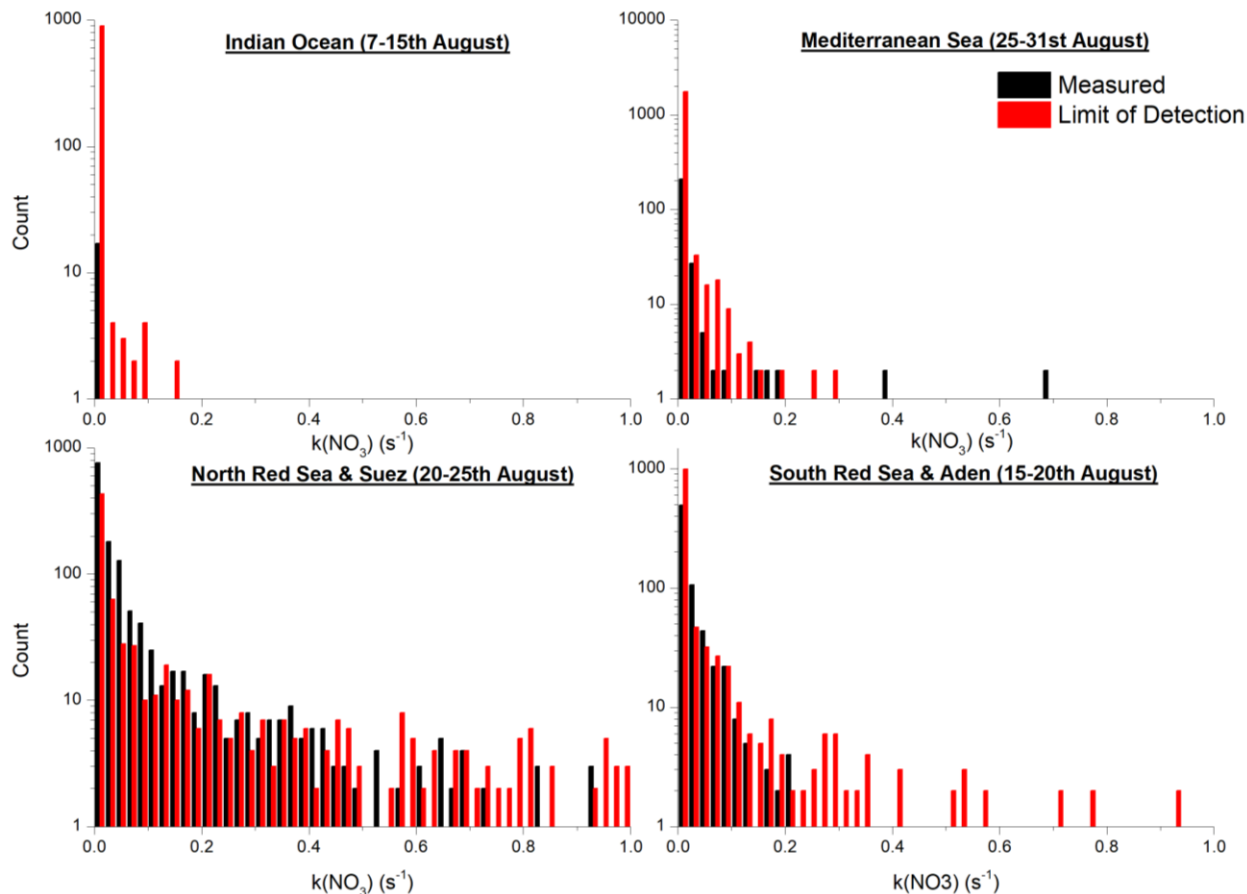


Figure 17. Histograms of NO_3 reactivity (bin size = 0.02 s^{-1}) from the AQABA campaign. This figure details the second leg of the campaign (Kuwait to La-Seyne-sur-Mer). The histograms show $k(\text{NO}_3)$ calculated directly from measurements of $K_{eq}(T) \times \text{N}_2\text{O}_5 (= \text{NO}_3)$ in black, while the red bars show the lower-limit to $k(\text{NO}_3)$, calculated from the limit of detection (LOD).

As described above, NO_3 measurements were taken on 30 nights of the AQABA with each geographic region of the campaign covered on at least one night. With exception of the Indian Ocean, observed lifetimes were short with medians of each region limited to generally between 30 to 200 seconds ($0.03 - 0.005 \text{ s}^{-1}$). Although $\text{NO}_3 / \text{N}_2\text{O}_5$ measurements have not been undertaken in many of the studied regions before, with exception of the Mediterranean, NO_3 lifetimes from the AQABA campaign broadly agree to ranges of NO_3 lifetimes reported from the field in other polluted marine environments, such as (Aldener et al. 2006) who observed lifetimes between 30 and 200 seconds ($0.03 - 0.005 \text{ s}^{-1}$) on a ship off the coast of the northeastern United States and (McLaren et al. 2010) who observed lifetimes of 60 – 130 seconds ($0.016 - 0.007 \text{ s}^{-1}$) from a station located on an island situated in the Vancouver archipelago in BC, Canada.

Table 4. Overview of measured and limit of detection (LOD-Limited) NO₃ reactivity by region. L1, L2 – Leg ½.

Region (L1, L2)	Median Reactivity (measured) (s ⁻¹)	Median Reactivity (LOD-limited) (s ⁻¹)
North Red Sea	0.0051	0.0464
South Red Sea	0.0168	0.0044
Persian Gulf	0.0145	0.0049
Persian Gulf	0.0350	0.0032
Indian Ocean	0.0003	0.0002
South Red Sea	0.0102	0.0014
North Red Sea	0.0156	0.0175
Mediterranean	0.0056	0.0002

The lowest median reactivity was found in the clean marine environment of the Indian Ocean, reflecting the relatively low concentrations of VOCs and other reaction partners for NO₃. Here the average lifetime of NO₃ was ~55 minutes (0.0003 s⁻¹), which is consistent with observations of extended NO₃ lifetimes in open marine environments such as the ~80 minutes seen by (Heintz, et al. 1996) in a remote region of the Baltic Sea in Northern Germany or > 30 minutes lifetimes reported by (Crowley, Thieser, Tang, Schuster, Bozem, Beygi, et al. 2011) when analyzing an air mass originating from the open Atlantic Ocean at a coastal site in southern Spain.

Conversely, high median reactivity was observed in areas such as the Red Sea, and Persian Gulf. Lifetimes in these regions were on the order of 30 – 60 s, suggesting enhanced roles of NO₃ + VOC reactivity, as these loss mechanisms would be favored in the higher temperatures (which favor partition towards NO₃ in the NO₃ / N₂O₅ equilibrium) and the increased concentrations of VOCs in these regions, related to regional-specific anthropogenic sources such as the oil and gas industry in the Persian Gulf or shipping emissions in the Red Sea. Particle surface concentration was also greater, which contributes to greater heterogeneous losses of N₂O₅ (see below), even for similar temperature and NO_x levels.

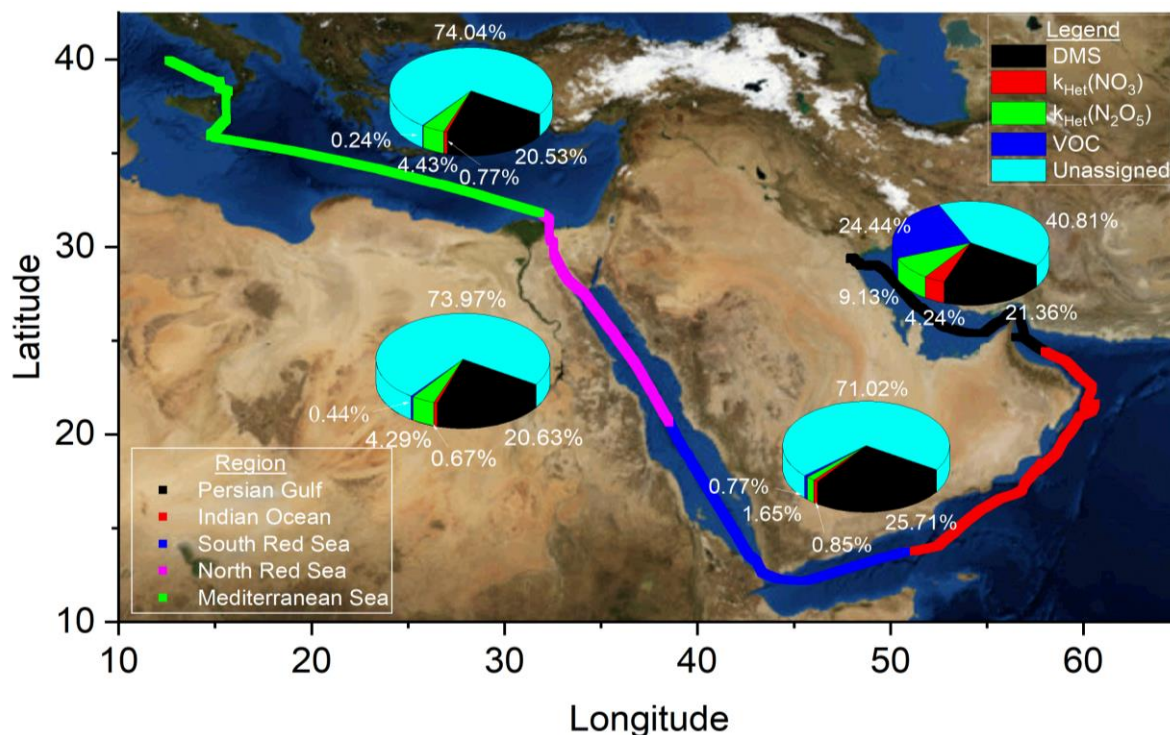


Figure 18. Course of the Kommandor Iona on the second leg of the AQABA campaign (3 - 31st August). The different regions are highlighted in different colors. The 4 pie charts represent the proportions of median $k(\text{NO}_3)$ assigned by known reaction partner of NO_3 and N_2O_5 for each of the regions, excluding the Indian Ocean.

In addition to the anthropogenic VOC suspected to contribute to $k(\text{NO}_3)$, biogenic gas-phase reaction partners were also measured on AQABA, including Isoprene from plant life and dimethyl sulfide (DMS), emitted from microbial sea organisms, such as phytoplankton. Fine-particulate matter is also a potential contributor to $k(\text{NO}_3)$, which, in the context of the Arabian Peninsula, can be derived from both natural (e.g. dust or sea salt) or anthropogenic (e.g. black carbon) sources. Figure 18 details the known contributions of each identified reaction partner of NO_3 by each region. $k_{\text{Het}}(\text{NO}_3)$ and $k_{\text{Het}}(\text{N}_2\text{O}_5)$ represent heterogeneous loss processes of NO_3 and N_2O_5 on to the surface of particles, respectively. $k(\text{VOC})$ is the combined contribution of all volatile organics (excluding DMS) known to react with NO_3 measured during AQABA, including short-chain (C2-C5) saturated and unsaturated hydrocarbons; longer chain (C6-C8) saturated hydrocarbons; aromatic compounds (benzene, toluene, xylenes); isoprene (C_5H_8); and formaldehyde (HCHO). Region-to-region, the contributions of heterogeneous activity remains fairly constant for both NO_3 ($< 1\%$) and N_2O_5 ($\approx 2 - 4\%$). The exception is in the Persian Gulf region where increased ambient fine particulate matter resulted in an increase of surface area. Note that depending on the value assumed for $\gamma(\text{NO}_3)$, the reactivity to $k_{\text{Het}}(\text{NO}_3)$ may vary by up to an order of magnitude (see section 5.2.2).

Compared to DMS, the sum of the contributions of other VOCs made up an extremely small proportion of $k(\text{NO}_3)$ in the Red Sea and Mediterranean Sea ($< 1\%$) while a significant proportion of the reactivity could be assigned to these VOCs in the Persian Gulf ($\approx 18\%$). The small contribution of VOC reactivity is a result of many of the measured VOCs having small rate coefficients with NO_3 (e.g. H-abstraction from $\text{C}_2\text{H}_6 < 1 \times 10^{-17} \text{ cm}^3 \text{ molecule}^{-1} \text{ s}^{-1}$ (J. A. Bagley, et al. 1990)) and / or relatively low concentrations, while in the Persian Gulf concentrations of VOCs were generally elevated (to a maximum of 166.5 ppb (Bourtsoukidis et al.

2019)) due to the presence of sources related to oil and gas extraction and refining. NO_3 typically reacts quickly with unsaturated hydrocarbons with an electrophilic attack on the electron-rich carbon-carbon double bond. During AQABA the most abundant VOCs which were measured were ethane, ethene, propane and propene, all of which have low rate coefficients with NO_3 , despite the double bond systems in ethene and propene. This remained true in the Persian Gulf where short-chain hydrocarbons were still the most prevalent of all measured VOCs but VOC mixing ratios in general were elevated relative to the rest of the AQABA campaign, leading to more significant contributions from longer chained VOCs, such as butenes and pentenes, which have larger rate coefficients with NO_3 .

Biogenic VOC reactivity by contrast was nearly entirely attributable to DMS. $k(\text{DMS})$ remained fairly constant throughout the campaign, contributing approximately 20 – 25% to total NO_3 steady state reactivity in all regions. A 20% contribution of DMS to NO_3 reactivity in the eastern Mediterranean is consistent with other Eastern Mediterranean studies conducted on land close to the shore in Cyprus and Crete (Vrekoussis et al. 2003, 2007), indicating that DMS was an important sink for NO_3 during AQABA as it has been shown in other marine and coastal environments in the past..

Below, a night of the campaign is analyzed in detail, attempting to identify the various direct and indirect loss processes controlling $k(\text{NO}_3)$ as discuss the importance of each species and consistency with other measurements taken under broadly similar conditions.

5.2.1 Assigning reactivity 22 – 23 August (North Red Sea)

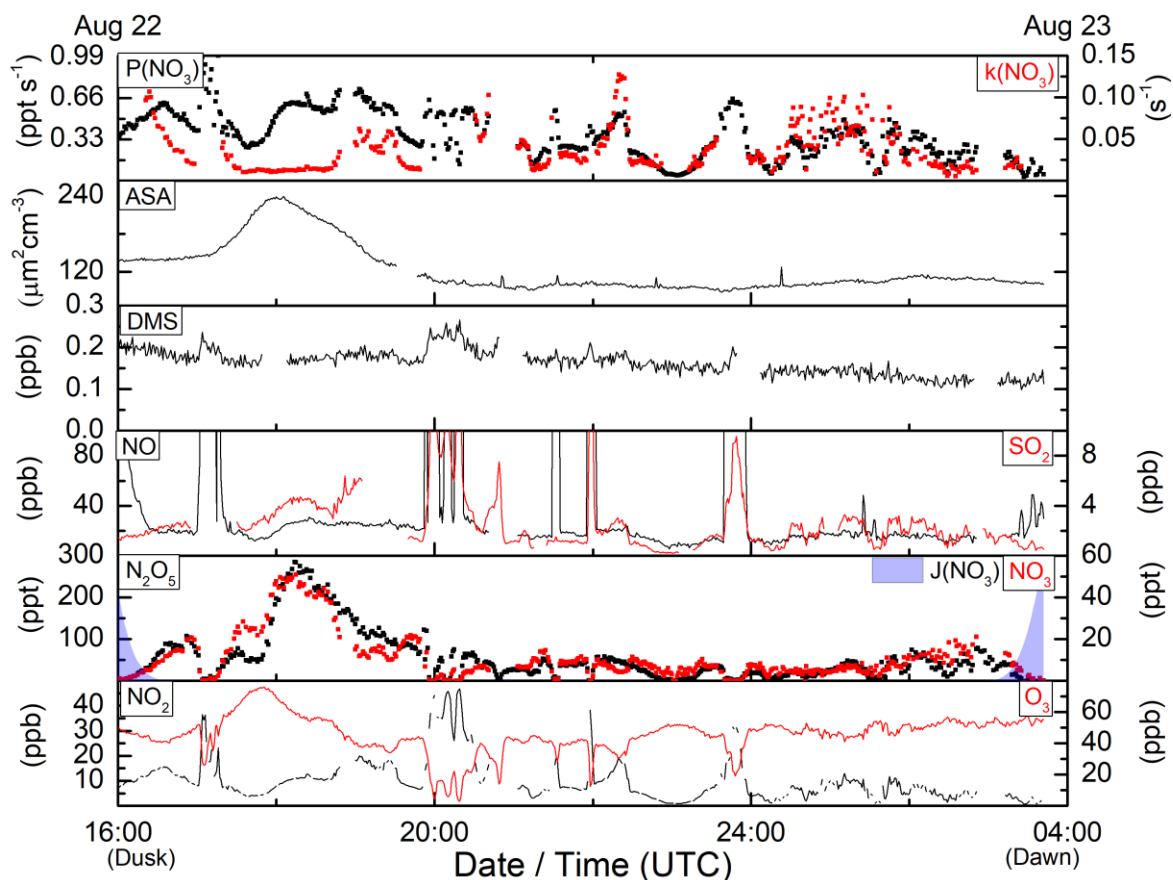


Figure 19. Overview of selected parameters from the night of 22-23rd August in the Gulf of Suez, in the North Red Sea. ASA = Aerosol surface Area. $P(\text{NO}_3)$ = ppt per-second production rate of NO_3 . NO_3 mixing ratios presented are calculated according to (Equation 12).

Measurements made on the 22-23rd of August, displayed in Figure 19, were taken in the Gulf of Suez at the northern end of the Red Sea and were expected to be strongly influenced by shipping emissions as this area, being so close to the Suez Canal, is one of the world's busiest shipping lanes. This is reflected in the highly variable, elevated NO_2 levels seen throughout the night between with a constant background between ~5 to ~20 ppb (excluding between 23:00 and 00:00 UTC where NO_2 decreased to approximately 1 ppb) and a number of short duration plumes (minutes) of up to 40 ppb. NO_2 mixing ratios co-varied strongly with SO_2 and anti-correlated with O_3 , which was otherwise stable between 60 – 70 ppb throughout the night. Sudden losses of O_3 which anti-correlate with NO_2 , such as those seen at ~20:00, are often indicative of combustion processes which produce NO, as the reaction of NO (the major NO_x product released by internal combustion engines) with O_3 produces NO_2 . While several terrestrial sources of NO_x emissions are possible, and it is noted that several small cities and industries are located along the Gulf of Suez coastline, at several points during the night large, ppb-scale increases of NO were seen (including 17:00, 20:00, 22:00 and shortly before 00:00). These must necessarily have a local source close to the *Kommandor Iona* as the lifetime of NO in the presence of 60 – 70 ppb of O_3 is on the order of a few minutes. Taking these kinetics, together with the location and the presence of SO_2 in the plumes (which is a known ship exhaust product) these NO and NO_2 plumes are most likely to be from nearby ship emissions in origin.

NO₃ and N₂O₅ mixing ratios co-varied mostly according to NO₂, with mixing ratios reaching a maximum of 280 ppt and 60 ppt, respectively close to 18:00 before declining to between ~20-50 ppt (N₂O₅) and ~5-15 ppt (NO₃) between 19:00 and 01:00. Towards the end of the night, from 01:00 onwards, N₂O₅ and NO₃ build up again to a maximum of ~100 ppt and ~20 ppt respectively, though are highly variable throughout this period. On several occasions (e.g. around 20:00) rapid reductions of NO₃ and N₂O₅ to below the detection limit were observed. This was always accompanied by a sudden increase of NO and SO₂ which, as mentioned above, are presumably from nearby ships' exhausts.

As shown in reactions (R14) and (R15a), the production rates of NO₃ and N₂O₅ are governed by the concentrations of [NO₂] and [O₃]. As the ambient concentrations of these trace gases were high and, at least in the case of NO₂, variable. The overall production rate of NO₃ varied throughout the night between less than 0.1 ppt s⁻¹ and up to 1 ppt s⁻¹. These production rates can be divided by the observed concentrations of NO₃ (or N₂O₅), to estimate a steady state loss coefficient according to (Equation 13). Below, the factors controlling the lifetimes of NO₃ are analyzed by estimating the contribution of each process to see if the sum is consistent with observations.

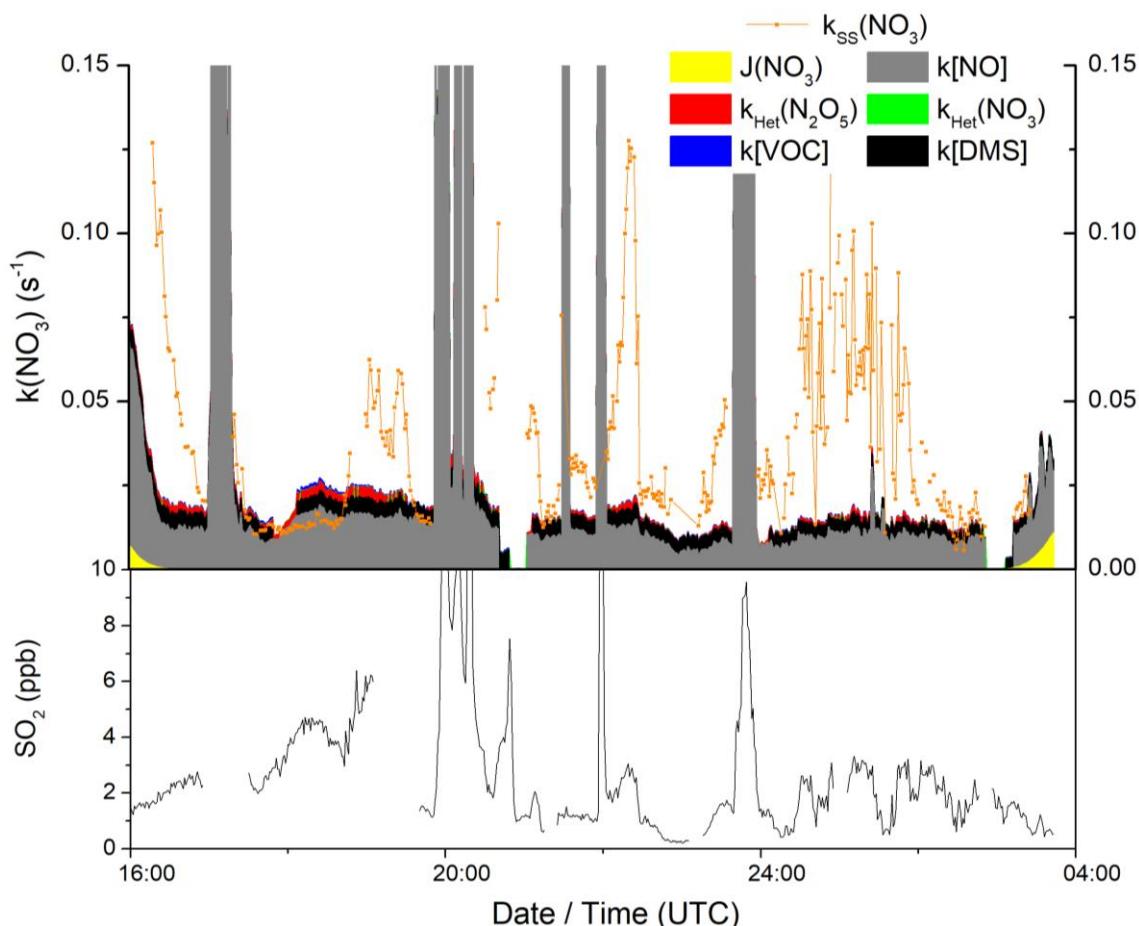


Figure 20. Overview of reactivity ($k(\text{NO}_3)$) on the night 22-23rd August. $k_{\text{Het}}(\text{NO}_3)$ and $k_{\text{Het}}(\text{N}_2\text{O}_5)$ refer to heterogeneous loss processes of NO₃ and N₂O₅ onto the surface of particles. $k(\text{VOC})$ includes the summed contribution of various VOCs measured during the AQABA campaign, detailed in section 3. $J(\text{NO}_3)$ is the photolysis rate of NO₃ and marks sunset and sunrise. Plotted below is the SO₂ mixing ratio (ppb) which tracks with unassigned $k(\text{NO}_3)$.

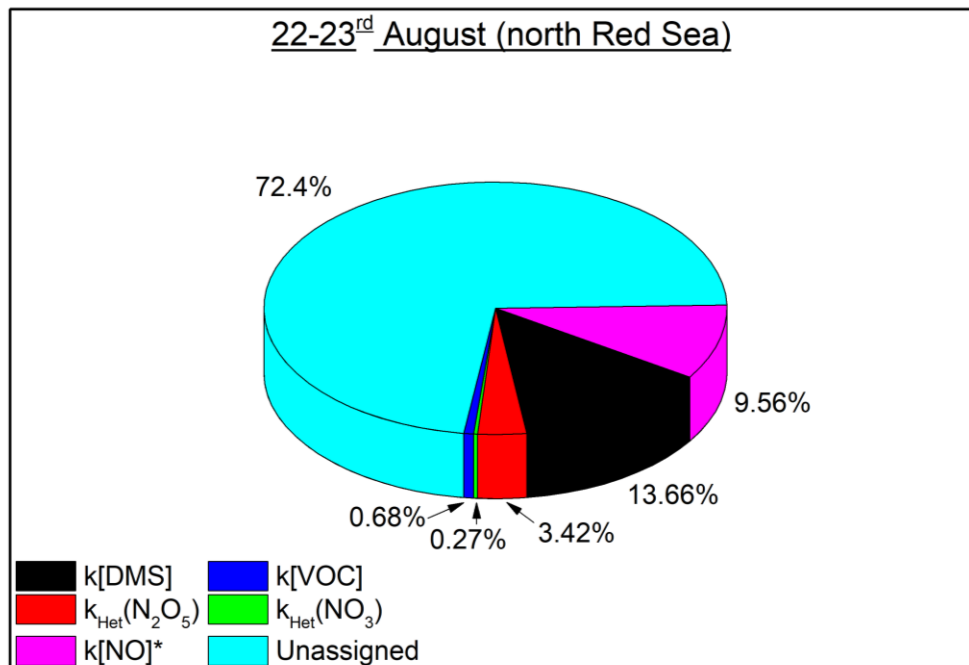


Figure 21. Contribution to median $k(\text{NO}_3)$ attributed to each known reaction partner during the night 22-23 August. * - $k[\text{NO}]$ calculated from limit of detection of NO measurement. Data from plumes excluded.

Figure 20 details the contributions of each known loss mechanism compared with the steady-state calculated reactivity of NO_3 . Between 18:00 – 19:00 and towards the end of the night, where $J(\text{NO}_3)$ becomes important as the sun begins to rise (~02:00 – 03:00), all calculated reactivity is accounted for with the summed photolysis, DMS, (anthropogenic) VOC and heterogeneous N_2O_5 and NO_3 loss. However, most reactivity throughout most of the night, as shown in Figure 21, could not be accounted for by these mechanisms. Below, each of the loss processes identified are examined and discussed with regard to both the night 22-23 August and the wider AQABA campaign.

5.2.2 Gas-Phase reactions of NO₃

Table 5. Rate coefficient of NO₃ + each gas-phase partner ([X]) measured during the AQABA campaign at 298 K. Lifetimes of each partner in the presence of 10 ppt NO₃ given to contextualize the relative importance of each VOC in controlling k(NO₃).

Molecule [X]	k[X]+NO ₃ (cm ³ molecule ⁻¹ s ⁻¹ , 298 K)	Lifetime of [X] (10 ppt* NO ₃ , 298 K)	Reference
NO	2.6 x 10 ⁻¹¹	158 seconds	(Brown, Ravishankara and Stark 2000)
Dimethyl Sulfide (DMS)	1.1 x 10 ⁻¹²	1 hour	(Wallington, et al. 1988)
HCHO	5.5 x 10 ⁻¹⁶	86.5 days	(Atkinson, Plum, et al. 1984)
Ethane	<1 x 10 ⁻¹⁷	> 4760 days	(J. A. Bagley, et al. 1990)
Ethene	2.1 x 10 ⁻¹⁶	226.8 days	(Atkinson, Aschmann and Pitts Jr. 1988)
Propane	< 7 x 10 ⁻¹⁷	> 680 days	(Boyd, et al. 1991)
Propene	9.5 x 10 ⁻¹⁵	5 days	(Atkinson, Plum, et al. 1984)
<i>i</i>-Butane	1.1 x 10 ⁻¹⁶	433 days	(J. A. Bagley, et al. 1990)
<i>n</i>-Butane	4.6 x 10 ⁻¹⁷	1035 days	(J. A. Bagley, et al. 1990)
<i>trans</i>-2-Butene	3.9 x 10 ⁻¹³	2.9 hours	(IUPAC, 2020)
<i>i</i>-Pentane	1.6 x 10 ⁻¹⁶	297 days	(Wayne, et al. 1990)
<i>n</i>-Pentane	2.4 – 8.0 x 10 ⁻¹⁷	~595 days	(Wayne, et al. 1990)
1-Pentene	1.5 x 10 ⁻¹⁴	3.2 days	(Aschmann and Atkinson 2010)
2-Methyl-Pentane	1.71 x 10 ⁻¹⁶	278 days	(Aschmann and Atkinson 1995)
<i>n</i>-Hexane	3.2 – 10.5 x 10 ⁻¹⁷	~453 days	(Wayne, et al. 1990)
<i>n</i>-Heptane	4.1 – 13.6 x 10 ⁻¹⁷	~350 days	(Wayne, et al. 1990)
Octane	5.5 – 18.1 x 10 ⁻¹⁷	~263 days	(Wayne, et al. 1990)
Benzene	< 3 x 10 ⁻¹⁷	> 1587 days	(IUPAC, 2020)
Toluene	7.8 x 10 ⁻¹⁷	610 days	(R. Atkinson 1991)
Isoprene	6.5 x 10 ⁻¹³	1.76 hours	(Atkinson, Plum, et al. 1984)

* - 10 ppt NO₃ ≈ 2.43 x 10⁸ molecule cm⁻³ at 298 K

Known reaction partners of NO₃ which were measured on AQABA (Table 5) include NO, HCHO, isoprene, DMS and several light hydrocarbon species (C2-C8), several heavier hydrocarbons (C6-C8) and aromatic compounds including benzene and toluene. Of these, NO and DMS are known to have large rate coefficients with NO₃, and while many of the measured hydrocarbons react only very slowly with NO₃. Isoprene, 1-pentene, *trans*-2-butene and, to a lesser extent, propene represent an intermediate case where, under high concentrations (several ppb) in the atmosphere, they may contribute significantly to k(NO₃).

5.2.2.1 Reaction with NO

Beginning with NO, while there are significant periods of large NO reactivity, such as those seen in Figure 20, at 19:00, 20:00, 22:00 and 00:00, the NO₃ reaction with excess NO disrupts the equilibrium between NO₃, N₂O₅ and NO₂ and therefore steady-state conditions cannot be assumed during these events, which

were common throughout the entirety of the AQABA campaign. High NO_3 loss rates and high temperatures typically favor the rapid establishment of steady state conditions, with FACSIMILE / CHEKMAT simulations (Curtis and Sweetenham 1987) (Appendix A) showing that under typical AQABA conditions (~ 50 ppb O_3) a sudden titration of NO_3 will reestablish steady state within 5 – 10 minutes under ambient temperatures and factoring in known loss rates. As a result, data following a large plume of NO is where steady state is not likely to have been reestablished is not further considered.

During the night 22 – 23 August, background NO mixing ratios remained high (≈ 20 ppt), which is nearly a factor of 4 times greater than the reported limit of detection (≈ 5 ppt) of the Chemiluminescence detector (CLD) measurements (see section 4). This is surprising, given the rapid reaction with O_3 to produce NO_2 and lack of photochemical production. As the background is constant, not dependent on wind direction, does not correlate with background NO_2 and no obvious (necessarily strong) source exists, it is more likely that the elevated background represents the sampling of some unknown chemical interference of the CLD measurement, with such interferences reported before (Grosjean and Harrison 1985) being a result of organosulfur species. Note that some contribution towards the total calculated steady state reactivity (Figure 21) has been described by reaction with NO, but it is difficult to quantify exactly how much of the NO signal and therefore contribution to $k(\text{NO}_3)$ comes from true NO at levels close to the detection limit. If it is assumed that NO is at its reported detection limit during these periods, this allows for an upper limit on NO contribution to $k(\text{NO}_3)$ to be set as ≈ 5 ppt of NO, which would be equivalent of 0.0028 s^{-1} , or approximately 9.5% of median reactivity on the 22 – 23rd August.

5.2.2.2 Reaction with DMS

DMS is an organosulfur biogenic VOC which is released directly into the sea by marine microorganisms, such as phytoplankton and zooplankton. From the Oceans, DMS diffuses into the atmosphere from the surface and undergoes oxidation reactions to produce organosulfur products including dimethyl sulfoxide (DMSO), methanesulfonic acid (MSA), SO_2 and ultimately sulfate (SO_4^{2-}) ions. Due to the fast reaction and source strength in open marine and coastal environments DMS has been shown consistently to be an important sink for NO_3 in such regions (Vrekoussis et al. 2007, 2006; Aldener et al. 2006; Matsumoto et al. 2006; Allan et al. 1999; S. S. Brown et al. 2004).

During the AQABA campaign, DMS mixing ratios varied slightly by region, with the lowest observed levels in the south Red Sea of 140 ± 30 ppt, and the highest in the Indian Ocean with an average $\approx 310 \pm 85$ ppt. The mean mixing ratio of DMS was 163 ± 99 ppt throughout the entire campaign. While measurements of atmospheric DMS concentrations in most of the studied regions are limited, the concentrations of DMS in the Indian Ocean during AQABA are similar to the results of another study of organosulfur compounds, including DMS, in the Indian Ocean by (Sciare, Baboukas, and Mihalopoulos 2001) which reported a mean DMS of 395 ± 285 ppt. These were however, recorded at a significantly different longitude, centered around Amsterdam Island ($37^\circ 48' \text{ S}$, $77^\circ 34' \text{ E}$) rather than the in the Arabian Sea. As previously discussed in (Edtbauer et al. 2020) the relatively high DMS concentrations observed in the Indian Ocean region could be accounted for by the upwelling effect, described by (Kämpf and Chapman 2016) where winds from the land (particularly off of the coast of Somalia) displace surface level ocean waters allowing for nutrient rich waters in the oceans to rise from a depth of 100 – 300 m. These nutrient rich waters can then stimulate the proliferation of DMS producing marine organisms, in turn leading to high atmospheric mixing ratios. Predictions of the natural sulfur (DMS) flux into the atmosphere can be predicted if surface level concentrations are known, and these have been reported for the Indian Ocean before (M. Zhang et al. 2017). (Lana et al. 2011) used these measurements to predict that particularly strong sulfur fluxes (30

$\mu\text{mol S m}^{-2} \text{ d}$) in the Gulf of Aden and Indian Ocean during the months of June and August, coincident with the timing of the AQABA campaign and consistent with elevated DMS mixing ratios reported by Edtbauer *et al.*

On the night 22 – 23rd August specifically, DMS mixing ratios were steady more-or-less all night beginning around 200 ppt and slowly declining down to around 100 ppt by the end, representing a large contribution of NO_3 reactivity. Noteworthy on this night, and several others, is the apparent increase of DMS during the large NO and SO_2 features seen in Figure 19 at approximately 20:00 UTC. This suggests a source of DMS which is combustive in origin, as these features are associated with ship emissions. While combustive sources of DMS have been reported before (Meinardi *et al.* 2003) in the form of biomass burning, to the best of the author's knowledge, DMS emissions from internal combustion engines are not known in the literature. Depending on the (bio)fuel, the emission factor (g DMS / kg fuel) can vary significantly (Andreae 2019), which may explain the observation that DMS was not observed during similar ship emission plumes throughout all of AQABA as different ships will contain different fuel and engine types. Other possibilities include a possible inlet transmission issue for the PTR-ToF-MS instrument measuring the DMS or a chemical interference on the DMS mass (mass 62). A chemical interference is unlikely due to the high mass sensitivity of the PTR-ToF-MS (up to $6000 \text{ m} / \Delta\text{m}$) (Jordan, *et al.* 2009) and would require a organosulfur trace gas which fragments on exactly the same mass as DMS. SO_2 , while not typically measured by the PTR-ToF-MS, could represent a pathway to DMS. Although this is unlikely, the covariance seen in Figure 19 when fitted in a linear regression during these events suggests that between 0.1 – 0.7 % of SO_2 would be detected as DMS. If true, then applied to the entire dataset this would only result data correction of 4.7 ± 22 ppt to the DMS signal, only making up a significant contribution to the total signal at low DMS mixing ratios or inside of shipping plumes, where SO_2 is high. As the cause of the DMS signal during the ship emission events cannot be determined, the DMS contribution to $k(\text{NO}_3)$ during these events is not further considered.

The median contribution of DMS to steady-state $k(\text{NO}_3)$ during the night 22 – 23 August was $\approx 14\%$, which is slightly lower than the average for the north Red Sea region ($\approx 20\%$) or the average of other regions (20 – 25%). These contributions to total $k(\text{NO}_3)$ are in agreement with previous evaluations of similar areas such as (Aldener *et al.* 2006) who reported an average but variable contribution of DMS to $k(\text{NO}_3)$ of 25% during the NEAQS campaign off the eastern coast of the United States and similar to (Matsumoto *et al.* 2006) who reported a contribution between 30 – 40%, dependent on the air mass, on an island close to a densely populated megacity in Japan. DMS contributions to $k(\text{NO}_3)$ are known to be seasonal and enhanced during the summer months (Vrekoussis *et al.* 2006; Steven S. Brown and Stutz 2012), over which the AQABA measurements were taken, which may reflect higher temperatures (in the northern hemisphere) favoring the partition towards NO_3 in the $\text{NO}_3\text{-N}_2\text{O}_5$ equilibrium, as well as enhanced DMS fluxes in many regions, including the Mediterranean, the seas around the Arabian Peninsula and the north Atlantic (Lana *et al.* 2011). Larger contributions of DMS to $k(\text{NO}_3)$ are known (80 – 90%) (Allan, *et al.* 2000) and these are comparable to the contribution to the lower limit of $k(\text{NO}_3)$ (calculated from the N_2O_5 limit of detection and scaled according to K_{eq}) observed in the Indian Ocean, where DMS contributed an average of 89% to this limit. Clearly, these results demonstrate DMS is an important sink for NO_3 in maritime environments.

5.2.2.3 Reaction with other VOCs

Gas phase reactions with other measured VOCs (i.e. excluding DMS) did not represent an important sink for NO_3 during the night 22 – 23 August, and this was the case for much of the campaign outside the

Persian Gulf region. NO_3 has relatively large rate coefficients with a number of VOCs, particularly biogenic VOCs such as isoprene, monoterpenes and sesquiterpenes, which are characteristic emissions from foliage. As the AQABA campaign was conducted around the seas of the Arabian Peninsula biogenic emissions of this kind were not expected to strongly influence NO_3 lifetimes due to the lack of source strength in either the seas nor the landmasses close to the seas which are mostly arid desert regions. Desert regions (southwestern United States) as a source of isoprene and monoterpenes have been examined before (Geron et al. 2006) and are not considered a strong source of isoprene, and generally not a strong source of monoterpenes compared with forested environments. These observations are supported by the measurements of isoprene and monoterpenes which were at the limits of detection throughout the majority of campaign and display no covariance with $k(\text{NO}_3)$ ($R^2 < 0.08$), suggesting neither was an important sink during AQABA.

VOC which are anthropogenic in origin, by contrast, were a regionally significant sink for NO_3 , particularly in the Persian Gulf where the sum of the loss rates of all VOCs measured during AQABA, shown in Table 5, contributed to $\approx 25\%$ of $k(\text{NO}_3)$. This figure should be taken as a strict lower limit as this likely presents only a fraction of the total VOCs in the atmosphere (Goldstein and Galbally 2007). This increased role of VOCs towards $k(\text{NO}_3)$ in the Persian Gulf is driven by relative increases, compared to other regions, in the concentrations of many of the VOC species measured during AQABA (Bourtsoukidis et al. 2019), including several molecules which have relatively large rate coefficients with NO_3 (e.g. butenes). While a relative increase in the sum of all VOCs is also seen across the Suez Canal, the contribution to total $k(\text{NO}_3)$ remains low ($< 2\%$), reflecting the relatively large concentrations of longer carbon-chain ($> \text{C}_4$) VOCs observed in the Persian Gulf, which are likely to be related to the petrochemical industries that are prominent in the region. A large contribution of anthropogenic VOC to $k(\text{NO}_3)$ is relatively uncommon in the literature as studies typically, but not always, focus on remote regions away major industrial emission sources. Aircraft studies (Steven S. Brown et al. 2009) passing over Houston, Texas found a that 46% of NO_3 reactivity could be assigned to anthropogenic VOCs, dominated by reactions with alkenes (87%) such as isobutene, 1,3-butadiene (neither of which was measured during the AQABA campaign) and isoprene, typically thought of as a natural product but also associated with the oil and gas industries (Steven S. Brown and Stutz 2012). Smaller contributions were given by alkanes (2%) and aromatic compounds (11%).

In the other studied regions during AQABA the contribution to $k(\text{NO}_3)$ from other (mostly anthropogenic) VOCs was largely determined to be insignificant, contributing $< 1\%$. VOC concentrations outside the Persian Gulf were considerably lower and were dominated by ethane and propane, both of which have small rate coefficients with NO_3 . These may represent products from combustion (e.g. from ships' engines) or long range transport, as both ethane and propane have lifetimes with the OH radical on the order of several days in addition to slow reactions with NO_3 . Overall, these results show that VOC reactivity as a sink for NO_3 was important in particular regions during the AQABA campaign but not in others, suggesting that different anthropogenic sources will produce different VOC molecules with structures which will contribute differently to $k(\text{NO}_3)$, thereby highlighting the selectivity of NO_3 .

5.2.2.4 Heterogeneous reactions of NO_3 and N_2O_5

N_2O_5 undergoes hydrolysis on the surface of particles, resulting in a heterogeneous, indirect loss process of NO_3 . As N_2O_5 is a product of the reaction of NO_3 with NO_2 , two equivalents of NO_x are lost from the gas-phase for every heterogeneous reaction which removes N_2O_5 . As discussed above, heterogeneous reactions are controlled by the concentrations of NO_2 , the temperature (via K_{eq}), the total surface area of the particles, and the value of the uptake coefficient, which varies with particle composition. For this

analysis, a $\gamma(\text{N}_2\text{O}_5) \approx 0.03$ was calculated. The large values of $\gamma(\text{N}_2\text{O}_5)$ reflect the low nitrate content in aerosol measurements which are controlled by the high temperatures during AQABA favoring partition towards gas phase HNO_3 . Suppression of γ in the presence of organics has been reported (Timothy H. Bertram et al. 2009) but the organic to sulfate ratio seen in particles during AQABA were low (generally < 2). Thus, a value of $\gamma(\text{N}_2\text{O}_5) \approx 0.03$ is consistent with both laboratory observations of N_2O_5 uptake and field determinations of γ such as the 0.03 ± 0.02 reported by (Aldener et al. 2006) for a polluted marine environment.

Heterogeneous reactions of N_2O_5 were only a minor sink on the 22 – 23 August, contributing 3.42% to $k(\text{NO}_3)$. This night is largely consistent with contributions on a regional scale, which varied from $\sim 2\%$ (in the south Red Sea) to $\sim 10\%$ in the Persian Gulf, with the variability driven by differences in aerosol surface area. These results suggest a much lesser role for N_2O_5 hydrolysis as a contributor to $k(\text{NO}_3)$ than previous field studies in marine environments have reported. While inefficient losses of N_2O_5 have been reported in air masses originating from such environments (Crowley, Thieser, Tang, Schuster, Bozem, Beygi, et al. 2011) (Heintz, et al. 1996), these are the results of low NO_x , low aerosol surface area conditions and typically coincide with long chemical lifetimes of NO_3 and N_2O_5 and a lack of permanent nocturnal sinks for NO_x in general. In more polluted environments, N_2O_5 hydrolysis is generally more significant due to high $\gamma(\text{N}_2\text{O}_5)$ and higher average NO_x concentrations. (Vrekoussis et al. 2006) reported that an average between 40 – 57% (depending on the season) of all NO_3 and N_2O_5 losses occurred due to heterogeneous losses of N_2O_5 at a coastal site in Greece. While this study, and several others from the time period (Allan et al. 1999; Monica Martinez et al. 2000), predict a $\gamma(\text{N}_2\text{O}_5) = 0.1$ as an upper limit, for the purposes of comparison, raising the $\gamma(\text{N}_2\text{O}_5)$ for AQABA to this value is not enough to close the discrepancy. A $\gamma(\text{N}_2\text{O}_5) = 0.1$ during AQABA would cause N_2O_5 hydrolysis to be the single largest contributor to $k(\text{NO}_3)$ in the Persian Gulf, raising from $\sim 10\%$ to $\sim 22\%$, while other regions would see an increase from $\sim 5\%$ to $\sim 15\%$. While these increased numbers are significant, they represent less than half of the contributions to $k(\text{NO}_3)$ reported in the literature for similar polluted marine environments. Moreover, more recent studies have shown that N_2O_5 hydrolysis is normally an important loss mechanism in such environments even when $\gamma(\text{N}_2\text{O}_5)$ can be determined directly from measurements (although this implies relatively stable loss processes of NO_3) or calculated from aerosol measurements, as is the case in this work. For example, (Aldener et al. 2006) show that N_2O_5 hydrolysis made up 47% of $k(\text{NO}_3)$ on average across the entire NEAQS campaign and as high as 80% for individual nights on the campaign.

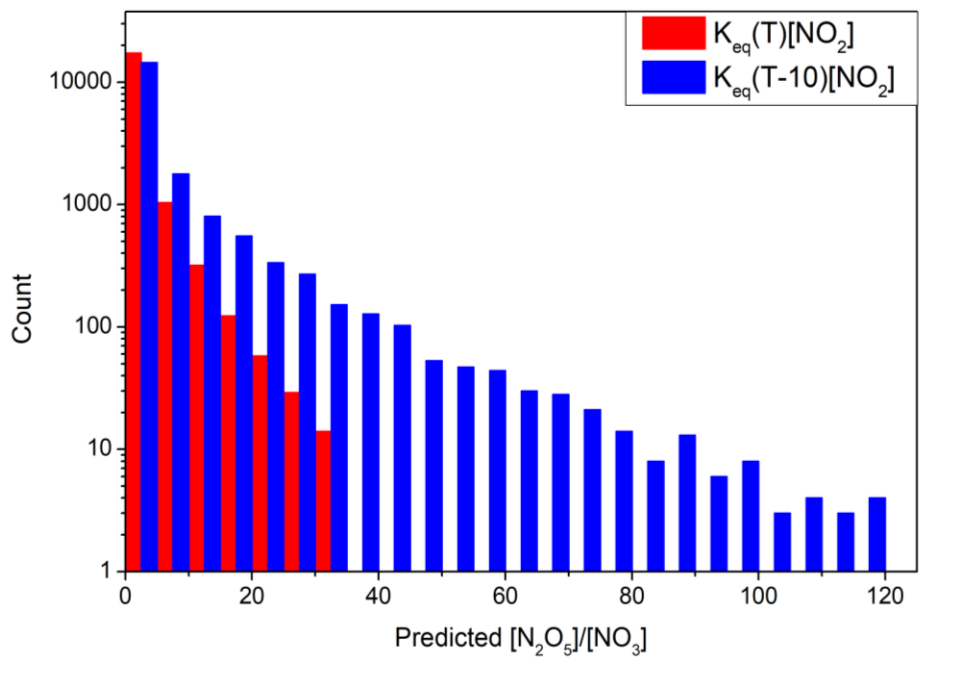


Figure 22. Histogram of predicted $N_2O_5/NO_3 (= K_{eq}[NO_2])$ ratios during AQABA. The red data are calculated from the observed temperatures and the blue data are the calculated with Temperature -10K.

The relatively small contribution of N_2O_5 to $k(NO_3)$ may be a result of the higher temperatures observed during AQABA which typically favor the partition towards NO_3 in the NO_3 - N_2O_5 equilibrium. As discussed in (Eger et al. 2019) in the context of halogen activation, the high temperatures result in a low thermal lifetime of N_2O_5 , inhibiting availability to react onto the surface of particles, despite otherwise favorable conditions, therefore making N_2O_5 hydrolysis less competitive with gas phase NO_3 reactivity. In terms of (Equation 12), this results in small N_2O_5/NO_3 ratios generally close to 1. Figure 22 compares $K_{eq}(T)[NO_2]$ at the temperatures observed during AQABA (red), compared with the same calculation while setting the temperature to 10 K lower (blue). In the red AQABA data ~90% of the (nighttime) data points predict a N_2O_5/NO_3 ratio between 1 – 3, while this reduces in the blue, temperature-reduced data to ~66% of data points in the same range.

The effect of direct heterogeneous NO_3 uptake onto the surface of aerosols were also calculated. NO_3 uptake coefficients are not well understood, with wide ranges reported in various laboratory studies for differing chemical compositions of particles (see section 2). They are also difficult to derive from field measurements due to the difficulty separating heterogeneous chemistry from other gas-phase NO_3 losses. Large values of γ have however been observed for unsaturated, organic particles, and soot ($\gamma \approx 0.33$) however these organics quickly react with oxidizing trace gases during the day (OH) and during the night (O_3) suppressing the uptake of NO_3 . For this evaluation, a value of $\gamma(NO_3) = 0.01$ has been used. This is a conservative, lower limit estimate of $\gamma(NO_3)$ based on the large fraction of sulfate observed in the composition of the fine particulate matter which dominates the contribution to the aerosol surface area during AQABA in most regions. Note that During a 3 – 5 period in the Indian Ocean / Gulf of Aden region the contribution of fine particulates to aerosol surface area (typically > 90%) decreased to ~50% due to the sampling of air masses from Ethiopia where the contribution of coarse dust particles to surface area increased. Taking this assumption of $\gamma(NO_3)$, $k_{Het}(NO_3)$ is occasionally competitive with, but usually lower

than, the contribution of $k_{\text{het}}(\text{N}_2\text{O}_5)$, depending on ambient NO_2 levels. On the 22-23rd specifically, the high NO_2 concentrations made the heterogeneous loss via N_2O_5 , the more important loss pathway of the two. Overall the NO_3 heterogeneous losses contributed $\approx 0.4\%$ to median $k(\text{NO}_3)$. Campaign wide, the contribution of direct NO_3 uptake to $k(\text{NO}_3)$ varied between $< 1\%$ in the Red Sea and Mediterranean regions and up to $\sim 4\%$ in the Persian Gulf. This is generally in agreement with other reports in the literature, e.g. (Aldener et al. 2006) who reports a campaign-wide average contribution 2% in the polluted marine boundary layer off the eastern coast of the United States.

5.2.3 Unknown loss processes

Heterogeneous loss processes and reactions with other trace gases which were measured during the AQABA campaign could only explain a fraction of the steady state $k(\text{NO}_3)$ observed. While short periods of time of several could be completely explained through the combined loss processes which were accounted for (e.g. at around 18:00 on 22 – 23 August in Figure 20), the majority of the reactivity remains unassigned ($> 72\%$). This reflects the broader observations across the AQABA campaign where in each region, the largest contributor to $k(\text{NO}_3)$ was some unknown loss process. While this can be a result of direct (gas phase reaction with NO_3) or indirect (via N_2O_5) loss processes, as discussed above, the high temperatures on AQABA favors the loss of NO_3 in the gas phase compared with N_2O_5 losses, where heterogeneous loss processes have been quantified and gas phase reactions are unknown.

5.2.3.1 – Reactions with NO

Some possibilities of reaction partners for NO_3 include NO, which was often above the limit of detection at night time. As discussed in 5.2.2.1, the NO signal during the night was likely a result of an interference in the CLD measurement system and shows no correlation with NO_2 outside of plumes. During the night 22 – 23 August, taking the assumption that the instrument's reported limit of detection represents the upper limit of NO's contribution to $k(\text{NO}_3)$, this results in 9% contribution. Applied to the entire campaign, this reduces the unassigned reactivity to $\sim 35\%$ in the Persian Gulf and approximately 65% in the other 3 regions and thus is not enough to close the discrepancy. Inside of the (fresh) plumes, where large mixing ratios of NO were often observed, NO would likely be the most important loss process of NO_3 , due to the large rate coefficient, but these conditions rapidly remove NO_3 and disrupt the equilibrium and therefore the validity of the steady state assumption and thus are not considered in the analysis.

5.2.3.2 – Reactions with RO_2 radicals

Another potential sink for NO_3 is reaction with various peroxy radicals (RO_2), which react with NO_3 in the gas phase to produce NO_2 , RO and O_2 . While the literature is limited to only a few R groups, the studies which do exist generally point to uncertain but significant rate coefficients with NO_3 , on the order of $10^{-12} \text{ cm}^3 \text{ molecule}^{-1} \text{ s}^{-1}$, such as the reaction with the methyl peroxy radical (CH_3O_2 , $1.2 - 2.3 \times 10^{-12} \text{ cm}^3 \text{ molecule}^{-1} \text{ s}^{-1}$ (IUPAC, 2020)). In the mechanisms discussed in section 2, sources of RO_2 most relevant to the AQABA NO_3 dataset are the reactions with VOCs with all major atmospheric oxidants, including OH, O_3 and NO_3 and thus sources of RO_2 exist throughout the day. OH initiated reactions and to a lesser extent, reactions with free halogens (e.g. Cl), are important at dawn and dusk as these radicals react in H-abstractions or additions to double bonds leaving unpaired electrons which react quickly with abundant molecular oxygen in the atmosphere to give RO_2 . Similar reactions occur with NO_3 . Reaction with O_3 proceeds via a 1,3 addition across VOCs containing a double bond forming a Criegee intermediate, also known as a primary ozonide, followed by a decomposition in the carbon chain (ozonolysis) yielding an alkyl radical which reacts with O_2 to give RO_2 . While reaction with DMS leads to generation of significant

concentration of $\text{CH}_3\text{SCH}_2\text{O}_2$ radicals which can compete with other sources (Carslaw et al. 1997), most notably O_3 -initiated VOC sources, the resulting RO_2 must compete with NO_3 in HO_2 , NO and RO_2 -self reactions. Nighttime $\text{HO}_2 + \text{RO}_2$ reactions are generally considered to be important within the context of isoprene and terpene chemistry (Schwantes et al. 2015; Beaver et al. 2012) as NO_3 reactions with large organics release HO_2 , though this would not be the case on AQABA due to a lack of significant emissions of the relevant precursors around the Arabian Peninsula, while reaction with NO is generally limited due to a lack of photolysis at night (though it is still present from combustive sources due to the polluted nature of the region). Additionally, modelling studies have come to opposing conclusions of whether $\text{NO}_3 + \text{RO}_2$ (Kirchner and Stockwell 1996) or $\text{RO}_2 + \text{RO}_2$ (Bey, Aumont, and Toupance 2001) reactions are more important in the nighttime boundary layer and in particular, the self-reaction of the $\text{CH}_3\text{SCH}_2\text{O}_2$ radical has not yet been assessed in the literature.

Unfortunately, RO_2 was not measured during the AQABA campaign. Due to the large uncertainties which still remain in the sources of RO_2 at night, and the rate coefficients of oxidant reactions ($\text{RO}_2 + \text{RO}_2$ or $\text{RO}_2 + \text{NO}_3$, etc.) it is difficult to predict how significant a sink RO_2 may be in the context of AQABA. For instance, (Steven S. Brown et al. 2011) determined that $\text{RO}_2 + \text{NO}_3$ reactions made up a lower limit of $\sim 3\%$ of the NO_3 reactivity budget in flights over polluted coastal region over Houston, Texas in conditions which were broadly similar to those within AQABA regions such as the Persian Gulf (high temperature, oil and gas industry emissions, large urban environments). The authors specifically note however, that DMS was not an important loss process for NO_3 during the flights, in contrast to what has been observed during AQABA, and note the uncertainty of the RO_2 measurements at night which were calculated from peroxyacetyl radicals known to be in equilibrium with PAN, which was measured. A stratified altitude profile in DMS is generally expected in aircraft measurements is generally expected as DMS emissions are released into the atmosphere from the surface of the oceans. This leads to higher concentrations closer to the surface which decline at higher altitudes as DMS reacts with NO_3 , formed from more varied elevation NO_x sources. In contrast, (Sommariva et al. 2009) made a modelling study using an adjusted Master Chemical Mechanism (MCM) of RO_2 , HO_2 and $\text{NO}_3 / \text{N}_2\text{O}_5$ concentrations, constrained by measurements made in the 2004 NEAQS campaign. This approach highlighted the potentially important role of $\text{NO}_3 + \text{RO}_2$ interactions in a polluted marine boundary layer, showing a median of 15% contribution to $k(\text{NO}_3)$ throughout the entire NEAQS campaign, with large contributions of the $\text{CH}_3\text{SCH}_2\text{O}_2$ radical under conditions where NO_3 mixing ratios were primarily controlled by DMS, and up to $\sim 22\%$ contribution of RO_2 from anthropogenic sources (i.e. non DMS, non-isoprene) when sampling off the coast of Massachusetts, near the large urban center of Boston. As has been shown above, the reactions with DMS and anthropogenic VOCs were important to losses of NO_3 during AQABA, perhaps more so than during NEAQS, as there were more potential sources of VOC emissions besides urban emissions, such as ships or industrial sources.

High O_3 levels, particularly in hotspots like the Persian Gulf or Suez Canal, presumably also contribute to an increase in nighttime RO_2 via the Criegee ozonolysis mechanism. These observations suggest that a box model study with MCM or similar may give some insight into the importance of $\text{RO}_2 + \text{NO}_3$ interactions in these regions and the other regions studied in AQABA, and this may help close some of the $k(\text{NO}_3)$ budget presented above.

5.2.3.3 – Reactivity from ship-based emissions

Some clues to the source of the unattributed reactivity may come from the observation that the unassigned contribution ($k_{ss}(\text{NO}_3) - k[\text{NO}] + k[\text{VOC}] \dots$) to the total NO_3 steady state loss rate ($k(\text{NO}_3)$) appears to correlate with both NO_2 and SO_2 .

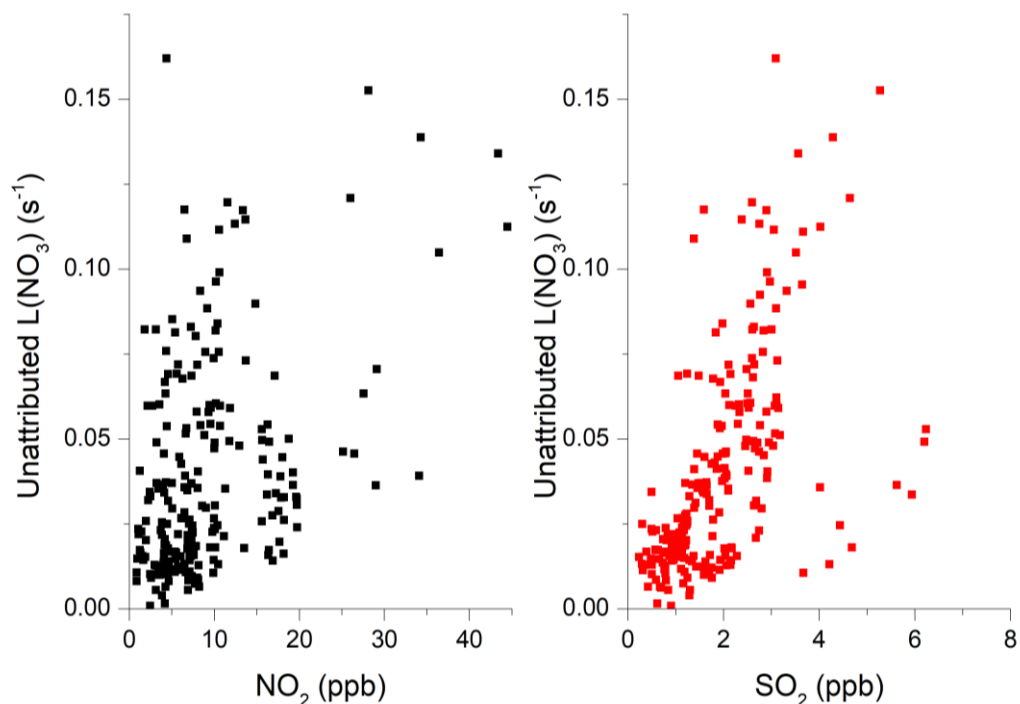


Figure 23. Unassigned contribution to the first order loss rate of NO_3 ($L(\text{NO}_3)$) vs. NO_2 / SO_2 for the night 22-23 August (North Red Sea)

NO_3 does not react directly with SO_2 , and reacts with NO_2 resulting in N_2O_5 , which is equilibrium. While one might expect a dependence of $k(\text{NO}_3)$ on NO_2 in circumstances where NO_3 losses proceeded primarily through the heterogeneous uptake of N_2O_5 , as high nighttime NO_2 concentrations normally favor partition towards N_2O_5 which increases the competitiveness of the heterogeneous reaction compared with gas phase losses of NO_3 . However, as presented above, these losses compared to the gas phase were relatively small during AQABA and therefore an alternative explanation is required for this dependence on the NO_2 (and SO_2) mixing ratios. One such explanation for this correlation could be that NO_2 and SO_2 likely share a common origin, which most likely is related to combustion. While many combustion processes release NO_x and SO_2 , the location of the measurements, taken in the Gulf of Suez close to the Suez Canal, and the repeated presence of large plumes of NO , implying proximity to the *Kommandor Iona*, suggest that the source of the reactivity may be the ships themselves. (Bourtsoukidis et al. 2019) shows that in the periods of measurements of contaminated by the exhaust gas of the *Kommandor Iona* the slope of the linear regression of the i-pentane to n-pentane mixing ratios during the AQABA campaign, which can be used as an indicator of sources of hydrocarbon emissions, was $1.59 \text{ ppb ppb}^{-1}$, which is similar to the $1.71 \text{ ppb ppb}^{-1}$ identified in the Suez Canal zone and consistent with the 1.7 ppb ppb^{-1} identified by (Blake et al. 2014) in a Texas shipping channel, suggesting the hydrocarbon mix in the Suez Canal was strongly influenced by ship exhausts.

Ship emissions are a major source of pollutants including NO_x , particulate matter, SO_2 and VOCs (Corbett, Fischbeck, and Pandis 1999; Eyring et al. 2005). To date, very few detailed studies exist on the speciation of VOCs emitted from ship's fuel combustion. From one of the only studies related to the topic, (Cooper, Peterson, and Simpson 1996) compared passenger ferries with difficult fuel types, gas oil and fuel oil, in the North Sea reporting that composition of the exhaust gas contained high levels of, among other species: ethane, propene, isobutene, polycyclic aromatic hydrocarbons (PAHs), and organic molecules containing chlorine. At least one of these molecules, isobutene, is known to have a large rate coefficient with NO_3 ($k_{\text{isobutene}} = 3.4 \times 10^{-13} \text{ cm}^3 \text{ molecule}^{-1} \text{ s}^{-1}$ (Atkinson, Plum, et al. 1984)), which is comparable to isoprene. As the origin of the high levels of reactivity are suspected to be tied to shipping emissions, below an analysis to describe the reactivity we observed in terms of the correlated NO_2 and SO_2 signals is attempted.

5.2.4 Reactivity from Ship Emissions.

Emissions from ships, or any other source, are subject to (photo)chemical aging within the troposphere, due to reactions with atmospheric oxidants O_3 , OH, and NO_3 . As a result, from the point of emission the NO_2 , SO_2 and other trace gases will age at differing rates according to the sum of their individual loss processes. The ratio of VOC emissions, which are likely to contribute to $k(\text{NO}_3)$, to NO_2 or SO_2 will change based on the age of the air mass.

The NO_x/NO_y ratio is a useful indicator of the age of an air mass as it gives the proportion of reactive nitrogen sequestered between gas-phase NO and NO_2 , which are direct emission products, and all other reactive nitrogen tied up in NO_y (organic nitrates, particles, HNO_3 and others). As NO_x is directly emitted and has a relatively short chemical lifetime (~ 1 day), high NO_x/NO_y ratios are typically associated with more recent emissions. Conversely, a low NO_x/NO_y ratio usually contains very little NO_x with most nitrogen oxidized and stored in other forms. If the NO_x/NO_y ratio is used to give an indication of the age of the air masses that were sampled during the AQABA campaign, the evolution of the NO_3 reactivity of a ship's plume may be explained.

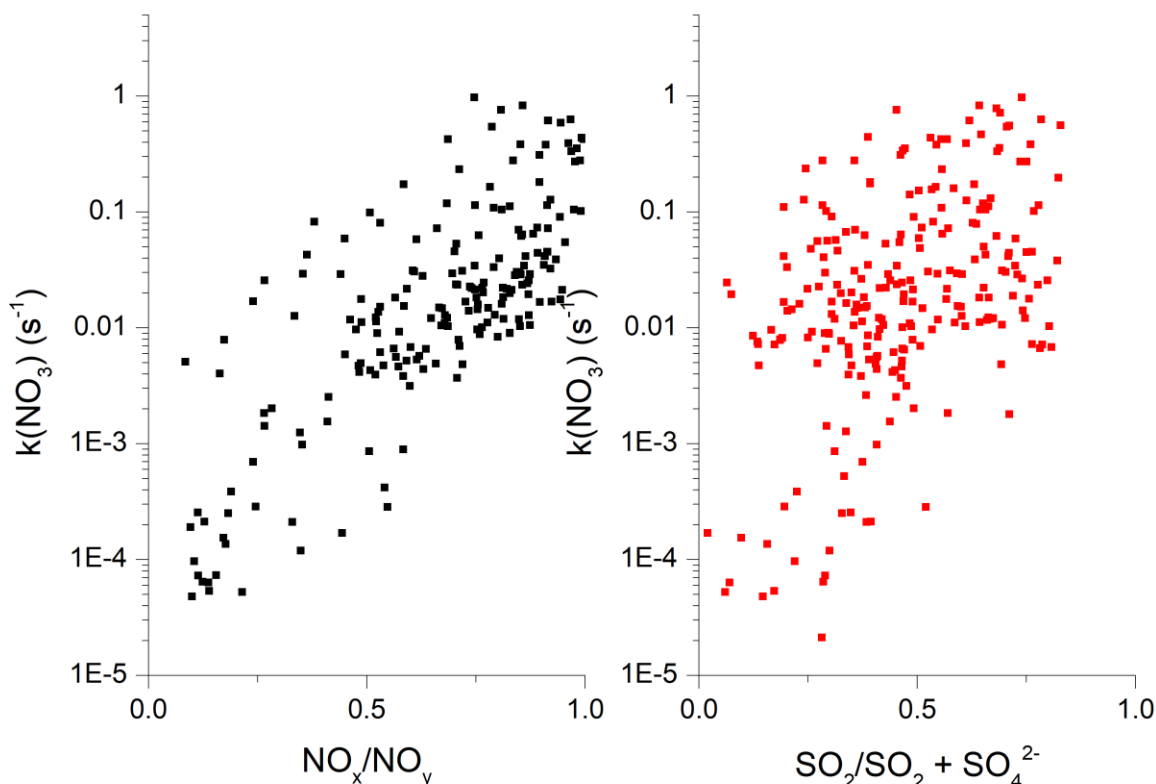


Figure 24. $k(\text{NO}_3)$ vs NO_x/NO_y , and $\text{SO}_2/\text{SO}_2+\text{SO}_4^{2-}$ ratio for the entire AQABA campaign

Figure 24 shows the steady-state derived, unattributed contribution to $k(\text{NO}_3)$ plotted against two indicators of chemically aged air masses, the NO_x/NO_y ratio and the ratio of SO_2 to $\text{SO}_2 + \text{SO}_4^{2-}$. As with NO_x , SO_2 is directly released into the atmosphere by ship emissions, and reacts with atmospheric oxidants (OH) to give sulfate ions. SO_2 has a longer chemical lifetime ($\sim 3 - 5$ days) compared to NO_x (~ 1 day) when considering the reaction with OH and zero reactivity towards NO_3 . SO_4^{2-} lifetimes (dry deposition rates) over the ocean have been characterized with an deposition rates parameterized between $0.1 - 1.0 \text{ cm s}^{-1}$ (Ganzeveld, Lelieveld, and Roelofs 1998), largely dependent on wind speed which drives surface roughness. Taking an average wind speed value for the AQABA campaign of 0.4 cm s^{-1} , this results in lifetime of SO_4^{2-} of ~ 2 days at 298 K and atmospheric pressure. This is longer than the lifetime of HNO_3 over the oceans (~ 1 day), and therefore suggests that the SO_2 to $\text{SO}_2 + \text{SO}_4^{2-}$ ratio indicates a much longer timescale relative to the NO_x/NO_y ratio. Assuming that the source of reactivity comes from VOCs from a ship emission, if the VOCs have lifetimes shorter than that of NO_x , then it would be expected that $k(\text{NO}_3)$ would decline more rapidly compared with NO_x when these are plotted against the NO_x/NO_y ratio. If the lifetimes are longer than NO_x , the opposite is true and significant $k(\text{NO}_3)$ will remain as the NO_x/NO_y ratio approaches zero.

For the analysis of ships plumes directly, it is necessary to normalize the signal of $k(\text{NO}_3)$, putting reactivity in terms of a concentration of a known ship emission product. This could be normalized in terms of either SO_2 or NO_2 . For this analysis, it was determined that $k(\text{NO}_3)/[\text{SO}_2]$ correlation was a better indicator of shipborne NO_3 reactivity when plotted against the NO_x/NO_y ratio. Unattributed $k(\text{NO}_3)$ had a stronger

correlation with SO_2 than NO_2 ($R^2_{\text{SO}_2} = 0.36$ vs. $R^2_{\text{NO}_2} = 0.19$) which may be a product of SO_2 's lower background mixing ratios compared with NO_2 , or that SO_2 is a better indicator of ship's emissions than NO_2 if NO_2 has more sources in the regions studied. Figure 25 shows the dependence of $k(\text{NO}_3)$, normalized per molecule of SO_2 , on the NO_x/NO_y ratio. The NO_x/NO_y ratio was converted into an approximate time scale taking the assumptions that daytime OH concentrations averaged 1.0×10^6 molecule cm^{-3} and nighttime O_3 , driving the production of NO_3 , concentrations averaged 50 ppb.

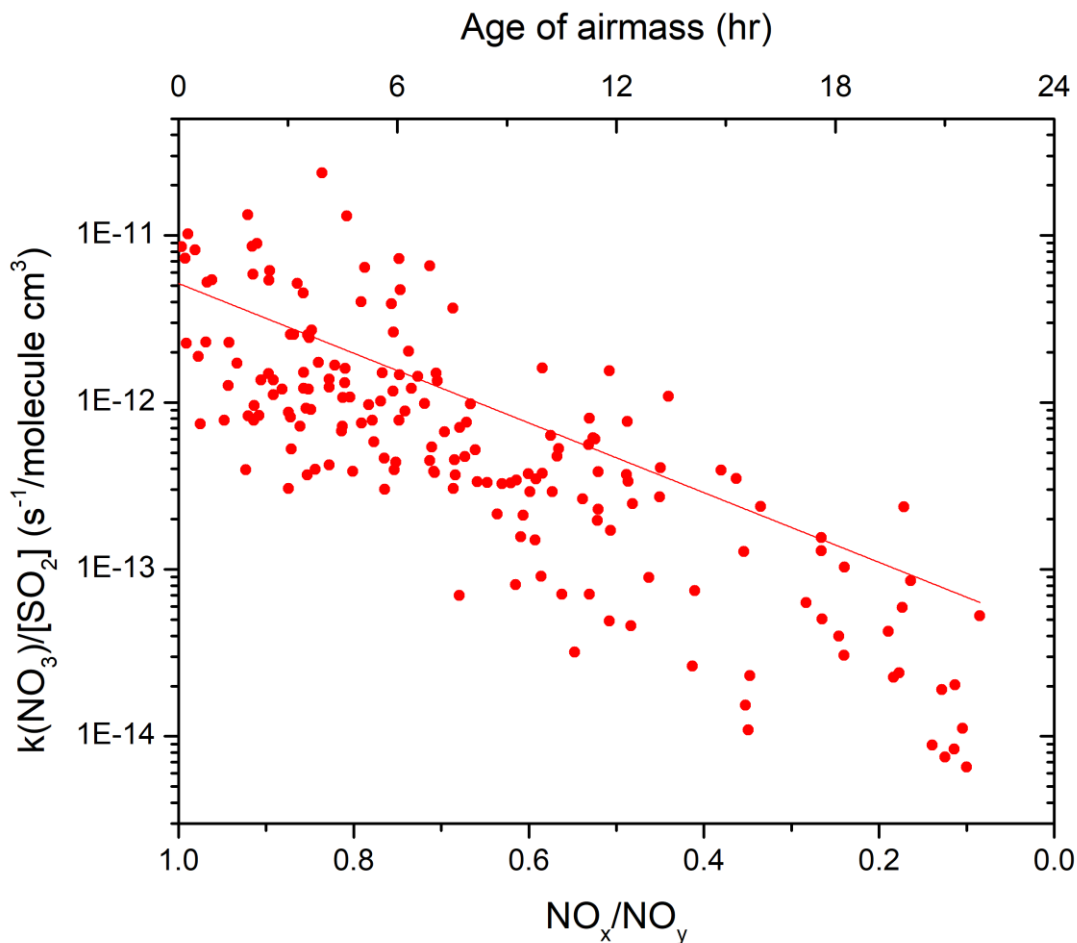


Figure 25. $k(\text{NO}_3)/[\text{SO}_2]$ vs the NO_x/NO_y ratio for the entire AQABA campaign.

A fit of Figure 25 with an exponential function ($y = ab^x$) allows us to relate the reactivity of $k(\text{NO}_3)$ per $[\text{SO}_2]$ from ship emissions to the NO_x/NO_y ratio, where $a = 4.2 \times 10^{-14}$ and $b = 122.45$ with an $R^2 = 0.24$. To put this into context, this implies within a factor of 4, that 1 ppb of freshly emitted SO_2 would be equivalent to 0.08 s^{-1} of NO_3 reactivity caused by a co-emitted VOC. The fitted approximate timescale indicates that the VOC emission(s) from a ship plume has a lifetime on the order ~ 1 day with combined OH and NO_3 processing. The significant scatter about the fit may be caused by a number of factors including:

- The ship size, engine design, and fuel type. These factors will determine the chemical composition of the ship emission; as different fuel or engine types may lead to different VOC mixtures, or ratios of those mixtures, which will result in different reactivity towards NO_3
- The timing of the emission. VOC emissions at day time will undergo photochemical processing with OH, which are likely to have different rate coefficients with OH than with NO_3 . If a ship emission is processed by OH before night time, the correlation with SO_2 or NO_2 is likely to be different than an emission that only sees night time processing, and vice-versa.
- Background $\text{NO}_2 / \text{SO}_2$. The NO_x/NO_y ratio was not observed to approach zero (min ≈ 0.1) as a constant background of NO_2 was seen in most of the polluted regions. Similarly, a background of unassigned $k(\text{NO}_3)$ unrelated to ship emissions would increase the rate at which the reactivity approaches the x-axis on NO_x/NO_y scale, biasing the results.
- Presence of other oxidizing species. Removal of VOCs (but not NO_x or SO_2) by non- NO_3 oxidation mechanisms during the night will cause a reduction in $k(\text{NO}_3)$ as this reduces the available VOC to react with NO_3 . As discussed in (Eger et al. 2019), the rates of oxidation of VOCs can be enhanced during the dawn, where NO_3 may still be present in small concentrations, as a result of release of free halogen atoms from the photodissociation of ClNO_2 and this is competitive with VOC oxidation by OH during the same period. Reactions with O_3 will also remove some VOC via the Criegee ozonolysis mechanism.
- Reaction with RO_2 . To the extent to which RO_2 radicals may act as a sink for NO_3 on the AQABA campaign (see above), RO_2 will contribute to $k(\text{NO}_3)$ but will reproduce NO_2 , impacting the rate at which the NO_x/NO_y ratio will approach zero.
- The uncertainty in the measurements of $[\text{N}_2\text{O}_5]$, $K_{\text{eq}}(\text{T})$, $[\text{SO}_2]$, $[\text{NO}_x]$, and $[\text{NO}_y]$. Which contribute to a considerable propagated uncertainty in both the x and y axis.

A similar plot of $k(\text{NO}_3)/[\text{NO}_2]$ is included in appendix A. The R^2 value = 0.11 was determined for the same fit as Figure 25.

5.2.5 comparison with OH reactivity

Reactivity of the OH radical was directly measured during the AQABA campaign with the results reported in (Pfannerstill et al. 2019). The analysis determined that OH reactivity was elevated in similar regions as the NO_3 reactivity reported here, i.e. with higher per-second loss rates in the more polluted regions of the north Red Sea and Persian Gulf and lower values in the open Indian Ocean. Large portions of the OH reactivity could similarly not be assigned, with speculation that this could be results of non-measured VOC species, such as branched alkanes and alkenes. A strong covariance between $k(\text{OH})$ and $k(\text{NO}_3)$ was not generally observed during AQABA ($R^2 \approx 0.05$ for the entire campaign). This is expected as NO_3 is far more selective than OH, which reacts quickly (relative to NO_3) with short and long-chain carbon molecules, such as alkanes, leading to significant $k(\text{OH})$ where $k(\text{NO}_3)$ is much lower while NO_3 reactivity can also be significant while OH reactivity is relatively low due to NO_3 and N_2O_5 's interactions with the aerosol phase. The presence of signals of both $k(\text{NO}_3)$ and $k(\text{OH})$ is therefore a more useful diagnostic for OH rather than NO_3 , as this implies the presence of a molecule which reacts quickly with both radicals, which may imply longer chained alkene species (or DMS), reducing the possibilities of possible reactivity sources.

Covariance was observed between the two inside ship plumes, which may bolster the arguments put forward above that the unattributed proportion of $k(\text{NO}_3)$ is caused by unsaturated VOC species co-emitted with NO_2 and SO_2 . However, elevated $k(\text{OH})$ during plumes would be expected regardless due to the reactions of OH with both NO_2 and SO_2 , as well as the short-chain alkanes (ethane, propane) which are known to be emitted with ships, all of which either do not (or only very slowly) react with NO_3 .

A relative plot of $k(\text{NO}_3)$ vs $k(\text{OH})$ can be a useful diagnostic tool in environments which are dominated by the reactivity of a certain trace gas for identifying particular molecules, particularly under low- NO_x and SO_2 conditions. Under these conditions one would expect a linear function, scaling with the concentration of trace gas [X] with a slope in a linear regression analysis of the ratio of the rate coefficients, as was shown for isoprene and some terpenes on a rural mountain top location in southern Germany by (J. M. Liebmann et al. 2018). During AQABA in general and particularly in ships plumes, where the strongest covariance was observed, plots of this kind did not produce any obvious linear functions, suggesting that several different types of molecules were responsible for both $k(\text{OH})$ and $k(\text{NO}_3)$ which would be consistent with the ship-plume theory as discussed above, where the exhaust fumes likely contain a range of different VOCs and other trace gases, including beyond what was measured during AQABA, which would be seen by OH and NO_3 differently.

5.2.6 Simulations

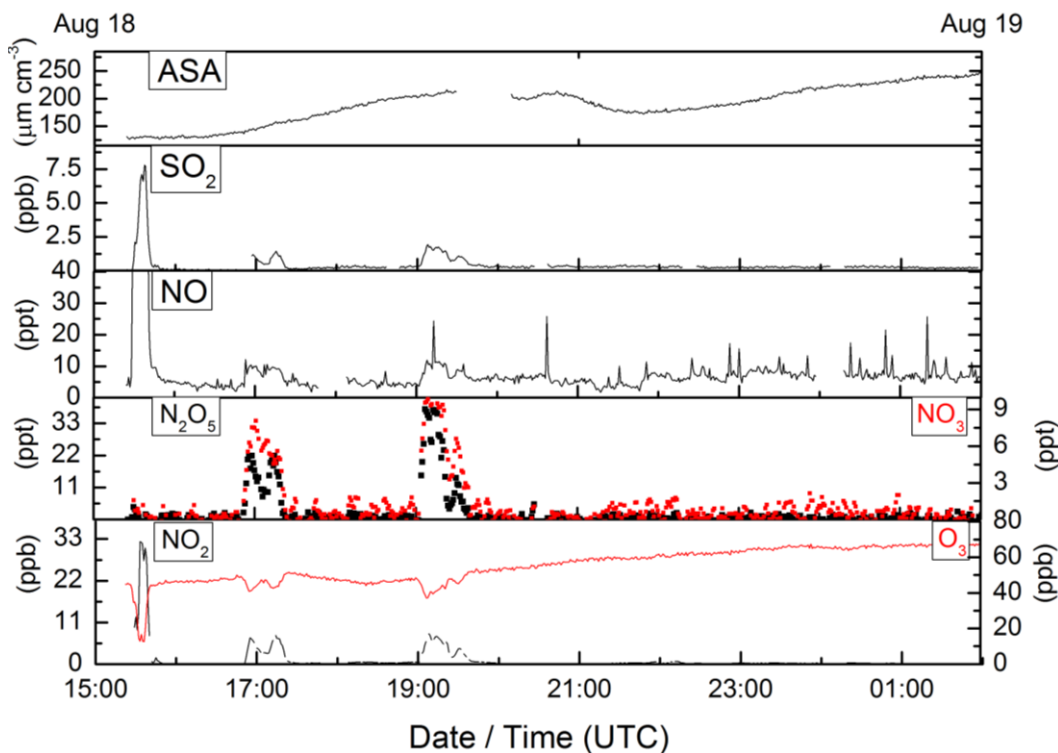


Figure 26. Overview of selected parameters from the night 18 - 19 August. ASA = Aerosol Surface Area

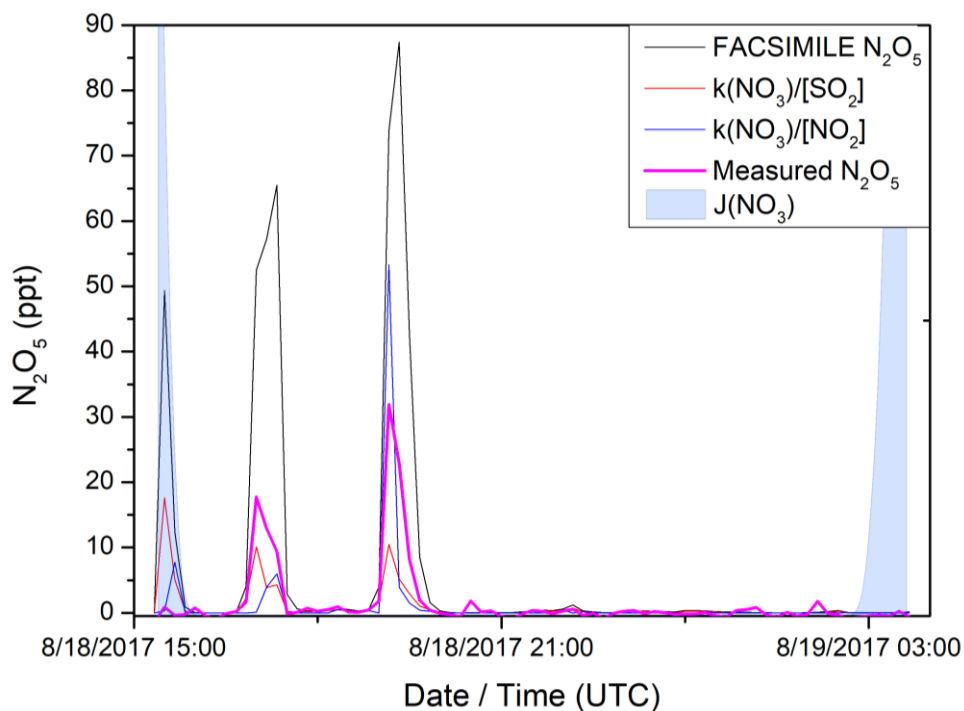


Figure 27. FACSIMILE simulated N_2O_5 mixing ratios compared with measured values (pink). The black, red and blue lines make different assumptions of the loss terms of NO_3 ($k(NO_3)$) where black includes the sum of all attributed loss processes (VOC, Heterogeneous, etc) and red and blue include the sum of all loss process plus an additional loss term derived from the relationships discussed in 5.3.4. Blue shaded area shows $J(NO_3)$, indicating dusk and dawn.

Figure 26 presents an overview of selected data from the night 18 – 19 August in the south Red Sea. Unlike the data from 22 – 23 August, on this night NO_3 and N_2O_5 were not observed above the limits of detection all throughout the night but rather appeared in two plumes at $\sim 17:00$ (4 ppt and 20 ppt, respectively) and $\sim 19:00$ UTC (9 ppt and 30 ppt, respectively). During the same periods of time, plumes of NO_2 and SO_2 increased to several ppb from a baseline of close to the respective detection limits while O_3 mixing ratios decreased from ~ 50 ppb to ~ 40 ppb concurrently. These observations suggest that the source of NO_2 (and thereby NO_3 and N_2O_5) and SO_2 were combustive in origin. As was case for the 22 – 23 August, the most likely source of these emissions was other ships in the region, as the (photo)chemical lifetime of NO_2 in this region (~ 1 day) requires the emissions to be in close proximity to the *Kommandor Iona*. Calculations of $P(NO_3)$ and $k(NO_3)$ were completed as before, yielding similar observations, that the sum of all loss processes (Reaction with DMS, other VOCs, and heterogeneous processes) was not in agreement with the calculated steady-state loss rates of NO_3 , implying the presence of unknown loss processes.

Figure 27 shows the results of numerical simulations, constrained by measurements of NO , NO_2 , O_3 , SO_2 and the sum of all known loss rates to reconstruct the N_2O_5 mixing ratios, compared against the measured mixing ratios in pink. The black data is a reconstruction using the sum of all the known loss processes previously discussed while the red and blue data show the result of all these processes plus the additional loss terms linked to the mixing ratios of NO_2 (blue) and SO_2 (red) and the age of the air mass (NO_x/NO_y ratio) in the relationships discussed in 5.2.3. Each of the simulations are able to regenerate the periods between the three observed plumes of NO_2 on this night, leading to the conclusion that, outside of the plumes, the combination of the known loss rates is enough to reduce NO_3 and N_2O_5 to below the instrument limits of detection. Inside of the plumes, each of the three simulations predict an N_2O_5 signal

which was not observed in the data in the first NO₂ plume. The numerical simulations did not contain the spectral radiometer data, thus the discrepancy can be entirely attributed to J(NO₃), which is highlighted in the shaded blue regions of Figure 27.

In the second plume, where N₂O₅ and NO₃ were measured, the SO₂ method performs best predicting the mixing ratio of the plume within a factor of < 2 (10 vs. 18 ppt), compared with slightly under a factor of 3 (~6 vs. 18 ppt) for the NO₂ method. The NO₂ method also predicts the maximum of the peak several minutes after the SO₂ method, which generally agrees in shape to the observed N₂O₅ data. In the third plume the NO₂ method overestimates the N₂O₅ mixing ratios (50 vs. 30 ppt), while the SO₂ data underestimates the data (10 vs. 30 ppt).

5.2.7 Summary of losses

Steady state-derived first order lost rates of NO₃ were calculated from observations of NO₃ (via the equilibrium with N₂O₅) in each of the regions studied during the AQABA campaign. While P(NO₃) remained high throughout many nights high due high background NO₂ and O₃, observations of NO₃ and N₂O₅ were rather sporadic with mixing ratios over the detection limit appearing primarily during large plumes of NO₂. Calculated lifetimes of NO₃ in most regions were short, implying that losses of NO₃ were efficient. In general, reaction with DMS was important to each region making up between one fifth to one quarter of median reactivity, affirming previous observations of the importance of DMS to the controlling NO₃ concentrations in coastal and maritime environments. Other VOCs, typically anthropogenic in origin, contributed strongly (approximately one quarter) to NO₃ losses in the Persian Gulf, reflecting the importance of emissions from the oil and gas industries as a sink for NO₃ in this region, but elsewhere were negligible contributing less than < 1% to median k(NO₃). Heterogeneous loss rates of N₂O₅ were limited by high temperatures during AQABA, contributing to short thermal lifetimes despite otherwise generally favorable conditions (high NO_x, high aerosol surface area). The maximum contributions to k(NO₃) from heterogeneous loss processes were approximately 9% for N₂O₅ and 4% for direct uptake of NO₃ in the Persian Gulf and approximately 2 – 4% and < 1% in other regions, respectively with the difference between these regions driven by an increase in aerosol surface area. Unknown loss processes made up the majority contribution to k(NO₃) in the Mediterranean and Red Sea regions (70 – 75%), and a plurality in the Persian Gulf (40%). Some of this unattributed reactivity could be assigned to reaction with NO, but unrealistic nighttime mixing ratios suggest possible chemical interferences which are significant when NO is close to the detection limit. Additionally, the unassigned proportion of k(NO₃) showed covariance with NO₂ and SO₂ plumes, generally thought to be from ship emissions which were the dominant source of hydrocarbons in the Red Sea and Suez canal regions. Comparison of k(NO₃), normalized to the concentration of SO₂, against an indicator of the age of an air mass, the NO_x/NO_y ratio, suggests that, under a reasonable assumption of the concentrations of oxidizing trace gases (OH and O₃) during AQABA, the lifetime of a co-emitted VOC responsible for the unattributed k(NO₃) was approximately one day. This analysis suggests that ship emissions may strongly influence both the production (via emissions of NO_x) and losses (via emissions of reactive VOCs) of NO₃ in polluted marine environment, particularly in warmer climates and in the absence of non-DMS biogenic VOC emissions such as isoprene or terpenes.

5.3.1 Integrated NO_x Loss

The efficiency of nocturnal loss of NO_x to the particle phase or to another long-lived reservoir species such as HNO₃ will depend on both the absolute and relative loss rates of NO₃ and N₂O₅. If NO₃ and N₂O₅ loss rates are both small then NO₃ and N₂O₅ represent a temporary reservoir of NO_x as NO₃ will undergo rapid photolysis beginning at sunrise, which releases NO_x back into the atmosphere. However if the losses of either NO₃ or N₂O₅ are efficient, then the lifetimes of NO₃ will be reduced suggesting that NO_x has undergone a reaction to produce an irreversible loss to the atmosphere. During AQABA the loss rates of NO₃ in the gas-phase were sufficiently high (a lifetime of just a few minutes) that the rate of loss NO_x in the marine boundary layer at night is approximately equal to the rate of NO₃ formation:

$$L(\text{NO}_x)_{\text{Night}} \approx S k_1[\text{NO}_2][\text{O}_3] \quad (\text{Equation 16})$$

Where S is a scaling factor and is equal to 1 if NO_x is lost only through NO₃ reactivity and is equal to 2 if NO_x is lost only indirectly through N₂O₅ uptake, as two molecules of NO₂ are required to form each molecule of N₂O₅. For the AQABA campaign, it has been shown above that during nighttime hours NO_x is predominantly lost via gas phase reactions of NO₃, as N₂O₅ uptake is limited, implying that S is close to 1. Integrating (summing up) over the ppt per-second production rates of NO₃ therefore gives a good approximation of the total loss of NO_x over the course of a night. Some reactions of NO₃ reproduce NO or NO₂ and thus are not an irreversible loss of NO_x to the atmosphere, in particular the reaction of NO₃ with NO. Although production of NO is not expected during the night due to a lack of photochemistry, it is emitted directly into the atmosphere from various anthropogenic activities and therefore periods of elevated NO mixing ratios have omitted from the final integration calculation.

These nighttime losses can be compared to the dominant daytime OH-initiated loss of NO₂ to form HNO₃:



As with NO₃ losses with VOCs, the production of HNO₃ during the day is considered an irreversible loss process of NO_x. HNO₃ is thermally stable up to 700 K and thus does not thermally decompose back to NO₂, while photolysis rates and reactions with other oxidants are slow in the troposphere (Finlayson-Pitts and Pitts Jr. 1999) when compared to deposition rates, which are high due to high deposition velocities (in the range 1 – 5 cm s⁻¹ (Finlayson-Pitts and Pitts Jr. 1999)) of HNO₃ and high solubility in water. This makes HNO₃ readily able to adsorb onto surfaces, particularly wet surfaces such as the ocean surface, removing reactive nitrogen from the atmosphere. As such, the loss of NO_x during the day can be estimated as approximately equal the formation of HNO₃

$$L(\text{NO}_x)_{\text{Day}} \approx k_2[\text{OH}][\text{NO}_2] \quad (\text{Equation 17})$$

As with the formation of NO₃, the formation of HNO₃ can be used to approximate the total NO_x loss during the day when the ppt per-second loss rates are integrated over the course of a day. Below follows a comparison of these two losses processes in each region of the campaign. Comparisons between NO_x losses between the day and night could only be made where a complete day / night cycle was available, as missing data points have been treated as adding nothing to the integration, which negatively biases the losses, and therefore should be considered a lower-limit. A summary of losses is given in Figure 28.

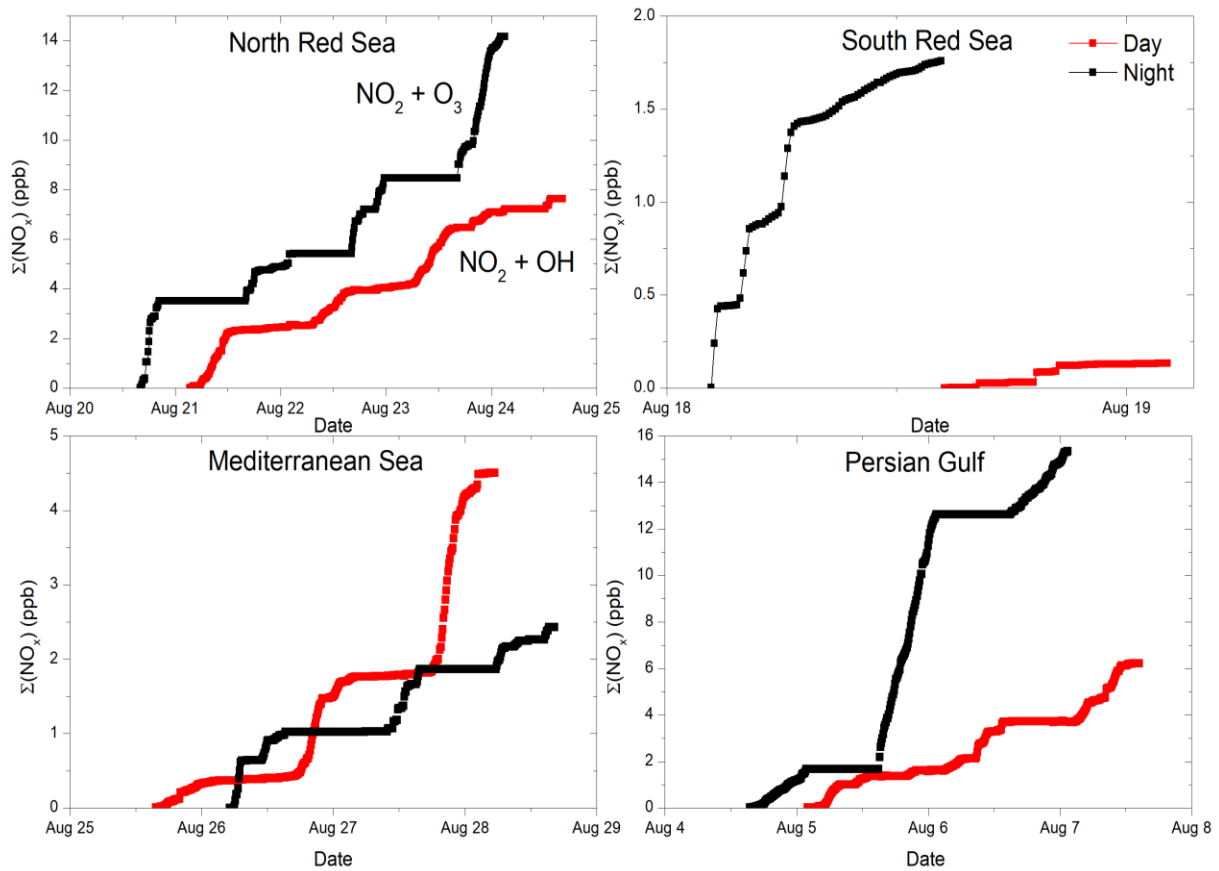


Figure 28. Integrated NO_x loss via day (red) and night (black) mechanisms for the Red Sea, Mediterranean Sea and Persian Gulf regions.

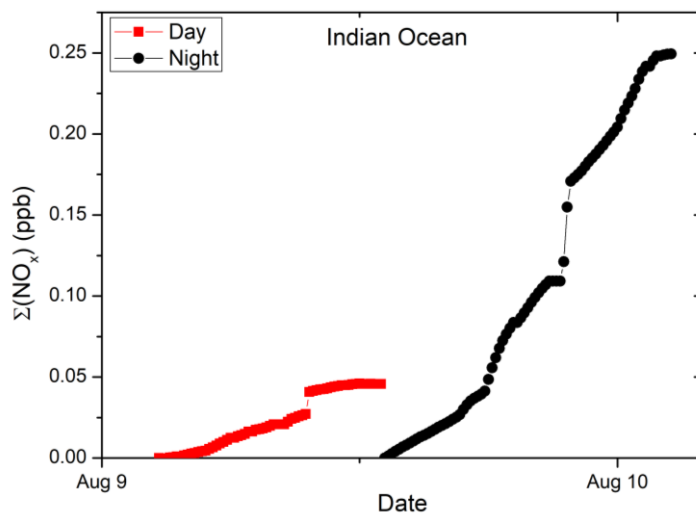


Figure 29. Integrated NO_x loss via day (red) and night (black) mechanisms for the Indian Ocean region

5.3.1.1 NO_x loss in the Persian Gulf

The Persian Gulf region was characterized by highly polluted air and strong solar irradiation. O₃ mixing ratios varied between 50 – 60 ppb in the south to well over 100 ppb in the north, near Kuwait and other large cities. OH concentrations were also high, but less dependent on location within the Gulf, reaching a daily maximum of 5 – 12 × 10⁶ molecule cm⁻³. NO₂ levels were highly variable (mean: 2.16 ± 3.05 ppb, max: 23.6 ppb). The Length of the day in the Persian Gulf averaged 13.5 hours (dateandtime.info 2020), while ERA5 boundary layer data (Copernicus Climate Change Service (C3S) 2017) (see section 4) gives a marine boundary layer of ~500 m with ~200 m variation between the day and night on the 5th and the 6th as the *Kommandor Iona* crossed close to the Straits of Hormuz. Figure 30 details the instantaneous production terms of HNO₃ and NO₃ in the Persian Gulf. Losses by nighttime NO₃-initiated oxidation outpace losses by daytime OH-initiated oxidation, reflecting the high mixing ratios of O₃ and high mixing ratios of NO₂ at night. This is particularly evident on the night 5 – 6th of August where NO₃ production averaged 10⁷ molecule cm⁻³ s⁻¹ for most of the night and resulted in nearly 10 ppb NO_x loss (Figure 28). For comparison, the loss of NO_x via the daytime mechanism during the day after (or before) averaged 2 ppb of loss of NO_x.

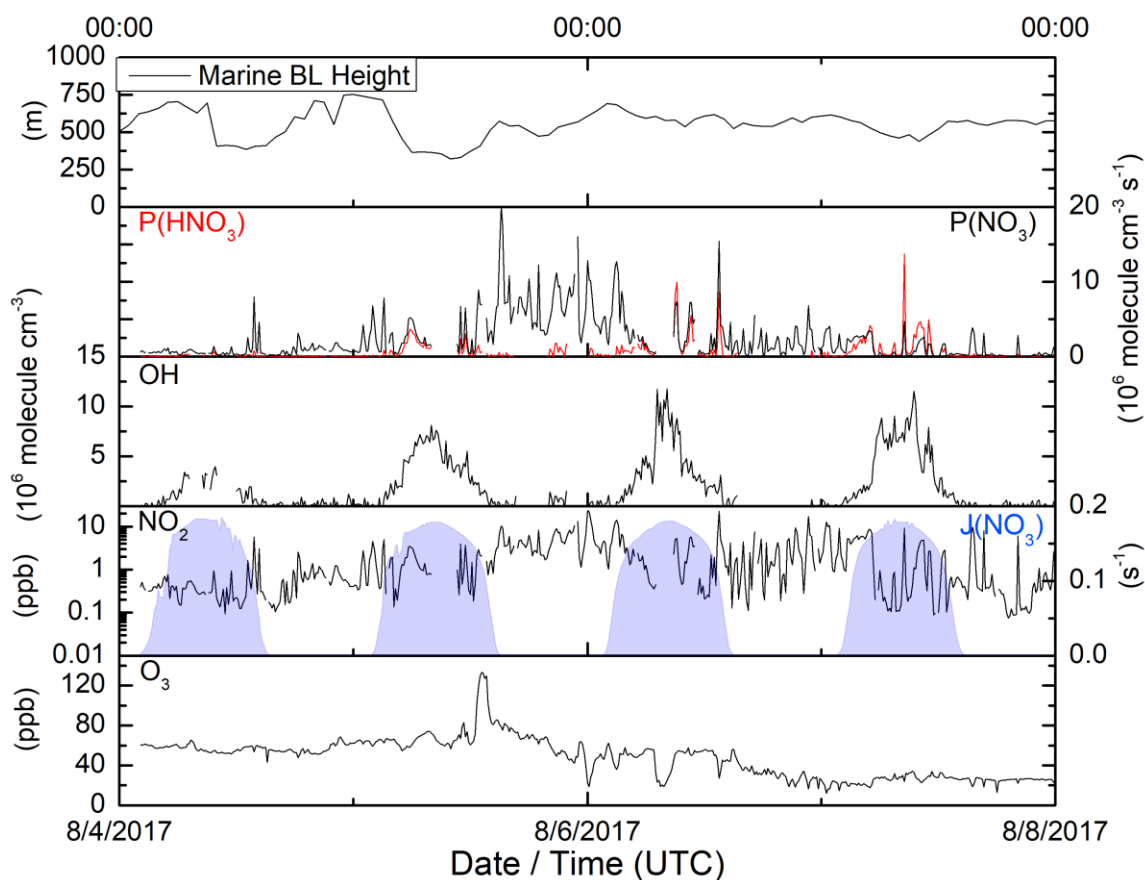


Figure 30. Selected parameters from 4-8th August in the Persian Gulf. $P(\text{HNO}_3)$ and $P(\text{NO}_3)$ refer to the gas-phase production of HNO₃ by OH oxidation of NO_x and the production of radical NO₃ from O₃ oxidation of NO_x, respectively.

5.3.1.2 NO_x Loss in the Indian Ocean

Compared with the Persian Gulf or Red Sea, conditions in the open Indian Ocean were starkly different with lower averages of nearly all trace gases and a lower average temperature. O₃ mixing ratios were among the lowest observed in the entire campaign at 15 – 20 ppb. Peak OH concentrations were 2 – 6 x 10⁶ molecule cm⁻³ while background NO_x levels ranged typically from near the detection limit up to ~1 ppb. However, short-term (of a few minutes) plumes of NO_x of a few ppb (up to 10 ppb) were also observed. The marine boundary layer ERA5 data gives a height of 500-600 m with essentially no diurnal variation. An integration over an entire day / night cycle was only possible on between the 8-9th of August, where NO_x loss during the night came to 250 ppt, and 60 ppt during the day (Figure 29), the lowest losses seen during the entire campaign.

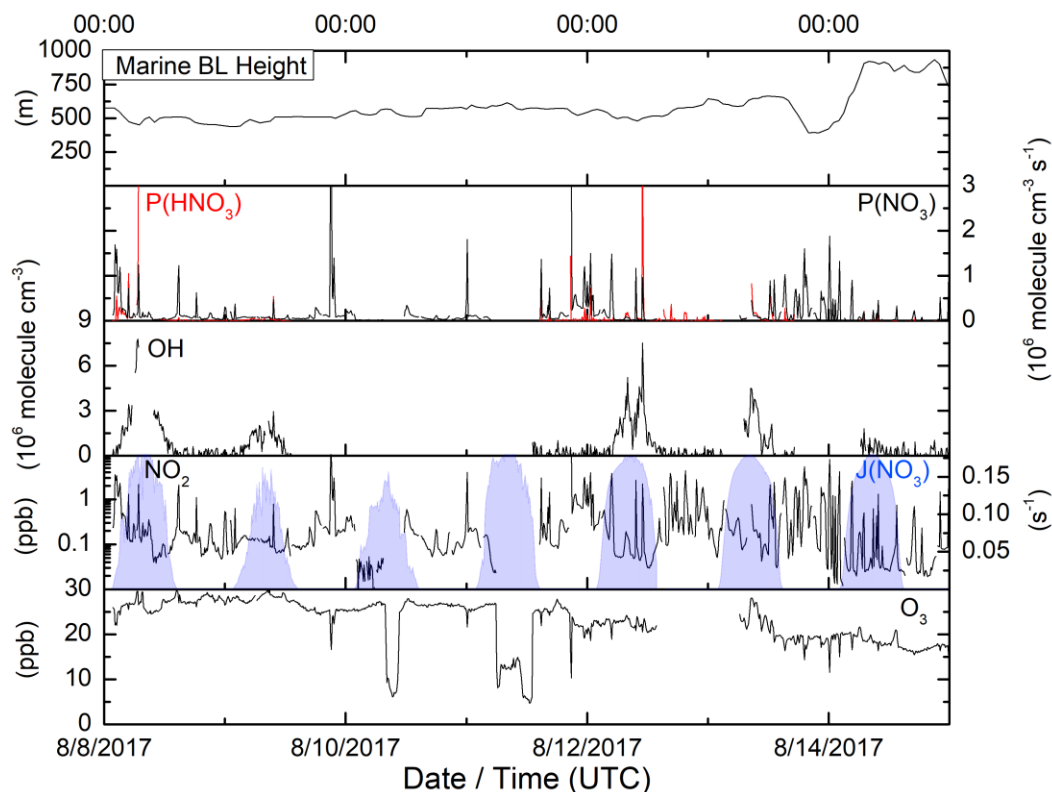


Figure 31. Selected parameters from 8-12th August in the Indian Ocean. $P(\text{HNO}_3)$ and $P(\text{NO}_3)$ refer to the gas-phase production of HNO_3 by OH oxidation of NO_x and the production of radical NO_3 from O_3 oxidation of NO_x , respectively.

5.3.1.3 NO_x Loss in the Red Sea

From the southern part (15 – 20 August) of the Red Sea heading northern part (20 – 25 August), background O₃ mixing ratios steadily increased from the ‘clean’ marine environment observed at the end of the open Indian Ocean (20 ppb) to the polluted regions of the Gulf of Suez and the Suez Canal zone (60 ppb). Strong diurnal cycles in O₃ were observed as the *Kommandor Iona* moved closer to Suez (Figure 33). OH concentrations were an average of 5 x 10⁶ molecule cm⁻³ with a maximum of 15 x 10⁶ molecule cm⁻³ seen on the 16th August. As ship traffic increased with the proximity to the Suez Canal, NO_x levels increased from a mean of 1.4 ± 2.68 ppb (max: 24.49 ppb) in the south Red Sea to a mean of 4.79 ± 6.72 ppb (max 54.18 ppb) in the North. ERA5 data gives a marine boundary layer height of ~750 m in the south of the

Red Sea, increasing to over 1000 m after the 20th August. A high boundary layer of ~1400 m, the highest in the campaign, was seen on the 22nd of August which was significantly higher than < 1000 m seen the night before and the night after indicating the proximity to land in the Gulf of Suez (The Gulf is 32 km wide on average). In total, integrations in the south Red Sea were completed over two full day / night cycles (16 – 17th and 18-19th) and over four full day / night cycles in the north Red Sea (20 – 24th). In both regions, the length of a day was approximately 13 hours. Loss of NO_x increased as the *Kommandor Iona* traveled north, particularly at night time. Between 16 – 17th August ~1.5 ppb NO_x was lost due to formation of NO₃, increasing to ~2.0 by 18 – 19th and > 3 ppb after the 19th (Figure 28). Loss due to OH also increased northwards, with < 1 ppb lost on 16 – 17th and 18 – 19th, and ~3 ppb lost after the 19th.

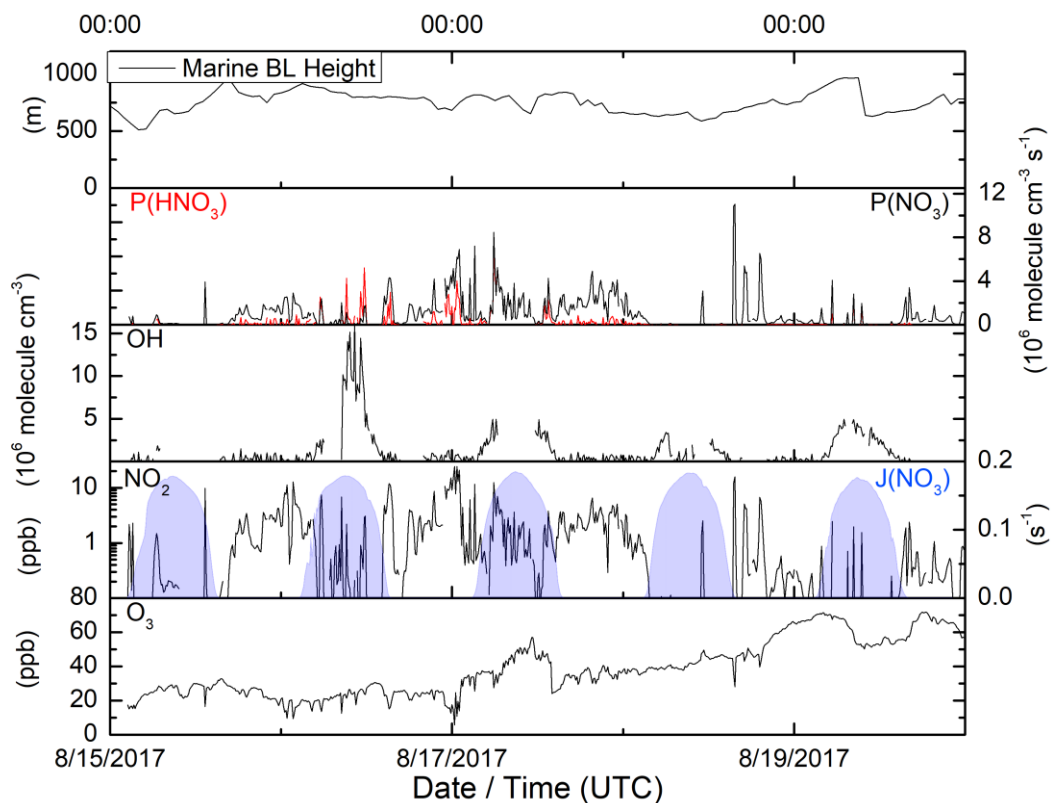


Figure 32. Selected parameters from 15-20th August in the Red Sea. $P(\text{HNO}_3)$ and $P(\text{NO}_3)$ refer to the gas-phase production of HNO_3 by OH oxidation of NO_x and the production of radical NO_3 from O_3 oxidation of NO_x , respectively.

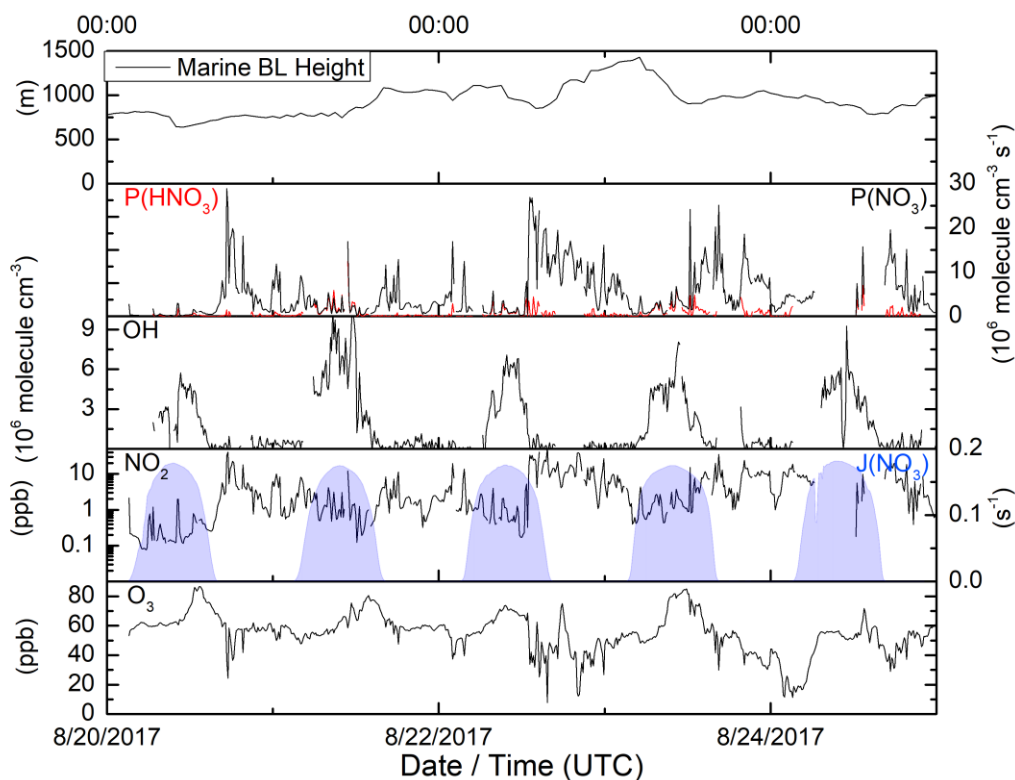


Figure 33. Selected parameters from 20-25th August in the North Red Sea. $P(\text{HNO}_3)$ and $P(\text{NO}_3)$ refer to the gas-phase production of HNO_3 by OH oxidation of NO_x and the production of radical NO_3 from O_3 oxidation of NO_x , respectively.

5.3.1.4 NO_x loss in the Mediterranean Sea

Conditions in the Mediterranean Sea changed as the *Kommandor Iona* sailed from the eastern Mediterranean (25 – 27th) to the west and past the Straits of Messina between Sicily and the Italian mainland (27 – 31st). O_3 mixing ratios decreased from $\sim 70 - 80$ ppb to ~ 60 ppb on the 25 – 27th before rising again to ~ 70 ppb 27 – 29th (Figure 34) and once again decreasing to 60 ppb from 29 – 31st. The periods of lower O_3 were over the open Mediterranean while higher periods were closer to landmasses. OH concentrations from $7 - 12 \times 10^6$ molecule cm^{-3} . NO_x levels ranged from the detection limit, over the open sea, to 3 – 6 ppb near the Straits of Messina (mean = 0.95 ± 1.94 ppb; max = 20.95 ppb). ERA5 data shows the marine boundary layer of 600 – 800 m with no diurnal variation. Losses of NO_x were integrated over three days (26 – 29th). A day was approximately 13 hours long with little variation between the east and west Mediterranean, despite travelling north. Approximately 1 ppb was lost each night due to formation of NO_3 while approximately 2 ppb was lost each day due to formation of HNO_3 .

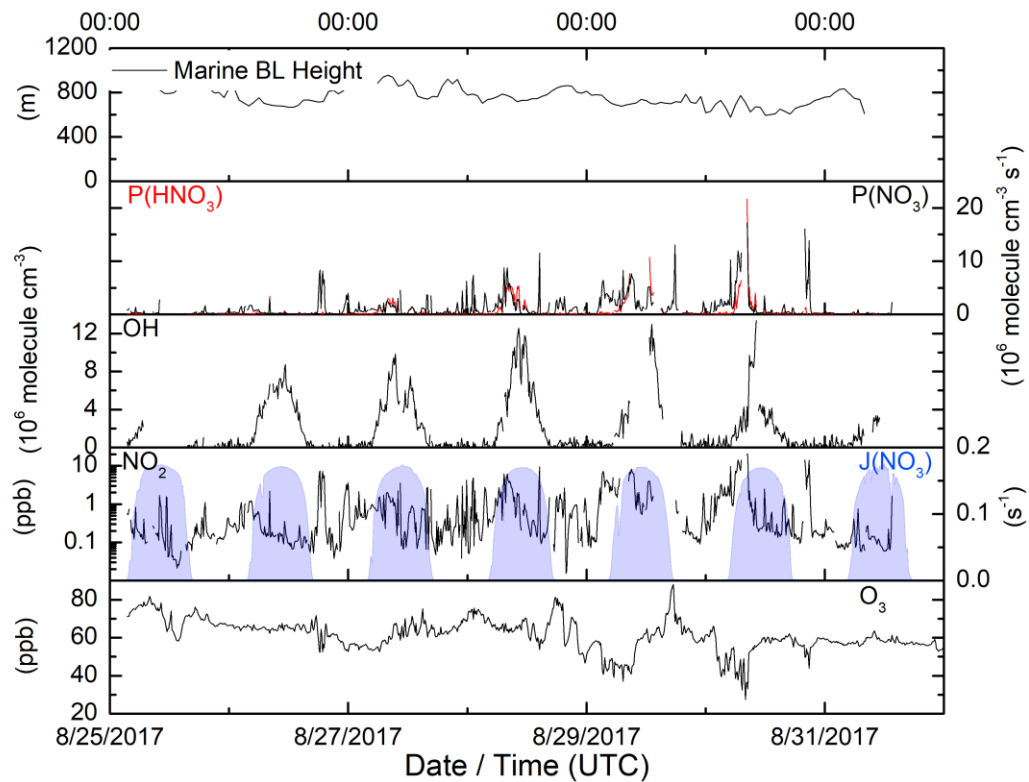


Figure 34. Selected parameters from 25-31st August in the Mediterranean Sea. $P(\text{HNO}_3)$ and $P(\text{NO}_3)$ refer to the gas-phase production of HNO_3 by OH oxidation of NO_x and the production of radical NO_3 from O_3 oxidation of NO_x , respectively.

5.3.1.5 Summary of NO_x Losses

Table 6. Summary of NO_x losses per region during the AQABA campaign. Mean L(NO_x) per hour is given for both day time and night time loss mechanisms. k(NO₂) is the average (mean) loss rate of NO₂ in s⁻¹

Region	Total L(NO _x) – Day (ppb)	Total L(NO _x) – Night (ppb)	Length of Day (hour)	Number of Day / Night cycles	L(NO _x) (ppb hour ⁻¹) Day	L(NO _x) (ppb hour ⁻¹) Night	k(NO ₂) day (x10 ⁻⁵ s ⁻¹)	k(NO ₂) night (x10 ⁻⁵ s ⁻¹)
Persian Gulf	6.20	15.07	13.5	3	0.15	0.48	2.73 ± 2.53	4.82 ± 2.82
Indian Ocean	0.06	0.25	12.75	1	0.005	0.02	1.02 ± 1.23	1.92 ± 3.44
South Red Sea	0.95	3.32	13	1	0.04	0.15	2.31 ± 2.60	4.37 ± 1.79
North Red Sea	7.63	13.88	13	4	0.15	0.32	2.93 ± 2.40	4.89 ± 1.26
Mediterranean Sea	4.77	2.43	13	3	0.12	0.07	2.99 ± 0.16	5.5 ± 0.77

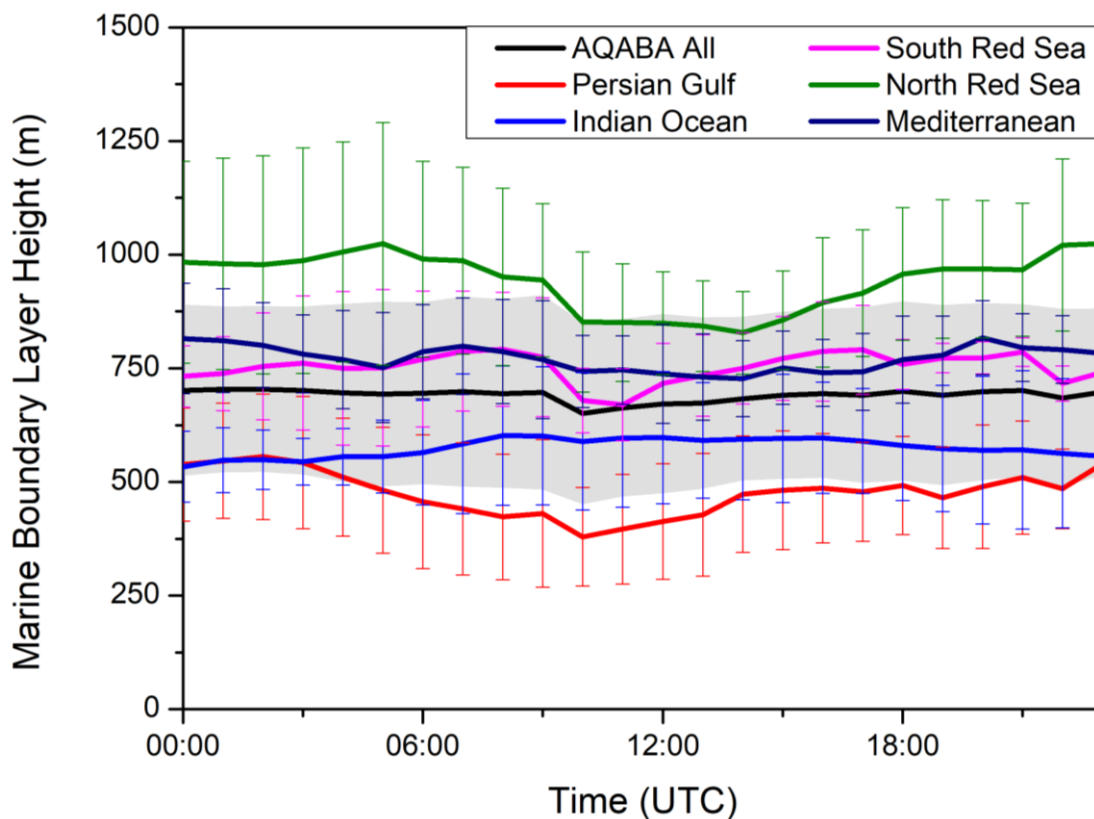


Figure 35. Averaged diurnal cycles of the marine Boundary Layer (BL) height. The shaded area represents the (1 σ) standard deviation of the BL throughout the entire AQABA campaign.

Table 6 summarizes the total losses of NO_x in each region of AQABA, as well as the losses normalized per hour for both day and night. In the Persian Gulf, Red Sea and Indian Ocean regions the rate of NO_x lost by reaction with O₃ outpaces the rates of loss with OH, with two times (Red Sea), three times (Persian Gulf) or four times (Indian Ocean) more NO_x lost per hour via the nighttime mechanism. In the Mediterranean Sea, the opposite is true and the OH mechanism is two times more efficient compared to the O₃ initiated losses. (Crowley, Thieser, Tang, Schuster, Bozem, Hosaynali Beygi, et al. 2011) report a total loss rate for NO₂ + O₃ between 1.9 – 4.2 x 10⁻⁵ s⁻¹ for differing air masses over a coastal site in rural Spain during the 2008 DOMINO campaign, which is comparable to the 5.5 ± 0.77 x 10⁻⁵ s⁻¹ in the Mediterranean on AQABA, the somewhat higher loss rates likely due to the difference in season, and therefore average temperature, between the AQABA (June – September) and DOMINO (November – December) campaigns. Crowley *et al.* posit that the OH mechanism is likely to dominate NO_x loss due to the differences in the boundary layer height, which was greater during the day, despite relatively short lengths of the day (10 hours) in the winter season in Southern Spain (dateandtime.com 2020). These conclusions are supported by summer time observations in the eastern Mediterranean by (Vrekoussis et al. 2003) where 83.82% of local HNO₃ was produced via the OH + NO₂ reaction, compared with 16.18% of all nighttime loss processes of NO₂ + O₃ via NO₃ and N₂O₅ during the MINOs campaign. Although this compares production of HNO₃ and not all NO_x losses the authors note that other VOC reactivity was only of minor importance for controlling the NO₃ budget, implying that formation of RONO₂ did not contribute significantly to NO_x loss. Similar results were reported for another region of the eastern Mediterranean over a year of measurements by (Vrekoussis et al. 2006) where ~75% of all local HNO₃ (and ~50% of all particle nitrate) production was a result of NO₂ oxidation by OH, although these measurements note that up to 10% of NO₃ losses were the result of reaction with isoprene, and therefore a loss pathway of NO_x which does not immediately result in formation of nitrate ions. For the AQABA campaign, comparisons to the eastern Mediterranean formation of nitrate ions are difficult to make as a large proportion of k(NO₃) remains unassigned; thus it is not possible to determine quantitatively whether loss processes of NO₃ in this unassigned contribution result in the formation of HNO₃ (via H-abstraction), NO₂ formation (via reaction with NO or RO₂), or RONO₂ formation (via addition to an unsaturated hydrocarbon). However, due to the selectivity of NO₃ reactions which generally have faster rate coefficients with unsaturated organics, and the previous analysis that a large proportion of the unassigned reactivity is caused by co-emitted VOCs it is reasonable to assume that much of the loss proceeds via the addition mechanism. Regardless, the data presented here show that the loss of all NO_x is favored by the daytime mechanism, which is described only by the NO₂ + OH reaction, meaning that a majority of NO_x is lost via daytime formation of nitrates. This implies that even if all unattributed NO₃ reactivity were to describe a reaction which directly formed nitrate, which is unlikely, this would necessarily have to describe a smaller fraction of the NO₃⁻ formation than the daytime mechanism and therefore the AQABA data are qualitatively consistent with the studies above.

Figure 35 shows the average (mean) marine boundary layer heights over a 24 hour period, broken down by region. The large error bars relative to the variation in the mean suggest that there was no significant diurnal variation in the Marine Boundary Layer between night and day and therefore it is possible to compare directly all NO_x losses between the day and night, as concentrations of NO_x and oxidants are not dependent on large differences in the relative volume of an air mass; nor the well-known sea breeze effect, which occurs at coastal regions where temperature and pressure differences between the air over the land and over the sea driven by the sun in a convection current which brings air masses (and therefore

pollutants) from the sea to the land during the day, as the land is warmed more rapidly by the Sun, and the reverse during the nights, as the land cools more rapidly than the sea. Sea breezes may extend several kilometers out to sea, driven by a number of meteorological factors such as the temperature gradient and wind speed (Igel, van den Heever, and Johnson 2018) and therefore may help explain some of the observations of higher NO_x at night relative to the preceding day, such as seen on the 22 – 24th August (Figure 33) as the *Kommandor Iona* passed through the northern part of the Gulf of Suez and Suez Canal. However, as this is highly speculative as the region around Suez is one of the busiest shipping lanes in the world, and thus is a bottleneck point for ships as well as other vehicular and urban emission sources which could account for the higher NO_x .

Observations of the higher losses of NO_x at night than day are relatively rare in the literature, but not unknown, and have been reported in maritime environments (S. S. Brown et al. 2004) and coastal environments (Ambrose et al. 2007). Brown *et al.* inferred the importance of nighttime NO_x removal by comparing production rates of gas phase HNO_3 at day, which represents a lower limit but likely a majority to NO_x loss (as formation of Peroxyacetyl Nitrates (PANs) do not represent a long-term sink for NO_x), and night and found that the calculated production rate at night was 80% of that during the day. The findings suggest that losses of NO_x were approximately equal to, and sometimes exceeded, the daytime losses when NO_3 + VOC addition reactions were also considered. This is similar to the findings of Ambrose *et al.* who determined that 50% of NO_x losses on an island off the coast of Maine, United States, occurred as a result of nighttime chemistry despite nighttime hours only making up ~40% of the diel cycle, implying that the dominance of nighttime chemistry for NO_x removal in this location.

These findings are similar to what was observed in AQABA as NO_x average nighttime loss rates in various regions, including the Red Sea and Persian Gulf, were similar to those experienced in the day and the daylight hours made up a majority of the diel cycle. The loss of NO_x per hour however, as described in Table 6, shows that despite longer days relative to the nights and roughly equivalent loss rates of NO_x that the nighttime mechanism was favored by a factor of 2 – 3. This observation suggests that there is a difference in the concentrations of NO_2 between the night and the day, which is not unexpected as photolysis cycles NO_x between the NO and NO_2 forms during the day, which would inhibit the formation of HNO_3 by limiting the available NO_2 to react with the OH radical. Other potential explanations for the increased NO_x loss during the night may include the *Kommandor Iona's* course, which was generally travelling within established shipping lanes and therefore closer to emission sources (other ships) during the night and more likely to leave them, for the purposes of lessening the chance of measurement contamination, during the day. Finally, as these measurements were made on board a moving platform, and each average potentially represents a wide geographic area with changing chemical conditions expressed only in 1 – 4 days, there exists a possibility that the increase of concentrations NO_x was a result of the *Kommandor Iona* being closer to emission sources during the nights of the campaign (the passing of the Strait of Hormuz was made at night, for example) which could positively bias the results. If this was the case, then while these results highlight the importance of nighttime chemistry to the regional NO_x budget, they also demonstrate the need for longer term measurements of NO_x , NO_3 , N_2O_5 , OH and O_3 (among others) in each of the studied regions of AQABA.

5.3.2 Day time losses due to NO_3 formation

It has recently been shown that NO_3 -oxidation of VOCs (thus an irreversible of NO_x), particularly biogenic VOCs, can be an important loss mechanism during the day. (J. Liebmann et al. 2018) made direct NO_3 reactivity measurements in the boreal forest which determined that the loss rates of NO_3 were sufficiently large that reaction with BVOC was competitive with the reaction with the NO_x -reproducing, gas phase

reaction with NO or photolysis rate. Contrasting against OH and O₃ data, (J. Liebmann et al. 2019) showed that 70% of all local production of ANs (RONO₂) was due to BVOC reaction with NO₃, including 21% of the production during the day. As O₃ and NO₂ concentrations remained high during the days of AQABA the production term of NO₃ also remained high suggesting that if VOC concentrations were sufficiently large, this could represent a significant loss process. This does not appear to be the case however, as the average per-second losses of NO₃ via photolysis, J(NO₃), and reaction with NO (median = 0.24, mean = 8 s⁻¹) were considerably higher than reactivity derived from shipping emissions, assumed to be VOC-related, using the relationship derived in section 5.2.4 (median = 0.01, mean = 0.04 s⁻¹) or from measured steady state reactivity throughout the whole AQABA campaign (median = 0.02, mean = 0.06 s⁻¹). This implies that losses due to local oxidation of ship-emitted VOCs during the day is a factor of 10 – 200 times slower than regeneration of NO_x due to photolysis or reaction with NO and therefore likely does not represent an important loss mechanism of NO₃ during the day.

5.4.1 Summary

Night time chemistry has been shown to be important during the AQABA campaign. High mixing ratios of O₃ and NO₂ led to high production terms of NO₃ and N₂O₅. Despite high production however, average lifetimes in most regions were on the order of a few seconds to ~5 minutes implying large loss terms. High temperatures during the AQABA campaign suggest that loss via NO₃, rather than N₂O₅, was the dominant mechanism, with DMS in particular as an important source of reactivity, in agreement with numerous previous works on nocturnal boundary layer chemistry. Large proportions of steady-state derived first order loss rates of NO₃ could not be assigned to the concentration(s) of any measured molecule(s) but likely are related to shipping emissions. A comparison of the loss of NO_x between the OH + NO₂ daytime mechanism (generally believed to be the most important) against the NO₂ + O₃ nighttime mechanisms revealed that in 4 of the 5 studied regions, the nighttime mechanism was dominant with per hour NO_x losses a factor 2 – 3 times more efficient than during the day. The dominance of the daytime mechanism was only seen in the Mediterranean Sea, which is consistent with several past studies of NO₃ reactivity in coastal sites across the region. The dominance of the nighttime mechanism in the other regions was determined despite comparable per second loss rates of NO₂ (k[OH], k[O₃]) and a longer day than night, suggesting the difference was driven by a relative increase in the concentration of NO₂ at night compared with the day. Diurnal cycles revealed that meteorological factors which could influence the concentrations of trace gases, such as the boundary layer height, were generally stable throughout a 24-hour period. This suggests that the increase of NO₂ concentrations were due to other factors and these may include influence from coastal sea breezes, which draw air masses (and therefore trace gases) away from sea to the land during the day and the reverse during the night, particularly when the *Kommandor Iona* passed close to coastal regions. The results may also simply reflect the averaging of measurements (each region only describes 2 – 4 day/night cycles) to describe a large, chemically diverse geographic regions on board a moving ship as it moved towards and away from emission sources and sinks. While these results highlight the importance of nighttime chemistry as a sink for NO_x and VOCs around the Arabian Peninsula, clearly further longer term studies of each region are required to determine to what extent NO₃ chemistry dominates compared against the OH initiated mechanism, and to compare these two over a broader range of conditions, such as seasonal differences.

6. NO₃ during the 2018 SAPHIR NO₃-Isoprene Campaign

6.1.1 Overview of Measurements

The 2018 SAPHIR campaign was a series of experiments looking at the nighttime oxidation of biogenic volatile organic compound (BVOC) isoprene with the NO₃ radical in a series of controlled chamber experiments. The SAPHIR chamber has been described and characterized before (Fuchs, Ball, et al. 2009; Rohrer et al. 2005; Bossmeyer et al. 2006) and is described in more detail in section 4. The main objectives of the 5-CRD measurements were to perform an intercomparison of NO₂ measurements (against 4 other instruments, with three using the CRD method) and NO₃ / N₂O₅ measurements (against two other instruments, both using the CRD method), with the goal of creating a ‘true’, harmonized dataset for further data analysis.

Another goal of the 5-CRD and other TD-CRD instruments was the calculation of organic nitrate (RONO₂) yields from the 5-CRD ΣANs data. The question of organic nitrate yields is discussed in section 7. While this chapter will focus on the intercomparisons with other instruments for NO₂, NO₃, and N₂O₅.

The experiments during the SAPHIR campaign were divided into two sections: gas phase and seed aerosol experiments. Gas phase experiments took place from 31st July, 2018 to 13th August. The basic conditions in each experiment were based around several injections of NO₂, O₃ and isoprene into the chamber and monitoring the formation of products over time. Different conditions imposed on experiments include varying the concentrations of Isoprene, NO₂ and O₃; different levels of relative humidity; the introduction of photochemistry by opening and closing of the chamber walls to expose the gases to natural sunlight; and the introduction of other trace gases e.g. CO as an OH scavenger or propene as an HO₂ source. Seed aerosol experiments mirrored the gas-phase experiment conditions but additionally introduced Ammonium Sulfate, (NH₄)₂SO₄, for the purposes for forming secondary organic aerosol (SOA).

6.2.1 Intercomparison of NO₂ measurements

NO₂ measurements form the basis of the experiments, as NO₂ is the main source of NO₃ in the chamber. Understanding the inputs of reactive nitrogen into the chamber is crucial to understanding how this nitrogen evolves and becomes sequestered in different NO_y species (NO_y = NO, NO₂, NO₃, N₂O₅, HNO₃, pNO₃⁻, Organic Nitrates) over time. NO₂ was measured by five different instruments during the SAPHIR campaign:

Table 7. Instruments measuring NO₂ during the NO₃-Isoprene SAPHIR chamber experiments with technical information on limit of detection, total uncertainty and total days of data coverage. CRD = Cavity ringdown. CLD = Chemiluminescence detector.

Instrument	Type	Limit of Detection (ppt)	Total Uncertainty (%)	Data Coverage (Experiments /22)
5-CRD	Cavity Ringdown	54	9% ± 10 ppt	19
MPI-TD-CRD*	Cavity Ringdown	98	11% ± 20 ppt	22
k(NO₃)-CRD	Cavity Ringdown	150	9%	18
Reed-TD-CRD	Cavity Ringdown	>1000	10%	21
IEK8-CLD	Chemiluminescence	10	5%	20

* - Instrument measures NO_x (NO_x = NO + NO₂).

Note that some of the uncertainties will cancel for the 5-CRD, TD-CRD and $k(\text{NO}_3)$ -CRD instruments as each of the instruments are known to have standardized the reference NO_2 spectrum (Vandaele et al. 2002) thus the total uncertainty associated with the measurement of NO_2 absorption spectrum is the same.

NO_2 comparisons were made for each experiment between each instrument which reported data, including only partial data, for a particular day. For the most part, as NO_3 oxidation of isoprene requires dark conditions (as NO_3 undergoes rapid photolysis when exposed to sunlight), measurements of NO_x by the MPI-TD-CRD were, in essence, measurements of NO_2 . Independent CLD measurements of NO were also taken which confirm that the NO mixing ratios were nearly always below the limit of detection (≤ 10 ppt). As discussed in section 3, measurements of NO are themselves also necessary for CRD data corrections, which would be significant during experiments where the chamber shutters were opened, allowing sunlight to enter and photolysis of NO_2 to occur. In order to make a comparison with the MPI-TD-CRD in the presence of NO , the independent measurement of NO must be subtracted from the total NO_x signal, leaving NO_2 . This does however have the disadvantage of introducing the uncertainty (5%) of the CLD into the comparisons with other instruments.

6.2.2 Comparison by experiment

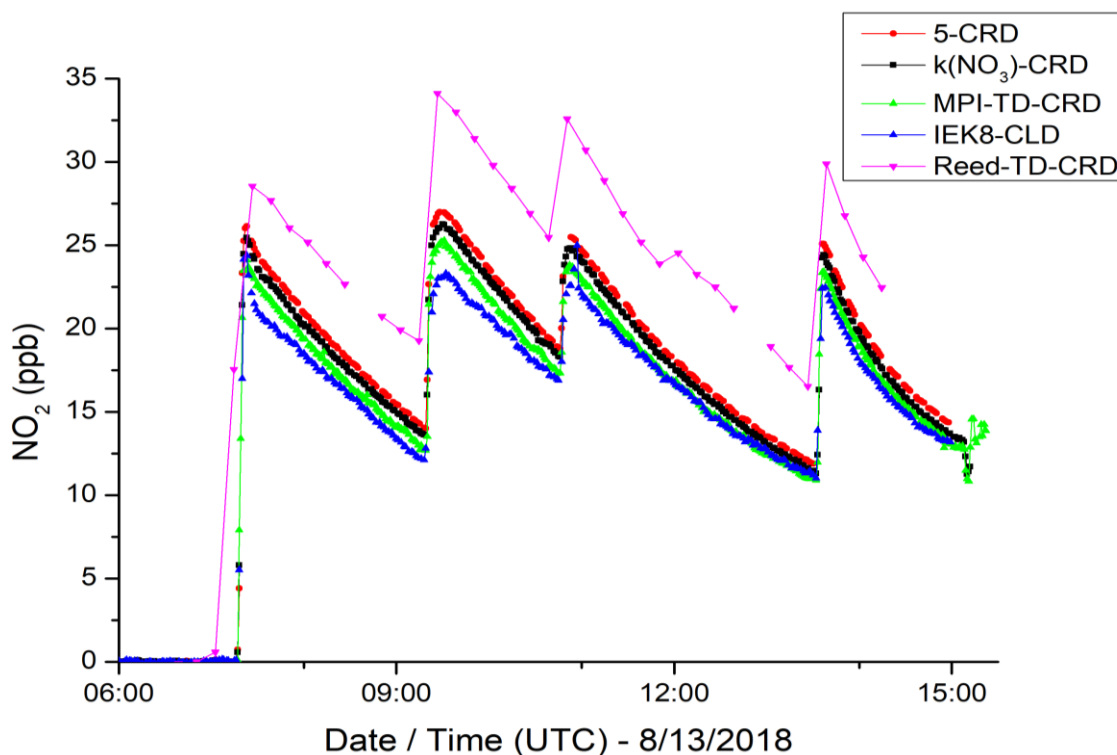


Figure 36. Corrected NO_2 signals for each instrument on 13th of August.

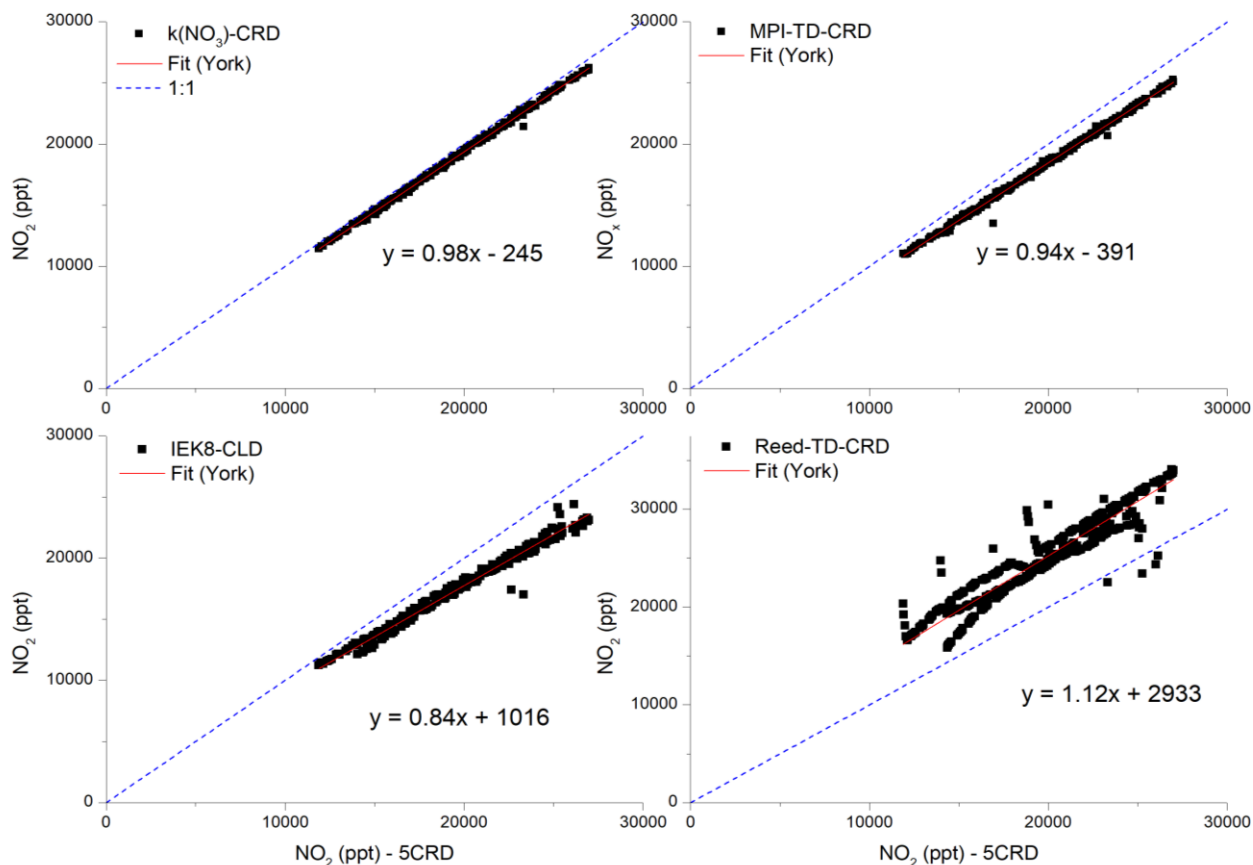


Figure 37. Comparison of NO₂ measurements from the experiment 8/13. All measurements are plotted against the 5-CRD in the x-axis.

Figure 36 and Figure 37 show a typical data comparison of NO₂ during the SAPHIR campaign, with Figure 36 showing the corrected NO₂ signals of all instruments as a time series of the experiment on 8/13 and Figure 37 in the form of a correlation plot where each of the instruments NO₂ signals are plotted in the y-axis against the NO₂ signal from the 5-CRD in the x-axis. As is the case in this example, in general, the best agreement was observed between the 5-CRD, MPI-TD-CRD and k(NO₃)-CRD instruments. The agreement was strong when determined in terms of the slopes between the two instruments, the intercepts of the y-axis and the coefficients of determination (R^2). These metrics are shown for each instrument which reported data for a particular experiment in Figure 38 for the gas phase experiments and Figure 39 for the seed aerosol experiments. The 5-CRD and the MPI-TD-CRD throughout all experiments report a mean slope of 0.896 ± 0.007 ; a mean intercept of -0.054 ± 0.319 ; and a mean R^2 of 0.967 ± 0.095 . The 5-CRD and the k(NO₃)-CRD report a mean slope of 0.941 ± 0.005 ; a mean intercept of -0.020 ± 0.252 ; and a mean R^2 of 0.970 ± 0.063 . These values are fully consistent with the reported combined uncertainties of the three instruments.

Agreement between the IEK8-CLD instrument and in particular the Reed-TD-CRD instrument was significantly worse and tended to vary considerably between each experiment. Compared to the 5-CRD the mean slope across all experiments with the Reed-TD-CRD was 0.936 ± 0.273 ; the mean intercept was 2.552 ± 2.202 ; and the mean R^2 was 0.694 ± 0.290 . While the mean slope is within the reported combined uncertainty of the 5-CRD and the Reed-TD-CRD, as the standard deviation suggests this is largely a function

of high variable slopes for each experiment which were often greater than the combined uncertainties. The Reed-TD-CRD was a newly built and deployed instrument and featured a single, 4 m, PTFE inlet line direct from the chamber to the oven system, which used a series of valves to divert the flow through several, ovens set to different temperatures for quantitative determination of NO₂ (ambient temperature), PNs, ANs and HNO₃ (heated). This design may be responsible for the shape of the signal seen in Figure 36 where the trace of the data was similar (resulting in a reasonably good slope and R²) but the presence of a large and non-constant offset (average 3 ppb equivalent) was obvious. This can be seen in several other experiments (Figure 39). This may indicate that the Reed-TD-CRD instrument may act as a source of NO₂ following sampling of reactive nitrogen containing air, due perhaps to gas-surface interactions; or the instrument experienced other technical difficulties perhaps related to pressure, flow or temperature regulations. On other experiments, particularly 8/9, the instrument showed almost no linear behavior compared to the 5-CRD, which was itself in strong agreement with the MPI-TD-CRD and k(NO₃)-CRD instruments. Some experiments do however report better agreement, according to these metrics, with the other instruments e.g. 8/19 and 8/23. As the variable behavior of the Reed-TD-CRD is subject to large divergences compared to the other four instruments, the NO₂ datasets produced by this instrument are not considered further when generating the final, harmonized NO₂ dataset.

The IEK8-CLD system reported a mean slope of 0.881 ± 0.113 ; a mean intercept of 0.484 ± 0.701 ; and a mean R² of 0.943 ± 0.128 . In contrast to the Reed-TD-CRD, the CLD system showed more consistent results even as this resulted in lesser agreement on average to the 5-CRD and other instruments. This is evidenced by the lower standard deviations on the slopes, which were less than half as variable, and a much higher and less variable mean R² value. It is noteworthy however, that the deviation of the mean slope is outside the combined uncertainties of the 5-CRD and CLD instruments. The CLD was the only instrument to use a completely different method for evaluation of NO₂, as CLD instruments must reduce NO₂ to NO for detection, compared to the absolute measurement of NO₂ (as a function of absorption) in CRD instruments. This introduces the need for regular calibrations, which introduce a series of additional uncertainties into the final NO₂ signal. In principle, an error in the calibration of the CLD would introduce deviation away from a slope of 1, assuming no systematic error in the 5-CRD, as different calibrations would give different slopes, depending on the accuracy. This may account for the high R² compared to the slopes, as the instruments give a different response to the same amount of NO₂. The relatively high (compared to the MPI-TD-CRD and k(NO₃)-CRD instruments) intercepts of the CLD suggest the presence of an interference in the CLD system. On several occasions (including 8/13, Figure 37) the correlation plots between the 5-CRD and CLD showed several parallel lines (i.e. same slope but different intercept) which may be a result of a contaminant in the calibrations. For example, if the CLD is calibrated with a bottles containing NO₂ and this source contains a contaminant of NO, this may manifest as an offset in the NO₂ signal. Additionally, on several occasions the CLD detected a signal of NO₂ in the chamber following an injection of O₃, but before an injection of NO₂. This signal appears to have been liberated from walls of the SAPHIR chamber and is not seen in any of the NO₂ or NO_x measurements. A similar effect is seen in the measurements of NO_y and NO_z (NO_y – NO_x) which also see an increase in signal following an injection of O₃ into the chamber before the first injection of NO₂ or isoprene. These observations may suggest that the molecule(s) liberated from the walls after interacting with O₃ undergo photolysis in the CLD detection cell (the CLD uses a photolysis method to reduce NO₂ to NO) to give NO₂, but are also thermally stable to up ~650 K as they are not detected by the 5-CRD heated channels. However, it is difficult to determine with certainty whether these signals are of the same molecule(s) as the NO_y signal is generally larger the NO₂-CLD and the NO_y instrument detects reactive nitrogen as NO₂ while the CLD

detects it as NO. As these discrepancies cannot be rigorously explained, and it is unknown to what extent the variable offsets and slopes associated with the CLD instrument are a function of calibration versus chemical interferences, the CLD NO₂ dataset is not further considered when generating the final, harmonized NO₂ dataset.

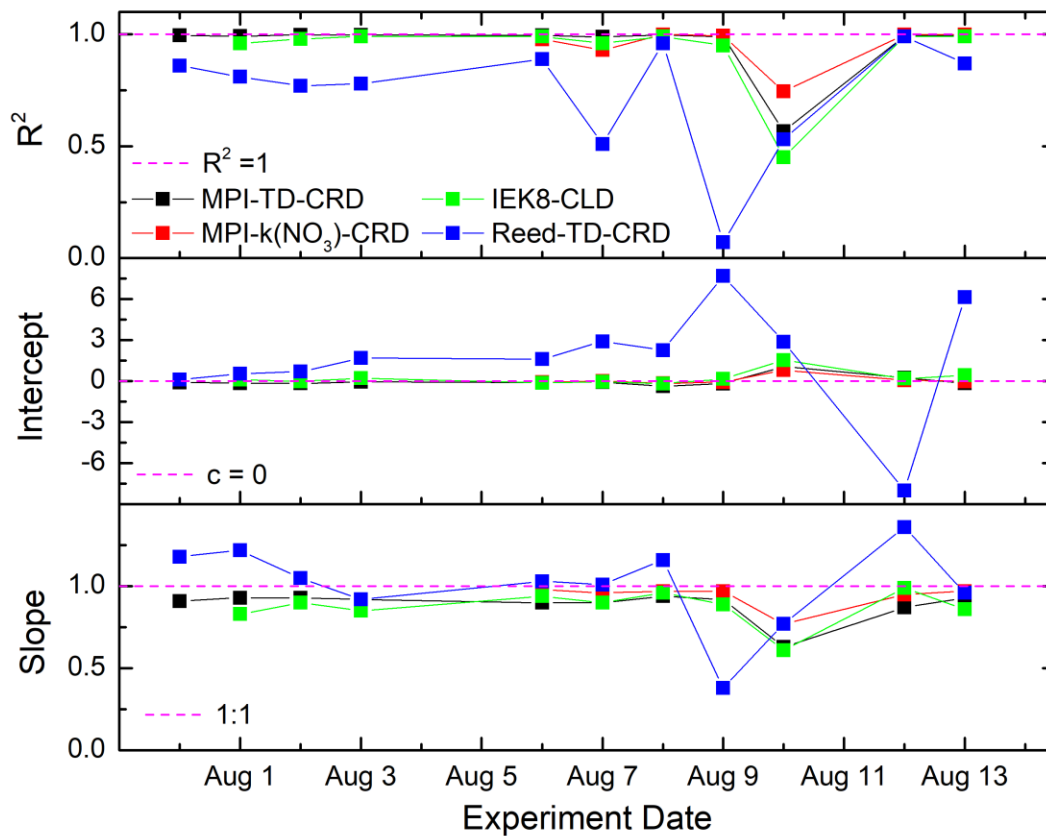


Figure 38. NO₂ intercomparisons against the 5-CRD for slope, intercepts and coefficient of determination for each instrument by date during the Gas Phase section of the 2017 SAPHIR campaign.

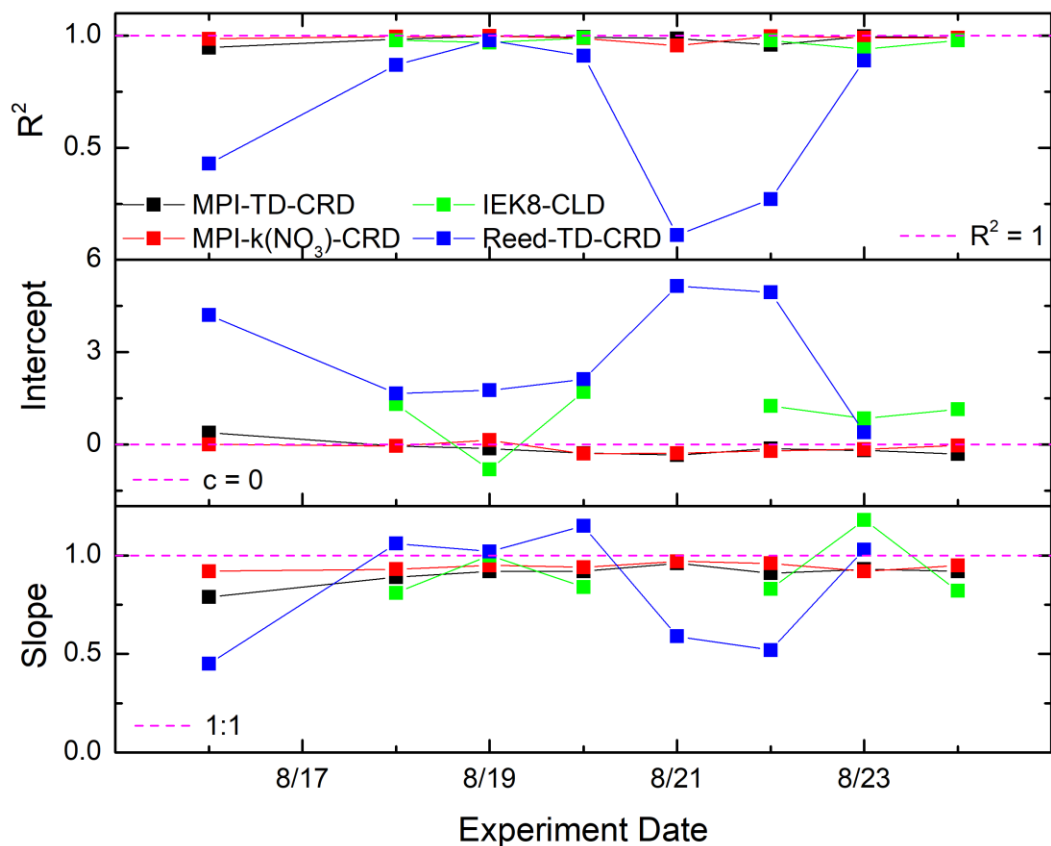


Figure 39. NO_2 intercomparisons against the 5-CRD for slope, intercepts and coefficient of determination for each instrument by date during the Seed Aerosol section of the 2017 SAPHIR campaign.

Following the analysis detailed above, the final NO_2 dataset was generated using the 5-CRD, MPI-TD-CRD and $\text{k}(\text{NO}_3)$ -CRD datasets. As the strongest agreement was between the 5-CRD and $\text{k}(\text{NO}_3)$ -CRD datasets and the MPI-TD-CRD dataset had the best coverage, as it reported NO_x data for every experiment, the final dataset was generated by scaling the MPI-TD-CRD data to an average of the other two datasets. This average was the geometric mean, i.e. the n^{th} root of n products, where for these experiments $n = 2$. Figure 40 shows a comparison of the finalized NO_2 dataset (pink) against the three datasets used to generate it.

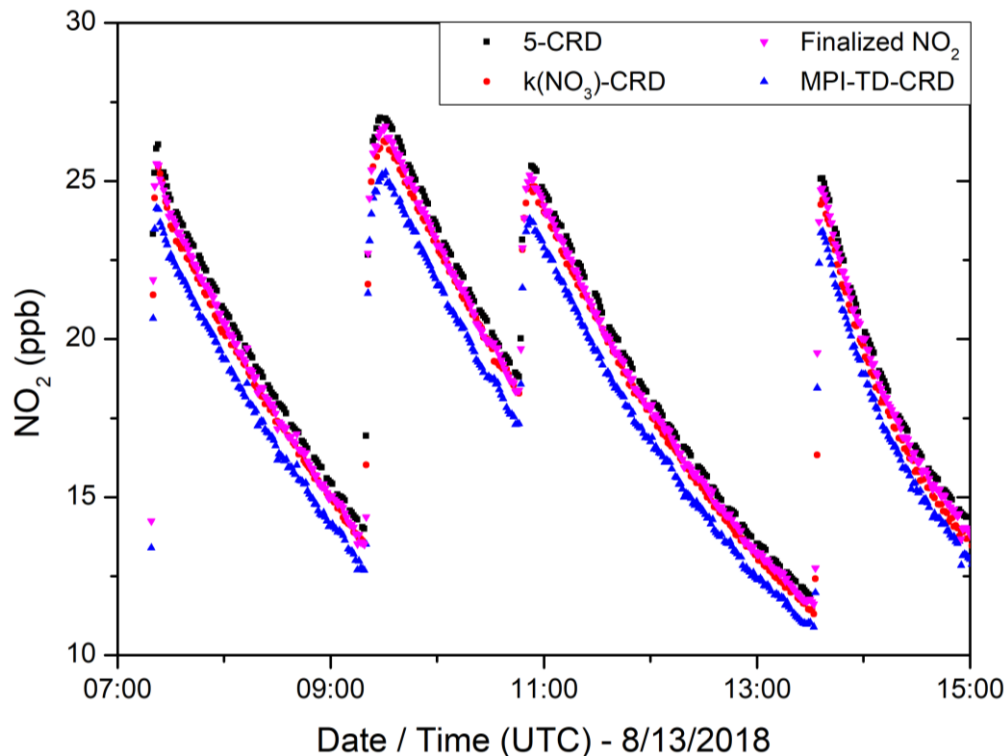


Figure 40. Comparison of finalized NO_2 dataset against the datasets used to calculate it. Zero signals and other NO_2 measurements omitted for clarity.

6.2.3 Conclusion and comparison with previous NO_2 intercomparison campaign.

The SAPHIR chamber has been host to instrument comparisons before, including for NO_2 and NO_3 (see below). The NO_2 intercomparison was reported on in (Fuchs, Ball, et al. 2009) and also included five different instruments. In contrast to this campaign however, which had three measurements of NO_2 performed by instruments utilizing nearly identical techniques (pulsed Cavity Ringdown spectroscopy), the 2010 campaign featured five different measurements using five different techniques, including laser induced fluorescence (LIF); different CRD techniques; incoherent broadband cavity-enhanced absorption spectroscopy (IBBCEAS); and (the same) CLD, though it is unknown to what extent the CLD has been modified since the campaign. Additionally, the 2010 campaign also featured a variety of different atmospheric ‘scenarios’, i.e. simulations of different conditions which are typical for a variety of urban and rural conditions. These featured much larger mixing ratios of NO_2 than experienced here (up to 75 ppb) and injections of aerosols, various biogenic and anthropogenic VOCs and other trace gases. Linear regression analyses of the instruments show that four of the five instruments gave R^2 values > 0.98 combined for each experiment and slopes which generally agreed within the instrument combined uncertainties, with intercepts close to zero. In general, these results of this previous intercomparison are comparable to the results presented here between the three CRD instruments ($R^2 > 0.97$; mean slope > 0.9) and to a lesser extent, the CLD.

These results show the reliability of the CRD technique for the measurement of atmospheric NO_2 , one of the atmosphere’s most prevalent and important trace gases. The results also highlight the usefulness of the SAPHIR chamber for the purposes of intercomparisons between different instruments for studying various trace gases.

6.3.1 Intercomparisons of NO₃ / N₂O₅ measurements

Following the generation of the NO₂ finalized dataset, the next most important step was to establish a similar finalized dataset for the NO₃ radical. As NO₃ was the principle oxidant in these experiments, understanding the evolution of its concentration over time is key in understanding the sequestration of reactive nitrogen over time, as well as the losses of atmospherically important trace gases such as O₃, NO₂ or isoprene. Below follows an intercomparison of measurements of NO₃ and its equilibrium partner, N₂O₅, made during the 2018 SAPHIR campaign. Direct measurements of NO₃ and N₂O₅ were made by three different Cavity Ringdown Systems:

Table 8. Cavity Ringdown (CRD) instruments for measuring NO₃ and N₂O₅ during the SAPHIR Campaign with reported technical data (Total Uncertainty, Limit of detection).

Instrument	Type	Limit of Detection NO ₃ (ppt)	Limit of Detection N ₂ O ₅ (ppt)	Total Uncertainty NO ₃ (%) (1σ)	Total Uncertainty N ₂ O ₅ (%) (1σ)	Data Coverage (Experiments /22)
5-CRD	Cavity Ringdown	0.5	3.8	25%	28%	20
CNRS-CRD	Cavity Ringdown	0.25	0.9	20%	15%	20
IEK8-CRD	Cavity Ringdown	1.6	2.3	15%	20%	4

Note both the 5-CRD and CNRS-CRD agreed on the use the same reference spectrum for the correction of the effective cross section of NO₃ (Orphal, Fellows, and Flaud 2003) which contributes 10% uncertainty to the measurement of NO₃ and N₂O₅. This common reference spectrum means that some of the uncertainty between the instrument is common and thus cancels in the comparison. Data coverage was minimal for the IEK8-CRD system due to technical issues with the instrument leading to heavy losses of NO₃ during sampling, and large corrections (with large associated uncertainties) for the experiments for which data were reported. As a result, all of the data from the intercomparisons used to generate a final, ‘true’ dataset comes from the measurements of the CNRS-CRD and 5-CRD.

6.3.2 Comparison by experiment

As it can be difficult to accurately measure a radical species, a useful identity for checking the consistency and accuracy of measurements is the dynamic equilibrium coefficient of the reaction between NO₂ and NO₃ to form N₂O₅. As previously discussed, K_{eq} can be expressed as the ratio between the reactants and products:

$$K_{eq}(T) = \frac{[N_2O_5]}{[NO_2][NO_3]} \quad (\text{Equation 12})$$

NO₂ was measured by various instruments during the campaign with efforts to generate a harmonized dataset with the goal of making the measurement as accurate as possible. Together with the literature values of K_{eq}(T), NO₂ can be used to derive an expected ratio between N₂O₅ and NO₃. This expected ratio can, in turn, be compared to the measured ratio of each instrument: within combined uncertainties, these should agree. The uncertainty of K_{eq}(T) can be estimated by the following equations from (JPL, 2020.):

$$\sigma(K_{eq}NO_2) = K_{eq}(T)[NO_2] \sqrt{\left(\frac{\sigma_{K_{eq}}}{K_{eq}}\right)^2 + \left(\frac{\sigma_{[NO_2]}}{[NO_2]}\right)^2} \quad (\text{Equation 18})$$

With,

$$\frac{\sigma_{K_{eq}}}{K_{eq}} = 1.2 \times e \left(75 \times \left(\frac{1}{T} - \frac{1}{298} \right) \right) - 1 \quad (\text{Equation 19})$$

$\sigma(K_{eq}NO_2)$ is the combined uncertainty of K_{eq} at a given T (K) and the given concentration of $[NO_2]$ (molecule cm^{-3}). $\sigma(K_{eq}(T))$ and $\sigma([NO_2])$ are the relative uncertainties (%) in the values of K_{eq} and NO_2 , respectively. No uncertainty is assumed in the measurement of temperature, which was actively monitored along with other parameters including pressure, relative humidity and gas replenishment flow in a suite of standard onboard instruments (Bossmeier et al. 2006).

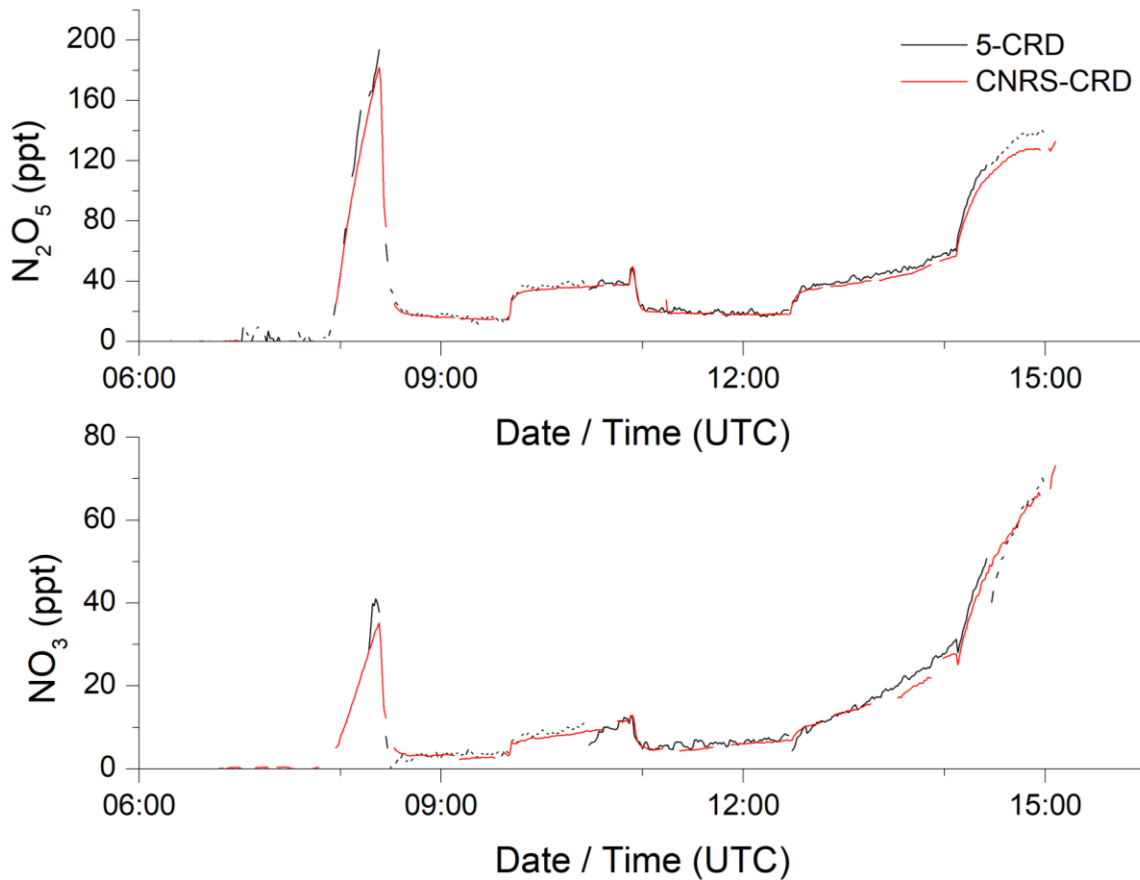


Figure 41. Measured NO_3 and N_2O_5 from each CRD instrument for the 8/10 NO_3 -Isoprene experiment plotted against time.

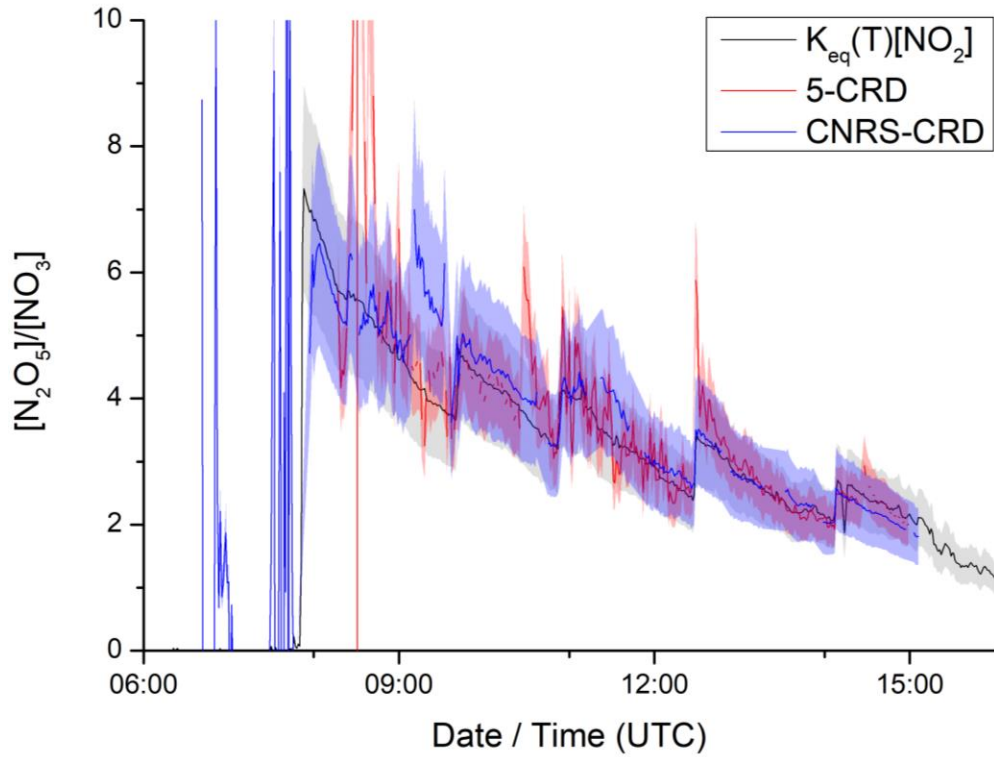


Figure 42. $[N_2O_5]/[NO_3]$ ratios against time for the experiment on 8/10. $K_{eq}(T)$ is calculated from (JPL. rec.). Shaded area surrounding lines represent 1- σ uncertainties of each measurement.

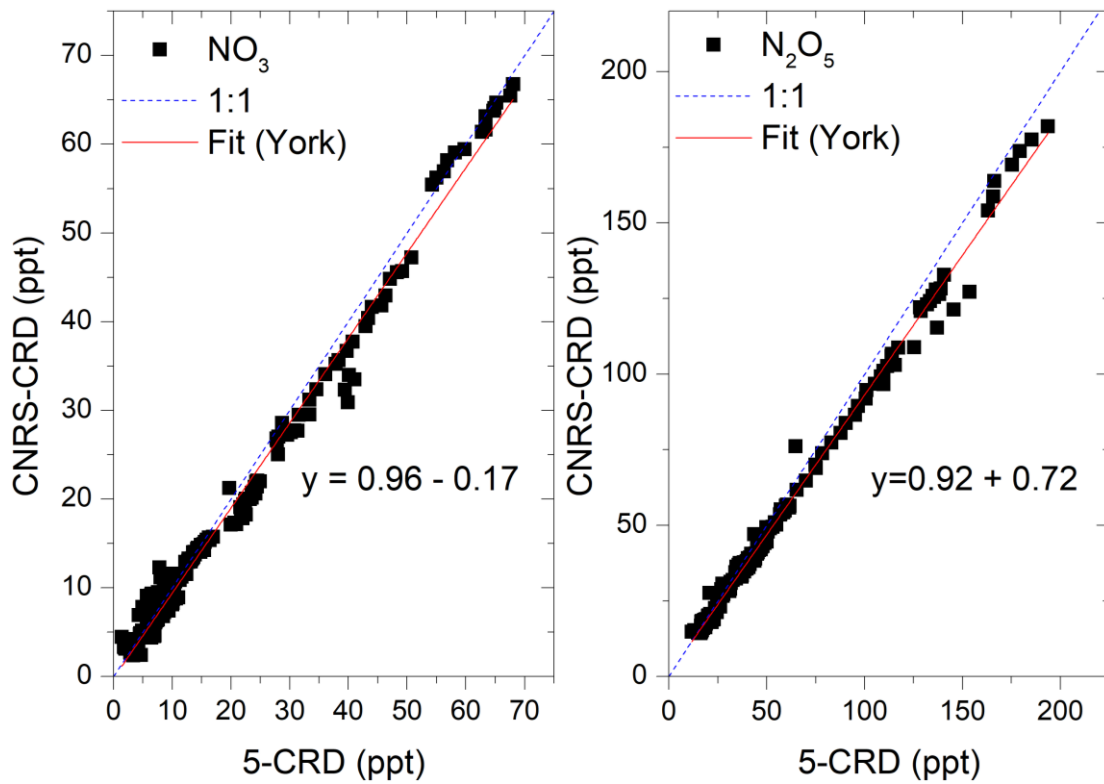


Figure 43. Plots of 5-CRD vs. CNRS-CRD for NO_3 and N_2O_5 mixing ratios for the 8/10 NO_3 -Isoprene experiments

Figure 41 shows the NO_3 and N_2O_5 mixing ratios (in ppt) over the run of an experiment (10th August) conducted during the NO_3 -Isoprene campaign. From this, the two datasets can be compared by plotting one against the other (Figure 43) and performing a linear regression analysis. For the 10th of August experiment, NO_3 and N_2O_5 had slopes of 0.96 and 0.92, respectively which is well within the combined uncertainties for each instrument and intercepts close to zero (-0.17 and +0.72 (ppt), respectively). These result in coefficients of determination (R^2) of > 0.999. Figure 42 compares the measured ratio of $\text{N}_2\text{O}_5/\text{NO}_3$ from each instrument, against $K_{\text{eq}}(T)[\text{NO}_2]$ for the 8/10 experiments. As per (Equation 12), these should be equal however, there are large uncertainties associated both with $K_{\text{eq}}(T)[\text{NO}_2]$ (20 – 22% for this experiment) and the measurements of NO_3 and N_2O_5 . The instruments therefore can be said to agree whenever the uncertainties (shaded regions) of all three measurements overlap. While no error is assumed in the measurement of temperature, an error is possible as the measurement of the temperature is given by an onboard instrument which reports a single average across the entire chamber, and thus the homogeneity of temperature in the chamber is not known. This can be problematic as the $\text{NO}_3/\text{N}_2\text{O}_5$ partitioning is strongly dependent on temperature. For instance, a 1-degree difference in temperature would introduce an additional 12% uncertainty into the $\sigma(K_{\text{eq}}[\text{NO}_2])$. Additionally, a temperature difference between the chamber and the measurement site (the temperature regulated cavities within temperature controlled shipping containers beneath the SAPHIR chamber) was known, and variable throughout the day. For the majority of the time in these experiments, the temperature in the chamber was higher than the measurement sites, reflecting the high summer temperatures experienced during the SAPHIR campaign, although this was occasionally reversed at the beginning of experiments in the early mornings where temperatures were lower. FACSIMILE simulations suggest, assuming a linear temperature gradient between the chamber and the cavity, that the residence time in the sampling lines and instruments (~2 s in the 5-CRD) produce a negligible difference in the concentrations detected at the instrument compared with those present in the chamber before entering the sampling line. For example, the mean temperature of the chamber was determined to be 299 ± 5 K while the cavity was maintained at a temperature of 300 K. A 5 K difference over 3 seconds would result in a difference in the NO_3 mixing ratios of < 1%.

Table 9 details the agreement (slope of linear regression) between the 5-CRD and the CNRS-CRD for NO_3 and N_2O_5 for each experiment with a description of the experimental conditions and which instrument, if either, agrees to $K_{\text{eq}}[\text{NO}_2]$ within combined uncertainties. The linear regression function used a least-squares solution (York Method) for each experiment.

Table 9. NO₃-Isoprene campaign experiments. 7/31 - 8/13 are gas-phase experiments and 8/14 - 8/24 include the addition of seed aerosol ((NH₄)₂SO₄). The slopes of the linear fit of 5-CRD vs. CNRS-CRD are displayed for NO₃ and N₂O₅. Agreement to K_{eq}[NO₂] details where the uncertainties of the measurements overlap with the uncertainties of K_{eq}[NO₂]. Note: CO = Carbon Monoxide; MVK = Methylvinyl Ketone; RH = Relative Humidity.

Date	Experiment	Slope NO ₃ - (5-CRD vs. CNRS-CRD)	Slope N ₂ O ₅ (5-CRD vs. CNRS-CRD)	Agreement to K _{eq} [NO ₂]
7/31	Reference NO ₃ (only 5 ppb NO ₂ / 100 ppb O ₃)	0.77	1.01	Both
8/1	100 ppb O ₃ , 5 ppb NO ₂ , 3 ppb Isoprene	0.85	0.96	5-CRD
8/2	Repeat 8/1	-	0.91	5-CRD
8/3	100 ppb O ₃ , 5 ppb NO ₂ , 3 ppb Isoprene, 80% RH, Open Chamber (day-to-night)	-	1.39	Neither
8/6	100 ppb O ₃ , 5 ppb NO ₂ , 3 ppb Isoprene, 80% RH, Open Chamber (night-to-day)	1.43	1.03	Both
8/7	50 ppb O ₃ , 5 ppb NO ₂ , 2 ppb Isoprene, 20% RH	-	0.71	5-CRD
8/8	100 ppb O ₃ , 25 ppb NO ₂ , 10 ppb Isoprene	-	-	5-CRD
8/9	100 ppb O ₃ , 5 ppb NO ₂ , 3 ppb Isoprene, 100 ppb propene, 120 ppm CO	-	0.88	5-CRD
8/10	Repeat 8/7	0.96	0.92	Both
8/12	100 ppb O ₃ , 5 ppb NO ₂ , 3 ppb Isoprene, 120 ppm CO, Open Chamber (night-to-day)	0.94	0.92	Both
8/13	Repeat 8/8	0.83	0.89	CNRS-CRD
8/14	100 ppb O ₃ , 25 ppb NO ₂ , 10 ppb Isoprene, Seed Aerosol	-	-	CNRS-CRD
8/15	100 ppb O ₃ , 25 ppb NO ₂ , 10 ppb Isoprene, Seed Aerosol, 60% RH	0.99	1.16	CNRS-CRD
8/16	100 ppb O ₃ , 100 ppb NO ₂ , 3 ppb Isoprene, Seed Aerosol, 80% RH, Open Chamber (night-to-day)	-	-	None
8/17	10 ppb Isobutyl Nitrate, 100 ppb O ₃ , 10 ppb acetaldehyde, 60% RH, Open Chamber	-	-	CNRS-CRD
8/18	120 ppb O ₃ , 5 ppb NO ₂ , 3 ppb Isoprene, 2 ppb Beta-Caryophyllene, Seed Aerosol, 60% RH, Open Chamber (night-to-day)	1.19	1.62	5-CRD
8/19	Frozen N ₂ O ₅ , 100 ppb O ₃ , 3 ppb Isoprene, 10 ppb MVK, Seed Aerosol	1.09	0.96	Both
8/20	120 ppb O ₃ , 5 ppb NO ₂ , 3 ppb Isoprene, 2 ppb Beta-Caryophyllene, Seed Aerosol, 60% RH	0.87	1.08	Both
8/21	100 ppb O ₃ , 5 ppb NO ₂ , 3 ppb Isoprene, 100 ppb propene, 120 ppm CO, Seed Aerosol, 60% RH	-	-	None
8/22	100 ppb O ₃ , 5 ppb NO ₂ , Isoprene Emitting Oak chamber (6 – 8 ppb), Seed Aerosol, 70% RH	1.51	1.06	Both
8/23	100 ppb O ₃ , 5 ppb NO ₂ , 3 ppb Isoprene, Seed Aerosol	-	-	None
8/24	100 ppb O ₃ , 5 ppb NO ₂ , 4 ppb Isoprene, 2 ppb Beta-Caryophyllene, Seed Aerosol, 60% RH	-	1.65	None

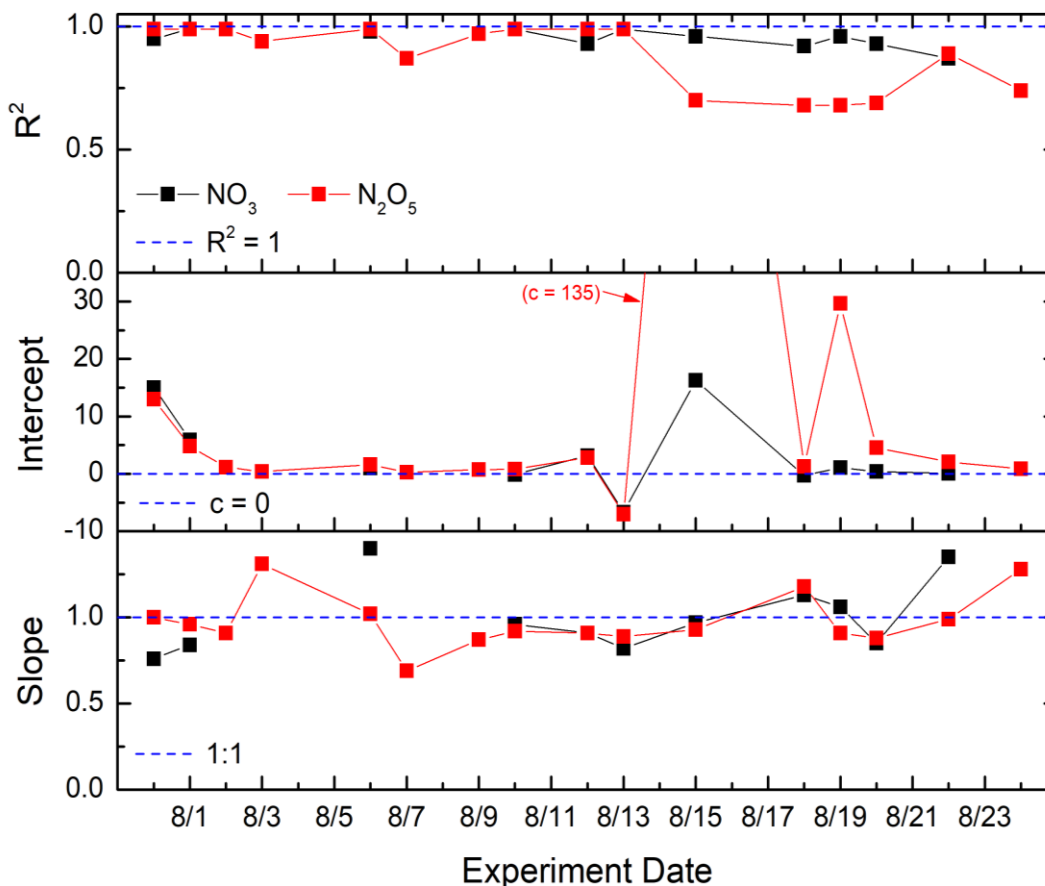


Figure 44. NO_3 (black) and N_2O_5 (red) intercomparisons against the 5-CRD for slope, intercepts and coefficient of determination for the CNRS-CRD by date during the 2017 SAPHIR campaign.

Figure 44 shows a graphical summary of the data in Table 8, together with the intercept of the y-axis and the coefficient of determination (R^2). During the 2018 SAPHIR campaign, the mean slopes between the two instruments were 1.00 ± 0.20 and 0.98 ± 0.15 ; the mean intercepts were 3.25 ± 6.5 and 12.03 ± 32.80 ; and the mean R^2 were 0.95 ± 0.04 and 0.89 ± 0.12 for NO_3 and N_2O_5 , respectively. The means in the N_2O_5 calculations are strongly impacted by the poor linearity of the function on 8/15 leading to a large intercept and relatively poor R^2 . Removal of this experiment results in a mean slope of 0.98; intercept of 3.78; and R^2 of 0.91 for N_2O_5 over the entire campaign. In general, these results suggest that the deviation away from unity in the linear regression were lower than the combined uncertainties of the two instruments ($\sim 32\%$ for both trace gases).

Considerable disagreement was observed in the first few days (not shown) with approximately a factor of three (8/2), a factor of five (8/1, 8/8) and a factor of seven (8/3) times more NO_3 seen by the 5-CRD than the CNRS-CRD. Similar divergence was not observed in the N_2O_5 signals, suggesting local losses of NO_3 to the CNRS-CRD. Losses were observed to have occurred on both the Teflon membrane filters where, following a filter change, the NO_3 signal appeared to decline relative to the signal before the change and then increased back into the overall experimental trend in an equilibrium-like curve. This effect was present in both instruments and can be seen in Figure 42 (though has been removed from the final comparison) for the 5-CRD at $\sim 13:00$ and at $\sim 09:00$ for the CNRS-CRD when the measured $\text{N}_2\text{O}_5/\text{NO}_3$ ratio most strongly diverges from $K_{\text{eq}}[\text{NO}_2]$, before returning into agreement. Additional losses were also

observed within the PFA sampling lines used by the CNRS system. While there are no rigorous explanations or characterizations at present for these losses, starting from 9th of August the CNRS-CRD operations involved the changing of the sampling lines each day before the beginning of each experiment. From this point onwards, the agreement between the two instruments improved markedly – strongly suggesting that the PFA inlet was responsible for the observed losses. While it would not be necessarily expected for controlled chamber experiments, one explanation for this effect could be that the produced organic compounds, which are highly polar (i.e. possessing a strong electrical dipole) and therefore ‘sticky’, in the chamber adhered to the surface of the PFA inlet creating a large surface area for NO₃ to undergo heterogeneous reactions, essentially residence time-dependent wall losses. Why similar losses were not observed in the 5-CRD system could be due to the differences in sampling methods employed by each instrument. The 5-CRD made use of a relatively large sampling flow, 15 SLM, subsampled perpendicular from an even larger flow, 25 SLM, for a total flow rate from the chamber to the point where the flow splits of 40 SLM. The CNRS-CRD system used a lower sampling flow (12 SLM) and no bypass flow. However, without a detailed understanding of the CNRS-CRD system, as total residence time is dependent on both the flow rate and the volume of the instrument and its sampling lines, this remains speculation.

Other noteworthy results to discuss are 8/3 or 8/7 where results showed slopes which diverged considerably from unity and R² values were poor. These experiments were characterized by relatively small mixing ratios of NO₃ due to either smaller injections of NO₂ (2 ppb vs. 5ppb) and O₃ (50 ppb vs. 100 ppb) or long periods of the chamber walls being open, thereby exposing the gas mixture to sunlight and photolysis. The low mixing ratios observed under 8/3, for example, (generally less than 5 ppt) are close to the 5-CRD limits of detection (0.5 and 3.8 ppt for NO₃ and N₂O₅, respectively) but somewhat higher than the limits of detection for the CNRS-CRD (0.25 and 0.9 ppt for NO₃ and N₂O₅, respectively) and lead to considerable scatter and poor linearity. Disagreement was also observed on 8/22 (low R², divergence from unity in slope) due to a failure in the fan system between ~11:00 – 14:00 UTC in the SAPHIR chamber and therefore is presumably a result of poor mixing in the chamber. In the absence of the fan system air within the SAPHIR chamber has a mixing time on the order ~1 h (Dorn et al. 2013), which is considerably longer than the lifetime of NO₃ in the chamber (~8.3 minutes, according to a derivation of the wall loss rate (Dewald et al. 2020)) and potentially leading to concentration gradients in the chamber.

From the results of the NO₃ / N₂O₅ comparisons, a finalized dataset for both trace gases was generated in a similar way to the NO₂, discussed in section 6.2.2. In this case a mathematical average (mean) between both signals was calculated, where data was available to compare, when the ratios of N₂O₅/NO₃ of both instruments within the uncertainties of K_{eq}[NO₂]. If data was available but one or both of the datasets were not within the uncertainties of K_{eq}[NO₂], the dataset which diverged less compared to K_{eq}[NO₂] was selected as the finalized dataset, as this was based on several independent measurements of NO₂ and well-established literature values of K_{eq}(T). In cases where NO₃ datasets were missing, incomplete or below the detection limits and therefore a comparison of the measured ratio against the expected ratio could not be made, NO₃ was calculated with N₂O₅ and K_{eq}[NO₂] according to (Equation 12) (there was no experiment without at least one N₂O₅ measurement). This approach is possible as N₂O₅ losses to the instrument(s) walls were not expected due to the previously discussed Teflon filters which block reactive aerosol particles (from 8/14 onwards with the introduction of seed aerosols) from coating the walls and where no selective losses of N₂O₅ had been observed in either the SAPHIR campaign nor in previous laboratory experiments for either instrument. Additionally, as NO₂ was measured by several different instruments during the campaign data were available for nearly every minute of every experiment,

meaning coverage was limited only to gaps in the N_2O_5 data. A downside of this approach is that it introduces additional uncertainty into final NO_3 measurement, particularly when N_2O_5 mixing ratios are close to the detection limits.

6.3.3 Comparison to previous intercomparisons

While no formal intercomparison campaigns have been attempted for the 5-CRD before, previous field measurements of NO_3 by (Sobanski, Tang, et al. 2016) during the 2011 PARADE campaign in a semi-rural mountain range in Germany were accompanied by NO_3 measurements by the Long-Path Differential Optical Absorption Spectroscopy (LP-DOAS) method. Compared with these results, the data presented in the intercomparison here are generally favorable, particularly at lower mixing ratios as PARADE results reported an average $[\text{NO}_3]_{\text{CRDS}}/[\text{NO}_3]_{\text{LP-DOAS}}$ ratio of 1.23 ± 0.07 . In more extreme cases, this ratio was < 0.5 when $[\text{NO}_3]$ mixing ratios were close to the 5-CRD limit of detection. When NO_3 lifetimes were higher (> 1500 s) however, (i.e. mixing ratios were larger) agreement between LP-DOAS and the 5-CRD was considerably stronger and closer to unity, with a ratio of 0.95 ± 0.05 , comparable to the results reported here. No previous N_2O_5 intercomparisons or concurrent field measurements have ever been attempted with the 5-CRD.

By contrast, the CNRS-CRD has undergone intercomparisons within the SAPHIR chamber before for NO_3 (Dorn et al. 2013) and N_2O_5 (Fuchs et al. 2012) as well as similar field data comparisons between NO_3 mixing ratios between CRD and LP-DOAS techniques (Steven S. Brown et al. 2007). The NO_3 intercomparison campaigns reported in Dorn *et al.* and Fuchs *et al.* were considerably larger in scope compared to this evaluation, featuring a variety of instruments and measurement techniques (seven for NO_3 , five for N_2O_5) including several cavity techniques (pulsed, off-axis, broadband), Laser induced fluorescence (LIF), DOAS, and cavity enhanced absorption. For NO_3 , the CNRS-CRD in the previous intercomparison reports a range of linear regression slopes between 0.91 – 1.18 (mean: 1.04) in the absence of aerosol and 0.85 – 1.34 (mean: 0.99) with seed aerosol addition. While the upper and lower limits to the slopes presented here were somewhat larger (0.85 – 1.35 in the gas phase; 0.77 – 1.43 with seed aerosol) the means are comparable (0.95 in the gas phase; 1.07 with seed aerosol). The median coefficient of determination during this campaign was 0.981 similar to the 0.96 determined for this work. The N_2O_5 intercomparisons report a linear regression slope range of 0.67 – 1.30 which is nearly identical to the 0.71 – 1.39 observed during this campaign. The reported R^2 values are also similar with a median value of 0.96 for the 2007 campaign compared with 0.97 reported for this campaign.

6.3.4 Conclusions

Multiple measurements of NO_3 and N_2O_5 allowed for a complete set of data to cover the entire 2018 SAPHIR NO_3 +Isoprene campaign. Where possible, these measurements allow for the generation of an accurate, harmonized dataset for use in further analysis related to this campaign. Where data was missing or otherwise flawed the multiple measurements allowed for gaps in the dataset to be filled, either with direct observations or indirectly, i.e. calculation of NO_3 via N_2O_5 , NO_2 and $K_{\text{eq}}(\text{T})$. In general, the measurements agreed with each other within the combined uncertainties of the instruments, in addition to the ratio $[\text{N}_2\text{O}_5]/[\text{NO}_3]$ predicted via the equilibrium calculation. Linear regression analysis of the revealed slopes close to unity and high coefficients of determination, particularly on experiments where both datasets overlapped with $K_{\text{eq}}[\text{NO}_2]$. Compared with previous intercomparisons, where possible, the 5-CRD performed better under a range of conditions compared with LP-DOAS measurements from NO_3 field data. The CNRS-CRD performed approximately the same as previous intercomparisons in the SAPHIR

chamber for both measurements of NO_3 and N_2O_5 . Initial disagreements between the instruments highlight the usefulness of intercomparisons for the purposes of instrumental troubleshooting and show the difficulty of measuring a radical trace gas in the presence of polar organic trace gases. These results suggest the state of the instrumentation used to detect the nitrate radical and its equilibrium partner, while accurate, have either not, or only modestly, improved since the 2007 intercomparison campaigns.

7. Organic Nitrates during the SAPHIR campaign

In this chapter, the results of the data analysis following measurements of organic nitrates (RONO_2) during the 2018 SAPHIR campaign are discussed. For analysis of the NO_2 , NO_3 and N_2O_5 measurements, see section 6.

7.1.1 Oxidation of Isoprene by NO_3

The 2018 SAPHIR campaign studied the reaction of Isoprene (C_5H_8) with NO_3 with in a series of controlled chamber experiments, with varying inputs of NO_2 , O_3 , Isoprene and others. In the presence of isoprene, NO_3 attacks the electron-rich double bond system resulting in an addition reaction and forming an alkyl nitrate functional group in a nitrooxy peroxy radical. The fate of this RO_2 radical is dependent on the conditions and will form suite of different organic products in the presence of NO_3 , HO_2 and other RO_2 , leading to mostly stabilized alkyl nitrate molecules but also organic products where NO_2 is ejected, particularly carbonyls. The 5-CRD is able to detect ΣANs via thermal decomposition and thus, the aims of these experiments with respect to the 5-CRD were to use the accurate isoprene data generated from an intercomparison similar to those completed for NO_2 and NO_3 in section 6 to can calculate the gas phase yield of this reaction and assess its sensitivity on the conditions of the experiments.

7.2.1 Detection of Isoprene Nitrates via TD-CRD

As detailed in section 2, there are many products of the NO_3 -Isoprene reaction scheme that can generate a relatively stable (i.e. with a lifetime long enough to sample) alkyl nitrate (AN) molecule. ANs, for the purposes of the analysis which follows, are defined as organic trace gases containing the RONO_2 functional group which dissociate to NO_2 when heated. The 5-CRD detects the sum of all organic nitrates ($\Sigma\text{ANs} + \Sigma\text{PNs}$) molecules at 690 K, together with all ambient gas-phase NO_2 and all NO_2 thermally derived from trace-gases which dissociate at temperatures lower than this, such nitryl chloride (ClNO_2) and dinitrogen pentoxide (N_2O_5). ClNO_2 was not expected to appear in this campaign lacking any obvious source, as ClNO_2 is liberated from chloride and nitrate containing particles. Peroxy nitrate species (RO_2NO_2) are formed by the interaction of RO_2 with NO_2 , but are generally considered unimportant as this reaction is highly reversible, as the $\text{RO}_2\text{-NO}_2$ bonding group is thermally unstable and quickly returns to the reactant trace gases.

690 K had been set as the new oven temperature of the ovens following a rebuilding of the ovens due to damage (rusting of components) sustained during the AQABA campaign. This temperature was significantly higher than the previously set temperature of 648 K but was determined in exactly the same manner as the previous temperatures, with laboratory thermogram experiments with iPN (section 3). This temperature would later be reduced down to 650 K following a calibration experiment during the SAPHIR campaign on 8/17 where iso-butyl nitrate (iBN), a direct analogue of iPN, was injected into the chamber. The comparison between the iPN and iBN thermograms suggest that the iPN source used for previous calibrations may have become contaminated over time, perhaps by conversion to HNO_3 , leading to a broadening of the thermogram and demonstrates the importance of regularly checking transmission of calibration sources.

7.2.2 Detection of 'PANs' at 448 K

The 5-CRD, described in detail in section 3, has two heated channels for detection of TD-derived NO_2 from, primarily, ΣPNs at 448 K and ΣANs 690 K. Peroxyacyl Nitrates ($\text{R(O)O}_2\text{NO}_2$) are more stable than the PNs

and while nighttime sources of PAN are known (Hanst 1971), these are not expected to contribute strongly to the products of the nighttime NO_3 + Isoprene system, as precursors to PAN (e.g. primary carbonyls) are produced in too small yields on the timescales of these experiments (3 – 7 hours), while other precursors such as acetone, MGLY or others, even if produced in significant amounts out of the NO_3 + isoprene scheme, require direct photolysis or oxidation with OH (indirect photolysis) in order to produce the $\text{R}(\text{O})\text{O}_2$ radical required to give a stabilized PAN molecules. Ozonolysis may supplement this by producing methacrolein and other RO_2 radicals, which may go on to form PANs in the presence of NO_x , however the reaction of isoprene with O_3 must compete with NO_3 , which has a far larger rate coefficient with isoprene, leading to larger loss rates. These may contribute significantly to the observed PNs signal towards the end of the experiments, when the isoprene has been consumed, with numerical simulations suggesting this may contribute 300 – 400 of PAN at the end of an experiment (with ~ 3 ppb isoprene).

However, on several occasions a large difference (up to 5 ppb) was detected between the room temperature NO_2 channel and the 448 K PNs + NO_2 channel (Figure 45).

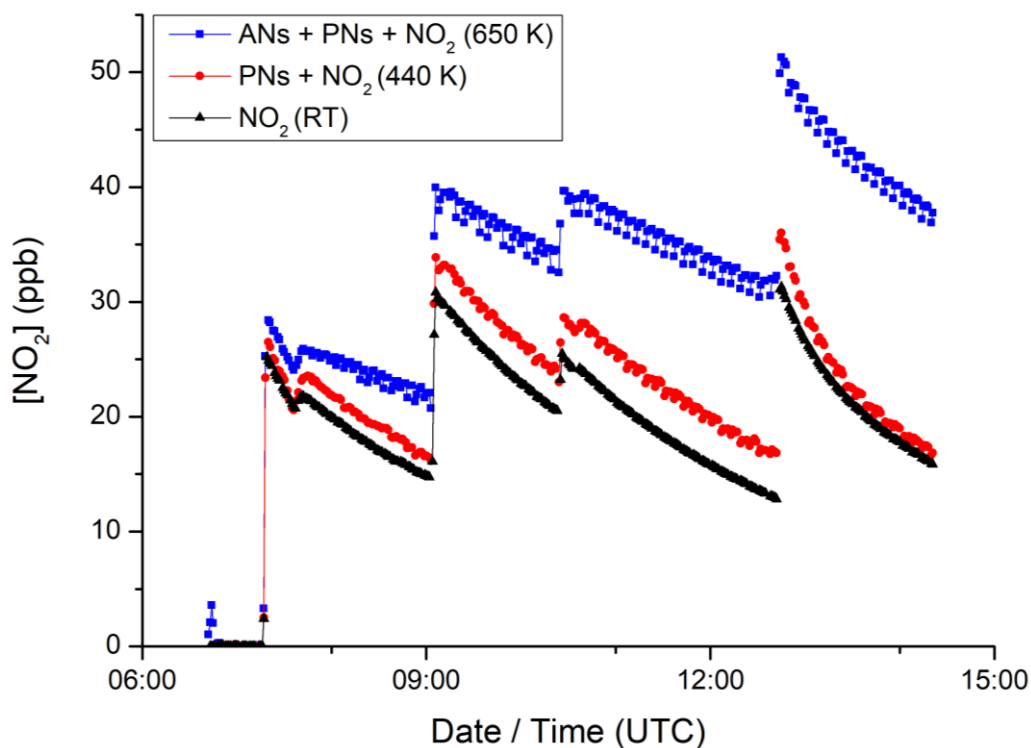


Figure 45. Corrected data from the experiment on the 8th August (100 ppb O_3 , 25 ppb NO_2 , 10 ppb Isoprene) showing a large difference between the NO_2 (black) and the PNs + NO_2 (red) signals. RT = Room Temperature.

This signal suggests that significant amounts of some trace gases were able to dissociate into NO_2 under operational conditions in this set-up. Below, several explanations for this phenomenon are posited.

7.2.3 Nighttime generation of PANs.

Nighttime formation of precursors to PANs are known to occur as a result of H-abstraction by NO_3 of primary, carbonyl group (RCHO) containing molecules:



In the presence of NO_2 , these can undergo addition reactions to form PAN:



This mechanism requires the generation of sufficient PAN precursors (e.g. aldehydes, RCHO) from a wholly nighttime chemical mechanism. The immediate precursor molecules to PAN and PAN analogues include acetaldehyde (44% of global PAN source), methylglyoxal (30%), acetone (7%) and the combined sum of all other isoprene and higher terpene oxidation products (19%), according to (Fischer et al. 2014). This suggests, as some of the direct precursors of PAN are formed by the oxidation of isoprene, that isoprene degradation therefore involved in ~37% of global PAN formation. Thus while the NO_3 -Isoprene system is clearly important to formation of PNs in the longer term, i.e. when looking at PAN formation on the scale of days within diurnal cycles, it is less important in the context of these several hour long chamber experiments with limited or no exposure to sunlight, and controlled chemical compositions.

From the NO_3 -Isoprene MCM mechanism (Jenkin, Young, and Rickard 2015) (shown in section 2), for instance, the most common non-nitrate aldehyde product, according to product studies of the reaction is methacrolein ($\text{C}_4\text{H}_6\text{O}$) with a product yield of ~2 – 3% (Perring et al. 2009; Schwantes et al. 2015; Rollins et al. 2009; Kwan et al. 2012). This implies that the isoprene injections seen in Figure 45 (10 ppb of Isoprene) one should expect ~200 – 300 ppt of methacrolein. Even if all this methacrolein was to react with NO_3 to form PAN or the methacrolein PAN (MPAN) analogue, this would be still far smaller than the observed difference between the NO_2 and $\text{NO}_2 + \Sigma\text{PN}$ channels. Further, when considering the short thermal lifetimes of PAN and other PNs, $\tau(\text{MPAN}) = \sim 48$ min; $\tau(\text{PAN}) = 50$ min at 298 K, (Finlayson-Pitts and Pitts Jr. 1999), mixing ratios of PANs should be reduced as they decompose back to R(O)O_2 radicals and NO_2 over the course of a six-hour (or longer) experiment in the relatively warm chamber.

In field studies, MPAN has been measured in rural areas where isoprene is present but generally lags several hours behind observations of methacrolein, which has been produced by NO_3 induced oxidation of isoprene at night, following sunrise and subsequent OH processing (Bertman and Roberts 1991) the next day. Note that the rate coefficient of methacrolein with NO_3 is also quite small ($k_{\text{methacrolein}} = 3.4 \times 10^{-14} \text{ cm}^3 \text{ molecule}^{-1} \text{ s}^{-1}$ at 298 K (Chew, Atkinson and Aschmann 1998)) which is an order of magnitude lower (x20) than the rate coefficient of NO_3 with isoprene, and it must also compete with other NO_3 reactions when isoprene has been depleted (such as the oxidation of the second double bond on isoprene) and many of these rate coefficients are not well described in the literature and are possibly larger than $k_{\text{methacrolein}}$. As such, one would expect that as this product is generated from isoprene in a small yield and has a smaller rate coefficient this would be seen in the experiment as an increase in the ΣPNs signal only after a period of time where significant isoprene (nearly all) has already been reacted away. The data in Figure 45 shows that this generation happens nearly immediately after injection of isoprene to the system and correlates strongly with the increase seen in the ANs cavity, which would not be expected (nor possible) in the PAN generation mechanisms described above.

While generation of other primary carbonyl containing carbon molecules (RCHO) is expected, looking closely at Figure 45 we can see that during the first injection of 10 ppb isoprene (between 06:00 – 09:00 UTC) that supposed PN generation by the point that most isoprene is consumed, approximately 2 – 3 ppb has been formed compared with 4 – 6 ppb of AN. This would imply the yield of PN from isoprene oxidation is between 20 – 30% while the yield of AN would be also 20 – 30%. This is extremely unlikely; it would

require the immediate generation of many high yielding PAN precursors, contrary to the current understanding of the mechanism, of which one of the largest expected (methacrolein) contributes only 300 ppt, while the formation of alkyl nitrate molecules would be far smaller than what has been observed in chamber experiments in the past. For these reasons, while generation of PANs is possible under the NO₃-Isoprene system, the mixing ratios observed do not line up with expectations in a reasonable way and therefore it is most unlikely that 'real' PANs were not the cause of the phenomenon.

7.2.4 Surface Catalyzed breakdown of ANs

The 5-CRD system uses quartz-glass ovens to measure organic nitrates using the thermal dissociation method, based on assumptions and characterizations of these ovens in how they respond to molecules chosen to be representative of PNs and ANs passing through them. A more detailed description of the TD-Method employed by the 5-CRD is available in section 3 but in short, the oven temperatures are set based on how high the set temperature of the heating element is required in order to dissociate a source of Peroxyacetyl nitrate (PAN, for PNs) or isopropyl nitrate (iPN, for ANs) until no more signal (NO₂) can be achieved. In order to prevent recombination, or other radical chemistry which would bias the downstream NO₂ measurement, the oven design includes a section filled with 400 – 600 μm glass beads, sitting on top of a fritted-glass section – both of which increase the surface area of the walls of the oven. It is possible that organic nitrate species derived from BVOC species like isoprene may undergo surface-catalyzed reactions on the glass beads. (Thieser et al. 2016) observed what was presumed to be a catalytic effect on the breakdown of PAN and iPN when using glass wool in a similar TD-CRD system, a finding also reported by (Sobanski, Schuladen, et al. 2016) on the 5-CRD. This finding by Sobanski *et al.* could not be replicated upon replacement of the glass wool with the glass beads, leading to the assumption that if the effect did not occur for iPN nor PAN, then this was likely representative for all PNs and ANs. These results then, may suggest that this assumption does not hold true for isoprene nitrates and perhaps other BVOC-derived organic nitrates.

The glass-surface catalysis theory is somewhat undermined however, by an experiment performed during the SAPHIR campaign (8/15, 100 ppb O₃, 25 ppb NO₂, 10 ppb Isoprene, Seed Aerosol, 60% RH) wherein a relative thermogram (Figure 46) between the two heated channels was taken, without the glass beads in the ΣPNs 448 K oven. The results of this thermogram showed that there was a constant rise in signal between 433 and 690 K suggesting that either catalysis was not a major factor in these findings, or that the glass surfaces which remained, including the oven walls and the fritted glass section built into the ovens, possessed a sufficient surface area to achieve the catalytic effects.

7.2.5 Thermal Dissociation of Alkyl Nitrates at T < 690 K

The underlying principle of the 5-CRD, and other TD instruments, for measurement of organic nitrate species, such as PNs and ANs, is that there exists a clear temperature step between these two classes of molecules such that other molecules which dissociate to NO₂ (e.g. N₂O₅, ClNO₂) when heated can be independently measured and then subtracted from this, giving the total concentrations of PNs and ANs. Many TD-CRD or TD-LIF instruments work according to this principle e.g. (Womack et al. 2017; Sobanski, Schuladen, et al. 2016; Thieser et al. 2016; Day et al. 2002). It has mostly been observed thus far that TD-yields of NO₂ follow a pattern where, due to the weaker bonds in the R(O)O₂NO₂ functional group, all PNs reach maximum yields before significant NO₂ is detected from ANs. Likewise, most NO₂ yields from ANs max out before significant signal is detected from HNO₃ or particulate nitrates, although large conversions, e.g. of HNO₃, have been observed in the past at 648 K (Wild et al. 2014).

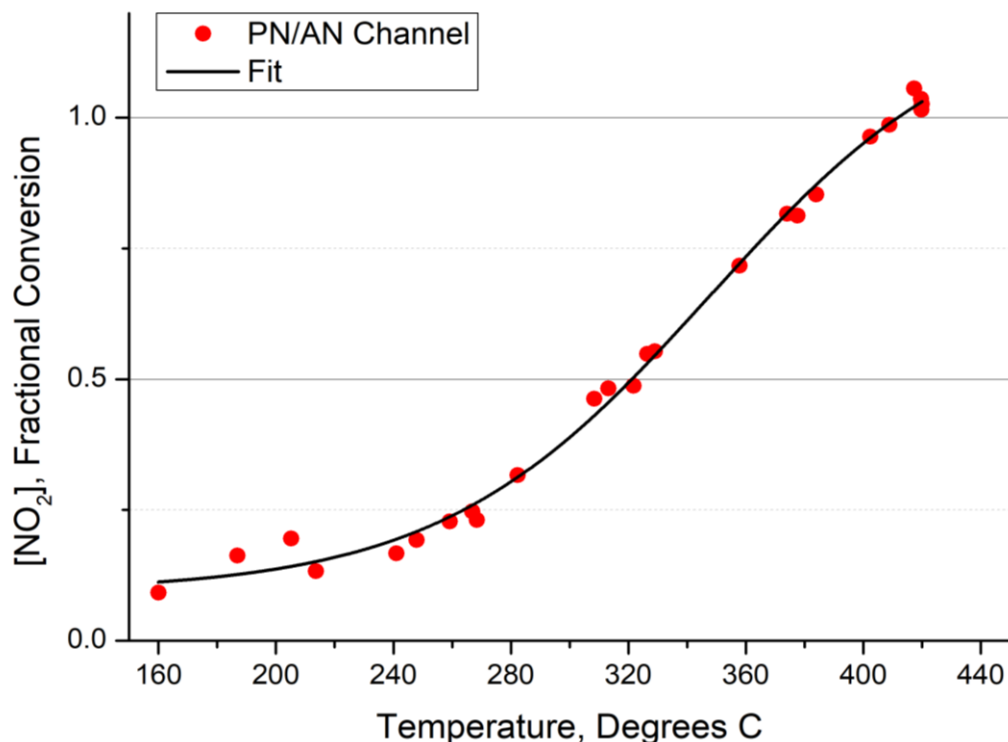


Figure 46. Relative thermogram of signal in the PNs + NO₂ channel vs. the ANs + PNs + NO₂ channel taken during the NO₃-Isoprene experiments. PN channel was taken without the glass beads described in section 3 and 7.2.5.

Figure 46 shows the results of a relative thermogram, that is the fractional conversion of NO₂ in one channel (Σ PNs + NO₂) vs. the hottest (Σ ANs + Σ PNs + NO₂) channel, over a range of set temperatures of the oven. Based on the results of the laboratory thermograms presented in Figure 11 (section 3) at 160 °C, a temperature which should be within the PNs plateau but well short of ANs conversion, it can already be seen that ~10% conversion has been achieved. As the temperature is increased the yield increases without ever reaching a plateau even up to 420 °C, the set temperature for the Σ ANs channel at the beginning of the SAPHIR experiments. At this temperature, the relative yield of NO₂ > 1, suggesting that for the 5-CRD under the SAPHIR experimental conditions even 420 °C was not high enough to dissociate all ANs generated by the NO₃-Isoprene system; however as previously noted in section 3, some small, reproducible losses of NO₂ have been observed, relative to the room-temperature NO₂ cavity, assumed to be as a result of catalytic removal from the gas phase by the glass beads (~5 % for the Σ ANs channel). As surface catalysis was posited as an explanation of the PANs signal, for this thermogram experiment the glass beads were removed from the oven. Therefore, it may be expected that the relative signal at the same temperature can exceed unity and it is noted that the difference between the two channels did not exceed 5% at the same temperature. It is however noteworthy that the fit of the relative signal does not appear to show any evidence of reaching a plateau up to 420 °C, a temperature chosen as well above the minimum required to reach the plateau in the previous iPN thermogram and suggests that the 5-CRD alkyl nitrates data may be under predicted (and PNs over predicted) both in these experiments and possibly in previous field experiments in environments dominated by biogenic emissions (Sobanski et al. 2017).

In order to understand this broad range over which the alkyl nitrate species appear to be dissociating over, it can be helpful to return to the NO₃-Isoprene schemes presented in section 2 (Figure 1, Figure 2, Figure 4, Figure 5). The 5-CRD, or any other TD-NO₂ instrument, detects NO₂ from the thermal dissociation of molecules with the functional group RONO₂. Thermal dissociation is based upon the energy required in order to overcome bond strengths between RO and NO₂, and these bonding energies are determined by the overall structure of the molecule. The NO₃-isoprene system generates a huge variety of variously functionalized organic products, many containing the RONO₂ group in various isomers and some containing more than one RONO₂ (dinitrates), the composition of which is subject to changes over time.

As the chemical structure of each of these products in the mix is different, it can be expected the bond energies in the RO-NO₂ bonding (nitrate ester) also vary. Bond lengths, therefore the energies required to break those bonds (e.g. by heating them), are not only influenced by the bonding atoms but also significantly by the R groups which surround them. While many of the nitrate ester bond dissociation energies and lengths are well-known, e.g. $\Delta H_{(iPN)} = 38.2 \text{ kcal mol}^{-1}$ at 473 – 698 K (Morin and Bedjanian 2016), several isoprene nitrates have yet to be investigated. It is generally well-known that the shorter the bond length for the same bonding atoms, the stronger that bond is (i.e. the higher the ΔH required to break it). (Zeng et al. 2007) showed in calculations that ΔH increased with increasing RO-NO₂ bond lengths in several, albeit not multifunctional, organic nitrate molecules, including dinitrates.

As none of these mechanisms for can fully account for the observed phenomenon of the NO₃-Isoprene PNs signal, the data analysis which follows was based on the assumptions that the vast majority of the non-NO₂ PNs signal was not caused by ‘real’ PANs or PNs, but was in fact NO₂ derived from ANs caused by some function of surface catalysis upon the high-surface area glass beads or the chemical bonding properties of isoprene nitrates which may decompose at significantly lower temperatures than the reference molecule, iPN. It is also assumed that in the hottest cavity of the 5-CRD does in fact measure the sum of all alkyl nitrates, as iPN is one of the strongest nitrate ester bonds known and therefore it is likely that isoprene-derived nitrate ester bonds should be weaker than this. If this assumption is not true, this will be seen in the analysis of alkyl nitrate yields per isoprene lost, which follows, as a systematically lower yield than other TD-NO₂ instruments.

7.3.1 Yields of Alkyl Nitrates

As previously stated, alkyl nitrates comprise many of the products in the isoprene reaction scheme as well as other products from rearrangements, decomposition and secondary reactions. As all organic carbon in the NO₃-isoprene comes from isoprene itself, the yield of alkyl nitrates can be defined in terms of isoprene lost over a given period of time:

$$\text{Yield} = \frac{\Delta AN}{\Delta \text{Isoprene}} \quad (\text{Equation 20})$$

With the yield (%) being the ratio of the change of AN over the change in isoprene (both ppt) over time. As the rate coefficient of NO₃ with isoprene is considerably faster than the rate coefficients governing most of the reactions describing NO₃ + isoprene products to give second-generation ANs, the function of the ratio of $\Delta ANs/\Delta \text{Isoprene}$ is expected to be linear. While the NO₃-Isoprene reaction is the main loss process of isoprene in the chamber, it is not the only one and this can bias the results and cause deviation from linearity. Isoprene is also consumed by reaction with O₃, wall losses and reaction with OH – relatively small concentrations of which are generated in the NO₃-isoprene reaction scheme. Similarly, the ANs produced in this system will undergo reaction with NO₃ and other oxidants which are generally

insignificant at the beginning of experiments and wall losses, which may or may not be significant depending of the specific chemical composition of the alkyl nitrate in question. Further, both isoprene and ANs will be consumed via the dilution effect of adding additional air into the chamber, however this should be the same for each molecule and cancel in (Equation 20). For isoprene, the combined effect of these additional, non-NO₃ loss processes were simulated in a box-model, allowing for a conversion of the isoprene PTR-ToF data into a dataset which describes the relative concentration of isoprene consumed by each above mechanism, constrained by the measurements of NO_x and O₃. The methodology of this model will be described in future publications elsewhere.

This isoprene consumed data (with respect to NO₃) can be compared to the production of ANs in a linear regression analysis to give the yields which can be compared against the experimental conditions (outlined in 6.2.1) to understand which factors (e.g. O₃ levels, RH, etc.), if any, have an influence on the yields.

7.3.2 Comparisons by experiment

Table 10. Alkyl Nitrate (ANs) yield per molecule isoprene and Alkyl Nitrate per molecule NO₂. NO₂ yields have been adjusted according to losses to the chamber walls via NO₃ and N₂O₅ estimated by (Dewald et al. 2020). N/A describes a situation where a yield could not be obtained.

Date	Experiment	Yield ANs per Isoprene	R ²
7/31	Reference NO ₃ (only 5 ppb NO ₂ / 100 ppb O ₃)	N/A	N/A
8/1	100 ppb O ₃ , 5 ppb NO ₂ , 3 ppb Isoprene	0.36 ± 0.28	0.09
8/2	Repeat 8/1	0.44 ± 0.23	0.66
8/3	100 ppb O ₃ , 5 ppb NO ₂ , 3 ppb Isoprene, 80% RH, Open Chamber (day-to-night)	N/A	N/A
8/6	100 ppb O ₃ , 5 ppb NO ₂ , 3 ppb Isoprene, 80% RH, Open Chamber (night-to-day)	0.94 ± 0.35	0.84
8/6	Injection 2	0.81 ± 0.35	0.93
8/7	50 ppb O ₃ , 5 ppb NO ₂ , 2 ppb Isoprene, 20% RH	N/A	N/A
8/8	100 ppb O ₃ , 25 ppb NO ₂ , 10 ppb Isoprene	0.87 ± 0.16	0.99
8/8	Injection 2	0.65 ± 0.11	0.97
8/8	Injection 3	0.89 ± 0.08	0.99
8/9	100 ppb O ₃ , 5 ppb NO ₂ , 3 ppb Isoprene, 100 ppb propene, 120 ppm CO	N/A	N/A
8/10	Repeat 8/7	0.71 ± 0.35	0.66
8/10	Injection 2	0.70 ± 0.14	0.39
8/12	100 ppb O ₃ , 5 ppb NO ₂ , 3 ppb Isoprene, 120 ppm CO, Open Chamber (night-to-day)	0.99 ± 0.36	0.96
8/12	Injection 2	1.11 ± 0.25	0.96
8/13	Repeat 8/8	0.62 ± 0.45	0.95
8/13	Injection 2	0.94 ± 0.05	0.99
Mean		0.77	0.72

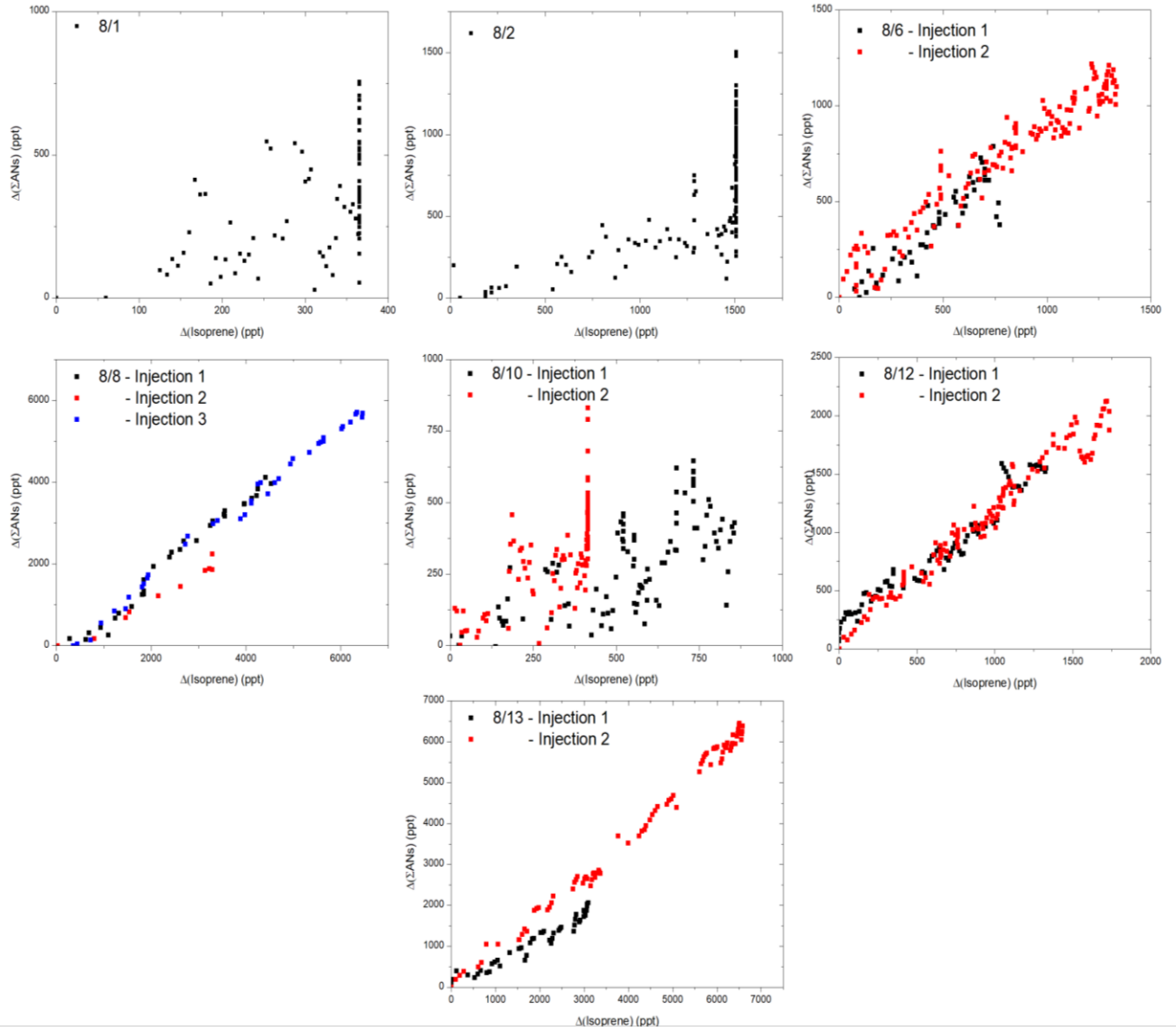


Figure 47. Change in AN vs. Change in isoprene for each evaluated experiment. Error bars excluded for clarity.

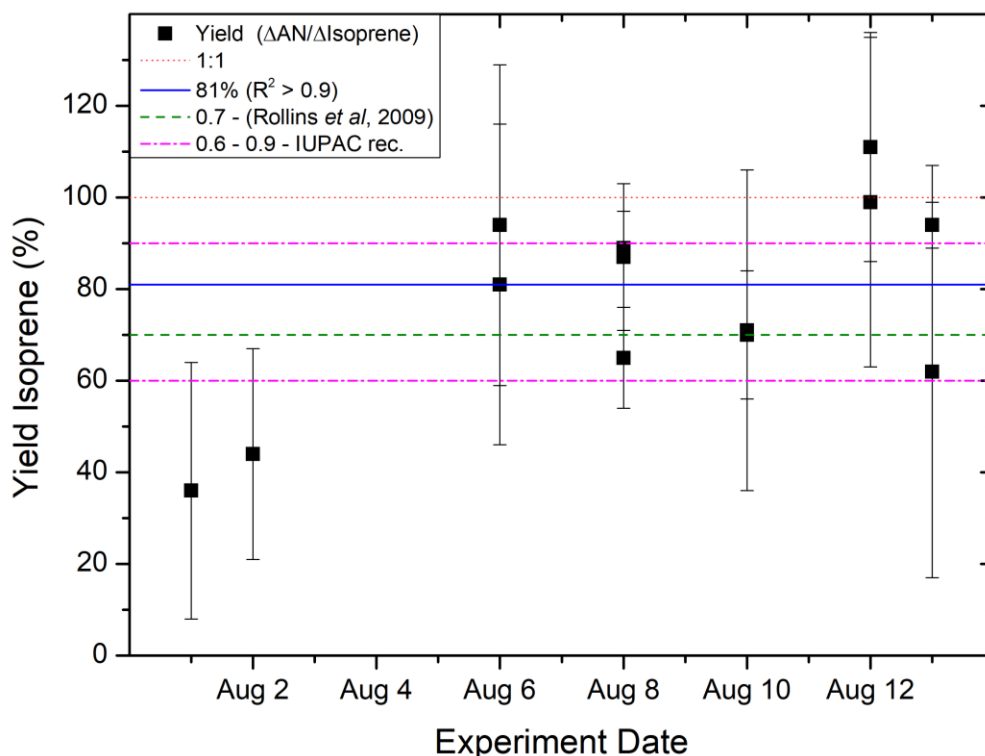


Figure 48. Yields of ANs per isoprene reacted with per experiment. Multiple data points for the same date represent multiple injections.

Table 10 reports the observed yields of AN from per molecule isoprene reacted when the chamber was closed and thus the where the main loss of isoprene expected is reaction with NO_3 . Observed yields of ANs were found to be extremely variable, ranging from 0.36 (8/2) to over 1.1 (second injection, 8/12) with a mean yield of 0.77 ± 0.22 and a mean coefficient of determination of 0.72. The standard deviation in this number reflects the statistical variability observed on a day-to-day basis (and sometimes even injection-to-injection during the same experiment, e.g. 8/13) and not the uncertainty in yield calculations, shown in Figure 48, which was considerable. The uncertainty in the yields were generated by estimating the upper and lower limits of the gradients in a linear regression analysis, defined by weighting the ΔANs data in the y-axis by the concentration-dependent errors propagated from uncertainty in the ΔANs calculation (including uncertainties in the NO_2 and $\text{NO}_2 + \Sigma\text{PNS} + \Sigma\text{ANs}$ signals) and $\Delta\text{Isoprene}$ signal (defined only by the uncertainties in the concentrations of both isoprene and NO_3 and the relevant rate coefficient k). This error therefore represents a lower-limit as the change in ANs assumes that all RONO_2 formation occurs as a result of isoprene oxidation, an assumption which becomes less valid towards the end of an injection as the isoprene has been consumed and new RONO_2 products start to be formed from oxidation of isoprene products. This may explain the data shown in Figure 47 where several experiments, such as 8/1, 8/2 and the second injection during 8/10 where distinct, sharp increase (vertical lines) of up to 500-1000 ppt can be seen at the end of a linear covariance relationship between ΔANs and $\Delta\text{Isoprene}$.

The relatively low mean R^2 suggests that for several experiments the dependence of ΔANs on $\Delta\text{Isoprene}$ was quite low, therefore the resulting function in the regression analysis was not very linear, in contrast to the expectations outlined above. Several of the low R^2 values were associated with low yields,

particularly 8/1 and 8/2, as shown in Figure 47. If only slopes with high R^2 (> 0.9) are chosen, the mean yield rises to 0.81 ± 0.17 . Both the evaluated average yield for all experiments and the yield derived from highly linear function yields are generally in agreement with previous studies of this reaction which have reported yields in the range of 0.65 – 0.8 (Rollins et al. 2009; Schwantes et al. 2015; Perring et al. 2009; Kwan et al. 2012; Barnes et al. 1990) while, if the upper and lower limits on each yield are considered, all yields may fall within the current recommended IUPAC ranges (0.6 – 0.9) which gives additional evidence that the yield falls within this range. While consistency with previous determinations is favorable, the SAPHIR campaign sought to test the effects of different experimental conditions, such as relative concentrations of NO_2 , O_3 , isoprene; relative humidity; or HO_2/RO_2 chemistry by introduction of other trace gases such as CO on the product distribution and yields of the NO_3 + isoprene reaction, including the total yield of ANs. The ANs data presented here are too uncertain to make an accurate, quantitative determination of this question other than that high yields are possible under a range of the tested conditions.

7.3.3 Technical issues in ANs measurements

The high uncertainties, and thus presumably the high day-to-day variability in the calculated yields reflect uncertainties on error corrections applied to the NO_2 , NO_3 , ΣANs and isoprene concentrations. In the case of both isoprene, NO_2 and NO_3 independent measurements of these trace gases were made by multiple instruments during the SAPHIR campaign which were used to generate harmonized datasets as described in section 6. Moreover, the isoprene measurements broadly agree with other datasets such as the NO_3 reactivity cavity ringdown which directly measures the sum of gas-phase losses of NO_3 . Through the $k(\text{NO}_3)$ dataset, modelling reconstructions of the observed NO_2 , O_3 , NO_3 , N_2O_5 and isoprene were shown for several experiments in (Dewald et al. 2020). Together, these observations imply that there were issues in the method used to detect ANs and indeed a large contribution to the total uncertainty propagated into the yield was due to the uncertainty associated with the subtraction of the ambient temperature NO_2 signal from the NO_2 + PAN + AN cavity channel when the difference between the two channels was close to the ANs limit of detection. In the data presented above, this can be seen in the fact that the yields associated with the later part of experiments, or on days with high NO_3 /Isoprene, the total uncertainties in the calculated yields are considerably smaller than in other experiments, as the ANs signal is much larger. The ANs LOD was difficult to define due to technical difficulties with the mass flow controller unit which introduced fluctuations in the flow rate through the cavity of up to 5%. These fluctuations were not observed in either the ΣPNs nor NO_2 cavities, only significantly affecting the ANs cavity where the flow rate (default setting 2100 sccm) would decrease between 50 – 100 sccm in a regular, approximately half an hour cycle, though the severity of the fluctuation was also variable on a day-to-day basis. The decreased flow rates consequently lead to changes pressure and temperature within the cavity and oven, and an increased residence time throughout the cavity. These effects largely went unnoticed during the campaign and have been addressed by increasing the ΣANs LOD by an equivalent NO_2 signal based on the Rayleigh scattering constant of NO_2 at different pressures described by (Thieser et al. 2016). The pressure difference compared to the pressure at 2100 sccm flow rate was typically on the order of $\sim 4\text{-}5$ torr, leading to a ~ 200 ppt increase in the ANs LOD.

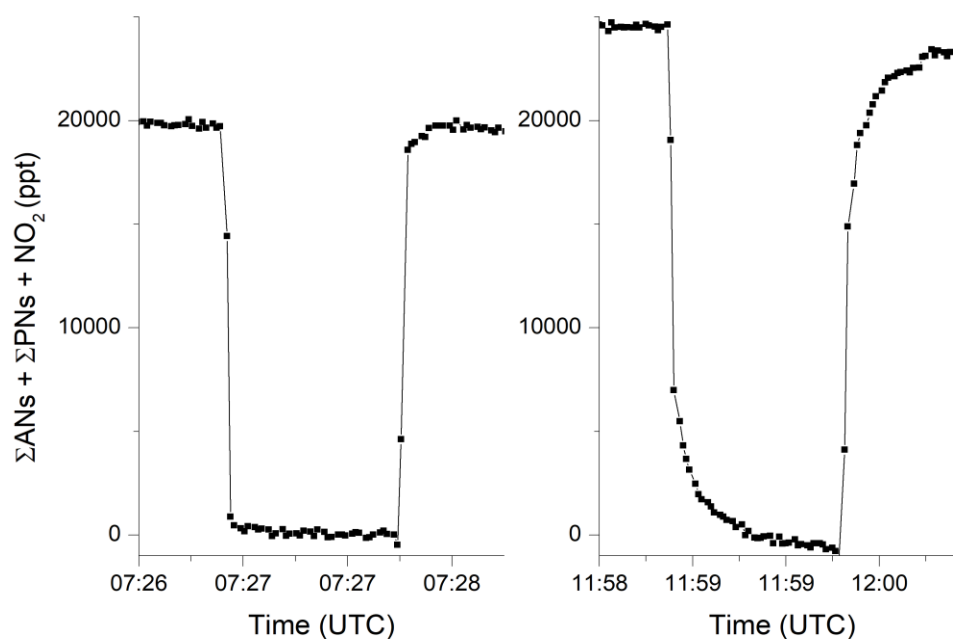


Figure 50. Raw alkyl nitrates before (left) and after (right) an injection of isoprene for a gas-phase experiment (8/8). The right side shows a significantly longer period of time for the slope to approach 0 ppt during a zeroing period, and significantly longer to return to the overall experimental trend after a zeroing period after exposure to isoprene nitrates compared with the signal earlier in the experiment.

Figure 50 shows another issue with the measurement of ANs which clearly impacted the evaluation of the LOD and uncertainty, related to issues in the zeroing method of the 5-CRD, which works by flooding the cavity with dry, low- NO_x containing zero air. As residence time in entire 5-CRD system, from the point of sampling to the exhaust of the cavity, is ~ 3 seconds. This implies the time taken to reach the baseline signal (set to 0 ppt), or return to full measurement after a zeroing period, should both take ~ 3 seconds. The left of Figure 50 compares the zero signal at the beginning of an experiment (8/8) where no isoprene has yet been added into the chamber; the right side shows several hours later where significant mixing ratios of ANs had been formed. Before the addition of isoprene and subsequent formation of ANs, the zero signal approaches the baseline at a much faster rate (seconds) compared with later in the experiment, where both the approach to zero and return into the larger experimental trend show a curved function which occurs on a significantly longer (minutes) time scale. These build-up and decay patterns are characteristic of absorption and desorption equilibria and are likely a result alkyl nitrates interacting with the surfaces of the 5-CRD. These apparent equilibria caused difficulty in experiments, particularly in high-isoprene conditions, in determining the instrument LOD, defined as the (average) difference between one zeroing period to the next. Many non-stable zeroing data points, which is to say zero data points which were still seeing the influence of $[\text{NO}_2]$ desorption and consequently had a visible slope to the data, needed to be discarded thereby increasing the statistical variability per zero. An attempt to nullify this effect was by making zeroing periods longer, from 20 seconds up to 1 minute, though despite this the calculated LOD using the consecutive zeroes method was considerably larger than in the laboratory or in previous deployments of the instrument, averaging ~ 300 ppt throughout all experiments from 8/1 to 8/13. Applying the additional error evaluated from the earlier described pressure fluctuations,

a value of ~500 ppt LOD is determined for the Σ ANs cavity. Note that previous deployments of the 5-CRD in field campaigns have not observed this effect in the PNs or ANs signals before, during either the AQABA campaign nor in past measurements in the rural environments where BVOC oxidations were prevalent studied in (Sobanski et al. 2017) during the previous PARADE and NOTOMO campaigns. This suggests this problem may be linked to solely to isoprene nitrates or some other issue(s) caused by the set-up of the chamber experiments.

Isoprene-derived nitrates are asymmetric molecules which contain many functional groups such as hydroperoxy (-OOH), nitrooxy (-ONO₂), carbonyl (C=O) or hydroxyl (OH). These groups are electron-dense relative to the molecule's carbon skeleton and thus determine a molecule's overall electric dipole moment, where electric charge is distributed unevenly across a molecule. A consequence of this is that it is possible for isoprene nitrates, through these electric dipoles, to adhere to the surfaces of the 5-CRD. Carbonyl and nitrooxy groups are frequently sampled into the 5-CRD as part of characterization tests such as the thermograms, where isopropyl nitrate (C₃H₇NO₃) or PAN (C₂H₃NO₅) are sampled into the instruments in ppb-level concentrations, comparable to the concentrations observed into the chamber experiments. This implies that the electric dipoles seen in these types molecules are not enough under typical operating conditions and concentrations to have a perceivable effect due to interactions with the instrument's perfluoroalkyl (PFA) tubing. Isoprene nitrates contain multiple functional groups, compared to the mono-functionalized iPN or PAN, including the hydroxyl and hydroperoxy hydrogen bond donor groups. It is not clear exactly where on the PFA tubing these groups could interact with, as the structure of PFA is a polymer with a repeating carbon chain, saturated with fluorine atoms and a branching -OCF₃ group. Perfluorinated alkyl polymers such as PFA or other polytetrafluoroethylene (PTFE) derivatives contain numerous strong C-F bonds leading to an even distribution of charge across the molecule and a low dipole moment, which results in the well-known properties which makes them useful for tubing applications: they are generally inert, have high thermal stability, low friction and low permeability. (Yeh and Ziemann 2015) note that a possible bonding site exists in the spaces between the alkoxy chains while a study of the gas-wall partitioning in (Deming et al. 2019) observed when sampling functionalized gas-phase organics including aldehydes, ketones and alkenes (all present in isoprene nitrates), a relatively small, non-humidity dependent delay occurred in various PTFE-derived tubing types, including PFA. (Z. Zhu et al. 2012) found at least 3% relative reduction in the concentration of gas-phase ammonia, itself a strong hydrogen bond donor, caused by adsorption on to the surfaces of several types of tubing, including PFA. In principle this effect could be corrected for, but in practice this would require a detailed understanding of the evolution of isoprene in the presence of NO₃, including the relative concentrations of each product and all of their interactions with PFA and each other for the purposes of displacement of one species for another on the bonding sites of PFA.

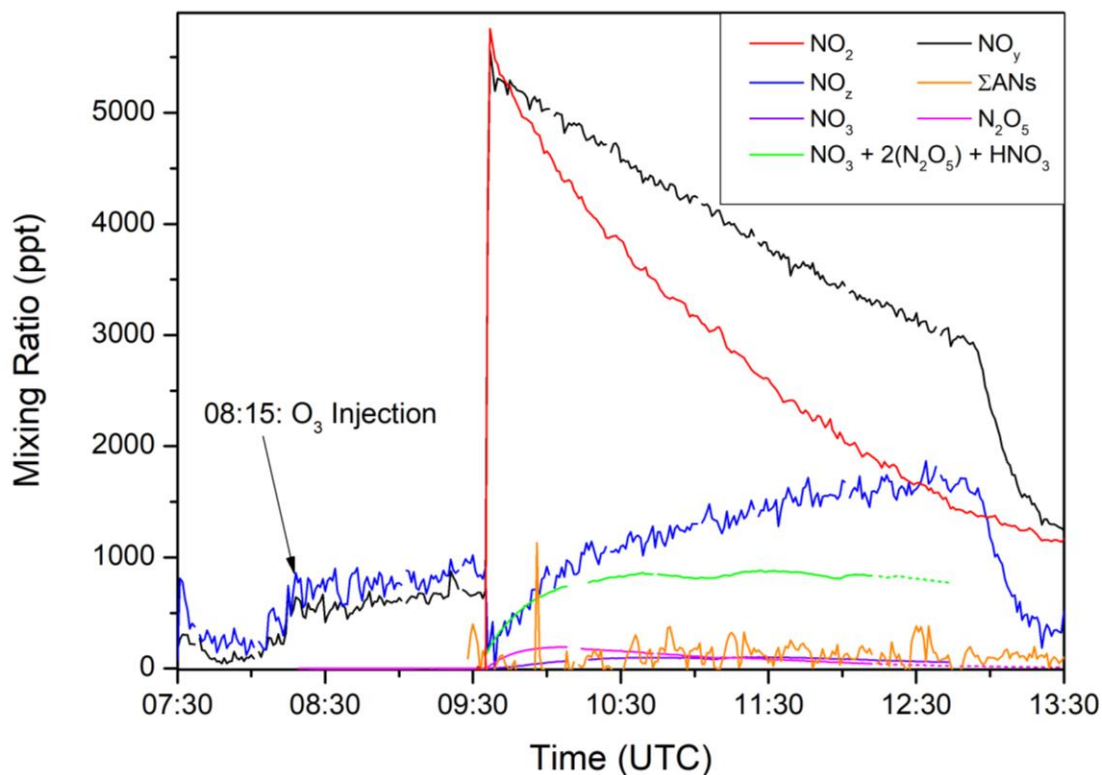


Figure 51. Selected trace gases from the experiment 7/31. No isoprene was injected in this experiment.

In several of the experiments listed above, including those with high mixing ratios well above the ANs limit of detection with high R^2 values showed large yields, most evident in the experiments on 8/12 where the yields either approached or exceeded unity. While this is most likely due to the uncertainties discussed above, a possibility exists of an alternative source of nitrogen which may be detected in the ANs channel, which would positively bias yields and thus the calculations presented above may represent an upper limit to the true yields. To investigate this possibility, Figure 51 shows selected reactive nitrogen trace gases from the experiment completed on 7/31. This experiment was unique in that NO_3 was generated by reaction of NO_2 and O_3 but no isoprene was injected, thus it can be used compare the signals of individual trace gases to the total NO_z ($\text{NO}_z = \text{NO}_y - \text{NO}_x$). From the thermograms discussed before, the signal observed in the ANs channel is expected to be a combination of injected NO_2 ; NO_2 from all dissociated organic nitrates, of which there should be none in this experiment; and NO_2 from the first thermal decomposition from N_2O_5 . These assumptions of NO_2 detection appear to be consistent to the ΣANs signal (orange line) in Figure 51, which remains at the detection limit (~ 300 ppt for this experiment). Note that the entire N_2O_5 signal (pink, ~ 200 ppt max) is lower than this. The green data points, which show a combination of the measurements of HNO_3 , $2x \text{N}_2\text{O}_5$ (as two NO_2 molecules are required to give one molecule of N_2O_5) and the NO_3 radical. The measurements show that there is approximately 700 ppt of HNO_3 in the chamber, when the peak N_2O_5 signal is observed ($\sim 10:00$ UTC). Assuming the second dissociation of N_2O_5 (and NO_3) is not observed, this would require $\sim 14\%$ of the HNO_3 to be detected in the ANs channel to raise the signal above the detection limit, which can be described as the upper limit during SAPHIR. It is likely however that that less than this is observed, based on the arguments provided in in section 3 where (Sobanski, Schuladen, et al. 2016) determined that the upper limit to HNO_3 decomposition in the 5-CRD ANs oven was $\sim 0.5\%$, though as the oven temperatures have been adjusted since this

characterization it is conceivable that a higher conversion efficiency of HNO₃ now exists, as the set temperature of the oven was higher than the original instrument operating parameters (375 °C vs. 420 °C), though evidence of significant HNO₃ decomposition had not been observed during previous field deployments (e.g. during AQABA), consistent with the findings by Sobanski *et al.*

The thermal decomposition of NO₃ is another potential source of detectable NO₂ in the system, although the radical itself is likely to experience large losses on the surfaces of the tubing, filter and ovens in the 405 nm cavities, particularly as the flow rate is significantly lower (~ 7 SLM vs. 40 SLM) than the sampling line in the 662 nm channels, and wall losses of NO₃ are exponential with time. This means that the only source of NO₃ at the ANs cavity like comes from the thermal decomposition of N₂O₅ in the oven, which may then go on to generate NO₂. However the unimolecular decomposition of NO₃ has been generally observed to proceed via the generation of NO and molecular oxygen (Johnston, Cantrell, and Calvert 1986), as this reaction would be thermodynamically favored compared to the alternative generation of NO₂ and an O atom, though small contributions of this branch are thought to occur (Graham and Johnston 1978). As the 5-CRD does not detect NO, this would not likely result in any perceivable increase in the ANs signal, even at 100% efficient decomposition of the N₂O₅.

These observations suggest that the high yields observed in Table 10 are not a result of HNO₃ or the thermal decomposition of NO₃ but rather the result of uncertainty or perhaps some other systematic error. If the error is systematic, one clue as to the high yields may also be visible in the NO_y and NO₂ data in Figure 51, at 08:15 UTC there is an unexpected increase in reactive nitrogen compounds (~1000 ppt) when O₃ is injected into the chamber, suggesting another source of nitrogen besides the NO₂ injections. This unassigned NO_y is larger than the sum of all HNO₃, N₂O₅ and NO₃ in the chamber. Although it appears as though this nitrogen compound is not seen significantly by the ΣANs channel of the 5-CRD, without positive identification, it is not possible to predict how this may influence later experiments using isoprene may react.

7.3.4 Discussion

Table 11. Summary of NO₃ + Isoprene yields and the methods used to derive them.

Work	Method	Chamber Size	Yield	Notes
(Barnes et al. 1990)	FT-IR	40 L	~80 ± 20%	Inferred from RONO ₂ IR spectra
(Rollins et al. 2009)	TD-LIF	SAPHIR (270 m ³)	70 ± 8%	Model fit of ΣANs experimental data
(Perring et al. 2009)	PTR-ToF-MS	28 m ³	65 ± 12%	Sum of isoprene, C-containing products
	TD-LIF		70 ± 10%	ΔANs vs. ΔIsoprene
(Kwan et al. 2012)	GC-FID	28 m ³	85 ± 5%	Sum of isoprene, C-containing products
	Nitrogen Balance		~80%	Inferred from NO ₂ losses / consumption of N ₂ O ₅
(Schwantes et al. 2015)	ToF-CIMS	24 m ³ / 1 m ³	76 ± 15%	Method not stated
This work	TD-CRD	SAPHIR (270 m ³)	77 ± 22%	ΔANs vs. ΔIsoprene
	High R ²		81 ± 17%	

Table 11 details the findings of several studies which have addressed the question of $\text{NO}_3 + \text{isoprene}$ gas phase RONO_2 yields together with the reported uncertainties and the methods used to derive them. The uncertainties for this work shown in Table 11 reports the statistical variability in the mean yield, though the uncertainties in the individual yield calculations are large. It is difficult to compare with the figures reported in the other studies as, while all of these studies detail the major sources of uncertainty in the measurements, it is not always clear how those uncertainties are propagated into the final calculation of the yield of $\text{NO}_3 + \text{isoprene}$, specifically. Despite this, yields determinations have remained rather constant over several years and with various methods of evaluation, implying accuracy, including analysis of carbon products e.g. Perring *et al.*, Kwan *et al.*, or Schwantes *et al.*; change in ANs vs isoprene e.g. Perring *et al.* or this work; or the methodology of Rollins *et al.* which used an adjusted MCM model to fit TD-LIF data ANs data. The Rollins method is also noteworthy in the way that they assign a wall loss constant ($2.2 \times 10^{-5} \text{ s}^{-1}$) to the fit of the ANs data, which is generally not addressed in the other studies beyond steps taken to minimize the losses. This is significant if ANs losses are significant in these (non-SAPHIR) chamber studies then the yields determined would therefore be underestimated, perhaps even to the extent that the average yield(s) might begin to approach 100%, as one might expect wall losses to be more significant on smaller chambers with larger surface area to volume ratios. Taking the Rollins *et al.* figure for the wall loss, although it describes the same chamber and applying it to the ANs data taken during this campaign would result in a modest increase in the yields presented here, e.g. numerical simulations suggest that if applied to the experimental conditions on 8/2 this would result in an 8% increase in the yield. While this may give some idea of the magnitude of the increase such as correction might make to the presented ANs, the Rollins *et al.* wall loss rate is likely not applicable to this campaign as the entire PFA interior of the SAPHIR chamber has been replaced between 2009 and the present. A future publication will explore in greater detail the question of wall losses of ANs and others in controlling the reactive nitrogen budget during the SAPHIR experiments with a box model analysis constrained by measurements made during the campaign. As a wall loss has not been applied to the ANs data presented here, this introduces a source of systematic error into the final ANs yield calculation and therefore the 0.77 / 0.81 figures presented here likely represent a lower limit to the true figure of the yield.

Assuming then, that the 0.81 figure is of a good approximation to the true value of the yield, this would strengthen the conclusions that the reaction of isoprene or its oxidation products with NO_3 is the strongest source (up to ~50%) of all isoprene nitrates in the continental boundary layer (Horowitz *et al.* 2007) compared against the OH or O_3 -initiated mechanisms. Model determinations of the global organic nitrate budgets are strongly sensitive to yields of isoprene nitrates, both with OH and NO_3 (von Kuhlmann *et al.* 2003), thus additional data which affirms the current understanding of isoprene nitrate formation will increase the confidence of these model predictions. This is important as isoprene nitrates make up the largest share and maybe a majority of all alkyl nitrates in the atmosphere globally (Fisher *et al.* 2016) and are particularly important in high isoprene (or other BVOC), high NO_x environments such as the north eastern US where a large fraction (~20%) of all emitted isoprene is oxidized by NO_3 , leading to recycling of NO_x due to rapid photolysis (Müller, Peeters, and Stavrou 2014) of NO_3 -derived isoprene nitrates (and therefore local O_3 and PAN levels) and large contribution to SOA formation which outpaces OH-initiated SOA formation by up to 50% (S. S. Brown *et al.* 2009). Field studies have noted however, that that currently a large source of organic aerosol appears to be missing from the models (Colette L. Heald *et al.* 2005). (Carlton, Wiedinmyer, and Kroll 2009) have detailed potential reasons for this underestimation of organic aerosols ranging from errors in source attribution, including primary particle emission and VOCs; uncertainties associated with measurements; effects of meteorological inputs; and the sensitivity of SOA

yields (in particular of isoprene) in chamber studies to temperature, humidity, NO_x levels and oxidant concentrations. They argue methacrolein is an important intermediate in the formation of isoprene SOA and chamber studies underestimate the true SOA yields as methacrolein oxidations tend to slow down considerably towards the end of experiments, preventing late determinations of yields as wall losses dominate.

7.4.1. Summary and conclusions

Measurements of alkyl nitrates were made during the 2018 SAPHIR chamber experiments campaign, where a difference between the reference NO₂ and the ANs + PN_s + NO₂ cavity could be observed following an injection of isoprene. An unexpected difference between the NO₂ and ΣPN_s + NO₂ cavity was also observed, implying the formation of PN_s/PAN_s in the chamber through a fully in the dark mechanism, which would contradict the NO₃-isoprene mechanism as it is currently understood. Possible explanations of this phenomenon are likely to be a combination of factors including the chemical explanation of the formation of PAN_s, particularly MPAN, though given the low yield of PAN precursors, such as methacrolein, this alone cannot explain the entire observed discrepancy in the signals. Other factors include the possibility of surface catalyzed breakdown of RONO₂ on the glass beads or other surfaces in the instrument, though this has not been observed for laboratory tested AN_s and PN_s, such as iPN and PAN, or previous field deployments of the 5-CRD. Physical chemistry is also a potential explanation as the NO₃ + Isoprene reaction gives a wide variety of multifunctionalized products and isomers in differing yields which have different chemical structures and which contribute to intramolecular forces that determine the length of the nitrate ester RO-NO₂ bonding group, where longer bonds possess a lower bond dissociation energy and are thus broken at lower temperatures. The thermogram presented above could thus be interpreted as a continuous series of overlapping thermal decomposition functions of many different isoprene nitrate molecules into NO₂. These results show the need for further research into the ability of the 5-CRD, and other TD instruments, to precisely see the partition of AN_s/PN_s in air mixtures which contain isoprene nitrates, other VOCs which may form a variety of products when oxidized by radicals, and mixtures of these plus PN_s.

Alkyl nitrate yields were calculated according to loss of isoprene fitted against gain of AN_s, where these yields showed unexpected variability on an experiment-to-experiment and sometimes injection-to-injection of isoprene basis. These ranged from extremely low (36%), relative to established yields in the literature, to very high (>100%) depending on the experiment. The linearity of experiments, which was expected to be high, was occasionally very low according to the coefficients of determination calculated from a linear regression analysis of the plot of ΔAN_s vs. ΔIsoprene. Low yields were associated with low R² and both generally occurred in experiments where smaller concentrations of AN_s were formed, which might imply an underestimation of the limits of detection for the AN_s signal. Contributing factors to the high LOD include gas-wall interactions between isoprene nitrates and the instrument surfaces, presumably the PFA-tubing lines, which contributed to absorption and desorption equilibria evident in the instrument zeroing, leading to a less accurate zero. Technical issues with one of the instrument's mass flow controller units additionally led to unexpected fluctuations in the flow rate, temperature and pressure of the AN_s cavity and oven. These factors together, when propagated with uncertainties in other datasets contributed a considerable uncertainty the final yield calculations. Despite this however, both the absolute mean of the yield and the upper or lower limits to the yield fell within established IUPAC (0.6 – 0.9) recommendations.

These yields should be taken as a lower limit, as wall losses of alkyl nitrates have yet evaluated for the SAPHIR chamber, with the most recent estimates more than a decade old and estimated on the SAPHIR's PFA surface, which has since been replaced. The yields are also potentially lower limits due to the question of whether or not the 5-CRD was able to detect the sum of all ANs accurately, with a relative thermogram of the $\text{NO}_2 + \Sigma\text{PNs}$ channel against the $\text{NO}_2 + \Sigma\text{PNs} + \Sigma\text{ANs}$ channel seeing no evidence of reaching a plateau, as would be expected as thermal decomposition approaches 100% and is seen in thermograms of the reference molecule, iPN. Conversely, the yields presented here may alternatively represent a lower limit to the yields, as while it does not appear that the 5-CRD detects significant signal of HNO_3 in the 5-CRD, other sources of nitrogen were detected in the SAPHIR chamber, according to the CLD and NO_y measurements, and without identification of this molecule (or molecules) it is difficult to predict what effect this may have on the ΣANs signal and may bias the yields upwards.

Isoprene nitrate yields as determined by this work averaged 0.81, which is consistent with previous determinations and therefore strengthens the conclusions of modelling groups that $\text{NO}_3 + \text{isoprene}$ is the strongest source of isoprene nitrates, and that isoprene nitrates are the strongest source of RONO_2 globally, a conclusion which requires a high and relatively robust and insensitive value of the yield. This is also true of modelling studies which estimate NO_x transport and recycling (and consequent ozone formation) in remote areas which rely heavily on photolysis of relatively short-lived, multifunctional RONO_2 such as those created by the NO_3 isoprene reaction; and is important in the secondary organic aerosol budget where a significant source of aerosol mass loading is known to come from the partition of isoprene nitrates into the aerosol phase.

8. Outlook

The results from the 2017 AQABA campaign highlight that, under certain conditions, the role of NO_3 as a sink for NO_x maybe be underestimated in highly polluted maritime regions which are strongly influenced by shipping emissions. As has been shown in the high NO_x , high O_3 environments studied during the campaign the rates at which NO_x is lost to the atmosphere via the nighttime O_3 -initiated mechanism can be competitive with the OH initiated mechanism during the day, even under conditions of strong solar irradiation. As NO_3 and N_2O_5 only represent a temporary reservoir of NO_x without suitable reaction partners to irreversibly convert NO_x , a detailed understanding of what these reaction partners are is necessary, beginning with a study on the speciation of VOCs emitted from the combustion engines of ships at sea in around the Arabian Peninsula, which first order loss rates of NO_3 have been shown to correlate with. As has been shown, the heterogeneous chemistry of N_2O_5 in these regions is largely unimportant compared to gas phase reactivity of the NO_3 radical and a list of quantified VOCs in a similar time resolution, on the order of 10 minutes or less, would allow for a reduction in proportions of unattributed reactivity, discussed in section 5. Further studies in other regions dominated by petrochemical industry and high shipping traffic, for example in the Gulf of Mexico and Panama Canal regions, should additionally be carried out, where possible, to determine if these results are consistent with observations made during the AQABA campaign. As shipping is global industry which is projected to grow in coming years, the extent to which shipping emissions act as a sink (and source) for local NO_x in polluted regions helps inform models seeking to describe the regional and global distribution of many trace gases, including short and long-lived organic nitrates, NO_x , SO_2 , VOCs as well secondary polluting effects including O_3 production rates and anthropogenic aerosol mass loading, all of which have consequences for climate, cloud condensation nuclei and human health.

The results of the AQABA NO_x -loss analysis also show the need for a longer term periods of field measurements to examine each of the regions. Comparing loss rates of NO_2 ($k[\text{OH}]$) at day compared with NO_2 ($k[\text{O}_3]$) at night reveals similar values, suggesting that that OH mechanism should be the more important of the two as daylight hours made up more than half of the diurnal cycle, though this was not the case for all of the studies regions except the Mediterranean. The difference appears to have been driven by higher NO_x concentrations during the nights, which may be a function of passing through global industrial and shipping hotspots, such as the Straits of Hormuz, at night which biases the averaged, per-hour losses at night, leading to the apparent domination of $\text{NO}_2 + \text{O}_3$ as the leading NO_x loss mechanism. A longer term study (months or even years) of similar measurements to those made on AQABA would be able to provide clarity on these observations, as well as contrast the relative importance of different loss mechanisms, particularly heterogeneous uptake, in the different seasons of the year when temperatures are consequently lower.

From the analysis of the 2018 SAPHIR NO_3 -Isoprene experiments, the most interesting aspect from which further studies could be based is the phenomenon of the PNs signal which, as discussed, is unlikely to be due to be caused by a real PN, as true PNs would necessarily be second-generation products (e.g. MPAN). These observations suggest that either surface level catalysis occurring in the heated sections of the instrument, which may affect all previous all previous data collected in remote, forested regions by the 5-CRD, or else a potential flaw in the Thermal Dissociation method for detecting alkyl nitrates in general, which could potentially impact all observations of ΣANs and ΣPNs in remote forested regions where isoprene, or potentially any other BVOC or alkene which reacts rapidly with NO_3 , is prevalent. A determination for whether this is just a 5-CRD problem will likely come down to a comparison of different

thermograms for different TD instruments to attempt isolate the cause of, presumably, the catalytic breakdown of isoprene nitrates. Should the cause be less to do with instrument design and more to do with physical chemistry a study looking into the thermal decomposition of isoprene nitrates under a wide variety of conditions is recommended. It should be noted however; these speculations are neither exhaustive nor mutually exclusive of one-another.

From looking at the results of the ANs data compared to the isoprene lost via reaction with NO_3 , the yields of this reaction, which were expected to be constant, showed unexpected day-to-day variability. This was likely due to the high uncertainties in the ΔANs and $\Delta\text{Isoprene}$ signals, propagated into the final linear regression analysis giving a wide range of possible slopes (yields). The fault may lie in the measurements of ANs and determinations of the limits of detection; ANs have been shown to undergo gas-wall partitioning reactions between the multifunctional isoprene nitrates and, most likely, the PFA tubing of the instrument. Investigations into these surface interactions with isoprene nitrates, and other common atmospheric trace gases, with common types of instrument tubing, such as PFA or PTFE, could provide insight into the best practices of sampling methods, instrument design or tubing types for a variety of different applications within the field of gas-phase atmospheric measurements.

For the instrument, several modifications could be made in order improve the overall performance. Simple measures such as replacing the mirrors, which have lost reflectivity over years of use, would improve the sensitivity of the cavities by extending ringdown times. Replacement of the mass flow controller unit which controls the outflow through the ANs cavity would likely help prevent fluctuations in flow observed during the SAPHIR campaign. In terms of modifications to the instrument design, one modification to side-step the PFA-ANs interactions altogether may be to relocate the ovens from a few cm before the cavities to the end of the main sampling inlet, avoiding issue of ANs traversing through > 4m of PFA before reaching the cavity. The approach would likely not work for PNs due to the recombination reaction of the peroxyacyl radicals with NO_2 leading to a potentially large, uncertain correction, relative to the method used now. Additional cavities could be added with potentially two additional cavities for detection of NO_x with an ambient temperature and a source of O_3 , where the difference between the NO_2 and NO_x channels would give NO ; and a cavity with an oven with temperatures even higher than the ANs cavity for detection of HNO_3 , which also decomposes to NO_2 , thereby giving the sum of all gas-phase reactive nitrogen. In the NO_3 and N_2O_5 channels, applying the FACSIMILE numerical simulations to the behavior of NO_3 and N_2O_5 in the cavity, as is the case for PNs and ANs, could potentially increase the accuracy of the corrections made when accounting for transmission across the instrument. This would require an accurate temperature and pressure profile of the 5-CRD and a quantified determination of the wall losses across the instrument. Finally, in a complete redesign of the frame of the instrument, a possible improvement for deployment purposes might be to vertically mount the cavities, which would allow for integration into space-controlled applications such as in an aircraft.

9. Appendix

Appendix A – Supplementary Figures AQABA

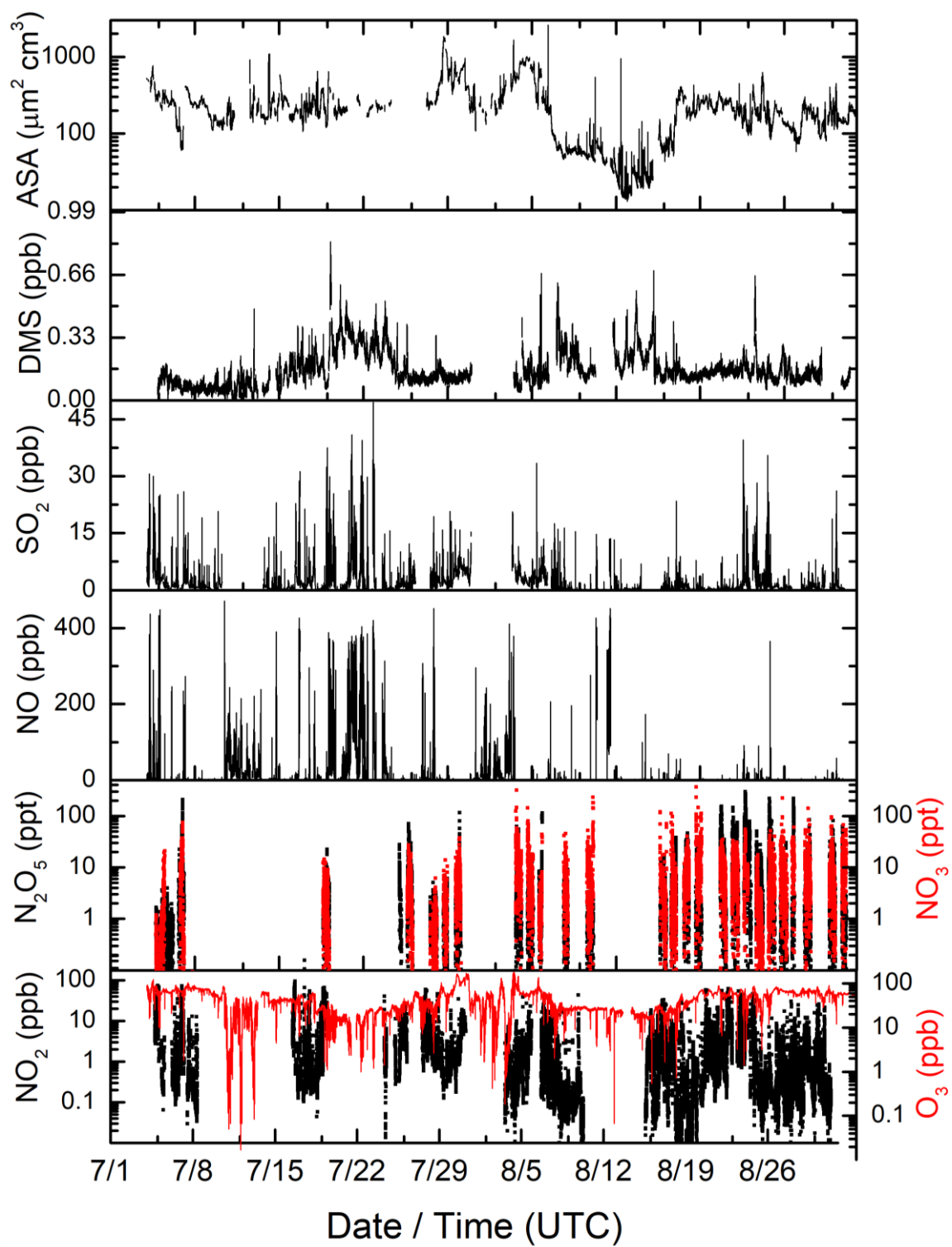


Figure 52. Overview of NO, NO_2 , NO_3 , N_2O_5 , SO_2 , DMS and aerosol surface area (ASA) measurements from the 2017 AQABA campaign.

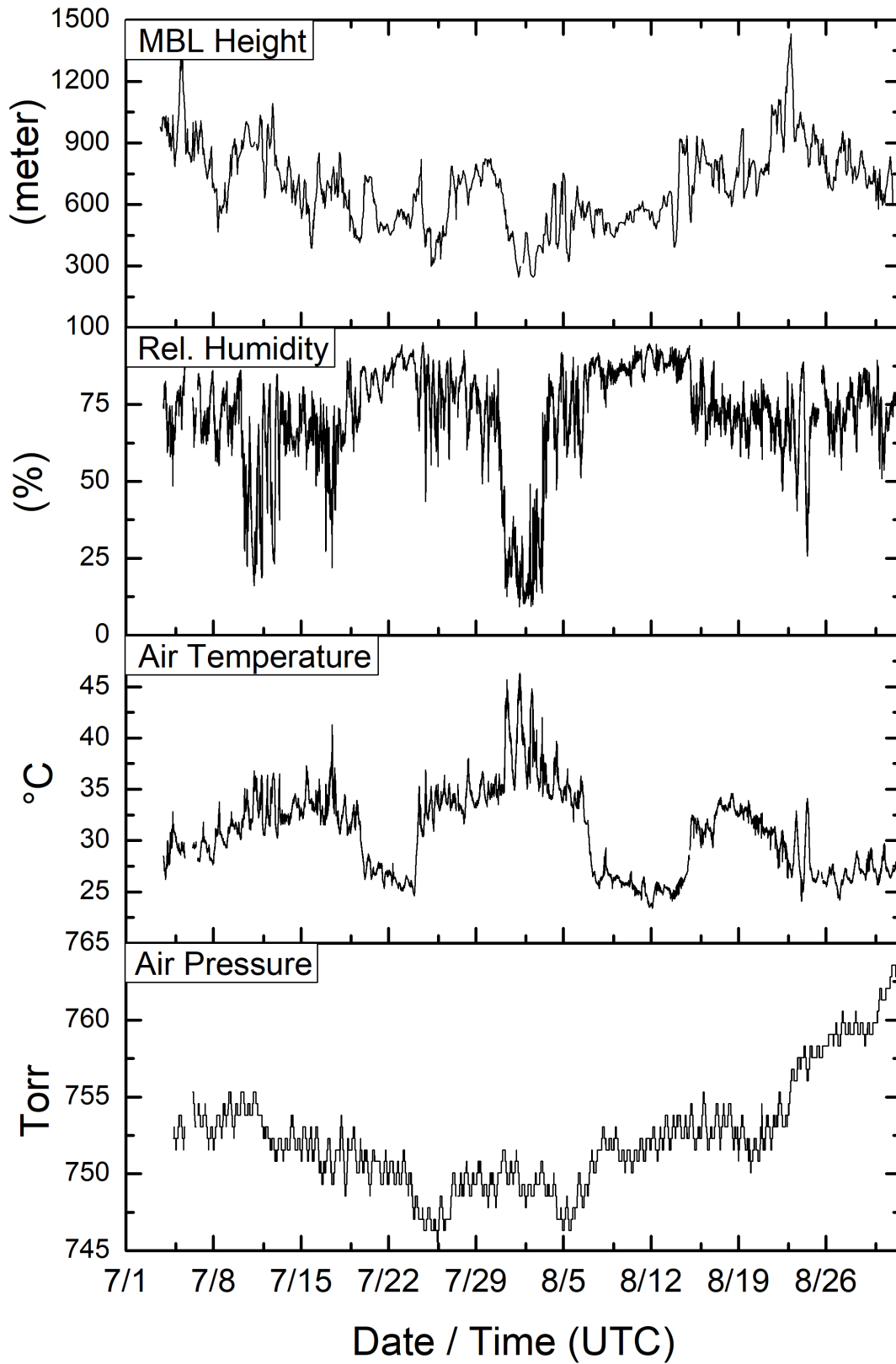


Figure 53. Supporting meteorological data of air temperature, air pressure (sea level), relative humidity and marine boundary layer height from the 2017 AQABA campaign

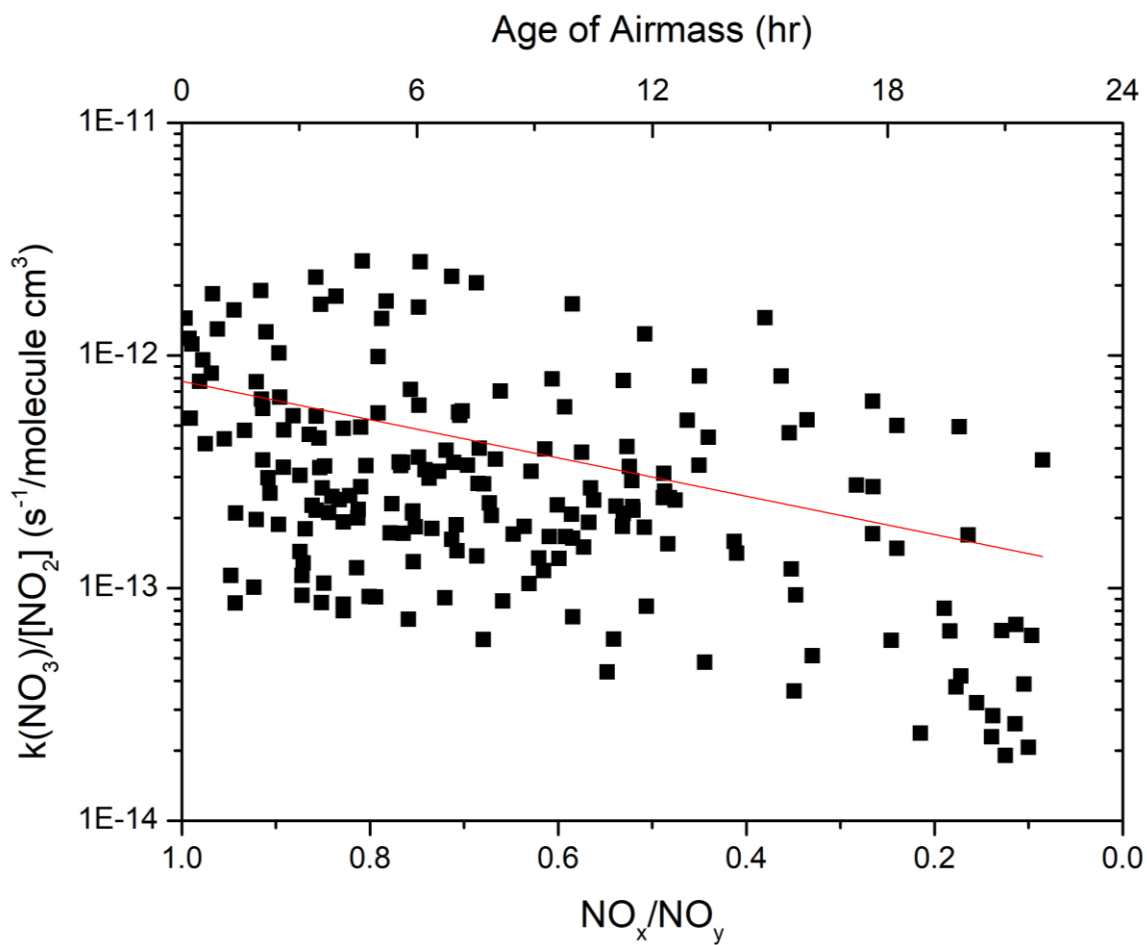


Figure 54. $k(NO_3)/[NO_2]$ vs. NO_x/NO_y ratio. Fit according to $y=ab^x$ where $a=1.16 \times 10^{-13}$, $b=666$. Analogous to $k(NO_3)/[SO_2]$ plot shown in 5.2.4, describing the dependence on co-emitted $k(NO_3)$ -contributing VOC from ship emissions on the age of the airmass as indicated by the NO_x/NO_y ratio, fitted to an approximate timescale based on reasonable assumptions of $[OH]$ and $[O_3]$.

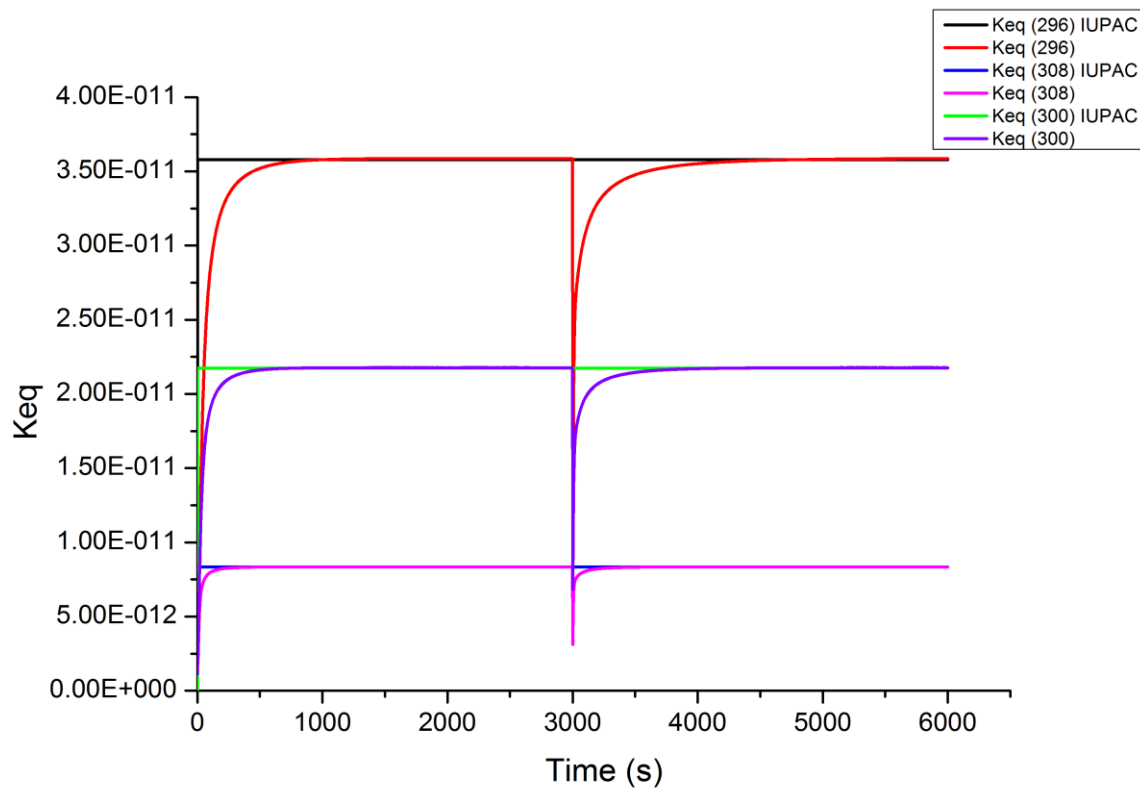


Figure 55. FACSIMILE simulations comparing time taken (in s) to reestablish $\text{NO}_2\text{-NO}_3\text{-N}_2\text{O}_5$ equilibrium following titration of all NO_3 by NO under AQABA temperature conditions. Simulation informed how long after a NO titration the data were likely to not be in equilibrium, necessary for determination of the mixing ratios of NO_3 via calculation and for calculation of steady state lifetimes.

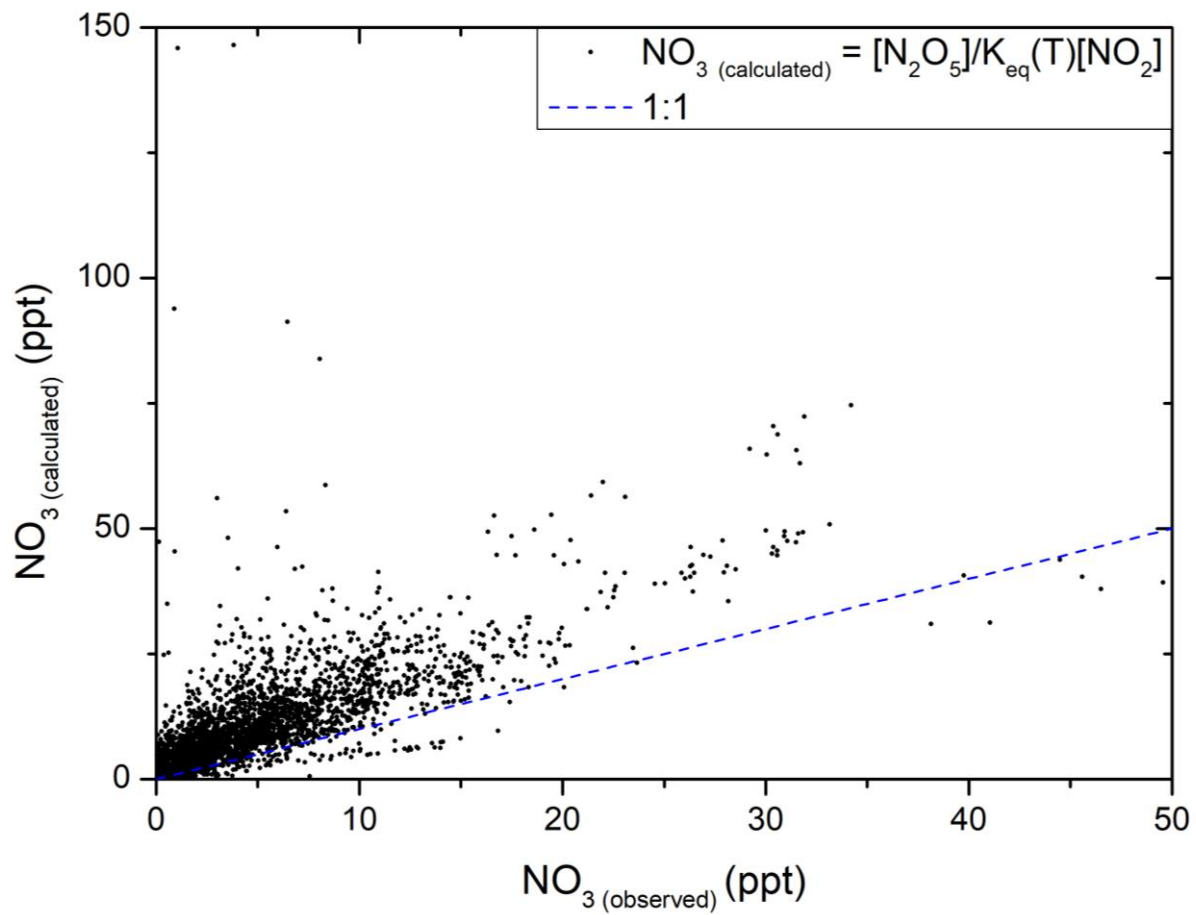


Figure 56. Comparison of $[\text{N}_2\text{O}_5]/K_{\text{eq}}(\text{T})[\text{NO}_2]$ -calculated NO_3 mixing ratios against NO_3 measured directly by the 5-CRD for the entire AQABA campaign. Calculated NO_3 mixing ratios are almost always systematically higher due to losses of NO_3 to the instrument walls.

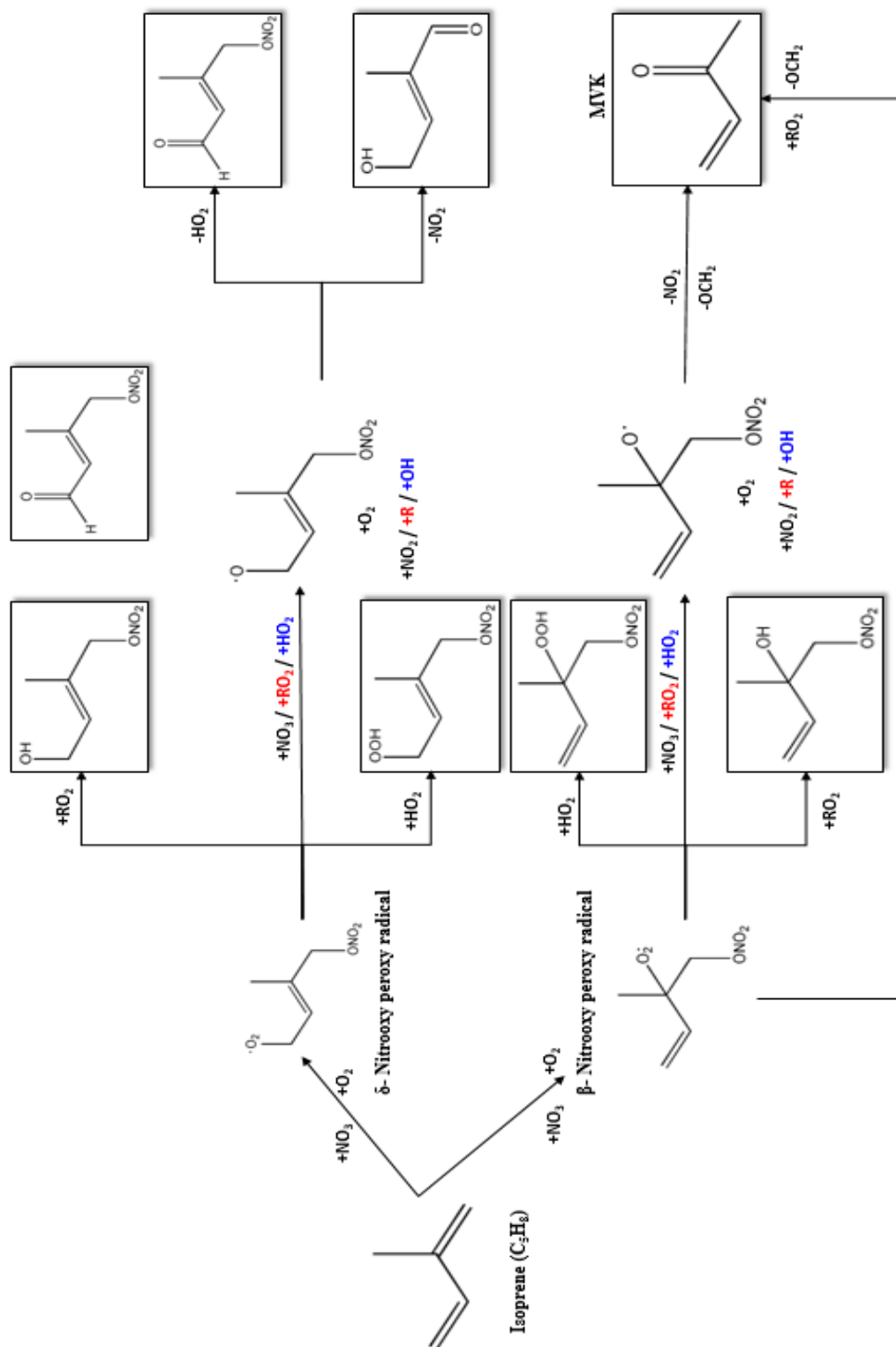


Figure 57. Reaction scheme of oxidation of Isoprene by NO_3

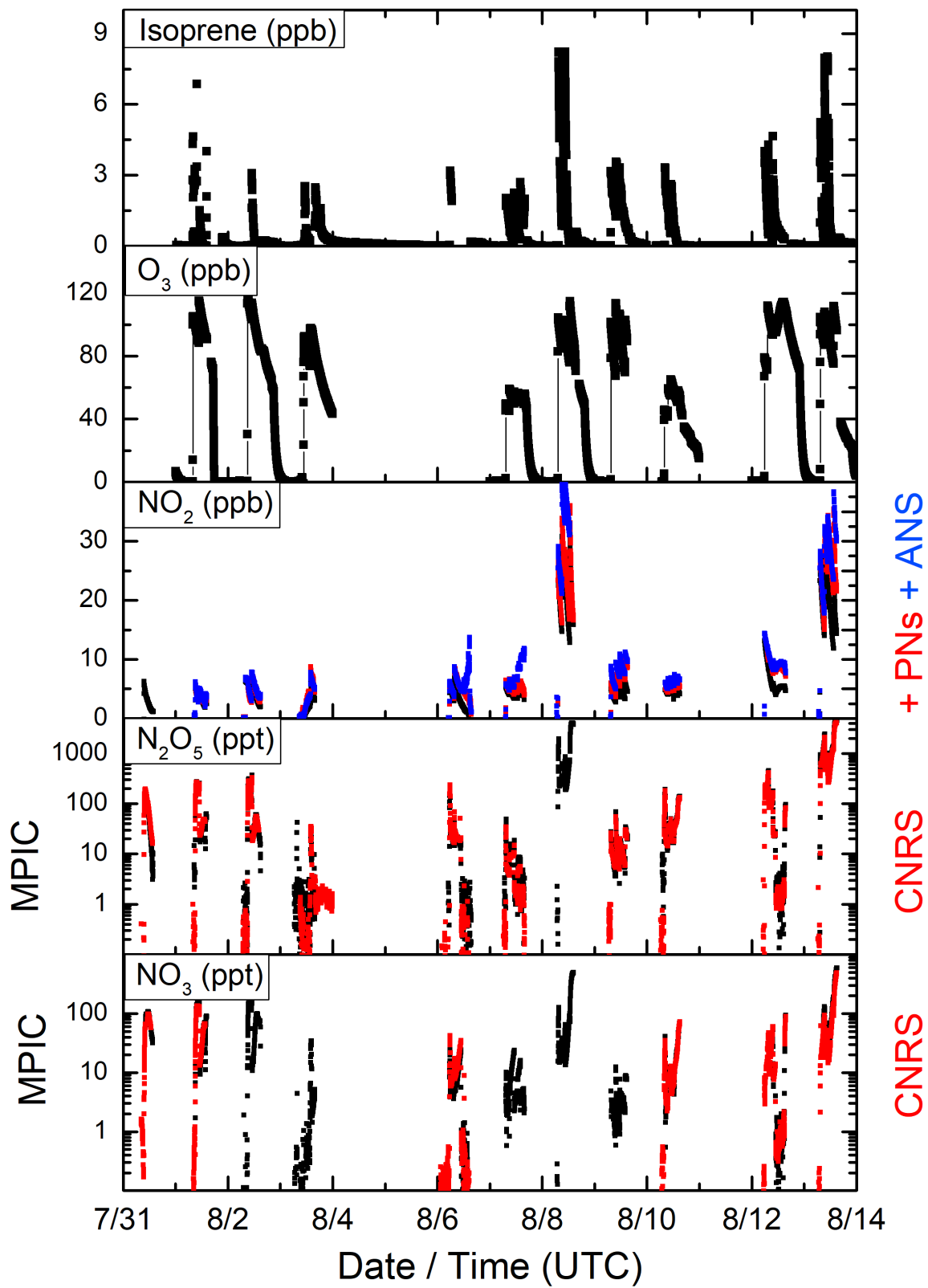


Figure 58. Overview of NO_3 , N_2O_5 , NO_2 , ΣPNs , ΣANs , O_3 and Isoprene measurements from SAPHIR experiments 7/31 – 8/13

Appendix C – List of abbreviations

Abbreviation	Meaning
ANs	Alkyl Nitrates
AQABA	2017 <u>A</u> ir <u>Q</u> uality and climate change in the <u>A</u> rabian <u>B</u> asin campaign
ASA	Aerosol Surface Area
(B)VOC	(Biogenic) Volatile Organic Compound
CI(Q)MS	Chemical Ionization (Quadrupole) Mass Spectroscopy
CLD	Chemiluminescence Detector
CNRS	Centre National de la Recherche Scientifique
DMS	Dimethyl Sulfide
DMSO	Dimethyl Sulfoxide
FACSIMILE	Flow And Chemistry SIMulator
iPN	Iso-propyl Nitrate
IUPAC	International Union of Pure and Applied Chemistry
JPL	Jet Propulsion Laboratory
LOD	Limit Of Detection
MBL	Marine Boundary Layer
MGLY	Methylglyoxal
MPAN	Methacrolein Peroxyacyl Nitrate
MPI(C)	Max Planck Institute (for Chemistry), Mainz
MS	Mass Spectroscopy
ONs	Organic Nitrates
PAN	Peroxyacetyl Nitrate
PANs	Peroxyacyl Nitrates
PFA	Perfluoroalkyl
POA	Primary Organic Aerosol
PNs	Peroxy Nitrates
PTR-ToF	Proton Transfer Reaction Time of Flight
RH	Relative Humidity
SAPHIR	<u>S</u> imulation of <u>A</u> tmospheric <u>P</u> hotochemistry <u>I</u> n a large <u>R</u> eaction <u>C</u> hamber
SCCM	Standard Cubic Centimetres per Minute
SLM	Standard Litres per Minute
SOA	Secondary Organic Aerosol
TD	Thermal Dissociation


```

k5 = 2.07e-12 * exp (-1400/T) ;IUPAC
kDMS = 1.9e-13 * exp (520/T) ;IUPAC
kx = 4.2e-14*(122.45@NOxy) ;
ky = loss ;
** ;
COMPILE INSTANT ;
open 7 "no3.sim" new ;
open 20 "Ships.txt" old ; if read in of parameters is needed
** ; define in block 4 and add as when 2)
COMPILE BLOCK 3 ;
PSTREAM 3 ;
** ;
COMPILE BLOCK 4 ;
Read 20 INPARAM <5> ;
NO2a = INPARAM <0> ;
O3a = INPARAM <1> ;
SO2a = INPARAM <2> ;
NOxya = INPARAM <3> ;
lossa = INPARAM <4> ;
NO2 = NO2a ;
O3 = O3a ;
SO2 = SO2a ;
NOxy = NOxya ;
loss = lossa ;
** ;
PSTREAM 3 7 ;
time NO3 NO2 O3 N2O5 M SO2 NOxy ;
** ;
when ;
1) time = 0 + 600*8200 call block 3 ;
2) time = time + 600 call block 4 restart ;
** ;
BEGIN ;
STOP ;

```

Correction of ΣANs or ΣPNs field data

```

* PAN artefact decomposition ;
* ===== ;
variable PAN ch3co3 NO2 NO ch3o2 ch3o2no2 ho2 h2o oh HCHO HO2NO2 IPN ;
variable ch3o o3 HONO HNO3 ch3co2 co2 RSO PAA AA CH3OOH h2o2 IPO ;
variable acet ch3cho ch3co ch2co2 ch2coooh OD ;
* ----- ;
parameter PANi 79.070911 ;
parameter NO2i 229.000000 ;
parameter NOi 3.000000 ;
parameter klang 0.001000 ;
parameter IPNi 0.000000 ;
parameter o3i 21785.000000 ;
parameter k1 k2 k3 k4 k5 k6 k7 k8 k9 k10 k11 k12 k13 k14 k15 k20 ;
parameter k16 k17 k18 k19 k21 k24a k23 k24 k25 k19a k26 k27 ;
parameter Dgoh Dgho2 DgMP DgCH3CO3 ;
parameter HPL24 LPL24 kint M Malt Z RC ;
parameter gamdiffoh gamdiffho2 gamdiffMP gamdiffCH3CO3 ;
parameter gamLangOH gamLangHO2 gamLangMP gamLangCH3CO3 ;
parameter gammaOH gammaHO2 gammaMP gammaCH3CO3 ;
parameter kwOH kwHO2 kwCH3O2 kwCH3CO3 f1 f2 f3 f4 f5 f6 ;
* ----- ;
parameter Voh 8.42 ;
parameter Mohair 21.4 ;
parameter Vho2 14.53 ;
parameter Mho2air 30.87 ;
parameter VMP 35.05 ;
parameter MMPair 35.87 ;
parameter VCH3CO3 57.06 ;
parameter MCH3CO3air 41.83 ;
parameter Vair 19.7 ;
parameter mmvOH ;
parameter mmvHO2 ;
parameter mmvMP ;
parameter mmvCH3CO3 ;

```

```

parameter O2 3.9e18 ;
parameter p 550 ;
parameter T 303.15 ;
parameter SSA 3.4 ;
parameter Dr 0.59 ;
parameter SS 1.0e12 ;
parameter Nmax 1.2e12 ;
parameter ks 1.2e-11 ;
parameter <5> INPARAM ;
* ----- ;
COMPILE GENERAL ;
M = P * 3.24E16 * 298 /T ;
** ;
COMPILE INITIAL ;
Malt = 550 * 3.24E16 * 298 /303.15 ;
PAN = PANi*Malt*1e-12 ;
NO = NOi*Malt*1e-12 ;
NO2 = NO2i*Malt*1e-12 ;
IPN = IPNi*Malt*1e-12 ;
o3 = o3i*Malt*1e-12 ;
** ;
COMPILE EQUATIONS ;
* ----- ;
% k1 : PAN = CH3CO3 + NO2 ;
f2 % k2 : CH3CO3 + NO2 = PAN ;
% k3 : CH3CO3 + NO = CH3CO2 + NO2 ;
% 1e6 : CH3CO2 = CH3O2 + CO2 ;
% k4 : CH3O2 + NO = HCHO + HO2 + NO2 ;
% k5 : CH3O2 + NO2 = CH3O2NO2 ;
% k6 : CH3O2NO2 = CH3O2 + NO2 ;
% k7 : HO2 + NO = NO2 + OH ;
% k8 : HO2 + NO2 = HO2NO2 ;
% k9 : HO2NO2 = HO2 + NO2 ;
% k10 : OH + NO2 = HNO3 ;
% k11 : OH + NO = HONO ;
% k12 : CH3CO3 + CH3CO3 = CH3CO2 + CH3CO2 ;
% k13 : CH3CO3 + CH3O2 = HCHO + HO2 + CH3O2 + co2 ;
% k14*0.29 : CH3CO3 + HO2 = PAA + O2 ; 0.29
% k14*0.1 : CH3CO3 + HO2 = AA + O3 ; 0.1
% k14*0.61 : CH3CO3 + HO2 = OH + CH3O2 ; 0.61
% k15 : CH3O2 + HO2 = CH3OOH ;
% k16 : HO2 + HO2 = H2O2 ;
% k17 : OH + HO2 = h2o + o2 ;
% k18 : IPN = IPO + NO2 ;
% k19 : IPO = HO2 + acet ; IPO + O2
% k19a : IPO = CH3O2 + CH3CHO ;
% k26 : OH + CH3CHO = CH3CO ;
% k20 : CH3CO3 = CH3CO ; diss to CH3CO + O2
% k21 : CH3CO3 = CH2COOOH ; isomerisation
% k23 : CH2COOOH = CH2CO2 + OH ;
% k24 : CH3CO + O2 = CH3CO3 ; add O2
% k24a : CH3CO + O2 = OH + CH2CO2 ;
% k25 : CH3CO = CH3O2 ; diss to CH3 + CO
% 2e-10 : OH + CH3O2 = HO2 + HO2 ; Assume HO2 + CH3O channel
only
% 2e-10 : OH + CH3CO3 = HO2 + CH3O2 + CO2 ;
% kwCH3CO3 : CH3CO3 = RSO ;
% kwCH3O2 : CH3O2 = RSO ;
% kwHO2 : HO2 = RSO ;
% kwOH : OH = RSO ;
% k27 : o3 + NO = NO2 + O2 ;
* ----- ;
z = M/Malt ;
RC = CH3CO3 + CH3O2 + HO2 ;
*Rate equations ;
DgOH = 1/p*1.0868*T@(1.75) / (Mohair)@(0.5) / ;
(VOH@(0.3333) + Vair@(0.3333) )**2 ;
DgHO2 = 1/p* 1.0868*T@(1.75) / (Mho2air)@(0.5) / ;
(VHO2@(0.3333) + Vair@(0.3333) )**2 ;
DgMP = 1/p* 1.0868*T@(1.75) / (MMPair)@(0.5) / ;
(VMP@(0.3333) + Vair@(0.3333) )**2 ;

```

```

DgCH3CO3 = 1/p* 1.0868*T@(1.75) / (Mch3co3air)@(0.5) /
(VCH3CO3@(0.3333) + Vair@(0.3333) )**2
;
mmvOH = 14600*(T/17)@0.5
;
mmvHO2 = 14600*(T/33)@0.5
;
mmvMP = 14600*(T/47)@0.5
;
mmvCH3CO3 = 14600*(T/75)@0.5
;
GamDiffOH = 3.66 * 2* DgOH/(mmvOH*Dr)
;
GamDiffHO2 = 3.66 * 2* DgHO2/(mmvHO2*Dr)
;
GamDiffMP = 3.66 * 2* DgMP/(mmvMP*Dr)
;
GamDiffCH3CO3 = 3.66 * 2* DgCH3CO3/(mmvCH3CO3*Dr)
;
gamLangOH = 4*ks*SS*Klang*1e-10*Nmax /
mmvOH/(1 + klang*1e-10*RC)
;
gamLangHO2 = 4*ks*SS*Klang*1e-10*Nmax /
mmvHO2/(1 + klang*1e-10*RC)
;
gamLangMP = 4*ks*SS*Klang*1e-10*Nmax /
mmvMP/(1 + klang*1e-10*RC)
;
gamLangCH3CO3 = 4*ks*SS*Klang*1e-10*Nmax /
mmvCH3CO3/(1 + klang*1e-10*RC)
;
gammaOH = 1/(1/GamDiffOH + 1/GamLangOH)
;
gammaHO2 = 1/(1/GamDiffHO2 + 1/GamLangHO2)
;
gammaMP = 1/(1/GamDiffMP + 1/GamLangMP)
;
gammaCH3CO3 = 1/(1/GamDiffCH3CO3 + 1/GamLangCH3CO3)
;
kwOH = gammaOH*mmvOH*SSA/4
;
kwHO2 = gammaHO2*mmvHO2*SSA/4
;
kwCH3O2 = gammaMP*mmvMP*SSA/4
;
kwCH3CO3 = gammaCH3CO3*mmvCH3CO3*SSA/4
;
k1 = z*((1.10e-5*exp(-10100/T))*M*
(1.9e17*exp(-14100/T)))/((1.10e-5*exp(-10100/T))*M+
(1.9e17*exp(-14100/T)))*10@(log10(0.3)/
(1+(log10((1.10e-5*exp(-10100/T))*M/
(1.9e17*exp(-14100/T)))/(0.75-1.27*log10(0.3))**2))
; PAN =
k2 = z*z*(3.28e-28*(T/300)@-6.87)*M*
(1.125e-11*(T/300)@-1.105)/((3.28e-28*(T/300)@-6.87)*M+
(1.125e-11*(T/300)@-1.105))*10@(log10(0.3)/
(1+(log10((3.28e-28*(T/300)@-6.87)*M/
(1.125e-11*(T/300)@-1.105)))/(0.75-1.27*log10(0.3))**2))
; CH3CO3 + NO2
k3 = z*z*7.5e-12*exp(290/T)
; CH3CO3 + NO
k4 = z*z*2.3e-12*exp(360/T)
; CH3O2 + NO
k5 = z*z*((2.5e-30*(T/300)@-5.5)*M*
(1.8e-11))/((2.5e-30*(T/300)@-5.5)*M+
(1.8e-11))*10@(log10(0.36)/(1+(log10((2.5e-30*(T/300)@-5.5)
*M/(1.8e-11))/(0.75-1.27*log10(0.36))**2))
; CH3O2 + NO2
k6 = z*((9e-5*exp(-9690/T))*M*
(1.1e16*exp(-10560/T)))/((9e-5*exp(-9690/T))*M+
(1.1e16*exp(-10560/T)))*10@(log10(0.36)/
(1+(log10((9e-5*exp(-9690/T))*M/
(1.1e16*exp(-10560/T)))/(0.75-1.27*log10(0.36))**2))
; CH3O2NO2 =
; HO2 + NO
k7 = z*z*3.45e-12*exp(270/T)
; HO2 + NO2
k8 = z*z*((1.4e-31*(T/300)@-3.1)*M*
(4.0e-12))/((1.4e-31*(T/300)@-3.1)*M+
(4.0e-12))*10@(log10(0.4)/(1+(log10((1.4e-31*(T/300)@-3.1)
*M/(4.0e-12))/(0.75-1.27*log10(0.4))**2))
; HO2 + NO2
k9 = z*((4.1e-5*exp(-10650/T))*M*
(6.0e15*exp(-11170/T)))/((4.1e-5*exp(-10650/T))*M+
(6.0e15*exp(-11170/T)))*10@(log10(0.4)/
(1+(log10((4.1e-5*exp(-10650/T))*M/
(6.0e15*exp(-11170/T)))/(0.75-1.27*log10(0.4))**2))
; HO2NO2 =
k10 = z*z*((3.2e-30*(T/300)@-4.5)*M*
(3.0e-11))/((3.2e-30*(T/300)@-4.5)*M+
(3.0e-11))*10@(log10(0.41)/(1+(log10((3.2e-30*(T/300)@-4.5)
*M/(3.0e-11))/(0.75-1.27*log10(0.41))**2))
; OH + NO2
k11 = z*z*((7.4e-31*(T/300)@-2.4)*M*
(3.3e-11*(T/300)@-0.3))/((7.4e-31*(T/300)@-2.4)*M+
(3.3e-11*(T/300)@-0.3))*10@(log10(0.81)/
(1+(log10((7.4e-31*(T/300)@-2.4)*M/
(3.3e-11*(T/300)@-0.3))/(0.75-1.27*log10(0.81))**2))
; OH + NO
k12 = z*z*2.9e-12*exp(500/T)*1
;
k13 = z*z*2.0e-12*exp(500/T)*1
;
k14 = z*z*7.6e-13*exp(980/T)
;
k15 = z*z*3.8e-13*exp(780/T)
;
k16 = z*z*(2.2e-13*exp(600/T) + 1.9e-33*M*exp(980/T))
;

```



```

k17 = z*z*4.8e-11*exp(250/T) ;
k18 = z*3.16e16*exp(-20129/T) ; IPN thermal decomp Day
k19 = 1*z*1.9e-14*exp(-300/T) ; IPO + O2 iupac
k19a = 1*z*5.33e19*T@-1.7*exp(-8630/T) ;
k20 = 1*z*1.5e16*exp(-20000/T) ; CH3CO3 = CH3CO
k21 = 0.2*z*1.6e16*exp(-20000/T) ; CH3CO3 = CH2COOOH
k23 = 1*z*1.8e18*exp(-20000/T) ; CH2COOOH = CH2CO2 + OH
LPL24 = 7.39e-30*(T/300)@-2.2 ;
HPL24 = 4.88e-12*(T/300)@-0.85 ;
k24 = (HPL24*LPL24*M/(LPL24*M+HPL24))* ;
0.8@((1+(log10(LPL24*M/HPL24))**2)**-1) ; Papadimitriou
kint = 6.4e-14*exp(820/T) ; Papadimitriou
k24a = kint*(1-k24/HPL24) ; Papadimitriou
k25 = ((1.0e-8*exp(-7080/T))*M*
(2.0e13*exp(-8630/T)))/((1.0e-8*exp(-7080/T))*M+
(2.0e13*exp(-8630/T))*10@(log10(0.5)/(1+(log10(
(1.0e-8 *exp(-7080/T))*M/(2.0e13*exp(-8630/T)))/
(0.75-1.27*log10(0.5))**2))) ; CH3CO = CH3 + CO Baulch
database
k26 = 4.7e-12*exp(345/T) ; OH + CH3CHO iupac
k27 = z*z*1.06*9e-19*exp(-850/T)*T@2.25 ; NO+ O3
** ;
compile instant ;
open 7 "PANfitAo.SIM" new ;
open 8 "PANfitAt.SIM" new ;
* open 9 "zzz.fit" new ;
* open 10 "zzz.gr2" new ;
open 20 "PAN0905.asc" old ;
** ;
COMPILE BLOCK 3 ;
PSTREAM 3 ;
PSTREAM 4 ;
** ;
compile block 4 ;
read 20 INPARAM <5> ;
T = INPARAM <0> ;
P = INPARAM <1> ;
SSA = INPARAM <2> ;
ks = INPARAM <3> ;
Dr = INPARAM <4> ;
** ;
PSTREAM 3 7 10 ;
time M NO2 PAN NO IPN GamDiffCH3CO3 gamLangCH3CO3 IPO ;
** ;
PSTREAM 4 8 10 ;
T P SSA Dr ks CH3CO3 ;
** ;
when ;
1) time = 0 + 1.325*1% call block 3 ;
2) time = time + 0.01 call block 4 restart ;
** ;
hmax 0.0025 ;
BEGIN ;
STOP ;

```

Appendix E – List of figures and tables

Figures

Figure 1. Isoprene + NO ₃ reaction forming β- and δ-nitrooxy peroxy isoprene (INP).	26
Figure 2. Reaction of INP with NO ₃ / RO ₂ / HO ₂ , producing alkoxy radicals	27
Figure 3. INP reaction with HO ₂ , producing hydroperoxy functionalized molecules	28
Figure 4. Reaction of INP with RO ₂ , forming carbonyl and hydroxyl functional groups	28
Figure 5. Rearrangement of isoprene nitrooxy alkoxy radicals to give multi-functionalized products	29
Figure 6. Reaction scheme of NO _x chemistry explored in this thesis. Includes major NO _x reactions from both day and nighttime processes	30
Figure 7. Cavity Ringdown set-up showing the initial laser intensity, I ₀ , entering the cavity and a transmitted intensity (I ₁ , I ₂ , I ₃ ...) leaving the cavity and arriving at the detector. This produces an exponential decay function where $I(t) = I_0 e^{(-t/\tau)}$	31
Figure 8. A ringdown signal comparing τ with τ_0 . The difference between the two is caused by the presence of a molecule which absorbs or scatters light at the wavelength(s) of the light source.	33
Figure 9. Instrument schematic of the five-channel cavity ringdown (5-CRD) system from (Sobanski, Schuladen, et al. 2016).	34
Figure 10. Absorption cross section of NO ₂ (Vandaele et al. 2003) with a typical 405 nm laser emission spectrum.	36
Figure 11. Thermogram of NO ₂ yield from peroxyacetyl nitrate (PAN) and isopropyl nitrate (iPN) as a function of set temperature.	37
Figure 12. NO ₃ absorption spectrum from (Orphal et al., 2003) and a typical 5-CRD laser diode emission spectrum centered about 662 nm.	45
Figure 13. Schematic of instrument locations relative to the SAPHIR campaign. MPIC = Max Planck Institut fuer Chemie, where the 5-CRD was located. NOAA/CNRS = Location of the other NO ₃ / N ₂ O ₅ instrument.	54
Figure 14. Overview of measurements of O ₃ , NO ₂ , NO ₃ , N ₂ O ₅ made during the 2017 AQABA ship campaign. $k(\text{NO}_3)$ = the loss rate (in s ⁻¹) of NO ₃ due to all processes, direct and indirect. Mixing ratios of NO ₃ shown are derived from calculations from [NO ₂], [N ₂ O ₅] measurements and the equilibrium constant K_{eq} from the literature. (N) = North, (S) = South.	57
Figure 15. $K_{\text{eq}}(\text{T})[\text{NO}_2]$ vs. $[\text{N}_2\text{O}_5]/[\text{NO}_3]$ for one night (22-23 August, north Red Sea) in the SAPHIR campaign compared with one experiment conducted during the 2018 SAPHIR campaign. Blue line indicates the 1:1 ratio.	59
Figure 16. Histograms of NO ₃ reactivity from the AQABA campaign. This figure details the first leg of the campaign (La Seyne-sur-Mer to Kuwait). The histograms show $k(\text{NO}_3)$ calculated directly from measurements of $K_{\text{eq}}(\text{T}) \times \text{N}_2\text{O}_5 (= \text{NO}_3)$ in black, while the red bars show the lower-limit to $k(\text{NO}_3)$, calculated from the limit of detection (LOD).	62
Figure 17. Histograms of NO ₃ reactivity (bin size = 0.02 s ⁻¹) from the AQABA campaign. This figure details the second leg of the campaign (Kuwait to La-Seyne-sur-Mer). The histograms show $k(\text{NO}_3)$ calculated directly from measurements of $K_{\text{eq}}(\text{T}) \times \text{N}_2\text{O}_5 (= \text{NO}_3)$ in black, while the red bars show the lower-limit to $k(\text{NO}_3)$, calculated from the limit of detection (LOD).	63
Figure 18. Course of the Kommandor Iona on the second leg of the AQABA campaign (3 - 31st August). The different regions are highlighted in different colors. The 4 pie charts represent the proportions of median $k(\text{NO}_3)$ assigned by known reaction partner of NO ₃ and N ₂ O ₅ for each of the regions, excluding the Indian Ocean.	65
Figure 19. Overview of selected parameters from the night of 22-23rd August in the Gulf of Suez, in the North Red Sea. ASA = Aerosol surface Area. P(NO ₃) = ppt per-second production rate of NO ₃ . NO ₃ mixing ratios presented are calculated according to (Equation 12).	67
Figure 20. Overview of reactivity ($k(\text{NO}_3)$) on the night 22-23 rd August. $k_{\text{Het}}(\text{NO}_3)$ and $k_{\text{Het}}(\text{N}_2\text{O}_5)$ refer to heterogeneous loss processes of NO ₃ and N ₂ O ₅ onto the surface of particles. $k(\text{VOC})$ includes the summed	

contribution of various VOCs measured during the AQABA campaign, detailed in section 3. $J(\text{NO}_3)$ is the photolysis rate of NO_3 and marks sunset and sunrise. Plotted below is the SO_2 mixing ratio (ppb) which tracks with unassigned $k(\text{NO}_3)$.	68
Figure 21. Contribution to median $k(\text{NO}_3)$ attributed to each known reaction partner during the night 22-23 August. * - $k[\text{NO}]$ calculated from limit of detection of NO measurement. Data from plumes excluded.	69
Figure 22. Histogram of predicted $\text{N}_2\text{O}_5/\text{NO}_3 (= K_{\text{eq}}[\text{NO}_2])$ ratios during AQABA. The red data are calculated from the observed temperatures and the blue data are the calculated with Temperature -10K.	75
Figure 23. Unassigned contribution to the first order loss rate of $\text{NO}_3 (L(\text{NO}_3))$ vs. $\text{NO}_2 / \text{SO}_2$ for the night 22-23 August (North Red Sea)	78
Figure 24. $k(\text{NO}_3)$ vs NO_x/NO_y , and $\text{SO}_2/\text{SO}_2+\text{SO}_4^{2-}$ ratio for the entire AQABA campaign	80
Figure 25. $k(\text{NO}_3)/[\text{SO}_2]$ vs the NO_x/NO_y ratio for the entire AQABA campaign.	81
Figure 26. Overview of selected parameters from the night 18 - 19 August. ASA = Aerosol Surface Area	83
Figure 27. FACSIMILE simulated N_2O_5 mixing ratios compared with measured values (pink). The black, red and blue lines make different assumptions of the loss terms of $\text{NO}_3 (k(\text{NO}_3))$ where black includes the sum of all attributed loss processes (VOC, Heterogeneous, etc) and red and blue include the sum of all loss process plus an additional loss term derived from the relationships discussed in 5.3.4. Blue shaded area shows $J(\text{NO}_3)$, indicating dusk and dawn.	84
Figure 28. Integrated NO_x loss via day (red) and night (black) mechanisms for the Red Sea, Mediterranean Sea and Persian Gulf regions.	87
Figure 29. Integrated NO_x loss via day (red) and night (black) mechanisms for the Indian Ocean region	87
Figure 30. Selected parameters from 4-8th August in the Persian Gulf. $P(\text{HNO}_3)$ and $P(\text{NO}_3)$ refer to the gas-phase production of HNO_3 by OH oxidation of NO_x and the production of radical NO_3 from O_3 oxidation of NO_x , respectively.	88
Figure 31. Selected parameters from 8-12th August in the Indian Ocean. $P(\text{HNO}_3)$ and $P(\text{NO}_3)$ refer to the gas-phase production of HNO_3 by OH oxidation of NO_x and the production of radical NO_3 from O_3 oxidation of NO_x , respectively.	89
Figure 32. Selected parameters from 15-20th August in the Red Sea. $P(\text{HNO}_3)$ and $P(\text{NO}_3)$ refer to the gas-phase production of HNO_3 by OH oxidation of NO_x and the production of radical NO_3 from O_3 oxidation of NO_x , respectively.	90
Figure 33. Selected parameters from 20-25th August in the North Red Sea. $P(\text{HNO}_3)$ and $P(\text{NO}_3)$ refer to the gas-phase production of HNO_3 by OH oxidation of NO_x and the production of radical NO_3 from O_3 oxidation of NO_x , respectively.	91
Figure 34. Selected parameters from 25-31st August in the Mediterranean Sea. $P(\text{HNO}_3)$ and $P(\text{NO}_3)$ refer to the gas-phase production of HNO_3 by OH oxidation of NO_x and the production of radical NO_3 from O_3 oxidation of NO_x , respectively.	92
Figure 35. Averaged diurnal cycles of the marine Boundary Layer (BL) height. The shaded area represents the (1 σ) standard deviation of the BL throughout the entire AQABA campaign.	93
Figure 36. Corrected NO_2 signals for each instrument on 13 th of August.	98
Figure 37. Comparison of NO_2 measurements from the experiment 8/13. All measurements are plotted against the 5-CRD in the x-axis.	99
Figure 38. NO_2 intercomparisons against the 5-CRD for slope, intercepts and coefficient of determination for each instrument by date during the Gas Phase section of the 2017 SAPHIR campaign.	101
Figure 39. NO_2 intercomparisons against the 5-CRD for slope, intercepts and coefficient of determination for each instrument by date during the Seed Aerosol section of the 2017 SAPHIR campaign.	102
Figure 40. Comparison of finalized NO_2 dataset against the datasets used to calculate it. Zero signals and other NO_2 measurements omitted for clarity.	103
Figure 41. Measured NO_3 and N_2O_5 from each CRD instrument for the 8/10 NO_3 -Isoprene experiment plotted against time.	105

Figure 42. $[\text{N}_2\text{O}_5]/[\text{NO}_3]$ ratios against time for the experiment on 8/10. $K_{\text{eq}}(\text{T})$ is calculated from (JPL. rec.). Shaded area surrounding lines represent 1- σ uncertainties of each measurement.	106
Figure 43. Plots of 5-CRD vs. CNRS-CRD for NO_3 and N_2O_5 mixing ratios for the 8/10 NO_3 -Isoprene experiments	106
Figure 44. NO_3 (black) and N_2O_5 (red) intercomparisons against the 5-CRD for slope, intercepts and coefficient of determination for the CNRS-CRD by date during the 2017 SAPHIR campaign.	109
Figure 45. Corrected data from the experiment on the 8th August (100 ppb O_3 , 25 ppb NO_2 , 10 ppb Isoprene) showing a large difference between the NO_2 (black) and the PNs + NO_2 (red) signals. RT = Room Temperature.	114
Figure 46. Relative thermogram of signal in the PNs + NO_2 channel vs. the ANs + PNs + NO_2 channel taken during the NO_3 -Isoprene experiments. PN channel was taken without the glass beads described in section 3 and 7.2.5.	117
Figure 47. Change in AN vs. Change in isoprene for each evaluated experiment. Error bars excluded for clarity.	120
Figure 48. Yields of ANs per isoprene reacted with per experiment. Multiple data points for the same date represent multiple injections.	121
Figure 49. Delta Isoprene vs. Delta ANs for each experiment	121
Figure 50. Raw alkyl nitrates before (left) and after (right) an injection of isoprene for a gas-phase experiment (8/8). The right side shows a significantly longer period of time for the slope to approach 0 ppt during a zeroing period, and significantly longer to return to the overall experimental trend after a zeroing period after exposure to isoprene nitrates compared with the signal earlier in the experiment.	123
Figure 51. Selected trace gases from the experiment 7/31. No isoprene was injected in this experiment.	125
Figure 52. Overview of NO , NO_2 , NO_3 , N_2O_5 , SO_2 , DMS and aerosol surface area (ASA) measurements from the 2017 AQABA campaign.	132
Figure 53. Supporting meteorological data of air temperature, air pressure (sea level), relative humidity and marine boundary layer height from the 2017 AQABA campaign	133
Figure 54. $k(\text{NO}_3)/[\text{NO}_2]$ vs. NO_x/NO_y ratio. Fit according to $y=ab^x$ where $a=1.16 \times 10^{-13}$, $b=666$. Analogous to $k(\text{NO}_3)/[\text{SO}_2]$ plot shown in 5.2.4, describing the dependence on co-emitted $k(\text{NO}_3)$ -contributing VOC from ship emissions on the age of the air mass as indicated by the NO_x/NO_y ratio, fitted to an approximate timescale based on reasonable assumptions of $[\text{OH}]$ and $[\text{O}_3]$.	134
Figure 55. FACSIMILE simulations comparing time taken (in s) to reestablish NO_2 - NO_3 - N_2O_5 equilibrium following titration of all NO_3 by NO under AQABA temperature conditions. Simulation informed how long after a NO titration the data were likely to not be in equilibrium, necessary for determination of the mixing ratios of NO_3 via calculation and for calculation of steady state lifetimes.	135
Figure 56. Comparison of $[\text{N}_2\text{O}_5]/K_{\text{eq}}(\text{T})[\text{NO}_2]$ -calculated NO_3 mixing ratios against NO_3 measured directly by the 5-CRD for the entire AQABA campaign. Calculated NO_3 mixing ratios were almost always systematically higher due to losses of NO_3 to the instrument walls.	136
Figure 57. Reaction scheme of oxidation of Isoprene by NO_3	137
Figure 58. Overview of NO_3 , N_2O_5 , NO_2 , ΣPNs , ΣANs , O_3 and Isoprene measurements from SAPHIR experiments 7/31 – 8/13	138

Tables

Table 1. Global Sources of NO_x (in TgN yr^{-1}) adapted from (Enhalt and Prather, 2001) to include most recent IPCC (2014) estimate. The next IPCC report (AR6) is predicted to be released in 2022.	11
Table 2. NO_3 uptake coefficients with ranges. Adapted from (Brown and Stutz, 2012). All γ coefficients given at 298 K.	18
Table 3. N_2O_5 uptake coefficients with ranges. Adapted from (Brown and Stutz, 2012). All γ coefficients given at 298 K	19

Table 4. Overview of measured and limit of detection (LOD-Limited) NO ₃ reactivity by region. L1, L2 – Leg ½.	64
Table 5. Rate coefficient of NO ₃ + each gas-phase partner ([X]) measured during the AQABA campaign at 298 K. Lifetimes of each partner in the presence of 10 ppt NO ₃ given to contextualize the relative importance of each VOC in controlling k(NO ₃).	70
Table 6. Summary of NO _x losses per region during the AQABA campaign. Mean L(NO _x) per hour is given for both day time and night time loss mechanisms. k(NO ₂) is the average (mean) loss rate of NO ₂ in s ⁻¹	93
Table 7. Instruments measuring NO ₂ during the NO ₃ -Isoprene SAPHIR chamber experiments with technical information on limit of detection, total uncertainty and total days of data coverage. CRD = Cavity ringdown. CLD = Chemiluminescence detector.	97
Table 8. Cavity Ringdown (CRD) instruments for measuring NO ₃ and N ₂ O ₅ during the SAPHIR Campaign with reported technical data (Total Uncertainty, Limit of detection).	104
Table 9. NO ₃ -Isoprene campaign experiments. 7/31 - 8/13 are gas-phase experiments and 8/14 - 8/24 include the addition of seed aerosol ((NH ₄) ₂ SO ₄). The slopes of the linear fit of 5-CRD vs. CNRS-CRD are display for NO ₃ and N ₂ O ₅ . Agreement to K _{eq} [NO ₂] details where the uncertainties of the measurements overlap with the uncertainties of K _{eq} [NO ₂]. Note: CO = Carbon Monoxide; MVK = Methylvinyl Ketone; RH = Relative Humidity.	108
Table 10. Alkyl Nitrate (ANs) yield per molecule isoprene and Alkyl Nitrate per molecule NO ₂ . NO ₂ yields have been adjusted according to losses to the chamber walls via NO ₃ and N ₂ O ₅ estimated by (Dewald et al., 2020). N/A describes a situation where a yield could not be obtained.	119
Table 11. Summary of NO ₃ + Isoprene yields and the methods used to derive them.	126

Appendix F – Bibliography

References

- Allan, B. J., G. McFiggans, J. M. C. Plane, H. Coe, and G. G. McFadyen. 2000. "The nitrate radical in the remote marine boundary layer." *J. Geophys. Res* 24 (204): 105.
- Aschmann, S.A., and R. Atkinson. 2010. "Effect of Structure on the Rate Constants for Reaction of NO₃ Radicals with a Series of Linear and Branched C-5-C-7 1-Alkenes at 296±2 K." *The Journal of Physical Chemistry* 115.
- Aschmann, S.M., and R. Atkinson. 1995. "Rate constants for the reactions of the NO₃ radical with alkanes at 296 ± 2 K." *Atmos. Environ.* 29 (17): 2311-2316.
- Atkinson, R. 1991. *J. Phys. Chem. Ref. Data.* 20: 459.
- Atkinson, R., C. N. Plum, W. P. L. Carter, A. M. Winer, and J. N. Pitts Jr. 1984. *J. Phys. Chem* 1210.
- Atkinson, R., S. M. Aschmann, and J. N. Pitts Jr. 1988. *J. Phys. Chem.* 94: 3454.
- Atkinson, Roger., Sara M. Aschmann, Arthur M. Winer, and James N. Pitts. 1984. "Kinetics of the gas-phase reactions of nitrate radicals with a series of dialkenes, cycloalkenes, and monoterpenes at 295 ± 1K." *Environ. Sci. Technol.* 370-375.
- Bagley, J. A., C. Canosa-Mas, M. R. Little, A. D. Parr, S. J. Smith, S. J. Waygood, and R.P. Wayne. 1990. *J. Chem. Soc. Faraday Trans.* 86: 2109.
- Bagley, Jane A., Carlos Canosa-Mas, Mark R. Little, A. Douglas Parr, Stuart J. Smith, Steven J. Waygood, and Richard P. Wayne. 1990. "Temperature dependence of reactions of the nitrate radical with alkanes." *Journal of the Chemical Society, Faraday Transactions* 2109-2114.
- Bertman, Steven B., and James M. Roberts. 1991. "A PAN analog from isoprene photooxidation." *Geophys. Research Letters* 1461-1464.
- Boyd, A. A., C. E. Canosa-Mas, A. D. King, R. P. Wayne, and M. R. Wilson. 1991. *J. Chem. Soc. Faraday* 87: 2913.
- Brown, Steven S., A. R. Ravishankara, and Harald Stark. 2000. "Simultaneous Kinetics and Ring-down: Rate Coefficients from Single Cavity Loss Temporal Profiles." *J. Phys. Chem. A* 7044-7054.
- Carr, S.A., David R. Glowacki, Chi-Hsiu Liang, Teresa Baeza-Romero, Mark A. Blitz, Michael J. Pilling, and Paul W. Seakins. 2011. "Experimental and Modeling Studies of the Pressure and Temperature Dependences of the Kinetics and the OH Yields in the Acetyl + O₂ Reaction." *Atmos. Chem. Phys.* 1069-1085.
- Chen, Sun-Yang, and Yuan-Pern Lee. 2010. "Transient infrared absorption of t-CH₃C(O)OO, c-CH₃C(O)OO, and α-lactone recorded in gaseous reactions of CH₃CO and O₂." *J. Chem. Phys.*
- Chew, Andrew A., Roger. Atkinson, and Sara M. Aschmann. 1998. "Kinetics of the gas-phase reactions of NO₃ radicals with a series of alcohols, glycol ethers, ethers and chloroalkenes." *J. Chem. Soc., Faraday Trans.* 1083-1089.

- Copernicus Climate Change Service (C3S). 2017. "ECMWF." *ERA5: Fifth generation of ECMWF atmospheric reanalyses of the global climate*. Accessed April 29, 2020. <https://cds.climate.copernicus.eu/cdsapp#!/home>.
- Curtis, A. R., and W. P. Sweetenham. 1987. *Facsimile*. R-12805, Atomic Energy Research Establishment.
- dateandtime.com. 2020. *dateandtime.com*. Accessed 6 7, 2020. <https://www.timeanddate.com/sun/spain/cadiz?month=11&year=2008>.
- dateandtime.info. 2020. *Sunrise and sunset time, day length in Nicosia, Cyprus*. March 19. <https://dateandtime.info/citysunrisesunset.php?id=146268&month=8&year=2017>.
- Dubé, W.P, S.S. Brown, H.D. Osthoff, M.R. Nunley, S.J. Ciciora, M.W. Paris, R.J. McLaughlin, and A.R. Ravishankara. 2006. "Aircraft instrument for simultaneous, in situ measurement of NO₃ and N₂O₅ via pulsed cavity ring-down spectroscopy." *Review of Scientific Instruments* 77.
- Finlayson-Pitts, Barbara J., and James N. Pitts Jr. 1999. *Chemistry of the upper and lower atmosphere*. Irvine, CA: Academic Press.
- George, C., J. L. Ponche, P. Mirabel, W. Behnke, V. Scheer, and C. Zetzsch. 1994. "Study of the Uptake of N₂O₅ by Water and NaCl Solutions." *J. Phys. Chem.* 8780-8784.
- Grosjean, Daniel., and Jeffery. Harrison. 1985. "Response of Chemiluminescence NO_x Analyzers and Ultraviolet Ozone Analyzers to Organic Air Pollutants." *Environ. Sci. Technol.* 862-865.
- Guenther, A. B., X. Jiang, C. L. Heald, T. Sakulyanontvittaya, T. Duhl, L. K. Emmons, and X. Wang. 2012. "The Model of Emissions of Gases and Aerosols from Nature version 2.1 (MEGAN2.1): an extended and updated framework for modeling biogenic emissions." *Geosci. Model. Dev.* 1472-1492.
- Guenther, A., T. Karl, P. Harley, C. Wiedinmyer, P. I. Palmer, and C. Geron. 2006. "Estimates of global terrestrial isoprene emissions using MEGAN (Model of Emissions of Gases and Aerosols from Nature)." *Atmos. Chem. Phys.* 3181-3210.
- Heintz, F., U. Platt, H. Flentje, and R Dubois. 1996. "Long term observation of Nitrate radicals at the Tor Stations, Kap Arkona (Ruegen)." *J. Geophys. Res.* 22891–22910.
- IQAir. 2019. *REPORT: Over 90% of global population breathes dangerously polluted air*. Accessed May 3, 2020. <https://www.iqair.com/blog/report-over-90-percent-of-global-population-breathes-dangerously-polluted-air>.
- ITF. 2019. *ITF Transport Outlook 2019*. Paris: OECD Publishing.
- Jordan, A., S. Haidacher, G. Hanel, E. Hartungen, L. Märk, H. Seehauser, R. Schottkowsky, P. Sulzer, and T.D. Märk. 2009. "A high resolution and high sensitivity proton-transfer-reaction time-of-flight mass spectrometer (PTR-TOF-MS)." *International Journal of Mass Spectrometry* 286: 122-128.
- Karagulian, F., C. Santschi, and M. J. Rossi. 2006. "The heterogeneous chemical kinetics of N₂O₅ on CaCO₃ and other atmospheric mineral dust surrogates." *Atmos. Chem. Phys.* 1373-1388.

- Kley, D., and M. McFarland. 1980. "Chemiluminescence Detector for NO and NO₂." *Atmospheric Technology* 63-69.
- Leighton, P.A. 1961. "Photochemistry of Air Pollution." *Academic Press*.
- Liss, P., and P. Slater. 1974. "Flux of Gases across the Air-Sea Interface." *Nature* 247: 181–184.
- Platt, U. F., A. M. Winer, H. W. Bierman, R. Atkinson, and Jr J. N. Pitts. 1984. *Environ. Sci. Technol.* 365–369.
- Platt, Ulrich F., Arthur M. Winer, Heinz W. Biermann, Roger. Atkinson, and James N. Pitts. 1984. "Measurement of nitrate radical concentrations in continental air." *Environ. Sci. Technol.* 18 (5): 365–369.
- Sanadze, G.A., and A.L. Kursanov. 1966. "On certain conditions of the evolution of the diene C₅H₈ from poplar leaves." *Sov. Plant Physiol.* 184-189.
- Special, Agis Salpukas. 1972. "Los Angeles Officials Insist the Air is Getting Cleaner." *The New York Times*, August 7: 54.
- Stein, A.F., Draxler, R.R, Rolph, G.D., Stunder, B.J.B., Cohen, M.D., and Ngan, F. 2015. "NOAA's HYSPLIT atmospheric transport and dispersion modeling system." *Bull. Amer. Meteor. Soc.* (Bull. Amer. Meteor. Soc.).
- Wallington, T. J., R. Atkinson, A. N. Winer, and J. N. Pitts. 1988. "Kinetics of the reaction of NO₃ radicals with CH₃SSCH₃." *J. Phys. Chem.* 4640.
- Walters, Robert. 1983. "Does Reagan still fear "Killer Trees"?" *The Southeast Missourian*, April 1: 3.
- Wayne, Richard P., I. Barnes, P. Biggs, J.P. Burrows, C.E. Canosa-Mas, J. Hjorth, G. Le Bras, et al. 1990. *The Nitrate Radical*. Oxford, U.K.: Oxford University Press.
- York, D. 1969. "Least squares fitting of a straight line with correlated errors." *Earth and Planet Sci. Lett.* 320-324.
- Zeldovich, Y.A. 1947. "The Oxidation of Nitrogen in Combustion Explosions."
- Aldener, Mattias, Steven S. Brown, Harald Stark, Eric J. Williams, Brian M. Lerner, William C. Kuster, Paul D. Goldan, et al. 2006. "Reactivity and Loss Mechanisms of NO₃ and N₂O₅ in a Polluted Marine Environment: Results from in Situ Measurements during New England Air Quality Study 2002." *Journal of Geophysical Research Atmospheres* 111 (23): 1–15.
<https://doi.org/10.1029/2006JD007252>.
- Allan, B. J., N. Carslaw, H. Coe, R. A. Burgess, and J. M.C. Plane. 1999. "Observations of the Nitrate Radical in the Marine Boundary Layer." *Journal of Atmospheric Chemistry* 33 (2): 129–54.
<https://doi.org/10.1023/A:1005917203307>.
- Ambrose, J. L., H. Mao, H. R. Mayne, J. Stutz, R. Talbot, and B. C. Sive. 2007. "Nighttime Nitrate Radical Chemistry at Appledore Island, Maine during the 2004 International Consortium for Atmospheric Research on Transport and Transformation." *Journal of Geophysical Research Atmospheres* 112

- (21): 1–19. <https://doi.org/10.1029/2007JD008756>.
- Andreae, Meinrat O. 1990. "Ocean-Atmosphere Interactions in the Global Biogeochemical Sulfur Cycle." *Marine Chemistry* 30 (C): 1–29. [https://doi.org/10.1016/0304-4203\(90\)90059-L](https://doi.org/10.1016/0304-4203(90)90059-L).
- . 2019. "Emission of Trace Gases and Aerosols from Biomass Burning – An Updated Assessment." *Atmospheric Chemistry and Physics Discussions* 19: 1–27. <https://doi.org/10.5194/acp-2019-303>.
- Avnery, Shiri, Denise L. Mauzerall, Junfeng Liu, and Larry W. Horowitz. 2011. "Global Crop Yield Reductions Due to Surface Ozone Exposure: 2. Year 2030 Potential Crop Production Losses and Economic Damage under Two Scenarios of O₃ Pollution." *Atmospheric Environment* 45 (13): 2297–2309. <https://doi.org/10.1016/j.atmosenv.2011.01.002>.
- Barkley, P. Michael, Gonzalo González Abad, P. Thomas Kurosu, Robert Spurr, Sara Torbatian, and Christophe Lerot. 2017. "OMI Air-Quality Monitoring over the Middle East." *Atmospheric Chemistry and Physics* 17 (7): 4687–4709. <https://doi.org/10.5194/acp-17-4687-2017>.
- Barnes, Ian, Volker Bastian, Karl H. Becker, and Zhu Tong. 1990. "Kinetics and Products of the Reactions of NO₃ with Monoalkenes, Dialkenes, and Monoterpenes." *Journal of Physical Chemistry* 94 (6): 2413–19. <https://doi.org/10.1021/j100369a041>.
- Beaver, M. R., J. M. St. Clair, F. Paulot, K. M. Spencer, J. D. Crouse, B. W. Lafranchi, K. E. Min, et al. 2012. "Importance of Biogenic Precursors to the Budget of Organic Nitrates: Observations of Multifunctional Organic Nitrates by CIMS and TD-LIF during BEARPEX 2009." *Atmospheric Chemistry and Physics* 12 (13): 5773–85. <https://doi.org/10.5194/acp-12-5773-2012>.
- Berden, Giel, Rudy Peeters, and Gerard Meijer. 2000. "Cavity Ring-down Spectroscopy: Experimental Schemes and Applications." *International Reviews in Physical Chemistry* 19 (4): 565–607. <https://doi.org/10.1080/014423500750040627>.
- Bertman, Steven B., and James M. Roberts. 1991. "A PAN Analog from Isoprene Photooxidation." *Geophysical Research Letters* 18 (8): 1461–64. <https://doi.org/10.1029/91GL01852>.
- Bertram, T. H., J. A. Thornton, and T. P. Riedel. 2009. "An Experimental Technique for the Direct Measurement of N₂O₅ Reactivity on Ambient Particles." *Atmospheric Measurement Techniques* 2 (1): 231–42. <https://doi.org/10.5194/amt-2-231-2009>.
- Bertram, Timothy H., Joel A. Thornton, Theran P. Riedel, Ann M. Middlebrook, Roya Bahreini, Timothy S. Bates, Patricia K. Quinn, and Derek J. Coffman. 2009. "Direct Observations of N₂O₅ Reactivity on Ambient Aerosol Particles." *Geophysical Research Letters* 36 (19): 1–5. <https://doi.org/10.1029/2009GL040248>.
- Bey, Isabelle, Bernard Aumont, and Gérard Toupance. 2001. "A Modeling Study of the Nighttime Radical Chemistry in the Lower Continental Troposphere 1. Development of a Detailed Chemical Mechanism Including Nighttime Chemistry." *Journal of Geophysical Research Atmospheres* 106 (D9): 9959–90. <https://doi.org/10.1029/2000JD900347>.
- Blake, N.~J., B Barletta, I.~J. Simpson, J Schroeder, S Hughes, J.~E. Marrero, S Meinardi, et al. 2014. "Spatial Distributions and Source Characterization of Trace Organic Gases during SEAC⁴RS and Comparison to DC3." In *AGU Fall Meeting Abstracts*, 2014:A33C-3197.
- Bossmeyer, J., T. Brauers, C. Richter, F. Rohrer, R. Wegener, and A. Wahner. 2006. "Simulation Chamber Studies on the NO₃ Chemistry of Atmospheric Aldehydes." *Geophysical Research Letters* 33 (18):

- 1–5. <https://doi.org/10.1029/2006GL026778>.
- Boucher, Olivier, and Ulrike Lohmann. 1995. "The Sulfate-CCN-Cloud Albedo Effect." *Tellus B: Chemical and Physical Meteorology* 47 (3): 281–300. <https://doi.org/10.3402/tellusb.v47i3.16048>.
- Boucher, Olivier, David Randall, Paulo Artaxo, Christopher Bretheron, Graham Feingold, Piers Forster, Veli-Matti Kerminen, et al. 2013. "Clouds and Aerosols." *Climate Change 2013 the Physical Science Basis: Working Group I Contribution to the Fifth Assessment Report of the Intergovernmental Panel on Climate Change* 9781107057: 571–658. <https://doi.org/10.1017/CBO9781107415324.016>.
- Bourtsoukidis, Efstratios, Lisa Ernle, John N. Crowley, Jos Lelieveld, Jean Daniel Paris, Andrea Pozzer, David Walter, and Jonathan Williams. 2019. "Non-Methane Hydrocarbon (C2-C8) Sources and Sinks around the Arabian Peninsula." *Atmospheric Chemistry and Physics* 19 (10): 7209–32. <https://doi.org/10.5194/acp-19-7209-2019>.
- Brown, S. S., J. A. Degouw, C. Warneke, T. B. Ryerson, W. P. Dubé, E. Atlas, R. J. Weber, et al. 2009. "Nocturnal Isoprene Oxidation over the Northeast United States in Summer and Its Impact on Reactive Nitrogen Partitioning and Secondary Organic Aerosol." *Atmospheric Chemistry and Physics* 9 (9): 3027–42. <https://doi.org/10.5194/acp-9-3027-2009>.
- Brown, S. S., J. E. Dibb, H. Stark, M. Aldener, M. Vozella, S. Whitlow, E. J. Williams, et al. 2004. "Nighttime Removal of NO_x in the Summer Marine Boundary Layer." *Geophysical Research Letters* 31 (7): 2–6. <https://doi.org/10.1029/2004GL019412>.
- Brown, Steven S. 2003. "Absorption Spectroscopy in High-Finesse Cavities for Atmospheric Studies." *Chemical Reviews* 103 (12): 5219–38. <https://doi.org/10.1021/cr020645c>.
- Brown, Steven S., Hyunjin An, Meehye Lee, Jeong Hoo Park, Sang Deok Lee, Dorothy L. Fibiger, Erin E. McDuffie, William P. Dubé, Nicholas L. Wagner, and Kyung Eun Min. 2017. "Cavity Enhanced Spectroscopy for Measurement of Nitrogen Oxides in the Anthropocene: Results from the Seoul Tower during MAPS 2015." *Faraday Discussions* 200: 529–57. <https://doi.org/10.1039/c7fd00001d>.
- Brown, Steven S., William P. Dubé, Hendrik Fuchs, Thomas B. Ryerson, Adam G. Wollny, Charles A. Brock, Roya Bahreini, et al. 2009. "Reactive Uptake Coefficients for N₂O₅ Determined from Aircraft Measurements during the Second Texas Air Quality Study: Comparison to Current Model Parameterizations." *Journal of Geophysical Research Atmospheres* 114 (11): 1–16. <https://doi.org/10.1029/2008JD011679>.
- Brown, Steven S., William P. Dubé, Hans D. Osthoff, Jochen Stutz, Thomas B. Ryerson, Adam G. Wollny, Charles A. Brock, et al. 2007. "Vertical Profiles in NO₃ and N₂O₅ Measured from an Aircraft: Results from the NOAA P-3 and Surface Platforms during the New England Air Quality Study 2004." *Journal of Geophysical Research Atmospheres* 112 (22): 1–17. <https://doi.org/10.1029/2007JD008883>.
- Brown, Steven S., William P. Dubé, Jeff Peischl, Thomas B. Ryerson, Elliot Atlas, Carsten Warneke, Joost A. De Gouw, et al. 2011. "Budgets for Nocturnal VOC Oxidation by Nitrate Radicals Aloft during the 2006 Texas Air Quality Study." *Journal of Geophysical Research Atmospheres* 116 (24): 1–15. <https://doi.org/10.1029/2011JD016544>.
- Brown, Steven S., Harald Stark, and A. R. Ravishankara. 2003. "Applicability of the Steady State Approximation to the Interpretation of Atmospheric Observations of NO₃ and N₂O₅." *Journal of Geophysical Research D: Atmospheres* 108 (17): 1–10. <https://doi.org/10.1029/2003jd003407>.

- Brown, Steven S., and Jochen Stutz. 2012. "Nighttime Radical Observations and Chemistry." *Chemical Society Reviews* 41 (19): 6405–47. <https://doi.org/10.1039/c2cs35181a>.
- Carlton, A. G., C. Wiedinmyer, and J. H. Kroll. 2009. "A Review of Secondary Organic Aerosol (SOA) Formation from Isoprene." *Atmospheric Chemistry and Physics* 9 (14): 4987–5005. <https://doi.org/10.5194/acp-9-4987-2009>.
- Carslaw, N., L. J. Carpenter, J. M.C. Plane, B. J. Allan, R. A. Burgess, K. C. Clemitshaw, H. Coe, and S. A. Penkett. 1997. "Simultaneous Observations of Nitrate and Peroxy Radicals in the Marine Boundary Layer." *Journal of Geophysical Research Atmospheres* 102 (15): 18917–33. <https://doi.org/10.1029/97jd00399>.
- Chameides, W. L., R. W. Lindsay, J. Richardson, and C. S. Kiang. 1988. "The Role of Biogenic Hydrocarbons in Urban Photochemical Smog: Atlanta as a Case Study." *Science* 241 (4872): 1473–75. <https://doi.org/10.1126/science.3420404>.
- Cooper, D. A., K. Peterson, and D. Simpson. 1996. "Hydrocarbon, PAH and PCB Emissions from Ferries: A Case Study in the Skagerak-Kattegatt-Öresund Region." *Atmospheric Environment* 30 (14): 2463–73. [https://doi.org/10.1016/1352-2310\(95\)00494-7](https://doi.org/10.1016/1352-2310(95)00494-7).
- Corbett, James J., Paul S. Fischbeck, and Spyros N. Pandis. 1999. "Global Nitrogen and Sulfur Inventories for Oceangoing Ships." *Journal of Geophysical Research Atmospheres* 104 (D3): 3457–70. <https://doi.org/10.1029/1998JD100040>.
- Crowley, J. N., M. Ammann, R. A. Cox, R. G. Hynes, M. E. Jenkin, A. Mellouki, M. J. Rossi, J. Troe, and T. J. Wallington. 2010. "Evaluated Kinetic and Photochemical Data for Atmospheric Chemistry: Volume v -Heterogeneous Reactions on Solid Substrates." *Atmospheric Chemistry and Physics* 10 (18): 9059–9223. <https://doi.org/10.5194/acp-10-9059-2010>.
- Crowley, J. N., G. Schuster, N. Pouvesle, U. Parchatka, H. Fischer, B. Bonn, H. Bingemer, and J. Lelieveld. 2010. "Nocturnal Nitrogen Oxides at a Rural Mountain-Site in South-Western Germany." *Atmospheric Chemistry and Physics* 10 (6): 2795–2812. <https://doi.org/10.5194/acp-10-2795-2010>.
- Crowley, J. N., J. Thieser, M. J. Tang, G. Schuster, H. Bozem, Z. H. Beygi, H. Fischer, et al. 2011. "Variable Lifetimes and Loss Mechanisms for NO₃ and N₂O₅ during the DOMINO Campaign: Contrasts between Marine, Urban and Continental Air." *Atmospheric Chemistry and Physics* 11 (21): 10853–70. <https://doi.org/10.5194/acp-11-10853-2011>.
- Crowley, J. N., J. Thieser, M. Tang, G. Schuster, H. Bozem, Z. Hosaynali Beygi, H. Fischer, et al. 2011. "Variable Lifetimes and Loss Mechanisms for NO₃ and N₂O₅ during the DOMINO Campaign: Contrasts between Marine, Urban and Continental Air." *Atmospheric Chemistry and Physics Discussions* 11 (6): 17825–77. <https://doi.org/10.5194/acpd-11-17825-2011>.
- Davis, J. M., P. V. Bhavsar, and K. M. Foley. 2008. "Parameterization of N₂O₅ Reaction Probabilities on the Surface of Particles Containing Ammonium, Sulfate, and Nitrate." *Atmospheric Chemistry and Physics* 8 (17): 5295–5311. <https://doi.org/10.5194/acp-8-5295-2008>.
- Day, D. A., P. J. Wooldridge, M. B. Dillon, J. A. Thornton, and R. C. Cohen. 2002. "A Thermal Dissociation Laser-Induced Fluorescence Instrument for in Situ Detection NO₂, Peroxy Nitrates, Alkyl Nitrates, and HNO₃." *Journal of Geophysical Research Atmospheres* 107 (5–6). <https://doi.org/10.1029/2001jd000779>.
- Delmas, R., D. Serça, and C. Jambert. 1997. "Global Inventory of NO_x Sources." *Nutrient Cycling in*

- Agroecosystems* 48 (1–2): 51–60. <https://doi.org/10.1023/A:1009793806086>.
- Deming, Benjamin L., Demetrios Pagonis, Xiaoxi Liu, Douglas A. Day, Ranajit Talukdar, Jordan E. Krechmer, Joost A. De Gouw, Jose L. Jimenez, and Paul J. Ziemann. 2019. “Measurements of Delays of Gas-Phase Compounds in a Wide Variety of Tubing Materials Due to Gas-Wall Interactions.” *Atmospheric Measurement Techniques* 12 (6): 3453–61. <https://doi.org/10.5194/amt-12-3453-2019>.
- Demore, W. B., J. J. Margitan, M. J. Molina, R. T. Watson, D. M. Golden, R. F. Hampson, M. J. Kurylo, C. J. Howard, and A. R. Ravishankara. 1985. “Tables of Rate Constants Extracted from Chemical Kinetics and Photochemical Data for Use in Stratospheric Modeling. Evaluation Number 7.” *International Journal of Chemical Kinetics* 17 (10): 1135–51. <https://doi.org/10.1002/kin.550171010>.
- DeMore, W B, S P Sander, C J Howard, A R Ravishankara, D M Golden, C E Kolb, R F Hampson, M J Kurylo, and M J Molina. 1997. “Chemical Kinetics and Photochemical Data for Use in Stratospheric Modeling.” *JPL Publication* 4 (12).
- Dewald, Patrick, Jonathan M Liebmann, Nils Friedrich, Justin Shenolikar, Jan Schuladen, David Reimer, Ralf Tillmann, et al. 2020. “Evolution of NO₃ Reactivity during the Oxidation of Isoprene.” *Atmospheric Chemistry and Physics*, no. 3: 1–29.
- Dockery, Douglas W., C. Arden Pope, Xiping xu, John D. Spengler, James H. Ware, Martha E. Fay, Benjamin G. Ferris, and Frank E. Speizer. 1993. “An Association between Air Pollution and Mortality in Six U.S. Cities.” *New England Journal of Medicine* 329 (24): 1753–59. <https://doi.org/10.1056/NEJM199312093292401>.
- Dorn, H. P., R. L. Apodaca, S. M. Ball, T. Brauers, S. S. Brown, J. N. Crowley, W. P. Dubé, et al. 2013. “Intercomparison of NO₃ Radical Detection Instruments in the Atmosphere Simulation Chamber SAPHIR.” *Atmospheric Measurement Techniques* 6 (5): 1111–40. <https://doi.org/10.5194/amt-6-1111-2013>.
- Dreyfus, Gabrielle B., Gunnar W. Schade, and Allen H. Goldstein. 2002. “Observational Constraints on the Contribution of Isoprene Oxidation to Ozone Production on the Western Slope of the Sierra Nevada, California.” *Journal of Geophysical Research Atmospheres* 107 (19): ACH 1-1-ACH 1-17. <https://doi.org/10.1029/2001JD001490>.
- Edtbauer, Achim, Christof Stönnner, Eva Y. Pfannerstill, Matias Berasategui, David Walter, John N. Crowley, Jos Lelieveld, and Jonathan Williams. 2020. “A New Marine Biogenic Emission: Methane Sulfonamide (MSAM), Dimethyl Sulfide (DMS), and Dimethyl Sulfone (DMSO₂) Measured in Air over the Arabian Sea.” *Atmospheric Chemistry and Physics* 20 (10): 6081–94. <https://doi.org/10.5194/acp-20-6081-2020>.
- EEA. 2003. “Nitrogen Oxides (NO_x) Emissions.” <https://doi.org/10.1201/9780203912782.pt2>.
- Eger, Philipp G., Nils Friedrich, Jan Schuladen, Justin Shenolikar, Horst Fischer, Ivan Tadic, Hartwig Harder, et al. 2019. “Shipborne Measurements of ClNO₂ in the Mediterranean Sea and around the Arabian Peninsula during Summer.” *Atmospheric Chemistry and Physics Discussions*, no. June: 1–37. <https://doi.org/10.5194/acp-2019-531>.
- Enhalt, D., and M. J. Prather. 2001. “Atmospheric Chemistry and Greenhouse Gases.” *IPCC*. <https://doi.org/10.2753/jes1097-203x330403>.
- Everest, Michael A., and Dean B. Atkinson. 2008. “Discrete Sums for the Rapid Determination of

- Exponential Decay Constants." *Review of Scientific Instruments* 79 (2).
<https://doi.org/10.1063/1.2839918>.
- Eyring, V., H. W. Köhler, J. Van Aardenne, and A. Lauer. 2005. "Emissions from International Shipping: 1. The Last 50 Years." *Journal of Geophysical Research D: Atmospheres* 110 (17): 171–82.
<https://doi.org/10.1029/2004JD005619>.
- Farahat, Ashraf. 2016. "Air Pollution in the Arabian Peninsula (Saudi Arabia, the United Arab Emirates, Kuwait, Qatar, Bahrain, and Oman): Causes, Effects, and Aerosol Categorization." *Arabian Journal of Geosciences* 9 (3). <https://doi.org/10.1007/s12517-015-2203-y>.
- Fenter, Frederick F., François Caloz, and Michel J. Rossi. 1996. "Heterogeneous Kinetics of N₂O₅ Uptake on Salt, with a Systematic Study of the Role of Surface Presentation (for N₂O₅ and HNO₃)." *Journal of Physical Chemistry* 100 (3): 1008–19. <https://doi.org/10.1021/jp9503829>.
- Fenter, Frederick F., and Michel J. Rossi. 2010. "ChemInform Abstract: Heterogeneous Reaction of NO₃ with Ice and Sulfuric Acid Solutions: Upper Limits for the Uptake Coefficients." *ChemInform* 28 (33): no-no. <https://doi.org/10.1002/chin.199733007>.
- Fischer, E. V., D. J. Jacob, R. M. Yantosca, M. P. Sulprizio, D. B. Millet, J. Mao, F. Paulot, et al. 2014. "Atmospheric Peroxyacetyl Nitrate (PAN): A Global Budget and Source Attribution." *Atmospheric Chemistry and Physics* 14 (5): 2679–98. <https://doi.org/10.5194/acp-14-2679-2014>.
- Fisher, Jenny A., Daniel J. Jacob, Katherine R. Travis, Patrick S. Kim, Eloise A. Marais, Christopher Chan Miller, Karen Yu, et al. 2016. "Organic Nitrate Chemistry and Its Implications for Nitrogen Budgets in an Isoprene- and Monoterpene-Rich Atmosphere: Constraints from Aircraft (SEAC4RS) and Ground-Based (SOAS) Observations in the Southeast US." *Atmospheric Chemistry and Physics* 16 (9): 5969–91. <https://doi.org/10.5194/acp-16-5969-2016>.
- Fontijn, Arthur, Alberto J. Sabadell, and Richard J. Ronco. 1970. "Homogeneous Chemiluminescent Measurement of Nitric Oxide with Ozone: Implications for Continuous Selective Monitoring of Gaseous Air Pollutants." *Analytical Chemistry* 42 (6): 575–79.
<https://doi.org/10.1021/ac60288a034>.
- Fry, J. L., A. Kiendler-Scharr, A. W. Rollins, T. Brauers, S. S. Brown, H. P. Dorn, W. P. Dubé, et al. 2011. "SOA from Limonene: Role of NO₃ in Its Generation and Degradation." *Atmospheric Chemistry and Physics* 11 (8): 3879–94. <https://doi.org/10.5194/acp-11-3879-2011>.
- Fry, Juliane L., Steven S. Brown, Ann M. Middlebrook, Peter M. Edwards, Pedro Campuzano-Jost, Douglas A. Day, José L. Jimenez, et al. 2018. "Secondary Organic Aerosol (SOA) Yields from NO₃ Radical + Isoprene Based on Nighttime Aircraft Power Plant Plume Transects." *Atmospheric Chemistry and Physics* 18 (16): 11663–82. <https://doi.org/10.5194/acp-18-11663-2018>.
- Fry, Juliane L., Danielle C. Draper, Kelley C. Barsanti, James N. Smith, John Ortega, Paul M. Winkler, Michael J. Lawler, et al. 2014. "Secondary Organic Aerosol Formation and Organic Nitrate Yield from NO₃ Oxidation of Biogenic Hydrocarbons." *Environmental Science and Technology* 48 (20): 11944–53. <https://doi.org/10.1021/es502204x>.
- Fuchs, H., S. M. Ball, B. Bohn, T. Brauers, R. C. Cohen, H.-P. Dorn, W. P. Dubé, et al. 2009. "Intercomparison of Measurements of NO₂ Concentrations in the Atmosphere Simulation Chamber SAPHIR during the NO₃Comp Campaign ." *Atmospheric Measurement Techniques Discussions* 2 (5): 2539–86. <https://doi.org/10.5194/amtd-2-2539-2009>.

- Fuchs, H., William P. Dubé, Brian M. Lerner, Nicholas L. Wagner, Eric J. Williams, and Steven S. Brown. 2009. "A Sensitive and Versatile Detector for Atmospheric NO₂ and NO_x Based on Blue Diode Laser Cavity Ring-down Spectroscopy." *Environmental Science and Technology* 43 (20): 7831–36. <https://doi.org/10.1021/es902067h>.
- Fuchs, H., W. R. Simpson, R. L. Apodaca, T. Brauers, R. C. Cohen, J. N. Crowley, H.-P. Dorn, et al. 2012. "Comparison of N₂O₅ Mixing Ratios during NO₃Comp 2007 in SAPHIR ." *Atmospheric Measurement Techniques Discussions* 5 (4): 4927–67. <https://doi.org/10.5194/amtd-5-4927-2012>.
- Ganzeveld, Laurens, Jos Lelieveld, and Geert Jan Roelofs. 1998. "A Dry Deposition Parameterization for Sulfur Oxides in a Chemistry and General Circulation Model." *Journal of Geophysical Research Atmospheres* 103 (D5): 5679–94. <https://doi.org/10.1029/97JD03077>.
- Geron, Chris, Alex Guenther, Jim Greenberg, Thomas Karl, and Rei Rasmussen. 2006. "Biogenic Volatile Organic Compound Emissions from Desert Vegetation of the Southwestern US." *Atmospheric Environment* 40 (9): 1645–60. <https://doi.org/10.1016/j.atmosenv.2005.11.011>.
- Goldstein, Allen H., and Ian E. Galbally. 2007. "Known and Unexplored Organic Constituents in the Earth's Atmosphere." *Environmental Science and Technology* 41 (5): 1514–21. <https://doi.org/10.1021/es072476p>.
- Graham, Richard A., and Harold S. Johnston. 1978. "The Photochemistry of NO₃ and the Kinetics of the N₂O₅-O₃ System." *Journal of Physical Chemistry* 82 (3): 254–68. <https://doi.org/10.1021/j100492a002>.
- Graus, Martin, Markus Müller, and Armin Hansel. 2010. "High Resolution PTR-TOF: Quantification and Formula Confirmation of VOC in Real Time." *Journal of the American Society for Mass Spectrometry* 21 (6): 1037–44. <https://doi.org/10.1016/j.jasms.2010.02.006>.
- Gross, Simone, and Allan K. Bertram. 2009. "Products and Kinetics of the Reactions of an Alkane Monolayer and a Terminal Alkene Monolayer with NO₃ Radicals." *Journal of Geophysical Research Atmospheres* 114 (2): 1–14. <https://doi.org/10.1029/2008JD010987>.
- Grossenbacher, John W., Tara Couch, Paul B. Shepson, Troy Thornberry, Maria Witmer-Rich, Mary Anne Carroll, Ian Faloon, et al. 2001. "Measurements of Isoprene Nitrates above a Forest Canopy." *Journal of Geophysical Research Atmospheres* 106 (D20): 24429–38. <https://doi.org/10.1029/2001JD900029>.
- Hallquist, M., J. C. Wenger, U. Baltensperger, Y. Rudich, D. Simpson, M. Claeys, J. Dommen, et al. 2009. "The Formation, Properties and Impact of Secondary Organic Aerosol: Current and Emerging Issues." *Atmospheric Chemistry and Physics* 9 (14): 5155–5236. <https://doi.org/10.5194/acp-9-5155-2009>.
- Hanst, Philip L. 1971. "Mechanism of Peroxyacetyl Nitrate Formation." *Journal of the Air Pollution Control Association* 21 (5): 269–71. <https://doi.org/10.1080/00022470.1971.10469527>.
- Hautefeuille, and Chappuis. 1882. "Annales Scientifiques De L'É.N.S." *Annales Scientifiques De L'É.N.S.* 11: 137–86.
- Heald, C. L., D. K. Henze, L. W. Horowitz, J. Feddema, J. F. Lamarque, A. Guenther, P. G. Hess, et al. 2008. "Predicted Change in Global Secondary Organic Aerosol Concentrations in Response to Future Climate, Emissions, and Land Use Change." *Journal of Geophysical Research Atmospheres* 113 (5): 1–16. <https://doi.org/10.1029/2007JD009092>.

- Heald, Colette L., Daniel J. Jacob, Rokjin J. Park, Lynn M. Russell, Barry J. Huebert, John H. Seinfeld, Hong Liao, and Rodney J. Weber. 2005. "A Large Organic Aerosol Source in the Free Troposphere Missing from Current Models." *Geophysical Research Letters* 32 (18): 1–4. <https://doi.org/10.1029/2005GL023831>.
- Horowitz, Larry W., Arlene M. Fiore, George P. Milly, Ronald C. Cohen, Anne Perring, Paul J. Wooldridge, Peter G. Hess, Louisa K. Emmons, and Jean François Lamarque. 2007. "Observational Constraints on the Chemistry of Isoprene Nitrates over the Eastern United States." *Journal of Geophysical Research Atmospheres* 112 (12): 1–13. <https://doi.org/10.1029/2006JD007747>.
- Hoyle, C. R., T. Berntsen, G. Myhre, and I. S.A. Isaksen. 2007. "Secondary Organic Aerosol in the Global Aerosol - Chemical Transport Model Oslo CTM2." *Atmospheric Chemistry and Physics* 7 (21): 5675–94. <https://doi.org/10.5194/acp-7-5675-2007>.
- Igel, Adele L., Susan C. van den Heever, and Jill S. Johnson. 2018. "Meteorological and Land Surface Properties Impacting Sea Breeze Extent and Aerosol Distribution in a Dry Environment." *Journal of Geophysical Research: Atmospheres* 123 (1): 22–37. <https://doi.org/10.1002/2017JD027339>.
- IPCC. 2013. *AR5 - Citations. CLIMATE CHANGE 2013 - The Physical Science Basis, Contribution of Working Group I to the Fifth Assessment Report of the Intergovernmental Panel on Climate Change*. <https://doi.org/10.1017/CBO9781107415324.Summary>.
- Jaoui, Mohammed, Tadeusz E. Kleindienst, Kenneth S. Docherty, Michael Lewandowski, and John H. Offenberg. 2013. "Secondary Organic Aerosol Formation from the Oxidation of a Series of Sesquiterpenes: α -Cedrene, β -Caryophyllene, α -Humulene and α -Farnesene with O₃, OH and NO₃ Radicals." *Environmental Chemistry* 10 (3): 178–93. <https://doi.org/10.1071/EN13025>.
- Jenkin, M. E., J. C. Young, and A. R. Rickard. 2015. "The MCM v3.3 Degradation Scheme for Isoprene." *Atmospheric Chemistry and Physics Discussions* 15 (6): 9709–66. <https://doi.org/10.5194/acpd-15-9709-2015>.
- Johnston, H. S., C. A. Cantrell, and J. G. Calvert. 1986. "Unimolecular Decomposition of NO₃ to Form NO and O₂ and a Review of N₂O₅/NO₃ Kinetics." *Journal of Geophysical Research* 91 (D4): 5159. <https://doi.org/10.1029/jd091id04p05159>.
- Jordan, A., S. Haidacher, G. Hanel, E. Hartungen, L. Märk, H. Seehauser, R. Schottkowsky, P. Sulzer, and T. D. Märk. 2009. "A High Resolution and High Sensitivity Proton-Transfer-Reaction Time-of-Flight Mass Spectrometer (PTR-TOF-MS)." *International Journal of Mass Spectrometry* 286 (2–3): 122–28. <https://doi.org/10.1016/j.ijms.2009.07.005>.
- Kämpf, Jochen, and Piers Chapman. 2016. *Upwelling Systems of the World. Upwelling Systems of the World*. <https://doi.org/10.1007/978-3-319-42524-5>.
- Kanakidou, M., J. H. Seinfeld, S. N. Pandis, I. Barnes, F. J. Dentener, M. C. Facchini, R. Van Dingenen, et al. 2005. "Organic Aerosol and Global Climate Modelling: A Review." *Atmospheric Chemistry and Physics* 5 (4): 1053–1123. <https://doi.org/10.5194/acp-5-1053-2005>.
- Kane, Sean M., Francois Caloz, and Ming Taun Leu. 2001. "Heterogeneous Uptake of Gaseous N₂O₅ by (NH₄)₂SO₄, NH₄HSO₄, and H₂SO₄ Aerosols." *Journal of Physical Chemistry A* 105 (26): 6465–70. <https://doi.org/10.1021/jp010490x>.
- Karagulian, F., C. Santschi, and M. J. Rossi. 2006. "The Heterogeneous Chemical Kinetics of N₂O₅ on CaCO₃ and Other Atmospheric Mineral Dust Surrogates." *Atmospheric Chemistry and Physics* 6 (5):

- 1373–88. <https://doi.org/10.5194/acp-6-1373-2006>.
- Kim, Michelle J., Delphine K. Farmer, and Timothy H. Bertram. 2014. "A Controlling Role for the Air-Sea Interface in the Chemical Processing of Reactive Nitrogen in the Coastal Marine Boundary Layer." *Proceedings of the National Academy of Sciences of the United States of America* 111 (11): 3943–48. <https://doi.org/10.1073/pnas.1318694111>.
- Kirchner, Frank, and William R. Stockwell. 1996. "Effect of Peroxy Radical Reactions on the Predicted Concentrations of Ozone, Nitrogenous Compounds, and Radicals." *Journal of Geophysical Research Atmospheres* 101 (15): 21007–22. <https://doi.org/10.1029/96jd01519>.
- Krechmer, Jordan, Felipe Lopez-Hilfiker, Abigail Koss, Manuel Hutterli, Carsten Stoermer, Benjamin Deming, Joel Kimmel, et al. 2018. "Evaluation of a New Reagent-Ion Source and Focusing Ion-Molecule Reactor for Use in Proton-Transfer-Reaction Mass Spectrometry." *Analytical Chemistry* 90 (20): 12011–18. <https://doi.org/10.1021/acs.analchem.8b02641>.
- Kuhlmann, R. von, M. G. Lawrence, U. Pöschl, and P. J. Crutzen. 2003. "Sensitivities in Global Scale Modeling of Isoprene." *Atmospheric Chemistry and Physics Discussions* 3 (3): 3095–3134. <https://doi.org/10.5194/acpd-3-3095-2003>.
- Kwan, A. J., A. W.H. Chan, N. L. Ng, H. G. Kjaergaard, J. H. Seinfeld, and P. O. Wennberg. 2012. "Peroxy Radical Chemistry and OH Radical Production during the NO₃-Initiated Oxidation of Isoprene." *Atmospheric Chemistry and Physics* 12 (16): 7499–7515. <https://doi.org/10.5194/acp-12-7499-2012>.
- Lana, A., T. G. Bell, R. Simó, S. M. Vallina, J. Ballabrera-Poy, A. J. Kettle, J. Dachs, et al. 2011. "An Updated Climatology of Surface Dimethylsulfide Concentrations and Emission Fluxes in the Global Ocean." *Global Biogeochemical Cycles* 25 (1): 1–17. <https://doi.org/10.1029/2010GB003850>.
- Lee Ng, Nga, Steven S. Brown, Alexander T. Archibald, Elliot Atlas, Ronald C. Cohen, John N. Crowley, Douglas A. Day, et al. 2017. "Nitrate Radicals and Biogenic Volatile Organic Compounds: Oxidation, Mechanisms, and Organic Aerosol." *Atmospheric Chemistry and Physics* 17 (3): 2103–62. <https://doi.org/10.5194/acp-17-2103-2017>.
- Lelieveld, J., P. Hoor, P. Jöckel, A. Pozzer, P. Hadjinicolaou, J. P. Cammas, and S. Beirle. 2009. "Severe Ozone Air Pollution in the Persian Gulf Region." *Atmospheric Chemistry and Physics* 9 (4): 1393–1406. <https://doi.org/10.5194/acp-9-1393-2009>.
- Liebmann, Jonathan, Einar Karu, Nicolas Sobanski, Jan Schuladen, Mikael Ehn, Simon Schallhart, Lauriane Quéléver, et al. 2018. "Direct Measurement of NO₃ Radical Reactivity in a Boreal Forest." *Atmospheric Chemistry and Physics* 18 (5): 3799–3815. <https://doi.org/10.5194/acp-18-3799-2018>.
- Liebmann, Jonathan M., Jennifer B.A. Muller, Dagmar Kubistin, Anja Claude, Robert Holla, Christian Plass-Dülmer, Jos Lelieveld, and John N. Crowley. 2018. "Direct Measurements of NO₃ Reactivity in and above the Boundary Layer of a Mountaintop Site: Identification of Reactive Trace Gases and Comparison with OH Reactivity." *Atmospheric Chemistry and Physics* 18 (16): 12045–59. <https://doi.org/10.5194/acp-18-12045-2018>.
- Liebmann, Jonathan M., Gerhard Schuster, Jan B. Schuladen, Nicolas Sobanski, Jos Lelieveld, and John N. Crowley. 2017. "Measurement of Ambient NO₃ Reactivity: Design, Characterization and First Deployment of a New Instrument." *Atmospheric Measurement Techniques* 10 (3): 1241–58. <https://doi.org/10.5194/amt-10-1241-2017>.

- Liebmann, Jonathan, Nicolas Sobanski, Jan Schuladen, Einar Karu, Heidi Hellén, Hannele Hakola, Qiaozhi Zha, et al. 2019. "Alkyl Nitrates in the Boreal Forest: Formation via the NO₃-, OH- And O₃-Induced Oxidation of Biogenic Volatile Organic Compounds and Ambient Lifetimes." *Atmospheric Chemistry and Physics* 19 (15): 10391–403. <https://doi.org/10.5194/acp-19-10391-2019>.
- Madronich, S., and J. G. Calvert. 1990. "Permutation Reactions of Organic Peroxy Radicals in the Troposphere." *Journal of Geophysical Research* 95 (D5): 5697–5715. <https://doi.org/10.1029/JD095iD05p05697>.
- Martinez, M., H. Harder, D. Kubistin, M. Rudolf, G. Eerdeken, H. Fischer, T. Klüpfel, et al. 2010. "Hydroxyl Radicals in the Tropical Troposphere over the Suriname Rainforest: Airborne Measurements." *Atmospheric Chemistry and Physics* 10 (8): 3759–73. <https://doi.org/10.5194/acp-10-3759-2010>.
- Martinez, Monica, Dieter Perner, Eva Maria Hackenthal, Stefan Külzer, and Lothar Schütz. 2000. "NO₃ at Helgoland during the NORDEX Campaign in October 1996." *Journal of Geophysical Research Atmospheres* 105 (D18): 22685–95. <https://doi.org/10.1029/2000JD900255>.
- Massoli, P., A. T. Lambe, A. T. Ahern, L. R. Williams, M. Ehn, J. Mikkilä, M. R. Canagaratna, et al. 2010. "Relationship between Aerosol Oxidation Level and Hygroscopic Properties of Laboratory Generated Secondary Organic Aerosol (SOA) Particles." *Geophysical Research Letters* 37 (24): 1–5. <https://doi.org/10.1029/2010GL045258>.
- Matsumoto, Jun, Kousuke Imagawa, Hidekazu Imai, Naohiro Kosugi, Masumi Ideguchi, Shungo Kato, and Yoshizumi Kajii. 2006. "Nocturnal Sink of NO_x via NO₃ and N₂O₅ in the Outflow from a Source Area in Japan." *Atmospheric Environment* 40 (33): 6294–6302. <https://doi.org/10.1016/j.atmosenv.2006.05.045>.
- McLaren, R., P. Wojtal, D. Majonis, J. McCourt, J. D. Halla, and J. Brook. 2010. "NO₃ Radical Measurements in a Polluted Marine Environment: Links to Ozone Formation." *Atmospheric Chemistry and Physics* 10 (9): 4187–4206. <https://doi.org/10.5194/acp-10-4187-2010>.
- Meinardi, Simone, Isobel J. Simpson, Nicola J. Blake, Donald R. Blake, and F. Sherwood Rowland. 2003. "Dimethyl Disulfide (DMDS) and Dimethyl Sulfide (DMS) Emissions from Biomass Burning in Australia." *Geophysical Research Letters* 30 (9): 1454. <https://doi.org/10.1029/2003GL016967>.
- Mogili, Praveen K., Paul D. Kleiber, Mark A. Young, and Vicki H. Grassian. 2006. "N₂O₅ Hydrolysis on the Components of Mineral Dust and Sea Salt Aerosol: Comparison Study in an Environmental Aerosol Reaction Chamber." *Atmospheric Environment* 40 (38): 7401–8. <https://doi.org/10.1016/j.atmosenv.2006.06.048>.
- Mohanakumar, K. 2008. "Stratosphere Troposphere Interactions: An Introduction." *Stratosphere Troposphere Interactions: An Introduction*, no. March: 1–416. <https://doi.org/10.1007/978-1-4020-8217-7>.
- Morin, Julien, and Yuri Bedjanian. 2016. "Thermal Decomposition of Isopropyl Nitrate: Kinetics and Products." *Journal of Physical Chemistry A* 120 (41): 8037–43. <https://doi.org/10.1021/acs.jpca.6b06552>.
- Müller, J. F., J. Peeters, and T. Stavrakou. 2014. "Fast Photolysis of Carbonyl Nitrates from Isoprene." *Atmospheric Chemistry and Physics* 14 (5): 2497–2508. <https://doi.org/10.5194/acp-14-2497-2014>.
- Ng, N. L., A. J. Kwan, J. D. Surratt, A. W.H. Chan, P. S. Chhabra, A. Sorooshian, H. O.T. Pye, et al. 2008.

- “Secondary Organic Aerosol (SOA) Formation from Reaction of Isoprene with Nitrate Radicals (NO₃).” *Atmospheric Chemistry and Physics* 8 (14): 4117–40. <https://doi.org/10.5194/acp-8-4117-2008>.
- O’Keefe, Anthony, and David A.G. Deacon. 1988. “Cavity Ring-down Optical Spectrometer for Absorption Measurements Using Pulsed Laser Sources.” *Review of Scientific Instruments* 59 (12): 2544–51. <https://doi.org/10.1063/1.1139895>.
- Orphal, J., C. E. Fellows, and P. M. Flaud. 2003. “The Visible Absorption Spectrum of NO₃ Measured by High-Resolution Fourier Transform Spectroscopy.” *Journal of Geophysical Research: Atmospheres* 108 (3): 1–11. <https://doi.org/10.1029/2002jd002489>.
- Osthoff, Hans D., Michael J. Pilling, A. R. Ravishankara, and Steven S. Brown. 2007. “Temperature Dependence of the NO₃ Absorption Cross-Section above 298 K and Determination of the Equilibrium Constant for NO₃ + NO₂ ↔ N₂O₅ at Atmospherically Relevant Conditions.” *Physical Chemistry Chemical Physics* 9 (43): 5785–93. <https://doi.org/10.1039/b709193a>.
- Park, Jinhae, and M. Carme Calderer. 2008. “Variational Problems and Modeling of Ferroelectricity in Chiral Smectic C Liquid Crystals.” *Modeling of Soft Matter*, 169–88. https://doi.org/10.1007/0-387-32153-5_7.
- Perring, A. E., A. Wisthaler, M. Graus, P. J. Wooldridge, A. L. Lockwood, L. H. Mielke, P. B. Shepson, A. Hansel, and R. C. Cohen. 2009. “A Product Study of the Isoprene+NO₃ Reaction.” *Atmospheric Chemistry and Physics* 9 (14): 4945–56. <https://doi.org/10.5194/acp-9-4945-2009>.
- Pfannerstill, Eva Y., Nijing Wang, Achim Edtbauer, Efstratios Bourtsoukidis, John N. Crowley, Dirk Dienhart, Philipp G. Eger, et al. 2019. “Shipborne Measurements of Total OH Reactivity around the Arabian Peninsula and Its Role in Ozone Chemistry.” *Atmospheric Chemistry and Physics Discussions*, no. x: 1–38. <https://doi.org/10.5194/acp-2019-416>.
- Phillips, G. J., M. J. Tang, J. Thieser, B. Brickwedde, G. Schuster, B. Bohn, J. Lelieveld, and J. N. Crowley. 2012. “Significant Concentrations of Nitryl Chloride Observed in Rural Continental Europe Associated with the Influence of Sea Salt Chloride and Anthropogenic Emissions.” *Geophysical Research Letters* 39 (10). <https://doi.org/10.1029/2012GL051912>.
- Phillips, Gavin J., Jim Thieser, Mingjin Tang, Nicolas Sobanski, Gerhard Schuster, Johannes Fachinger, Frank Drewnick, et al. 2016. “Estimating N₂O₅ Uptake Coefficients Using Ambient Measurements of NO₃, N₂O₅, ClNO₂ and Particle-Phase Nitrate.” *Atmospheric Chemistry and Physics* 16 (20): 13231–49. <https://doi.org/10.5194/acp-16-13231-2016>.
- Platt, U., and G. Le Bras. 1997. “Influence of DMS on the Ox - NO_y Partitioning and the NO_x Distribution in the Marine Background Atmosphere.” *Geophysical Research Letters* 24 (15): 1935–38. <https://doi.org/10.1029/97GL01821>.
- Platt, Ulrich, Dieter Perner, Arthur M. Winer, Geoffrey W. Harris, and James N. Pitts. 1980. “Detection of NO₃ in the Polluted Troposphere by Differential Optical Absorption.” *Geophysical Research Letters* 7 (1): 89–92. <https://doi.org/10.1029/GL007i001p00089>.
- Pope, C. Arden, and Douglas W. Dockery. 2006. “Health Effects of Fine Particulate Air Pollution: Lines That Connect.” *Journal of the Air and Waste Management Association* 56 (6): 709–42. <https://doi.org/10.1080/10473289.2006.10464485>.
- Presto, Albert A., and Neil M. Donahue. 2004. “Ozonolysis Fragment Quenching by Nitrate Formation:

- The Pressure Dependence of Prompt OH Radical Formation." *Journal of Physical Chemistry A* 108 (42): 9096–9104. <https://doi.org/10.1021/jp047162s>.
- RattanaVaraha, Weruka, Kevin Chu, Sri Hapsari Budisulistiorini, Matthieu Riva, Ying Hsuan Lin, Eric S. Edgerton, Karsten Baumann, et al. 2016. "Assessing the Impact of Anthropogenic Pollution on Isoprene-Derived Secondary Organic Aerosol Formation in PM_{2.5} Collected from the Birmingham, Alabama, Ground Site during the 2013 Southern Oxidant and Aerosol Study." *Atmospheric Chemistry and Physics* 16 (8): 4897–4914. <https://doi.org/10.5194/acp-16-4897-2016>.
- Ridley, B. A., F. E. Grahek, and J. G. Walega. 1992. "A Small, High-Sensitivity, Medium-Response Ozone Detector Suitable for Measurements from Light Aircraft." *Journal of Atmospheric & Oceanic Technology*. [https://doi.org/10.1175/1520-0426\(1992\)009<0142:ASHSMR>2.0.CO;2](https://doi.org/10.1175/1520-0426(1992)009<0142:ASHSMR>2.0.CO;2).
- Riedel, Theran P., Nicholas L. Wagner, William P. Dubé, Ann M. Middlebrook, Cora J. Young, Fatma Öztürk, Roya Bahreini, et al. 2013. "Chlorine Activation within Urban or Power Plant Plumes: Vertically Resolved ClNO₂ and Cl₂ Measurements from a Tall Tower in a Polluted Continental Setting." *Journal of Geophysical Research Atmospheres* 118 (15): 8702–15. <https://doi.org/10.1002/jgrd.50637>.
- Roberts, James M., Frank Flocke, Craig A. Stroud, Daniel Hereid, Eric Williams, Fred Fehsenfeld, William Brune, Monica Martinez, and Hartwig Harder. 2002. "Ground-Based Measurements of Peroxycarboxylic Nitric Anhydrides (PANs) during the 1999 Southern Oxidants Study Nashville Intensive." *Journal of Geophysical Research Atmospheres* 107 (21): 1–10. <https://doi.org/10.1029/2001JD000947>.
- Roberts, James M., Jonathan Williams, Karsten Baumann, Martin P. Buhr, Paul D. Goldan, John Holloway, Gerhard Hübler, et al. 1998. "Measurements of PAN, PPN, and MPAN Made during the 1994 and 1995 Nashville Intensives of the Southern Oxidant Study: Implications for Regional Ozone Production from Biogenic Hydrocarbons." *Journal of Geophysical Research Atmospheres* 103 (D17): 22473–90. <https://doi.org/10.1029/98JD01637>.
- Rohrer, F., B. Bohn, T. Brauers, D. Brüning, F. J. Johnen, A. Wahner, and J. Kleffmann. 2005. "Characterisation of the Photolytic HONO-Source in the Atmosphere Simulation Chamber SAPHIR." *Atmospheric Chemistry and Physics* 5 (8): 2189–2201. <https://doi.org/10.5194/acp-5-2189-2005>.
- Rollins, A. W., A. Kiendler-Scharr, J. L. Fry, T. Brauers, S. S. Brown, H. P. Dorn, W. P. Dubé, et al. 2009. "Isoprene Oxidation by Nitrate Radical: Alkyl Nitrate and Secondary Organic Aerosol Yields." *Atmospheric Chemistry and Physics* 9 (18): 6685–6703. <https://doi.org/10.5194/acp-9-6685-2009>.
- Rollins, A. W., S. Pusede, P. Wooldridge, K. E. Min, D. R. Gentner, A. H. Goldstein, S. Liu, et al. 2013. "Gas/Particle Partitioning of Total Alkyl Nitrates Observed with TD-LIF in Bakersfield." *Journal of Geophysical Research Atmospheres* 118 (12): 6651–62. <https://doi.org/10.1002/jgrd.50522>.
- Rudich, Yinon, Ranajit K. Talukdar, A. R. Ravishankara, and R. W. Fox. 1996. "Reactive Uptake of NO₃ on Pure Water and Ionic Solutions." *Journal of Geophysical Research Atmospheres* 101 (15): 21023–31. <https://doi.org/10.1029/96jd01844>.
- Sarwar, G., H. Simon, P. Bhave, and G. Yarwood. 2012. "Examining the Impact of Heterogeneous Nitryl Chloride Production on Air Quality across the United States." *Atmospheric Chemistry and Physics* 12 (14): 6455–73. <https://doi.org/10.5194/acp-12-6455-2012>.
- Sarwar, Golam, Heather Simon, Jia Xing, and Rohit Mathur. 2014. "Importance of Tropospheric ClNO₂

- Chemistry across the Northern Hemisphere.” *Geophysical Research Letters* 41 (11): 4050–58. <https://doi.org/10.1002/2014GL059962>.
- Scheret, J. J., J. B. Paul, A. O’Keefe, and R. J. Saykally. 1997. “Cavity Ringdown Laser Absorption Spectroscopy: History, Development, and Application to Pulsed Molecular Beams.” *Chemical Reviews* 97 (1): 25–51. <https://doi.org/10.1021/cr930048d>.
- Schwantes, Rebecca H., Alexander P. Teng, Tran B. Nguyen, Matthew M. Coggon, John D. Crouse, Jason M. St. Clair, Xuan Zhang, Katherine A. Schilling, John H. Seinfeld, and Paul O. Wennberg. 2015. “Isoprene NO₃ Oxidation Products from the RO₂ + HO₂ Pathway.” *Journal of Physical Chemistry A* 119 (40): 10158–71. <https://doi.org/10.1021/acs.jpca.5b06355>.
- Sciare, J., E. Baboukas, and N. Mihalopoulos. 2001. “Short-Term Variability of Atmospheric DMS and Its Oxidation Products at Amsterdam Island during Summer Time.” *Journal of Atmospheric Chemistry* 39 (3): 281–302. <https://doi.org/10.1023/A:1010631305307>.
- Seisel, Sabine, François Caloz, Frederick F. Fenter, Hubert Van Den Bergh, and Michel J. Rossi. 1997. “The Heterogeneous Reaction of NO₃ with NaCl and KBr: A Nonphotolytic Source of Halogen Atoms.” *Geophysical Research Letters* 24 (22): 2757–60. <https://doi.org/10.1029/97GL02857>.
- Sharkey, Thomas D., Amy E. Wiberley, and Autumn R. Donohue. 2008. “Isoprene Emission from Plants: Why and How.” *Annals of Botany* 101 (1): 5–18. <https://doi.org/10.1093/aob/mcm240>.
- Sharkey, Thomas D., and Sansun Yeh. 2001. “Isoprene Emission from Plants.” *Annual Review of Plant Biology* 52: 407–36. <https://doi.org/10.1146/annurev.arplant.52.1.407>.
- Simpson, Isobel J., Omar S. Aburizaiza, Azhar Siddique, Barbara Barletta, Nicola J. Blake, Aaron Gartner, Haider Khwaja, Simone Meinardi, Jahan Zeb, and Donald R. Blake. 2014. “Air Quality in Mecca and Surrounding Holy Places in Saudi Arabia during Hajj: Initial Survey.” *Environmental Science and Technology* 48 (15): 8529–37. <https://doi.org/10.1021/es5017476>.
- Singh, Hanwant B. 1987. “Reactive Nitrogen in the Troposphere.” *Environmental Science and Technology* 21 (4): 320–27. <https://doi.org/10.1021/es00158a001>.
- Smoydzin, L., M. Fnais, and J. Lelieveld. 2012. *Ozone Pollution over the Arabian Gulf &Ndash; Role of Meteorological Conditions. Atmospheric Chemistry and Physics Discussions*. Vol. 12. <https://doi.org/10.5194/acpd-12-6331-2012>.
- Sobanski, Nicolas, Jan Schuladen, Gerhard Schuster, Jos Lelieveld, and John N. Crowley. 2016. “A Five-Channel Cavity Ring-down Spectrometer for the Detection of NO₂, NO₃, N₂O₅, Total Peroxy Nitrates and Total Alkyl Nitrates.” *Atmospheric Measurement Techniques* 9 (10): 5103–18. <https://doi.org/10.5194/amt-9-5103-2016>.
- Sobanski, Nicolas, M. J. Tang, J. Thieser, G. Schuster, D. Pöhler, H. Fischer, W. Song, et al. 2016. “Chemical and Meteorological Influences on the Lifetime of NO₃ at a Semi-Rural Mountain Site during PARADE.” *Atmospheric Chemistry and Physics* 16 (8): 4867–83. <https://doi.org/10.5194/acp-16-4867-2016>.
- Sobanski, Nicolas, Jim Thieser, Jan Schuladen, Carina Sauvage, Wei Song, Jonathan Williams, Jos Lelieveld, and John N. Crowley. 2017. “Day and Night-Time Formation of Organic Nitrates at a Forested Mountain Site in South-West Germany.” *Atmospheric Chemistry and Physics* 17 (6): 4115–30. <https://doi.org/10.5194/acp-17-4115-2017>.

- Sommariva, R., H. D. Osthoff, S. S. Brown, T. S. Bates, T. Baynard, D. Coffman, J. A. De Gouw, et al. 2009. "Radicals in the Marine Boundary Layer during NEAQS 2004: A Model Study of Day-Time and Night-Time Sources and Sinks." *Atmospheric Chemistry and Physics* 9 (9): 3075–93. <https://doi.org/10.5194/acp-9-3075-2009>.
- Sommariva, R., M. J. Pilling, W. J. Bloss, D. E. Heard, J. D. Lee, Z. L. Fleming, P. S. Monks, et al. 2007. "Night-Time Radical Chemistry during the NAMBLEX Campaign." *Atmospheric Chemistry and Physics* 7 (3): 587–98. <https://doi.org/10.5194/acp-7-587-2007>.
- Stanaway, Jeffrey D., Ashkan Afshin, Emmanuela Gakidou, Stephen S. Lim, Degu Abate, Kalkidan Hassen Abate, Cristiana Abbafati, et al. 2018. "Global, Regional, and National Comparative Risk Assessment of 84 Behavioural, Environmental and Occupational, and Metabolic Risks or Clusters of Risks for 195 Countries and Territories, 1990-2017: A Systematic Analysis for the Global Burden of Disease Study." *The Lancet* 392 (10159): 1923–94. [https://doi.org/10.1016/S0140-6736\(18\)32225-6](https://doi.org/10.1016/S0140-6736(18)32225-6).
- Sun, En Jang, and Ming Huei Huang. 1995. "Detection of Peroxyacetyl Nitrate at Phytotoxic Level and Its Effects on Vegetation in Taiwan." *Atmospheric Environment* 29 (21): 2899–2904. [https://doi.org/10.1016/1352-2310\(94\)00329-J](https://doi.org/10.1016/1352-2310(94)00329-J).
- Sutugin, A G, and N A Fuchs. 1971. "FORMATION of Condensation Aerosols UNDER" 2: 361–68.
- Tadic, Ivan, John Crowley, Dirk Dienhart, Philipp Eger, Hartwig Harder, Bettina Hottmann, Monica Martinez, et al. 2019. "Net Ozone Production and Its Relationship to NO_x and VOCs in the Marine Boundary Layer around the Arabian Peninsula." *Atmospheric Chemistry and Physics*, no. 2: 1–35. <https://doi.org/10.5194/acp-2019-1031>.
- Tang, M. J., G. Schuster, and J. N. Crowley. 2014. "Heterogeneous Reaction of N₂O₅ with Illite and Arizona Test Dust Particles." *Atmospheric Chemistry and Physics* 14 (1): 245–54. <https://doi.org/10.5194/acp-14-245-2014>.
- Tang, M. J., J. Thieser, G. Schuster, and J. N. Crowley. 2010. "Uptake of NO₃ and N₂O₅ to Saharan Dust, Ambient Urban Aerosol and Soot: A Relative Rate Study." *Atmospheric Chemistry and Physics* 10 (6): 2965–74. <https://doi.org/10.5194/acp-10-2965-2010>.
- Terink, Wilco, Walter Willem Immerzeel, and Peter Droogers. 2013. "Climate Change Projections of Precipitation and Reference Evapotranspiration for the Middle East and Northern Africa until 2050." *International Journal of Climatology* 33 (14): 3055–72. <https://doi.org/10.1002/joc.3650>.
- Thieser, J., G. Schuster, J. Schuladen, G. J. Phillips, A. Reiffs, U. Parchatka, D. Pöhler, J. Lelieveld, and J. N. Crowley. 2016. "A Two-Channel Thermal Dissociation Cavity Ring-down Spectrometer for the Detection of Ambient NO₂, RO₂NO₂ and RONO₂." *Atmospheric Measurement Techniques* 9 (2): 553–76. <https://doi.org/10.5194/amt-9-553-2016>.
- Vandaele, A. C., C. Hermans, S. Fally, M. Carleer, R. Colin, M. F. Mérienne, A. Jenouvrier, and B. Coquart. 2002. "High-Resolution Fourier Transform Measurement of the NO₂ Visible and near-Infrared Absorption Cross Sections: Temperature and Pressure Effects." *Journal of Geophysical Research Atmospheres* 107 (18): ACH 3-1-ACH 3-12. <https://doi.org/10.1029/2001JD000971>.
- Vandaele, A. C., C. Hermans, S. Fally, M. Carleer, M. F. Mérienne, A. Jenouvrier, B. Coquart, and R. Colin. 2003. "Absorption Cross-Sections of NO₂: Simulation of Temperature and Pressure Effects." *Journal of Quantitative Spectroscopy and Radiative Transfer* 76 (3–4): 373–91. [https://doi.org/10.1016/S0022-4073\(02\)00064-X](https://doi.org/10.1016/S0022-4073(02)00064-X).

- Voigt, S., J. Orphal, and J. P. Burrows. 2002. "The Temperature and Pressure Dependence of the Absorption Cross-Sections of NO₂ in the 250-800 Nm Region Measured by Fourier-Transform Spectroscopy." *Journal of Photochemistry and Photobiology A: Chemistry* 149 (1–3): 1–7. [https://doi.org/10.1016/S1010-6030\(01\)00650-5](https://doi.org/10.1016/S1010-6030(01)00650-5).
- Vrekoussis, M., M. Kanakidou, N. Mihalopoulos, P. J. Crutzen, J. Lelieveld, D. Perner, H. Berresheim, and E. Baboukas. 2003. "Role of NO₃ Radical in Oxidation Processes in the Eastern Mediterranean Troposphere during the MINOS Campaign." *Atmospheric Chemistry and Physics Discussions* 3 (3): 3135–69. <https://doi.org/10.5194/acpd-3-3135-2003>.
- Vrekoussis, M., E. Liakakou, N. Mihalopoulos, Maria Kanakidou, P. J. Crutzen, and J. Lelieveld. 2006. "Formation of HNO₃ and NO₃- in the Anthropogenically-Influenced Eastern Mediterranean Marine Boundary Layer." *Geophysical Research Letters* 33 (5): 3–6. <https://doi.org/10.1029/2005GL025069>.
- Vrekoussis, M., N. Mihalopoulos, E. Gerasopoulos, M. Kanakidou, P. J. Crutzen, and J. Lelieveld. 2007. "Two-Years of NO₃ Radical Observations in the Boundary Layer over the Eastern Mediterranean." *Atmospheric Chemistry and Physics* 7 (2): 315–27. <https://doi.org/10.5194/acp-7-315-2007>.
- Vyskocil, Adolf, Claude Viau, and Serge Lamy. 1998. "Peroxyacetyl Nitrate: Review of Toxicity." *Human and Experimental Toxicology* 17 (4): 212–20. <https://doi.org/10.1191/096032798678908585>.
- Wild, Robert J., Peter M. Edwards, William P. Dubé, Karsten Baumann, Eric S. Edgerton, Patricia K. Quinn, James M. Roberts, et al. 2014. "A Measurement of Total Reactive Nitrogen, NO_y, Together with NO₂, NO, and O₃ via Cavity Ring-down Spectroscopy." *Environmental Science and Technology* 48 (16): 9609–15. <https://doi.org/10.1021/es501896w>.
- Womack, Caroline C., J. Andrew Neuman, Patrick R. Veres, Scott J. Eilerman, Charles A. Brock, Zachary C.J. Decker, Kyle J. Zarzana, et al. 2017. "Evaluation of the Accuracy of Thermal Dissociation CRDS and LIF Techniques for Atmospheric Measurement of Reactive Nitrogen Species." *Atmospheric Measurement Techniques* 10 (5): 1911–26. <https://doi.org/10.5194/amt-10-1911-2017>.
- Yeh, Geoffrey K., and Paul J. Ziemann. 2015. "Gas-Wall Partitioning of Oxygenated Organic Compounds: Measurements, Structure-Activity Relationships, and Correlation with Gas Chromatographic Retention Factor." *Aerosol Science and Technology* 49 (9): 727–38. <https://doi.org/10.1080/02786826.2015.1068427>.
- Yüceşahin, M. Murat, and A. Yiğitalp Tulga. 2017. "Demographic and Social Change in the Middle East and North Africa: Processes, Spatial Patterns, and Outcomes." *Population Horizons* 14 (2): 47–60. <https://doi.org/10.1515/pophzn-2017-0003>.
- Z. Zhu, H. Xin, H. Li, and H. Dong. 2012. "Assessment of Tubing Type on Ammonia Gas Adsorption." *Applied Engineering in Agriculture* 28 (2): 265–69. <https://doi.org/10.13031/2013.41343>.
- Zeng, Xiu Lin, Wang Hua Chen, Jia Cong Liu, and Jin Lin Kan. 2007. "A Theoretical Study of Five Nitrates: Electronic Structure and Bond Dissociation Energies." *Journal of Molecular Structure: THEOCHEM* 810 (1–3): 47–51. <https://doi.org/10.1016/j.theochem.2007.01.040>.
- Zetzsch, C., and W. Behnke. 1992. "Heterogeneous Photochemical Sources of Atomic Cl in the Troposphere." *Berichte Der Bunsengesellschaft Für Physikalische Chemie* 96 (3): 488–93. <https://doi.org/10.1002/bbpc.19920960351>.
- Zhang, Miming, C. A. Marandino, Liqi Chen, Heng Sun, Zhongyong Gao, Keyhong Park, Intae Kim, et al.

2017. "Characteristics of the Surface Water DMS and PCO₂ Distributions and Their Relationships in the Southern Ocean, Southeast Indian Ocean, and Northwest Pacific Ocean." *Global Biogeochemical Cycles* 31 (8): 1318–31. <https://doi.org/10.1002/2017GB005637>.
- Zhang, Q., Jose L. Jimenez, M. R. Canagaratna, J. D. Allan, H. Coe, I. Ulbrich, M. R. Alfarra, et al. 2007. "Ubiquity and Dominance of Oxygenated Species in Organic Aerosols in Anthropogenically-Influenced Northern Hemisphere Midlatitudes." *Geophysical Research Letters* 34 (13). <https://doi.org/10.1029/2007GL029979>.
- Zhang, Xuebin, Enric Aguilar, Serhat Sensoy, Hamlet Melkonyan, Umayra Tagiyeva, Nader Ahmed, Nato Kotaladze, et al. 2005. "Trends in Middle East Climate Extreme Indices from 1950 to 2003." *Journal of Geophysical Research Atmospheres* 110 (22): 1–12. <https://doi.org/10.1029/2005JD006181>.
- Zheng, Huang, Shaofei Kong, Xinli Xing, Yao Mao, Tianpeng Hu, Yang Ding, Gang Li, Dantong Liu, Shuanglin Li, and Shihua Qi. 2018. "Monitoring of Volatile Organic Compounds (VOCs) from an Oil and Gas Station in Northwest China for 1 Year." *Atmospheric Chemistry and Physics* 18 (7): 4567–95. <https://doi.org/10.5194/acp-18-4567-2018>.

Justin Shenolikar

🏠 Töpferweg 2, Mainz, Germany, 55130

✉️ justin.shenolikar@mpic.de

📞 +49 162 921 2723

Nationality: British citizen



Education

2016-present PhD Candidate in atmospheric chemistry in AG-Crowley
Max-Planck-Institut für Chemie, Mainz, Germany

- PhD candidate in the field of atmospheric chemistry responsible for the use, maintenance and improvements of built-in-house thermal dissociation Cavity Ringdown (TD-CRD) system for measurements of atmospheric reactive nitrogen trace gases including NO₂, NO₃, N₂O₅ and organic nitrates.
- Operation of instrument deployed into remote environments, including first-of-its-kind project onboard a ship around the Arabian Peninsula and eastern Mediterranean, leading to publications on halogen activation (Eger *et al.*, 2019) and net ozone formation in the Persian Gulf (Tadic *et al.*, 2019).
- Use of instrument in large-scale chamber experiments for studying the reaction between radicals and organic gases, with kinetic modelling results published (Dewald *et al.*, 2020) and further publications in preparation.
- Data analysis of complex, interconnected chemical systems with Origin and designing and running model simulations of data through FACSIMILE software.
- Worked with scientists from around the world on large-scale atmospheric science research projects requiring international coordination and networking skills.
- Taught analytical chemistry techniques and supervised practical lab courses for Bachelor students at Johannes Gutenberg University, 2018.
- Presented data to public in a poster during the European Geosciences Union 2019 annual general meeting in Vienna, Austria.

PhD Representative Elected representative to the PhD students of the Max Planck Institute for Chemistry, 2017. Reelected 2018, serving two consecutive 1-year terms

- Duties included planning and holding scientific seminars, organization of social events for students, arranging regular sports matches and other non-academic activities and managing a budget
- Organized and hosted annual *Paul Crutzen Day* event, a daylong scientific seminar for PhD students to present their data and other career-relevant skills in talks and poster sessions. Event planning involved signing up participants, delegation of tasks, invitation of an external keynote speaker and opening and chairing the event.
- Attended the PhDNet annual general meeting of representatives from each of the Max Planck Institutes across Germany where contracts, post-PhD employment opportunities, workloads and more were discussed.

2014-15 & 2016 Erasmus & research-student placement

Dr. Matthew Johnson, Copenhagen University

- Placement position focused on study and lectures related to atmospheric chemistry, air pollution and climate change and assisting active research projects with sample analysis related to ambient air quality and industrial emissions.
- Following academic Erasmus+ placement, employed to work as a research assistant at Copenhagen University in the summer of 2015 and again in 2016.
- Performed analysis of VOC samples from academic sources on behalf of Shandong University, leading to a publication on reaction kinetics (Zhang *et al.*, 2017) and commercial sources from Danish company Infuser, used in tailoring solutions for emissions and air quality by companies in Europe and Asia.
- Designed and ran a research project on the chemical origin of line-dried laundry (Pugliese *et al.*, 2020), later published in the New York Times.
- Assisted supervision of Bachelor student research projects at Copenhagen University, 2016.

2011-16

MSci Chemistry (Honours of the Second Class, division 1)

University of Glasgow, Glasgow, UK

- Master's thesis project focused on experiments related to the chemical origins of life on Earth.
- Use of analytical chemistry techniques including NMR, GC/MS, HPLC and LC/MS to identify liquid-phase organic products.
- Private tutoring of SQA higher and advanced higher level chemistry students in Glasgow.

Skills and Interests

Language skills English (Mother Tongue), Spanish (Intermediate), German (Basic)

Charity work with Raleigh International in Costa Rica and Nicaragua

- Expedition in Summer of 2011 with projects divided into three sections: Community, Environmental and Trek
- Community project in Nicaragua: worked as part of a team of volunteers and locals to build a running-water system for a remote village in rural Nicaragua.
- Environmental Project in Costa Rica: Assisted rangers in *La Cangreja* National Park and Playa Hermosa protected coastline in the care of new-born sea turtles and construction of new walking paths through forested regions to promote sustainable tourism.

Software

- Use of various data acquisition software for commercial GC/MS and HPLC instruments.
- Knowledge of LabView software use data acquisition purposes.
- Modelling software including FACSIMILE and PhreeqC.
- Data analysis software including Origin and Igor Pro.
- Proficient in use of Microsoft Word, Excel, and Powerpoint.

References

Available on request